

UNIVERSITÀ DI PADOVA



FACOLTÀ DI INGEGNERIA

Dipartimento di Ingegneria dell'Informazione

Scuola di Dottorato di Ricerca in Ingegneria dell'Informazione

Indirizzo: Bioingegneria

Ciclo XXI

QUANTIFICATION OF CEREBRAL HEMODYNAMIC FROM  
DYNAMIC SUSCEPTIBILITY CONTRAST - MAGNETIC RESONANCE IMAGING  
TECHNIQUE

Dottorando: ing. Denis Peruzzo

Supervisore: Ch.mo Prof. Claudio Cobelli

Co-Supervisore: Dott. ing. Alessandra Bertoldo

Direttore della Scuola: Ch.mo Prof. Matteo Bertocco

Gennaio 2009



UNIVERSITY OF PADUA



FACULTY OF ENGINEERING

Department of Information Engineering

Ph.D. School on Information Engineering  
Section of Bioengineering

21<sup>st</sup> cycle

QUANTIFICATION OF CEREBRAL HEMODYNAMIC FROM  
DYNAMIC SUSCEPTIBILITY CONTRAST - MAGNETIC RESONANCE IMAGING  
TECHNIQUE

Ph. D. student: Dr. Denis Peruzzo

Supervisor: Prof. Claudio Cobelli, Ph. D.  
Co-Supervisor: Dr. Alessandra Bertoldo, Ph. D.

School Head: Prof. Matteo Bertocco, Ph. D.

January 2009



*Measure what is measurable, and make measurable what is not so.*  
Galileo Galilei



# Prefazione

La *Risonanza Magnetica* (RM) è una tecnica di imaging medico che viene utilizzata in radiologia sia per le strutture anatomiche sia per le funzionalità del corpo umano. Grazie all'elevata risoluzione spaziale di cui dispone e al notevole livello di contrasto tra le differenti tipologie di tessuto, la RM è diventata lo strumento per la generazione di immagini anatomiche più diffuso. Negli ultimi decenni, la RM è stata oggetto di studi approfonditi e notevoli sviluppi, tanto che oggi sono disponibili macchinari ad elevate prestazioni e un ampio numero di protocolli d'acquisizione differenti. Di conseguenza, la RM ha cominciato a essere utilizzata anche per studi funzionali. Attualmente, la *Tomografia ad Emissione di Positroni* (PET) è la tecnica di riferimento per gli studi funzionali, ma la RM sta diventando una valida alternativa grazie alla sua maggiore risoluzione spaziale, alla sua maggiore diffusione e al fatto che non utilizza radiazioni ionizzanti nocive.

Attualmente, la risonanza magnetica di perfusione che ricorre all'uso di un agente di contrasto esogeno, come il gadolinio, è la tecnica più interessante per lo studio quantitativo dell'emodinamica. La *Dynamic Susceptibility Contrast - Magnetic Resonance Imaging* (DSC-MRI) permette di ricavare importanti parametri emodinamici che ricoprono un ruolo chiave nello studio di svariate patologie, quali la neoplasia cerebrale, l'ischemia, l'infarto, l'epilessia, la demenza e la schizofrenia.

Per caratterizzare il segnale ottenuto con la DSC-MRI viene generalmente utilizzato un modello basato sulla teoria dei traccianti non diffusibili (la *teoria della diluizione*). Basandosi sulle ipotesi che il tracciante sia intravascolare, che la barriera emato-encefalica sia intatta e che non ci sia ricircolo di tracciante, il modello permette di ricavare il *Volume Ematico Cerebrale* (CBV), il *Flusso Ematico Cerebrale* (CBF) e il *Tempo Medio di Transito* (MTT).

Il passaggio chiave per la stima di tali parametri è la quantificazione della funzione residuo, che presenta tuttavia alcuni problemi. In questa tesi saranno trattati i più importanti tra essi:

- la necessità di ricavare la *Funzione d'Ingresso Arteriale* (AIF), che rappresenta l'andamento nel tempo della concentrazione di tracciante nei vasi che irrorano il tessuto;
- la necessità di ricorrere ad un'operazione di deconvoluzione per ricavare la funzione residuo.

La AIF è solitamente ricavata selezionando alcuni pixel che rappresentano i vasi arteriali principali direttamente sulle immagini di RM. La selezione dei pixel può essere fatta sia manualmente da un radiologo sia tramite un algoritmo di selezione automatica. Recentemente sono stati proposti numerosi algoritmi per svolgere tale compito, ma non si è ancora raggiunto uno standard. In questo lavoro il problema relativo all'estrazione della AIF viene discusso approfonditamente. Si propone un nuovo metodo per la selezione dei pixel arteriali che combina le informazioni anatomiche con l'analisi del segnale DSC-MRI. L'algoritmo è testato su dati simulati e confrontato con i più interessanti algoritmi proposti in letteratura. Successivamente viene applicato anche su dati reali e confrontato con la AIF ottenuta tramite selezione manuale al fine di valutare l'impatto che la scelta della AIF ha sulla stima dei parametri CBF, CBV e MTT. Il metodo proposto ha dimostrato di essere in grado di ricostruire la AIF originale, fornendo sia stime accurate che intervalli di confidenza molto stretti. Inoltre ha dimostrato di essere robusto nei confronti di diversi livelli di rumorosità nei dati, contribuendo quindi all'aumento della riproducibilità nello studio dell'emodinamica cerebrale. Infine, le AIF ottenute tramite il nuovo algoritmo hanno permesso di effettuare diagnosi più accurate rispetto a quelle ottenute tramite selezione manuale.

Un altro passaggio critico per l'analisi dei dati DSC-MRI è rappresentato dall'operazione di deconvoluzione necessaria per la stima della funzione residuo. I problemi in quest'ambito sono legati sia ai problemi intrinseci della deconvoluzione (ad esempio il fatto che è un problema matematico mal condizionato e mal posto), sia ad aspetti dovuti al fatto che si tratta di un sistema fisiologico (ad esempio vincoli di non negatività). Inoltre, la possibile presenza di dispersione e ritardo nella AIF costituisce un'altra importante fonte di errore per la stima della funzione residuo. Ad oggi, i metodi di deconvoluzione più diffusi sono la *Singular Value Decomposition* (SVD) e la *block-Circulant Singular Value Decomposition* (cSVD). La SVD è storicamente il primo metodo proposto per lo studio dei dati DSC-MRI e rappresenta ancora il metodo di riferimento in quest'ambito. La cSVD è invece la naturale evoluzione della SVD, proposta per eliminare i problemi dovuti al ritardo nella AIF che caratterizzano la SVD. Numerosi metodi sono stati proposti negli anni in letteratura. Tra i vari, citiamo la *Nonlinear Stochastic Regularization* (NSR), che permette di tener conto sia dei vincoli di non negatività sia della regolarità della funzione residuo.

In questo lavoro si presenta un nuovo metodo di deconvoluzione. La *Population Deconvolution* (PD) che analizza contemporaneamente un ampio numero di voxel simili sfruttando un approccio di popolazione, quindi migliorando la qualità dei dati utilizzati per l'operazione di deconvoluzione. Il metodo PD è stato validato su dati simulati e confrontato sia con la SVD che con la cSVD. PD riesce a ricostruire funzioni residuo che risultato credibili e fisiologiche in quanto presentano oscillazioni poco ampie e più smorzate rispetto a quelle presenti nelle funzioni residuo ottenuto con la SVD e la cSVD. PD permette inoltre di ricavare stime accurate di CBF, sia in presenza che in assenza di dispersione nella AIF, fornendo risultati migliori rispetto alla SVD e alla cSVD. PD, SVD e cSVD sono stati inoltre utilizzati per l'analisi di dati reali e sono stati confrontati anche con NSR. Le mappe di CBF e MTT ottenute tramite PD presentano un livello di contrasto migliore rispetto a quelle ottenute con SVD e cSVD, enfatizzando maggiormente le aree caratterizzate da un diverso flusso

ematico. Anche le mappe ottenute tramite NSR presentano un alto livello di contrasto, risultando però più rumorose rispetto a quelle ottenute tramite PD. Si è inoltre introdotto un nuovo indicatore fisiologico, l'*indice di lateralità*, che permette di fornire una rappresentazione grafica e di integrare le informazioni contenute nelle mappe di CBF e MTT. NSR fornisce valori di lateralità molto ampi, evidenziando notevolmente le zone caratterizzate da diversi flussi ematici. Tuttavia, l'individuazione delle aree colpite dalla patologia è resa difficoltosa dal fatto che anche le aree sane sono caratterizzate da ampi indici di lateralità. L'opposto si verifica considerando gli indici di lateralità ottenuti tramite SVD o cSVD; in questo caso l'individuazione delle aree malate è resa difficile dal fatto che gli indici forniti sono molto piccoli. PD invece permette di ottenere degli indici di lateralità che evidenziano le aree malate più di quanto non facciano SVD o cSVD, ma con valori meno ampi rispetto a NSR, soprattutto nelle regioni sane. In questo modo, PD permette di ottenere diagnosi più accurate.

Infine, in questo lavoro viene presentato un ulteriore promettente metodo di deconvoluzione, chiamato DNP. A differenza di PD, che deve essere utilizzato per l'analisi di un elevato numero di voxel a causa dell'approccio di popolazione, DNP è un metodo di deconvoluzione di singoli voxel, quindi può essere applicato anche all'analisi di regioni contenenti pochi voxel. L'aspetto più interessante del metodo DNP è che permette di tenere conto sia del fatto che la funzione residuo deve essere continua, sia del fatto che un sistema fisiologico è, naturalmente, BIBO stabile. Inoltre, tale metodo permette di stimare anche il ritardo normalmente presente nella AIF, migliorando la precisione nella stima della funzione residuo. Dato che il metodo è ancora in fase di sviluppo, nella tesi sono riportati solo dei risultati preliminari. Tali risultati mostrano che DNP è in grado di fornire stime di CBF più accurate rispetto a SVD e cSVD, sia in presenza che in assenza di dispersione e ritardo. Inoltre, le funzioni residuo ottenute tramite DNP non presentano valori negativi e le oscillazioni non fisiologiche generalmente presenti nei risultati forniti da SVD e cSVD. D'altro canto, DNP presenta ancora dei problemi, il più importante dei quali è il calcolo del ritardo nella AIF, poco preciso e generalmente sovrastimato, soprattutto in presenza di dispersione. Inoltre, DNP non riesce ancora a caratterizzare bene l'andamento della funzione residuo. Un altro problema non ancora risolto è legato alla stima degli iper-parametri. Infatti questo aspetto richiede alcuni passaggi non lineari che incrementano notevolmente i tempi di calcolo necessari all'algoritmo.

In conclusione, anche se presenta ancora numerosi limiti nella fase di analisi del segnale, la DSC-MRI sta diventando uno strumento molto importante sia nella pratica clinica che nella fase di ricerca medica. Gli algoritmi di selezione della AIF e di deconvoluzione che sono stati proposti in questa tesi permettono di migliorare l'informazione clinica e scientifica che si può ottenere dall'analisi dei dati ottenuti tramite DSC-MRI.



# Preface

*Magnetic Resonance Imaging* (MRI) is a medical imaging technique used in radiology to visualize the anatomical structures and the functions of the body. Thanks to its fine spatial resolution and to the great contrast between the different soft tissues, MRI has become the most used method for the anatomical image generation. During the last two decades, MRI was widely studied and developed, so high performance devices and new analysis protocols are now available. As an outcome, MR can now be used also to perform functional analysis. Currently, the *Positron Emission Tomography* (PET) is the gold standard technique in functional imaging. However, MRI is becoming a valid alternative to PET in functional analysis because of its greater spatial resolution, its wide diffusion and the absence of ionizing radiations.

Currently, perfusion magnetic resonance using an exogenous tracer, such as gadolinium, is the most interesting technique for the quantitative study of the hemodynamic. The *Dynamic Susceptibility Contrast - Magnetic Resonance Imaging* (DSC-MRI) allows to quantify important hemodynamic parameters that play an important role in the study of several pathologies, such as cerebral neoplasia, ischemia or infarction, epilepsy, dementia and schizophrenia.

The commonly used model for describing the DSC-MRI signal is based on the non diffusible tracer theory, also called *dilution theory*. It assumes that the tracer remains intravascular, the blood-brain-barrier (BBB) is intact and there is no tracer recirculation. Under these assumptions, the model allows to estimate the *Cerebral Blood Volume* (CBV), the *Cerebral Blood Flow* (CBF) and the *Mean Transit Time* (MTT).

The most crucial step in the DSC-MRI image quantification is the residue function estimate that presents some limitations. The most important ones, that are considered in this work, are:

- the necessity to know the *Arterial Input Function* (AIF), which is the concentration time curve in the vessels feeding the tissue;
- the assessment of the residue function requiring to perform a deconvolution operation, which is a well-known difficult mathematical problem.

Currently, AIF is measured directly on the MR images, by selecting a small number of pixels containing one of the principal arterial vessels. The pixel selection can be made either manually, by a physician, or by means of automatic

algorithms. During the past years, several automatic and semiautomatic methods for the AIF extraction have been proposed, but a standard has not been achieved, yet. In this work, the AIF selection and deconvolution problems are discussed in depth. A new selection method, combining anatomical information with MR-signal analysis is presented. It is compared to the other AIF selection algorithms proposed in literature on a simulated data set. Then, a comparison with the manual selection method on a clinical data set is performed and the AIF selection impact on CBF, CBV and MTT estimate is investigated. The proposed method has been shown to reliably reconstruct the true AIF, providing accurate estimates and very narrow confidence bands. Moreover, it is robust against the different noise levels, thus increasing the reproducibility level in DSC-MRI image quantification. Furthermore, AIFs obtained with the new method have been shown to lead to a more accurate diagnosis than the manual ones.

Another critical step in DSC-MRI data analysis is the deconvolution operation, that allows to estimate the residue function. Problems in this step are due to the deconvolution intrinsic problems (e.g. the ill-posedness and the ill-conditioning) and to the physiological system specific problems (e.g. non negative constrains). Moreover, another important source of error in the residue function estimate is the possible presence of *delay* and/or *dispersion* in AIF. Currently, the most used deconvolution methods are the *Singular Value Decomposition* (SVD) and the *block-Circulant Singular Value Decomposition* (cSVD). SVD is historically the first and the most important deconvolution method proposed in the DSC-MRI context and it is currently the reference method. The cSVD method is the natural evolution of SVD and it has been proposed to overcome the problem of delay in the AIF. Several other deconvolution methods have been proposed in literature. Among them all, we focus on a recently proposed method, the *Nonlinear Stochastic Regularization* (NSR), that accounts for both the smoothness and the non-negativity constraint of the residue function.

In this work, a new deconvolution method is presented. The *Population Deconvolution* (PD) method exploits a population approach to analyse a large set of similar voxels at the same time, thus improving the data quality in the deconvolution operation. PD has been validated on simulated data and compared to SVD and cSVD. PD can reconstruct reliable and physiological residue functions. The residue functions obtained using PD present very small and damped oscillations compared to SVD and cSVD ones. Furthermore, PD has been shown to accurately estimate the CBF both in presence and in absence of dispersion, providing better results than SVD and cSVD. SVD, cSVD and PD have been compared also to NSR on clinical data. CBF and MTT maps provided by PD present a greater contrast level than SVD and cSVD ones, as they emphasize the flow and transit time differences. Also NSR maps are extremely contrasted, but they appear noisier than the PD ones. A new physiological indicator, the *Laterality Index*, has also been introduced. It provides a graphical representation of the CBF and MTT map information, integrating all the information provided by the different parameters. NSR provides very large laterality indices, thus emphasizing the disease affected regions. Nevertheless, the detection of the pathological areas is not easy because of the large LI variability also in the healthy regions. On the contrary, SVD and cSVD laterality indices make the disease detection difficult because they do not emphasize the pathological

areas. PD meets the need to underline the pathologic areas without showing false positive results, providing larger LIs than the SVD and cSVD ones, but smaller than the NSR ones. Therefore, PD has been shown to lead to a more accurate diagnosis than the other methods.

Finally, another promising deconvolution method, called DNP, is presented. Differently from PD, that has to be applied to large data sets because of its population approach, DNP is a voxel based method, thus it can be applied also to a small number of voxels. The most interesting DNP feature is that it accounts for both the residue function continuity and the system BIBO-stability. Moreover, it can estimate the AIF delay, thus improving the accuracy in the  $R(t)$  estimation. Since it is still under development, only the DNP preliminary results are presented in this work. DNP has been shown to provide more accurate CBF estimates than SVD and cSVD, both in presence and absence of delay and dispersion. Furthermore, the DNP reconstructed residue functions show neither the negative values nor the spurious oscillations usually present in the SVD and cSVD ones. However, DNP bears some limitations too. Currently, the most important DNP limitation is the delay estimation. DNP usually overestimates the delay, above all in presence of dispersion, thus providing a non accurate characterization of the residue function. Another DNP problem is that the hyper-parameter quantification requires a non-linear step, which increases the computation time of the algorithm.

In conclusion, although they present some limitations in the post-processing analysis, DSC-MRI techniques are becoming an important tool in medical research and in clinical practice. The development of a fully automatic algorithm for the AIF selection and of a deconvolution method based on a population approach would improve the clinical and scientific information provided by DSC-MRI analysis.



# List of Abbreviations

Abbreviation	Description
AIF	Arterial Input Function
BIBO	Bounded-Input Bounded-Output
CBF	Cerebral Blood Flow
CBV	Cerebral Blood Volume
cSVD	Block-Circulant SVD
DSC-MRI	Dynamic Susceptibility Contrast-MRI
DNP	De Nicolao & Pillonetto deconvolution method
EPI	Echo-Planar Imaging
GE	Gradient Echo
LI	Laterality Indices
ML	Maximum Likelihood
MR	Magnetic Resonance
MRI	Magnetic Resonance Imaging
MTT	Mean Transit Time
NSR	Nonlinear Stochastic Regularization
PD	Population Deconvolution method
RKHS	Reproducing Kernel Hilbert Space
SD	Standard Deviation
SE	Spin Echo
SNR	Signal to Noise Ratio
SVD	Singular Value Decomposition

Table 1: Abbreviation Table



# Contents

<b>1</b>	<b>Introduction</b>	<b>1</b>
<b>2</b>	<b>Dynamic Susceptibility Contrast -MRI: Protocol and Theory</b>	<b>5</b>
2.1	Experiment Protocol and Acquisition Sequence . . . . .	5
2.2	Dilution Theory . . . . .	6
2.3	Practice . . . . .	10
2.3.1	Paradigm . . . . .	10
2.3.2	From signal to concentration . . . . .	11
2.3.3	Recirculation . . . . .	12
2.3.4	Model and Paradigm limitations . . . . .	12
<b>3</b>	<b>Dynamic Susceptibility Contrast -MRI: State of the Art and Open Issues</b>	<b>15</b>
3.1	Arterial Input Function . . . . .	15
3.1.1	AIF problems . . . . .	16
3.1.2	Manual Selection . . . . .	17
3.1.3	Automatic Selection . . . . .	18
3.2	Deconvolution . . . . .	20
3.2.1	Singular Value Decomposition . . . . .	23
3.2.2	Block-Circulant Singular Value Decomposition . . . . .	25
3.2.3	Non linear Stochastic Regularization . . . . .	27
<b>4</b>	<b>The Arterial Input Function Selection</b>	<b>31</b>
4.1	Theory . . . . .	31
4.2	Simulation: Set up . . . . .	33
4.3	Simulation: Results . . . . .	39
4.3.1	Arterial Input Function reconstruction . . . . .	39
4.3.2	Impact of the Arterial Input Function on estimating the hemodynamic parameters . . . . .	46

4.4	Simulation: Discussion . . . . .	50
4.5	Clinical data: Experimental set up and subjects . . . . .	52
4.6	Clinical Data: Results . . . . .	54
4.7	Clinical Data: Discussion . . . . .	69
<b>5</b>	<b>Dynamic Susceptibility Contrast -MRI: Population Deconvolution</b>	<b>71</b>
5.1	Theory . . . . .	71
5.2	Simulation: Set up . . . . .	75
5.3	Simulation: Results . . . . .	77
5.3.1	Residue Function Reconstruction . . . . .	77
5.3.2	Impact on Cerebral Blood Flow Estimates . . . . .	77
5.4	Simulation: Discussion . . . . .	84
5.5	Clinical Data: Analysis . . . . .	86
5.6	Clinical Data: Results . . . . .	88
5.6.1	Cerebral Blood Volume maps . . . . .	88
5.6.2	Cerebral Blood Flow maps . . . . .	92
5.6.3	Mean Transit Time maps . . . . .	105
5.6.4	Laterality Indices . . . . .	118
5.7	Clinical Data: Discussion . . . . .	124
<b>6</b>	<b>Dynamic Susceptibility Contrast -MRI: a New Kernel-Based Deconvolution Approach</b>	<b>127</b>
6.1	Theory . . . . .	127
6.2	Simulation: Set up . . . . .	130
6.3	Simulation: Results . . . . .	131
6.4	Assessment on Clinical Data . . . . .	140
6.4.1	Data Set & Analysis . . . . .	140
6.4.2	Results . . . . .	140
6.5	Discussion . . . . .	143
<b>7</b>	<b>Conclusions</b>	<b>145</b>





# Chapter 1

## Introduction

*Magnetic Resonance imaging* (MRI) is a medical imaging technique used in radiology to visualize the anatomical structures and the functions of the body. Thanks to its fine spatial resolution and to the great contrast level between the different soft tissues, MRI has become the most used method for anatomical image generation. During the last two decades, MRI was widely studied and developed. Modern *magnetic resonance* (MR) scanners are equipped with a high-field magnet, high performance radio frequency amplifiers and they have components which generate high intensity gradients. Moreover, a deeper knowledge of the MR signal physics principles allowed to develop new analysis protocols. As an outcome of this fast development, MR can now be used also to perform functional analysis. Currently, the *Positron Emission Tomography* (PET) is the gold standard technique in functional imaging. However, MRI has a greater spatial resolution than PET, it is widely used in medical centres and it does not use ionizing radiations. For these reasons, MRI is becoming a valid alternative to PET in functional analysis.

Currently, the perfusion magnetic resonance using an exogenous tracer, such as gadolinium, is the most interesting technique for the quantitative hemodynamic study. Cerebral hemodynamic plays an important role in the study of several pathologies, such as cerebral neoplasia, ischemia or infarction, epilepsy, dementia and schizophrenia. *Dynamic Susceptibility Contrast - Magnetic Resonance Imaging* (DSC-MRI) allows to quantify important hemodynamic parameters using a non radioactive contrast agent and without requiring an arterial sampling.

DSC-MRI measures the  $T_2^*$  variations due to the tracer passage through the brain, then it analyses the tracer bolus time course to derive the perfusion parameters. The commonly used model for describing the DSC-MRI signal is based on the non diffusible tracer theory, also called *dilution theory*. It assumes that the tracer remains intravascular, the blood-brain-barrier (BBB) is intact and there is no tracer recirculation. Under these assumptions, the model allows to reconstruct the *residue function*, i.e. the fraction of contrast agent remaining inside the tissue at time  $t$ . It is therefore possible to estimate the *Cerebral Blood Volume* (CBV), the *Cerebral Blood Flow* (CBF) and the *Mean Transit Time* (MTT).

The most crucial step in the DSC-MRI image quantification is the residue function estimate. Its estimation requires to perform a deconvolution operation, which is a well-known difficult mathematical problem. Troubles in this step are due to the deconvolution intrinsic problems (e.g. the ill-posedness and the ill-conditioning) and to the physiological system specific problems (e.g. non negative constrains). Several methods have been proposed in literature to estimate the residue function in the DSC-MRI context, but no standard has been achieved yet.

Another important issue in DSC-MRI is that the deconvolution operation requires the knowledge of the *Arterial Input Function* (AIF), which is the concentration time curve in the vessels feeding the tissue. AIF can be measured directly by arterial sampling, but its invasiveness has promoted the development of alternative approaches. Currently, AIF is measured directly on the MR images, by selecting a small number of pixels containing one of the principal arterial vessels. The pixel selection can be made either manually, by a physician, or by means of automatic algorithms. During the past years, the need of a fully automatic method has emerged in order to avoid both the need of trained personnel and the subjectivity in the arterial pixel choice. Such AIF is also called *global AIF*, since a unique AIF is used to analyse the whole brain tissue. However, different brain sites have different feeding vessels, thus they can present different AIFs. Therefore, AIF should be measured for each brain site. This solution is called *local AIF*. Several attempts to measure a local AIF have been proposed, but they have to face many other problems, such as the partial volume effect. As for the deconvolution operation, several methods have been proposed in literature to estimate the AIF in the DSC-MRI images, but no standard has been achieved yet.

In this work, the above mentioned limitations are considered. An arterial pixel selection method and two deconvolution approaches will be proposed to overcome the DSC-MRI open issues.

The outline of the thesis is the following one.

In *Chapter 2* the DSC-MRI acquisition experiment using gadolinium as contrast agent is presented. Contrast agent effects and experimental protocol are explained. Then, the DSC-MRI signal model is explained, focussing on its assumptions and problems, such as the recirculation presence and the proportionality constant value. Finally, the dilution theory is presented and the CBF, CBV and MTT quantification procedure is explained.

In *Chapter 3* the AIF selection and deconvolution problems are discussed in depth. Firstly, the problems due to the AIF selection are explained and the manual selection method expounded. The AIF selection methods proposed in literature are also briefly reviewed. Then, the deconvolution problem is faced, focussing on its mathematical formulation. The singular value decomposition (SVD) and the block-circulant SVD (cSVD) are currently the most used deconvolution method in DSC-MRI. They are described with particular attention to their performances and limitations. A non linear stochastic regularization (NSR) algorithm, developed in the University of Padua Bioengineer Group, is also presented.

*Chapter 4* is dedicated to the AIF selection. Firstly, a new selection method, combining anatomical information with MR-signal analysis is presented. Sec-

only, it is compared to the other AIF selection algorithms proposed in literature on a simulated data set. Then, a comparison with the manual selection method on a clinical data set is performed and the AIF selection impact on CBF, CBV and MTT estimate is investigated.

In *Chapter 5* a *Population Deconvolution* (PD) method is presented. It exploits a population approach to improve the data quality in the deconvolution operation. PD is validated on simulated data and compared to SVD and cSVD. Then, SVD, cSVD, NSR and PD are compared on clinical data, with particular attention to the impact on the clinical diagnosis.

In *Chapter 6* a new pixel based deconvolution algorithm is presented. The original method has been proposed by De Nicolao & Pillonetto (DNP). The DNP application on DSC-MRI context is presented. SVD, cSVD and DNP are assessed and compared on simulated data, focussing on DNP merits and defects. SVD, cSVD and DNP are assessed and briefly compared on clinical data.



## Chapter 2

# Dynamic Susceptibility Contrast -MRI: Protocol and Theory

This chapter presents the DSC-MRI protocol and the acquisition sequences. Afterwards, the dilution theory (i.e. the model employed) is discussed, with particular attention to the model assumptions. In the end, the main steps of the standard paradigm used in DSC-MRI image quantification are presented, pointing out both the recirculation problem and the limitations of the model and quantification paradigm.

### 2.1 Experiment Protocol and Acquisition Sequence

DSC-MRI is a first-pass bolus tracking technique, which consists of the injection of a bolus of high-concentrated contrast agent and of the acquisition of a sequence of MR-images to observe the signal changes caused by the bolus passage through the brain.

Figure 2.1 shows a typical acquisition protocol: a bolus of contrast agent (i.e. Gadolinium at 0.1-0.3 mmol per kg body weight) is delivered to the patient by a MRI-compatible power injector at a 5-10 ml sec<sup>-1</sup> rate via an antecubital vein. A saline flush of 0.2-0.3 ml kg<sup>-1</sup> follows the bolus injection. Since bolus transit time is only few seconds, rapid imaging techniques are necessary to obtain sequential images in the wash-in and wash-out periods. Finally, the contrast agent was eliminated by the hepatic biliary system. Typically paramagnetic tracers are employed, such as gadolinium chelate. The paramagnetic solution causes the presence of inhomogeneities in the applied magnetic field, hence it de-phases the transverse magnetization in the surrounding tissue. Thus, it affects both  $T_2$  and  $T_2^*$  relaxation times.  $T_1$ ,  $T_2$  and  $T_2^*$  are parameters which characterise the MR-signal and they are properties of the tissue, i.e. they are

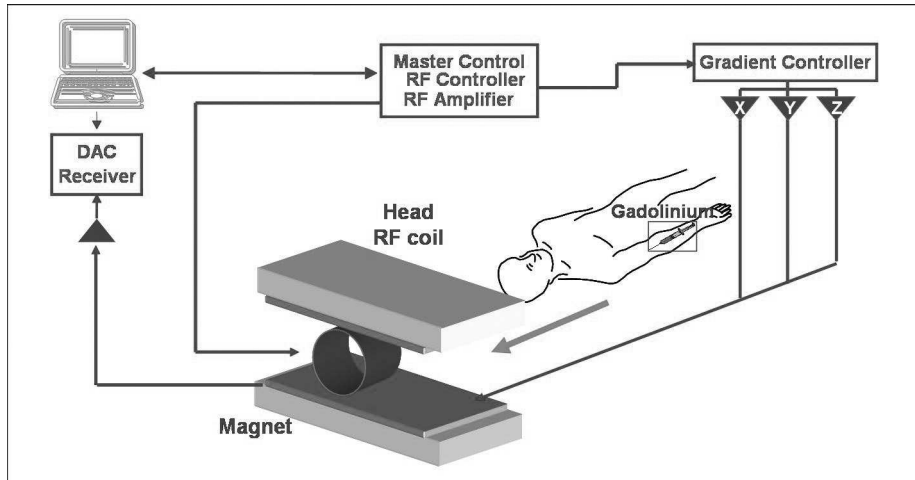


Figure 2.1: A typical acquisition setting.

fixed for a specific tissue at a given magnetic field strength.  $T_1$  is the *longitudinal relaxation time*, it refers to the time the spins take to realign along the longitudinal axis after the stimulation.  $T_2$  and  $T_2^*$  are the *transverse relaxation time*.  $T_2$  depends primarily on the spin-spin interactions, while  $T_2^*$  depends on the external magnetic field too. DSC-MRI can be performed by using either *Spin Echo* (SE) or *Gradient Echo* (GE) sequences, which are sufficiently fast to track bolus injection [74]. It has been shown that  $T_2^*$ -weighted GE sequences are more sensitive to the agent passage than  $T_2$ -weighted SE ones [34]. It has also been shown that the GE relaxation is more sensitive to the vessels larger than  $\sim 20 \mu\text{m}$  in diameter. Therefore, the GE signal derives from tissues with both large vessels and microcirculatory contributions [10]. Differently, SE sequences are mostly influenced by the capillary bed [39]. Refocusing the signal from larger vessels, SE sequences also allow improve the image quality in particular brain regions, such as the temporal lobes and the frontal sinus. Nonetheless, GE is the sequence usually chosen because of the high sensitivity of  $T_2^*$  in DSC-MRI. Commonly, sequences used in DSC-MRI include fast GE imaging, GE-weighted Echo Planar Imaging (EPI), SE-weighted EPI, different forms of fast SE imaging, spiral variants of EPI and three dimensional volume acquisition. A typical protocol consists of a single shot GE sequence with TE varying from 40 to 60 ms and TR from 800 to 1200 ms with a magnetic field strength of 1.5T. Flip angles of 60-80 are chosen to maximize signal to noise ratios and minimize any  $T_1$  effect.

## 2.2 Dilution Theory

The model used to characterize the dynamic of the tracer which passes through a volume of interest (VOI) follows the principles of tracer kinetics [4, 95, 96] and it is based on the following assumptions:

1. the contrast agent is totally nondiffusible;
2. there is no recirculation of the contrast agent;
3. the Blood Brain Barrier (BBB) is intact, i.e. no tracer leakage can occur from the intravascular to the extra-vascular space;
4. the system is in steady state during the experiment. This means that the blood flow is assumed constant. As a consequence, DSC-MRI technique can be used to estimate either constant flows, or flows varying very slowly within the experiment duration. The latter can be quantified by a series of consecutive experiments;
5. the contrast agent dose must not appreciably perturb the system.

Under these assumptions, the model allows to describe the tissue concentration ( $C_{VOI}(t)$ ) of the contrast agent in a considered VOI at time t using the following functions

- the *transport function*  $h(t)$ : consider a unitary amplitude bolus of nondiffusible tracer given in the vessels feeding a VOI at time t=0;  $h(t)$  is the density probability function of the transit times of the individual tracer particles passing through the VOI at time t. When a generic input function  $C_{AIF}(t)$  is given instead of the bolus, the tracer concentration leaving the VOI at time t ( $C_V(t)$ ) is given by

$$C_V(t) = C_{AIF}(t) \otimes h(t) \quad (2.1)$$

$h(t)$  is a system characteristic, it depends on the flow and on the vascular structure of the VOI. It has the dimension 1/time and, when integrated over all time, the area is unitary and dimensionless

$$\int_0^{\infty} h(\tau) d\tau = 1 \quad (2.2)$$

- the *residue function*  $R(t)$ : it is defined as

$$R(t) = 1 - \int_0^t h(\tau) d\tau \quad (2.3)$$

It represents the tracer fraction present in the VOI at time t after the injection of a nondiffusible tracer bolus with unitary amplitude into the vessels feeding the VOI at time t=0.  $R(t)$  is a dimensionless, positive and decreasing function.  $R(0)=1$ , that means that at time t=0 the total bolus of contrast agent is ideally present in the VOI.  $R(t)$  and, consequently,  $h(t)$  completely describe the system; once they are known, the concentration curves of the tracer leaving and remaining in the VOI can be predicted for any given input function.

- the *Arterial Input Function* (AIF)  $C_{AIF}(t)$ : is the concentration of contrast agent in the vessels feeding the VOI at time t.

Considering the previously defined functions, the model allows to quantify three important parameters characterising the hemodynamic:

- the *Cerebral Blood Volume* (CBV);
- the *Cerebral Blood Flow* (CBF);
- the *Mean Transit Time* (MTT).

In case of intact BBB, the CBV is defined as the ratio between the blood volume contained in a considered VOI and the VOI volume. CBV can be determined from DSC-MRI images as the ratio between the area under the concentration time curve of the tracer in the VOI ( $C_{VOI}(t)$ ) and the area under the concentration time curve in the vessels feeding the VOI ( $C_{AIF}(t)$ )

$$CBV = \frac{k_H \int_0^\infty C_{VOI}(\tau) d\tau}{\rho \int_0^\infty C_{AIF}(\tau) d\tau} \quad (2.4)$$

where  $\rho$  represents the brain tissue density and  $k_h$  accounts for the difference in hematocrit between large and small vessels. Since only plasma volume is accessible to the tracer, CBV may be split into cerebral plasma volume (CPV) and red cell volume (CRCV) [5], i.e.  $CBV = CPV + CRCV$ . Defining hematocrit as the ratio  $H = 100 \cdot CRCV / CBV$  one can obtain  $CBV = CPV + H \cdot CBV = CPV / (1 - H)$ . Starting from the definition of CBV

$$CBV = \frac{\text{amount of blood in a VOI}}{\rho \cdot \text{area under the blood input curve}} \quad (2.5)$$

defining

$$k_h = (1 - H_{LV}) / (1 - H_{SV}) \quad (2.6)$$

and, as the tracer is only in the plasma

$$CBV = \frac{\text{amount of plasma in a VOI}}{\rho(1 - H_{SV})} \frac{1 - H_{LV}}{\text{area under the plasma input curve}} \quad (2.7)$$

one can obtain Eq. (2.4)

$$CBV = \frac{\int_0^\infty C_{VOI}(\tau) d\tau}{\rho(1 - H_{SV})} \frac{1 - H_{LV}}{\int_0^\infty C_{AIF}(\tau) d\tau} = \frac{k_H \int_0^\infty C_{VOI}(\tau) d\tau}{\rho \int_0^\infty C_{AIF}(\tau) d\tau} \quad (2.8)$$

Commonly, CBV units are millilitres per 100 grams of tissue ( $ml/100g$ ) and microliters per gram ( $\mu ml/g$ ).

Another parameter characterising the VOI is MTT. It is defined as the center of mass of the distribution  $h(t)$ , that is the probability density function of the tracer transit time through the VOI. In other words, MTT represents the

average time required for any given particle of tracer to pass through the VOI. It can be calculated as

$$MTT = \frac{\int_0^{\infty} t \times h(\tau) d\tau}{\int_0^{\infty} h(\tau) d\tau} \quad (2.9)$$

keeping in mind Eq. (2.2) and (2.3) one can obtain

$$MTT = \int_0^{\infty} t \times h(\tau) d\tau = \int_0^{\infty} R(\tau) d\tau \quad (2.10)$$

Applying the *Central Volume theorem* of indicator dilution theory [4, 50, 79] MTT can be computed also as the ration between CBV and CBF

$$MTT = \frac{CBV}{CBF} \quad (2.11)$$

MTT has dimension of time and it is usually expressed in seconds (s).

Considering the above given definition CBF can be related to the tracer concentration inside a given VOI, the residue function and the AIF

$$C_{VOI}(t) = \frac{\rho}{k_H} \cdot CBF(C_{AIF}(t) \otimes R(t)) = \frac{\rho}{k_H} \cdot CBF \int_0^t C_{AIF}(t) R(t - \tau) d\tau \quad (2.12)$$

Eq. (2.12) can also be derived from Eq. (2.11), (2.4) and (2.10)

$$CBF = \frac{CBV}{MTT} = \frac{k_H \int_0^{\infty} C_{VOI}(\tau) d\tau}{\rho \int_0^{\infty} C_{AIF}(\tau) d\tau \int_0^{\infty} R(\tau) d\tau} \quad (2.13)$$

from which

$$\int_0^{\infty} C_{VOI}(\tau) d\tau = \frac{\rho}{k_H} CBF \int_0^{\infty} C_{AIF}(\tau) \cdot \int_0^{\infty} R(\tau) d\tau \quad (2.14)$$

thus obtaining Eq. (2.12).

The convolution operator can be explained by considering AIF as a sum of consecutive ideal boluses. In the simplest case, i.e. if AIF is an ideal single impulse of amplitude  $C_{AIF}(0)$ , the tracer concentration within the VOI is the residue function multiplied by the proportionality factor given by the constants  $\frac{\rho}{k_H} \cdot CBF \cdot C_{AIF}(0)$ . In the generalized case the AIF can be divided into a series of impulses with different amplitudes. The tracer concentration is then given by the integral (i.e. the sum) of the responses to each AIF impulse.

Commonly, CBF units are millilitres per 100 grams of tissue per minute ( $ml/100g/min$ ) and microliters per gram per second ( $\mu ml/g/sec$ ).

## 2.3 Practice

### 2.3.1 Paradigm

Eq. (2.12) is the central equation in the standard approach to determine CBF by using a nondiffusible tracer. Starting from DSC-MRI signal time curves the tracer concentration time curves for tissue ( $C_{VOI}(t)$ ) and AIF ( $C_{AIF}(t)$ ) are to be computed [80]. The correct estimation of the arterial concentration is one of the most delicate steps and the commonly used approach will be discussed in the next chapter.

Given  $C_{VOI}(t)$  and  $C_{AIF}(t)$ , CBV can be easily obtained using Eq. (2.4). To calculate CBF, a deconvolution operation must be performed between  $C_{VOI}(t)$  and  $C_{AIF}(t)$  in order to obtain the product function  $R^*(t) = CBF \cdot R(t)$ . From  $R^*(t)$  CBF value can be easily obtained as  $CBF = R^*(0)$ , since  $R(0) = 1$ . The deconvolution operation is another important open issue in DSC-MRI image quantification, the principal methods proposed in literature will be exposed in the next chapter.

Once CBV and CBF values are computed, MTT can be derived using Eq. (2.11).

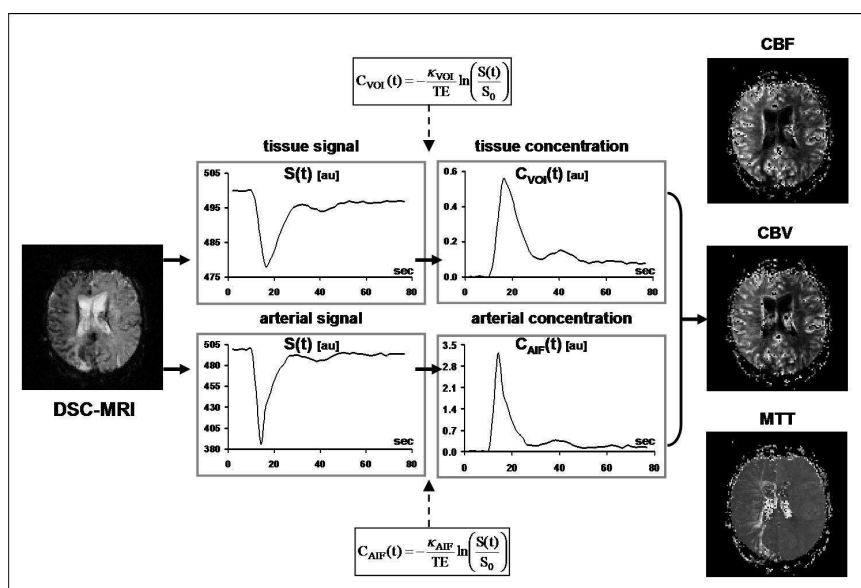


Figure 2.2: The quantification process of DSC-MRI image: from signal acquisition (left) to parametric mapping generation (right) of CBF, CBV, and MTT [9].

Figure 2.2 summarizes the principal steps in the DSC-MRI image quantification.

### 2.3.2 From signal to concentration

The contrast agent present within a VOI locally perturbs the total magnetic field, decreasing the relaxation time constants. Assuming a mono-exponential relaxation, the MR signal intensity in  $T_2$ - and  $T_2^*$ -weighted sequences are given by [60]

$$S = S_0(PD, TR, T_1)e^{-TE/T_2}$$

$$S = S_0(PD, TR, T_1)e^{-TE/T_2^*} \quad (2.15)$$

where  $S_0(PD, TR, T_1)$  includes terms depending on the longitudinal relaxation time ( $T_1$ ), the *repetition time* ( $TR$ ) and the proton density ( $PD$ ). The second term describes the loss of transverse relaxation determined by the *echo time* ( $TE$ ) and transverse relaxation time ( $T_2$  or  $T_2^*$ ). When passing through the vascular bed, the paramagnetic tracer generates a susceptibility difference between the intra- and the extra-vascular space, leading to field distortions and de-phasing. De-phasing increases the *relaxation rates*  $R_2 = \frac{1}{T_2}$  and  $R_2^* = \frac{1}{T_2^*}$  almost linearly in proportion to the intravascular blood concentration of the agent  $C_b$  [42]

$$R_2 = R_{20} + r_2 C_b$$

$$R_2^* = R_{20}^* + r_2^* C_b \quad (2.16)$$

where  $r_2$  and  $r_2^*$  are the transverse relaxivities which depend on the blood volume and vascular morphology [10, 39] and  $R_{20}$  and  $R_{20}^*$  are the intrinsic spin echo and gradient echo relaxation rates without the agent.

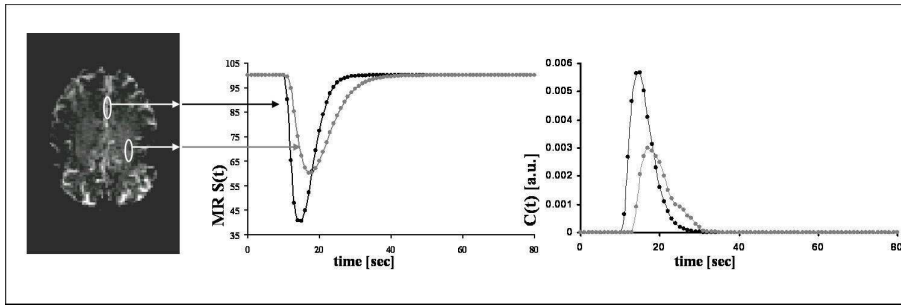


Figure 2.3: The effects of the passage of a paramagnetic agent bolus on MR signal.

The effects of the passage of a bolus of paramagnetic agent are schematically shown in figure 2.3, when the contrast agent enters the VOI, it increases the tracer concentration and decreases the MR signal.

Assuming a linear relationship between paramagnetic tracer concentration and the change in transverse relaxation rate, the kinetics of the tracer concentration inside the tissue can be related to the time curve of the observed MR signal intensity. If  $S_0$  and  $S(t)$  are the SE signal intensities in the baseline state (i.e. before the bolus arrival) and at a time  $t$  after the injection of agent, then concentration  $C_t(t)$  can be derived from Eq.(2.16) and (2.15), thus obtaining

$$C_t(t) = \frac{1}{r_2} [R_2(t) - R_2(0)] = -\frac{\kappa_{VOI}}{TE} \log \left[ \frac{S(t)}{S(0)} \right] \quad (2.17)$$

in which  $\kappa_{VOI}$  is an unknown proportionality constant of the VOI depending on the tissue, the contrast agent, the field strength, and the pulse sequence. A similar equation can be derived for the GE signal.

### 2.3.3 Recirculation

One of the assumptions of the dilution theory is the recirculation absence. However, this is not usually true in DSC-MRI experiments. The measured  $C_{VOI}(t)$  can include contributions from recirculation, which can be recognized as a second, smaller, concentration peak or an incomplete return to the baseline after the first pass. Therefore, the first pass tracer concentration profile needs to be separated from these undesired contributions.

A first approach consists in considering only data which include the initial peak, from the experiment beginning up until the time of recirculation, or the exceeding of a certain amplitude threshold. The intrinsic arbitrariness of the threshold choice and the partially overlapping between the first pass and the recirculation profile, making the bimodal pattern vague, are the main limitations of this method.

A more refined technique uses a *Gamma-variate* function to fit a portion of the  $C_{VOI}(t)$  data [7, 61, 62, 70]. The Gamma-variate general form is:

$$\Gamma(t; A, \alpha, \beta, t_0) = A \cdot (t - t_0)^\alpha \cdot e^{-\frac{t-t_0}{\beta}} \quad (2.18)$$

where  $A$ ,  $\alpha$ ,  $\beta$  and  $t_0$  are parameters to be estimated.

An example of Gamma-variate fit is presented in Figure 2.4 along with concentration samples from a typical VOI profile. In general, if recirculation is not accounted for, the calculated blood volume will be systematically larger and the other parameters will be similarly affected.

### 2.3.4 Model and Paradigm limitations

An important assumption in the conversion of the MR signal time course to a concentration time curve is that the *relaxivity* between the MR signal and the agent concentration (see Eq.(2.16) and (2.17)) is the same in different tissues [49]. Theoretical models show that the coupling constant can strongly depend on the choice of acquisition sequence and vascular morphology. For example, the extravascular relaxivity in a GE sequence is relatively independent from

the vessel size for vessels larger than 10-20  $\mu m$  in diameter [10], giving equal weighting to venules and arterioles and lesser weighting to capillaries. Thus, tissues with different vessels proportions may have different relaxivities.

The intravascular relaxivity is often assumed to be the molar relaxivity of the agent, but this is not perfectly true in a GE sequence. In GE sequences, the relaxation depends on specific geometrical properties. Besides, using intravascular sources for the AIF, one has to consider that the relaxivity is not the same as in the microvascular bed.

Using SE sequences, the extravascular signal is more sensitive to the non re-focusable signal from capillaries and has significantly reduced relaxivity for large vessels. In this situation, intravascular arterial sources are to be used for the AIF and the correct molar relaxivity of the agent must be used to convert the MR signal into concentration.

Another important assumption is the presence of an *intact Blood-Brain Barrier*. The presence of a damaged BBB results in tracer leakage to the extravascular space. This effect is often exploited to localize BBB breakdown in some diseases. However, this leads to a great confusion in vascular measurements, since the tracer has more direct access to the tissue and exerts stronger relaxation effects on  $T_1$ ,  $T_2$  and  $T_2^*$ . The most direct consequence is a decrease in the tissue  $T_1$  and  $T_2^*$ , thus altering the image contrast depending on the degree of  $T_1$  and  $T_2^*$  weighting. This leads to a systematic error in the DSC-MRI signal change.

The MR tracer model assumes that the relaxation rate is *linearly proportional* to the intravascular concentration of the agent (see Eq.(2.16)). Some recent studies suggest that in SE-based measurements this may not always be true: in the limit of high agent concentrations, the relaxation rate varies with concentration raise, thus introducing systematic errors for absolute quantification [39]. Theoretical models also suggest that the extravascular relaxivity from

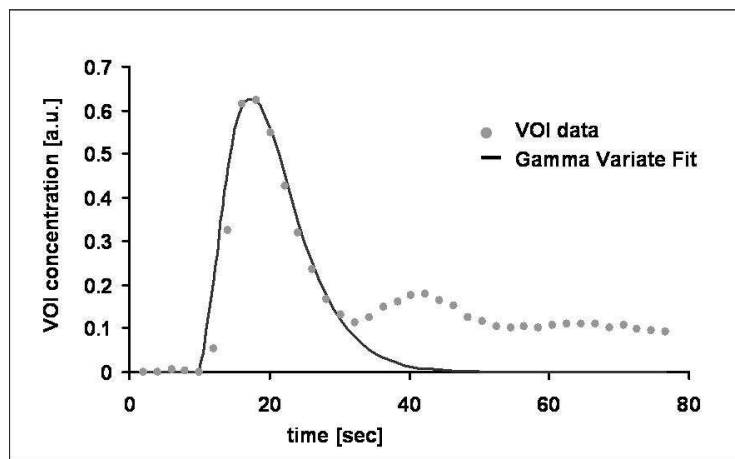


Figure 2.4: A typical tissue concentration time course (dot curve) in presence of tracer recirculation and the resulting gamma-variate fit (solid line).

capillaries in GE sequences may be nonlinear at low agent concentrations.

In general, a *recirculation correction* must be performed, if recirculation is not accounted for, the calculated CBV will be systematically larger. Likewise, also the other parameters will be affected. However, although the Gamma-variate function is the most commonly used model for the first pass of the concentration time curve, the model may not be valid in certain pathologies, such as in severe stroke lesions and tumours. Therefore, the use of Gamma-variate fitting can potentially introduce errors due to poor fitting. A better solution is to use the Gamma-variate fit strategy, which better performs with the type of available data.

*Absolute quantification* of CBF and CBV values is strongly dependent on the values of the constant  $k_{VOI}$ ,  $\rho$ ,  $H_{LV}$  and  $H_{SV}$  present in Eq. (2.17), (2.4), (2.6) and (2.12) [77].  $k_{VOI}$  depends on the tissue, the contrast agent, the magnetic field strength and the pulse sequence. This means that it is unknown and usually assumed unitary. As a consequence the tracer concentration curves obtained from Eq. (2.17) do not result in absolute unit. Moreover, the frequently used values for the other constants ( $\rho = 1.04g/ml$ ,  $H_{LV} = 0.45$  and  $H_{SV} = 0.25$  [72]) have been shown to vary among different populations. According to [72, 73], the values proposed for  $\rho$  and  $k_H$  generated CBF values which agree with the flow values obtained with other techniques (such as PET) in normal subjects. Nevertheless the same values used in healthy smoker subjects are unable to provide reliable CBF values [22]. Moreover, the validity of these values in pathologic conditions has not been investigated yet. Several approaches have been proposed to overcome these limitations, in [62] the authors obtained absolute CBF values by assuming a constant microvascular hematocrit across the brain and by assigning the mean relative CBF values in white matter to a standard value of  $22ml/100ml/min$ . The absolute CBF values in the other brain regions are obtained with a ratio with the white matter. This approach is based on PET studies, which showed that white matter in normal subjects has a relative uniform and age-independent blood flow of  $22ml/100ml/min$  [44]. In [54, 63, 64] a conversion factor to convert relative MRI CBF values to absolute ones was derived by comparison studies between MRI and PET CBF measurements.

Issues connected with the AIF estimate and deconvolution operation will be presented and investigated in the next chapter.

## Chapter 3

# Dynamic Susceptibility Contrast -MRI: State of the Art and Open Issues

This chapter is devoted to introducing the main aspects of the DSC-MRI image quantification which are investigated in this thesis. In the first part, the role of the *Arterial Input Function* (AIF) and the problems due to its selection are explained. The most interesting AIF selection methods proposed in literature are also briefly reviewed. The second part of the chapter faces the deconvolution operation, providing also a mathematical formulation of the problem. Then, the most widespread deconvolution algorithms in DSC-MRI are presented: the *Singular Value Decomposition* (SVD), currently considered the gold-standard technique and the *block-Circulant Singular Value Decomposition* (cSVD), proposed to solve the problem of delay in the tracer arrival. Finally, a recently proposed nonlinear stochastic deconvolution method called *Nonlinear Stochastic Regularization* (NSR) is presented.

### 3.1 Arterial Input Function

AIF is the tracer concentration in the vessels feeding the voxel (i.e. the basic volume unit in MRI image) at time  $t$ . Since the AIF has to be known in order to compute CBF, CBV and MTT, its correct measurement is one of the most delicate steps in the DSC-MRI image quantification.

AIF depends on the shape of the injected bolus, on the cardiac output, on the vascular geometry and on the cerebral vascular resistance. As a consequence, the arterial concentration time curve ( $C_{AIF}(t)$ ) has to be measured for each subject and for each experiment. Ideally, AIF has to be determined for each voxel, as it is different for each one. This is called *local AIF* [2, 20, 33]. This is not possible in practice and an overall AIF is computed on the basis of the signal contributions from many voxels, which are assumed to contain a portion of large vessel feeding the whole image slice [13, 62, 70]. This solution neglects

any finite distance between the AIF measurement site and the voxels and it is called *global AIF*. In this case, AIF should be measured as closest as possible to the region of interest (ROI) [1, 16], thus reducing the differences between the true and the measured AIFs. The Middle Cerebral Artery (MCA) is usually the preferred measurement site because its symmetric position reasonably guarantees a minimum delay whenever the whole slice is considered [35, 46, 62]. Other measurement sites used in DSC-MRI are the Anterior Cerebral Artery (ACA) and the Internal Cerebral Artery (ICA) [16].

### 3.1.1 AIF problems

AIF is involved in the CBF quantification; thus, a biased AIF can concur to generate inaccurate CBF maps. Unfortunately, the AIF estimates can be easily influenced by many unwanted effects.

One of the most important problems in estimating AIF is the *partial volume effect*. As DSC-MRI images have a relatively low spatial resolution, a selected arterial voxel might contain both the arterial vessel and the surrounding tissue. As a consequence, the measured AIF signal also includes tissue contributes, which introduce bias in the AIF estimate. The partial volume effect depends on the vessel size, location and orientation [29, 81] and it leads to a CBF overestimation. Many correction methods have been proposed: they are either based on an appropriate scaling factor [45], or on ad-hoc algorithms to obtain a corrected AIF [81, 83].

A linear relationship between the tracer concentration and the relaxation rate is assumed to compute the concentration ( $C_{VOI}(t)$ ) from the MR signal ( $S(t)$ ) using Eq. (2.17). When the tracer concentration into a voxel increases, this assumption is no longer valid and systematic errors are introduced [29, 30, 39, 41, 71]. This is called *saturation effect*. In [11] a correction method is proposed: the authors divide the arterial concentration time curve into reliable samples (low concentration) and unreliable ones (high concentration). Subsequently, the unreliable component of the concentration profile is reconstructed using a 3 order polynomial combination.

Since there is a finite distance between the AIF measurement site and the voxels, AIF may be affected by *delay* and *dispersion*, especially in presence of pathology. The bolus dispersion in the AIF estimate has been shown to be a significant source of errors in DSC-MRI data quantification [14, 65, 85]. If  $d(t)$  denotes the *dispersion function*, the residue function ( $R^*(t)$ ), obtained by deconvolution between the tissue concentration and the AIF, is

$$R^*(t) = CBF \cdot R(t) \otimes d(t) \quad (3.1)$$

with  $R^*(0) = 0$  and  $\int_0^\infty R^*(\tau) d\tau = CBF \cdot MTT$ . Examples of dispersed and non dispersed AIFs are shown in figure 3.1. Delay and dispersion modify the AIF shape and, consequently, the  $R^*(t)$  shape. As a consequence, CBF is no more computed as  $R^*(t)$  in  $t=0$  (see subsection 2.3.1 at page 10), but as its maximum value ( $CBF = \max\{R^*(t)\}$ ) [14, 17, 62]. An error in the CBF quantification is therefore introduced. In [14] the authors showed that 1-2 second delay can introduce a 40% CBF underestimation and a 60% MTT

overestimation. Noticeably, delays between the measured and the true AIFs are common in cerebral regions affected by cerebrovascular diseases. Consequently, the quality of information provided by MRI image quantification is reduced in important pathologies, such as cerebral ischemia and carotid stenosis.

A *local AIF* should be estimated to reduce the delay and dispersion impact [1, 16], but only few attempts have been carried out in this way [20, 48]. However, although the use of a local AIF instead of a global AIF can reduce delay and dispersion, it can increase the presence of partial-volume effect. Thus, as previously pointed out, particular care is required in selecting the best place for AIF measurement, by evaluating all technical limitations and physiopathological conditions. Using local AIF could be significant not only to minimize delay and dispersion but also to study patients with cerebral ischemia or stenosis. Differences among the voxel AIFs can be used by the physicians to detect the pathological tissue.

AIF is also dependent on the *acquisition sequence* used in the experiment. In [10], the authors demonstrated that SE functional images have great microvascular sensitivity, providing good quality images. On the other hand, the AIF obtained with these sequences better reflects the situation of the small vessels and may consequently underestimate the true AIF, as reported in [62]. Although, the GE sequence signal arises from both large and small vessels, but AIF results are more affected by partial-volume effect errors[82].

### 3.1.2 Manual Selection

Since the AIF determination is a delicate step in DSC-MRI image quantification, it is usually carried out by a physician. He/she manually selects the arterial voxels on an anatomical MR image or directly on a DSC-MRI image. In the first case, a coregistration operation between the anatomical and the functional MR images must be performed. This further transformation can introduce bias in the AIF because of the different slice position or the data rescaling operation.

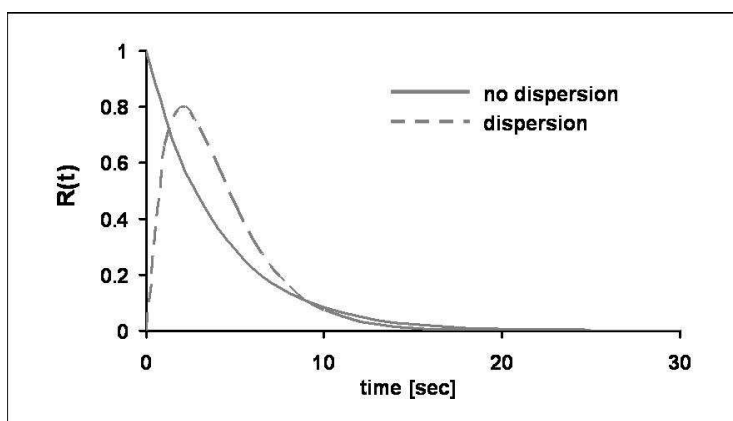


Figure 3.1: Residue function  $R(t)$  in absence (solid) or presence (dashed line) of arterial dispersion.

In the second case, the image low spatial resolution can lead to errors in the arterial voxel selection.

Other manual AIF limitations are the need of trained personnel, the intrinsic subjectivity and the low reproducibility. Despite all its problems, the manual AIF is still the most used AIF estimate method in the DSC-MRI image quantification.

### 3.1.3 Automatic Selection

Many automatic and semiautomatic selection methods have been proposed in literature to overcome the manual AIF limitations.

#### Rempp Method

One of the first attempts is reported in [72]. Here, the authors define several parameters describing the concentration time curve of each voxel, such as the *maximum concentration* (MC), the *moment of maximum concentration* (MMC) and the *full width at half maximum* (FWHM). Since AIF is expected to be characterized by an earlier MMC and a smaller FWHM, the candidate arterial voxels have to respect the following conditions

$$\begin{aligned} FWHM_{AIF} &< \overline{FWHM} - 1.5 \cdot \sigma_{FWHM} \\ MMC_{AIF} &< \overline{MMC} - 1.5 \cdot \sigma_{MMC} \end{aligned} \quad (3.2)$$

where  $\overline{FWHM}$  and  $\sigma_{FWHM}$  are the FWHM mean and standard deviation (SD) above the whole slice respectively. Likewise,  $\overline{MMC}$  and  $\sigma_{MMC}$  are respectively the MMC mean and SD. At last, only the voxels whose MC is at least 75% of the highest value are selected to reduce the partial volume effect. The AIF was computed as the mean concentration time curve of the remaining voxels.

#### Ibaraki Method

In [35] AIF was measured with a semiautomatic method. Firstly, a rectangular ROI containing the MCA was manually drawn by a physician. Secondly, the ratio between the MC and the MMC was computed for each voxel in the selected ROI. Finally, AIF was determined by averaging the five largest ratio voxels.

#### Butman Method

Another method, based on the concentration time course SD, was proposed in [12]. Firstly, the bolus arrival time was computed above the whole brain time course and an initial concentration rise time was defined 3-6 seconds later. Secondly, the SD of the concentration time curve in the baseline (i.e. from the beginning to the bolus arrival time) was computed for each voxel in order to obtain a baseline SD map ( $SDmap_b$ ). A second map containing the SD in the baseline plus the initial raise was also computed ( $SDmap_r$ ). Thirdly, both

SD maps were subtracted, thus obtaining a third map ( $SDmap_s = SDmap_r - SDmap_b$ ). The arterial voxels are expected to present high values in  $SDmap_s$ . Then, several thresholds were compared. Consider two consecutive threshold values. For each one, all voxels having SD values above the threshold were used to compute the mean concentration time curve. The width of both curves was obtained by assessing their widths at 95% of maximum. If the curve originating from the lower threshold is narrower than the one originating from the higher one, then voxels having SD values above the threshold are discarded and a new comparison is performed. Finally, AIF is determined as the mean concentration curve obtained with the final threshold.

### Carroll Method

Unlike the previously described methods, [23] selected the arterial voxel on the basis of the voxel MR signal rather than on the concentration time curve. In the first step, the mean whole brain signal was considered and the precontrast time frames were detected by the algorithm. Mean and SD ( $\sigma$ ) were computed among the frames acquired before the contrast agent injection. Then, each following frame was compared to the mean one. If the difference is smaller than  $3\sigma$ , then the frame is considered precontrast. The first frame, which differs from the mean for more than  $10\sigma$ , defines the precontrast arrival time. In the second step the tracer arrival time was computed on a voxel basis. The mean signal intensity ( $S_0$ ) and the SD ( $\sigma_v$ ) were computed on the precontrast frames selected in the previous step. The tracer arrival time is the first sample which differs from  $S_0$  for more than  $5\sigma_v$ . In the third step, the difference between the tracer arrival time and the precontrast arrival time was computed for each voxel. Voxels having a difference larger than 2 seconds were discarded. In the final step, the algorithm computes a depletion index for each remaining voxel. The depletion index is defined as the sum of the difference from  $S_0$  of the four samples measured after the tracer arrival time. AIF was defined as the voxel having the greatest depletion index.

### Clustering Methods

In [52, 55] the arterial voxels were selected using a cluster analysis algorithm. Clustering is a data analysis technique which classifies a set of objects into groups (called *clusters*). Its purpose is to sort the objects so that objects from the same cluster are more similar to each other than objects from different clusters. Commonly, similarity is according to a distance measure. The most widely used cluster algorithms are the *k-means clustering* and the *fuzzy c-means clustering*. The k-means algorithm assumes that the objects to be divided form a vector space and it minimizes intra-cluster variance:

$$V = \sum_{i=1}^k \sum_{x_j \in C_i} (x_j - \mu_i)^2 \quad (3.3)$$

where  $k$  is the number of clusters,  $C_i$  is the  $i$ -th cluster,  $\mu_i$  is the centroid of the  $i$ -th cluster (i.e. the curve representing the whole cluster population,

defined as the mean point) and  $x_j$  is the  $j$ -th object of the data set. Noticeably,  $k$ -means algorithm assigns each object to one single cluster (hard assignment). In fuzzy  $c$ -means clustering, objects can belong to more than one cluster (soft assignment). The algorithm assigns each object a certain degree of belonging to each cluster and minimizes the following objective function:

$$O = \sum_{j=1}^n \sum_{i=1}^k p_{ji}^m (x_j - \mu_i)^2 \quad (3.4)$$

where  $k$  is the number of clusters,  $n$  is the number of objects in the data set,  $\mu_i$  is the centroid of the  $i$ -th cluster,  $x_j$  is the  $j$ -th object of the data set,  $m$  is the fuzziness parameter (usually an integer value between 1 and 5) and  $p_{jk}$  is the degree level for the  $j$ -th object to belong to the  $i$ -th cluster. Noticeably, in fuzzy  $c$ -means clustering the cluster centroid is defined as the object mean, weighted by the degree of belonging to the cluster.

In [55] a rectangular ROI containing the ICA was first manually drawn. Then a fuzzy cluster analysis was performed. For each cluster centroid the MC, MMC and FWHM were computed and used to obtain an index  $M = MC/(MMC \cdot FWHM)$ . The cluster with the greatest  $M$  was selected as AIF.

The method proposed in [52] can be delineated in 5 steps. Firstly, 90% of voxels with the smallest area under the concentration time curve ( $C_{VOI}(t)$ ) are discarded. Secondly, 25% of the remaining voxels with highest roughness index ( $\Lambda(C) = \int_0^T (C''_{VOI}(t))^2 dt$ ) are excluded. Thirdly, all voxel concentration time curves are normalized to have a unitary area under the curve. Furthermore, a  $k$ -means cluster analysis is performed to divide the remaining voxels in 5 clusters. The cluster with the greatest first moment was selected. Finally, a second cluster analysis was performed on the selected cluster and the arterial cluster was selected as in the fourth step.

## 3.2 Deconvolution

As pointed out in subsection 2.3.1 (page 10) a deconvolution operation between  $C_{VOI}(t)$  and  $C_{AIF}(t)$  must be performed in order to quantify the CBF from (2.17).

Deconvolution is a mathematical operation that allows to reconstruct the unknown system impulse response starting from the input and the output signals. The main issues about this mathematical problem are its *ill-posedness* and *ill-conditioning*. Ill-posedness means that the same input and output discrete signals can lead to different equivalent solutions to the deconvolution problem. Ill-conditioning indicates that a low noise level in the output signal leads to high errors in the impulse response quantification. This means that low variations in the output signal can be amplified by the deconvolution operation, thus providing high variations in the impulse response. Moreover, the ill-conditioning problem gets worse if the sampling rate increases and in case of slow response systems. Besides the ill-posedness and the ill-conditioning, deconvolution is also complicated by some *physiological system characteristics* [26]. First of all, the

sampling rate is usually rare and non uniform because of ethical and economical reasons. Furthermore, signals are usually intrinsically positive, thus the negative estimates which can be achieved have no physiological meaning.

Deconvolution methods can be classified in two main categories: *model-dependent* and *model-independent* approaches, also called *parametric* and *non-parametric* methods.

In the *model-dependent* approaches, the unknown function to be deconvolved is described by a parametric function. In this way, the deconvolution operation becomes a parameter estimation problem, overcoming the ill-posedness and the ill-conditioning problems. Moreover, unphysiological solutions are discarded by the model assumed for  $R(t)$ . On the other hand, these methods introduce heavy assumptions on the  $R(t)$  shape and may introduce bias on CBF estimates. Examples of model-dependent approaches in DSC-MRI image quantification can be found in [43, 53, 65, 93].

The *model-independent* approaches make no assumption on the  $R(t)$ : they are therefore more powerful and less biased than the model-dependent ones. On the other hand, they are affected by the ill-posedness and ill-conditioning deconvolution problems. One of the simplest model-independent methods is to use the convolution theorem of Fourier transform. It states that the Fourier transform of two convolved functions is equal to the product of the single function transforms. Applying the theorem to Eq. (2.17)

$$\mathcal{F}\{CBF \cdot R(t) \otimes C_{AIF}(t)\} = \mathcal{F}\{C_{VOI}(t)\} \quad (3.5)$$

CBF can be easily deduced

$$CBF \cdot R(t) = \mathcal{F}^{-1} \left[ \frac{\mathcal{F}\{C_{VOI}(t)\}}{\mathcal{F}\{C_{AIF}(t)\}} \right] \quad (3.6)$$

where  $\mathcal{F}^{-1}$  denotes the inverse of the Fourier transform  $\mathcal{F}$ . Dissonant results were obtained with this method. Whereas [75] showed satisfactory CBF estimates, in [62] the authors pointed out a systematic CBF underestimation in presence of high flow.

Another model-independent method is based on the following assumption: tissue and arterial concentration samples are measured at equidistant time points,  $t_i = t_{i+1} - \Delta t$ , and  $R^*(t) = CBF \cdot R(t)$  is reasonably approximated by a staircase function in each  $\Delta t$  interval. Under these assumptions the discrete deconvolution problem in DSC-MRI can be written as

$$C_{VOI}(t_j) \cong CBF \cdot \Delta t \sum_{i=0}^j C_{AIF}(t_i) R(t_j - t_i) \quad (3.7)$$

which is equivalent to the matrix form

$$\mathbf{C}_{VOI} = CBF \cdot \Delta t \cdot \mathbf{C}_{AIF} \cdot \mathbf{R} \quad (3.8)$$

where  $\mathbf{C}_{\mathbf{VOI}}$  is a  $N \times 1$  vector,  $\mathbf{C}_{\mathbf{AIF}}$  is a  $N \times N$  matrix,  $\mathbf{R}$  is a  $N \times 1$  vector ( $N$  is the number of  $C_{VOI}(t)$  samples). Eq. (3.8) is a standard matrix equation with an explicit solution if  $\mathbf{C}_{\mathbf{AIF}}$  is invertible (i.e.  $\det(\mathbf{C}_{\mathbf{AIF}}) \neq 0$ )

$$CBF \cdot \Delta t \cdot \mathbf{R} = \mathbf{C}_{\mathbf{AIF}}^{-1} \cdot \mathbf{C}_{\mathbf{VOI}} \quad (3.9)$$

This approach is called *raw deconvolution* [25] and provides a perfect agreement between the measured and the re-convolved data. Nonetheless, the reconstructed residue function presents un-physiological wide oscillations.

Philips and Tikhonov separately developed the *Philips-Tikhonov regularization* method to improve the performances of the raw deconvolution. In this method the deconvolution problem is reformulated as an optimization problem (i.e. the minimum of a cost function has to be found). The cost function can be divided into two terms. The first one coincides with the raw deconvolution one and accounts for the adherence to the experimental data. The second one represents an estimate irregularity index, it is computed as the  $m$ -derivative energy of the estimated residue function and it accounts for the regularity of the solution. In the DSC-MRI context, the optimization problem can be written as

$$\hat{\mathbf{R}} = \min_{\hat{\mathbf{R}}} \{ (\mathbf{C}_{\mathbf{VOI}} - \mathbf{C}_{\mathbf{AIF}} \hat{\mathbf{R}})^T \Sigma_{\mathbf{C}_{\mathbf{VOI}}}^{-1} (\mathbf{C}_{\mathbf{VOI}} - \mathbf{C}_{\mathbf{AIF}} \hat{\mathbf{R}}) + \gamma \hat{\mathbf{R}}^T \mathbf{F}^T \mathbf{F} \hat{\mathbf{R}} \} \quad (3.10)$$

where the matrix  $\Sigma_{\mathbf{C}_{\mathbf{VOI}}}$  represents the noise covariance matrix,  $\mathbf{F}$  is the  $N \times N$  penalty matrix, chosen so that  $\mathbf{F} \hat{\mathbf{R}}$  represents the vector of the  $m$ -derivatives of  $\hat{\mathbf{R}}$ .  $\gamma$  is a scalar non negative parameter, called *regularization parameter*, that makes the trade-off between the two terms in the cost function, assigning them different relative weights (e.g. high  $\gamma$  values provide extreme regular solutions; low  $\gamma$  values provide a better adherence to the data). Since the method key step is selecting the optimum  $\gamma$  value, several methods have been proposed to fix the regularization parameter, such as the discrepancy criterion, the minimum risk criterion, the ordinary cross-validation criterion, the generalized cross-validation criterion and the L-curve criterion.

A different interpretation of the regularization problem can be proposed in a *stochastic context*. In this case,  $\mathbf{R}$  and  $\mathbf{C}_{\mathbf{VOI}}$  are assumed to be zero mean vectors with covariance matrices  $\Sigma_{\mathbf{R}}$  and  $\Sigma_{\mathbf{C}_{\mathbf{VOI}}}$ . The deconvolution problem can therefore be solved by means of a *Bayesian* estimation. In this case the covariance matrix of  $\mathbf{R}$ ,  $\Sigma_{\mathbf{R}} = \frac{1}{\gamma} (\mathbf{F}^T \mathbf{F})^{-1}$ , is needed. The Bayesian estimation is based on the *a priori knowledge* of the residue function regularity. A simple statistical *a priori* description of a smooth residue function considers  $\mathbf{R}(t)$  as the realization of a stochastic process obtained from a series of  $m$  integrators driven by a zero mean white noise with variance  $\frac{1}{\gamma}$ . E.g. for  $m = 1$  the residue function is modelled with a random walk model.

During the last decade, several non-parametric deconvolution methods have been proposed in literature [3, 57, 61, 84, 87, 88]. They show that the deconvolution operation is one of the most important open issues in CBF quantification. Even if its limitations have been largely reported, SVD currently represents the gold-standard technique in DSC-MRI image analysis [61, 62]; its evolution, the cSVD, overcomes some of the SVD limits and it is also widely used in clinical

practice. In this work the author chose to focus also on a new parametric deconvolution method, the *Nonlinear Stochastic Regularization* (NSR) [6, 67]. This method overcomes the SVD limits by imposing a non negative constrain on the residue function and estimating the dispersion function.

### 3.2.1 Singular Value Decomposition

In linear algebra, SVD is an important factorization of rectangular real or complex matrix, with several applications in signal processing and statistics. SVD can be seen as a generalization of the spectral theorem, which says that normal matrices can be diagonalized to arbitrary matrices using a basis of eigenvectors. SVD can be used, for example, to compute the pseudo-inverse of a matrix; SVD also provides an explicit representation of the range and null space of a matrix. Therefore, it can be used to determine the effective rank of a matrix. SVD is also extensively applied to the study of *linear inverse problems* and is useful to analyse of Regularization methods. It is widely used in statistics, where it is related to the Principal Component Analysis (PCA) in signal processing and pattern recognition and in output-only modal analysis.

A modified version of SVD, called truncated SVD, was introduced for the first time in the DSC-MRI context in 1996 by Østergaard and colleagues, becoming the gold-standard technique to quantify cerebral hemodynamic from bolus tracking experiments [61, 62].

Each algebraic approach to perform deconvolution is based on a algebraic reformulation of the convolution integral in Eq.(2.12). Assuming that the arterial and cerebral concentrations are measured at a set of equally spaced time points  $t_1, t_2, \dots, t_N$ , and that the residue function and arterial input values are constant over small time intervals  $\Delta t = t_{i+1} - t_i$ , the convolution in Eq.(2.12) can be formulated as a matrix equation

$$C_{VOI}(t_j) = \int_0^{t_j} C_{AIF}(\tau)R(t - \tau)d\tau \approx \Delta t \sum_{i=0}^j C_{AIF}(t_i)R(t_j - t_i) \quad (3.11)$$

or

$$\Delta t \begin{pmatrix} C_{AIF}(t_1) & 0 & \dots & 0 \\ C_{AIF}(t_2) & C_{AIF}(t_2) & \dots & 0 \\ \dots & \dots & \dots & \dots \\ C_{AIF}(t_N) & C_{AIF}(t_{N-1}) & \dots & C_{AIF}(t_1) \end{pmatrix} \cdot \begin{pmatrix} R(t_1) \\ R(t_2) \\ \dots \\ R(t_N) \end{pmatrix} = \begin{pmatrix} C_{VOI}(t_1) \\ C_{VOI}(t_2) \\ \dots \\ C_{VOI}(t_N) \end{pmatrix}$$

The vector notation can be used for Eq.(3.11)

$$\mathbf{A} \cdot \mathbf{b} = \mathbf{c} \quad (3.12)$$

where  $\mathbf{b}$  contains the elements of  $R(t_i)$ ,  $i = 1, 2, \dots, N$ , and  $\mathbf{c}$  are the measured tissue tracer concentrations. Eq.(3.11) can be solved iteratively for  $\mathbf{b}$  elements. However, this approach is extremely sensitive to noise, hence causes

the presence of oscillations in  $R(t)$ . In order to solve Eq.(3.12), both the noise effects and the distance between predicted and measured data are to be minimized

$$| \mathbf{A} \cdot \mathbf{b} - \mathbf{c} | \quad (3.13)$$

where  $| |$  in Eq.(3.13) represents the vector norm operation.

The algebraic approach assumes that arterial and tissue concentrations are constant between measurements. In the DSC-MRI context, both AIF and the Residue function are expected to vary over small time scales compared to the measurement temporal resolution. The constancy of both functions between consecutive measurements is a poor approximation, so  $C_{AIF}(t)$  and  $R(t)$  are assumed to vary linearly with time. The elements  $a_{ij}$  of the matrix  $\mathbf{A}$  in Eq.(3.13) become

$$a_{ij} = \begin{cases} \Delta t [C_{AIF}(t_{i-j-1}) + 4 \cdot C_{AIF}(t_{i-j}) + C_{AIF}(t_{i-j+1})] / 6 & 0 \leq j \leq i \\ 0 & \text{otherwise} \end{cases}$$

Considering these elements for matrix  $\mathbf{A}$ , SVD solves Eq.(3.13) constructing matrices  $\mathbf{V}$ ,  $\mathbf{W}$  and  $\mathbf{U}^T$  so that the inverse of  $\mathbf{A}$  ( $\mathbf{A}^{-1}$ ) can be written as

$$\mathbf{A}^{-1} = \mathbf{V} \cdot \mathbf{W} \cdot \mathbf{U}^T \quad (3.14)$$

where  $\mathbf{W}$  is a diagonal matrix (i.e. the off-diagonal elements equal to zero) containing the eigenvalues of  $\mathbf{A}$  and  $\mathbf{V}$  and  $\mathbf{U}^T$  are respectively orthogonal and transpose orthogonal matrices. Given the inverse matrix,  $\mathbf{b}$  and consequently  $R(t)$  are calculated as

$$\mathbf{b} = \mathbf{V} \cdot \mathbf{W} \cdot (\mathbf{U}^T \cdot \mathbf{c}) \quad (3.15)$$

The main quality of SVD is that the diagonal elements in  $\mathbf{W}$  are zero or close to zero and correspond to the linear equations of Eq.(3.11); moreover, they are almost linear combinations of each other. This allows to identify elements in matrix  $\mathbf{A}$  that cause the solution  $\mathbf{b}$  to oscillate or otherwise be meaningless in a biomedical modeling context. In other words, the smaller eigenvalues of  $\mathbf{W}$ , linked to the slow modes of the system, are mainly responsible for the deconvolution ill-conditioning. SVD eliminates these eigenvalues, thus increasing the regularity of the solution. In terms of sampling data from bolus tracking experiments, that equations in Eq.(3.11) being close to be linear combinations of each other allow data to be sampled at time points where changes in concentration time curves are small relative to the noise. If the diagonal elements below a certain threshold in  $\mathbf{W}$  are set to zero, the effects can be minimized before calculating  $\mathbf{b}$ .

SVD represents the most used approach to quantify DSC-MRI data. However, in the last years its limitations have been widely pointed out [46, 56, 76, 78, 86, 88]. In particular, it has been shown that CBF values obtained by SVD largely depend on the threshold value ( $P_{SVD}$ ) selected to eliminate diagonal elements in  $\mathbf{W}$ . The commonly used threshold is 20% of the maximum

singular value. This value was selected in a simulation study at the typical signal-to-noise ratio of DSC-MRI data [61, 62]. Although the study presented in [46] suggests that the threshold has to be optimized for each SNR, the 20% value remains the most commonly used threshold. The single threshold value is indeed convenient, and calculating the noise dependence can be a complex operation. Andersen and colleagues found that the empirical relationship between threshold value and noise proposed by Liu and colleagues is not optimal for non-exponential Residue function models [3]. Liu and colleagues' approach is better than the fixed-threshold approach only in the simulation conditions, whereas the curve is better estimated by the fixed threshold method in other tested circumstances. This suggests that, although the noise dependence for the threshold level proposed in [46] is real, the actual relationship is probably very complex and influenced by different factors. In addition, SVD introduces undesirable oscillations and negative values in the reconstructed  $CBF \cdot R(t)$ , producing a nonphysiological Residue function. This is far from ideal: in certain situations the whole shape of the Residue function is of interest, not just its maximum value. For instance, in presence of bolus delay and dispersion only an accurate determination of the  $CBF \cdot R(t)$  shape can assess and correct the error. In such cases, the conventional SVD method is not suitable.

### 3.2.2 Block-Circulant Singular Value Decomposition

In 2003, Wu and colleagues proposed a modified version of SVD, the cSVD. This method improves the flow estimates by performing deconvolution with a block-Circulant matrix. Therefore, it reduces sensitivity to tracer arrival time difference in AIF and in tissue signal [88].

One of the assumptions built into Eq.(3.11) is that the tissue signal cannot arrive before the AIF (i.e. *causality*). In practice, AIF can lag  $C_{VOI}(t)$  by a delay time  $t_d$ , since the measured AIF ( $C_{AIF}^*(t)$ ) is not necessarily the true AIF for that tissue ( $C_{AIF}(t)$ ), thus resulting in  $C_{AIF}^*(t) = C_{AIF}(t - t_d)$ . Therefore, the calculated  $R^*(t)$  should be  $R(t + t_d)$  for  $C_{VOI}(t)$ , but, if causality is assumed,  $R^*(t)$  cannot be correctly estimated by inversion of Eq.(3.11) using SVD.

By means of *circular deconvolution* instead of linear deconvolution,  $R^*(t)$  can be represented with  $R(t)$  circularly time shifted by  $t_d$ . Circular deconvolution has been shown to be equivalent to linear deconvolution with time aliasing. By zero-padding the  $N$ -point time series  $C_{AIF}(t)$  and  $C_{VOI}(t)$  to length  $L$ , with  $L \geq 2N$ , time aliasing can be avoided. Replacing matrix  $\mathbf{A}$  in Eq.(3.13) with a block-Circulant matrix  $\mathbf{D}$  whose elements are

$$d_{i,j} = \begin{cases} a_{i,j} & \text{for } j \leq i \\ a_{L+i-j,0} & \text{otherwise} \end{cases}$$

Eq.(3.12) can be reformulated as

$$\mathbf{g} = \mathbf{D} \cdot \mathbf{b} \quad (3.16)$$

where  $\mathbf{g}$  is the zero-padded  $\mathbf{c}$ . Using SVD, the inverse of  $\mathbf{D}$  can be decomposed to

$$\mathbf{D}^{-1} = \mathbf{V}_c \cdot \mathbf{W}_c \cdot \mathbf{U}_c^T \quad (3.17)$$

and, solving for  $\mathbf{b}$

$$\mathbf{b} = \mathbf{V}_c \cdot \mathbf{W}_c \cdot (\mathbf{U}_c^T \cdot \mathbf{g}) \quad (3.18)$$

When using circular deconvolution, due to the discontinuities at  $t = 0$  and  $t = L$ , leakage frequencies may be amplified, giving rise to spurious oscillations dominating the deconvolved signal. If the SVD threshold  $P_{SVD}$  increases, the oscillations are reduced.  $P_{SVD}$  can thus be varied until the estimated Residue function oscillations fall below a desired level. In [88], the optimal  $P_{SVD}$  was determined by computer simulations. It was computed by minimizing the average CBF estimation error over all considered Residue functions, assuming a zero time delay.

Results reported by Wu and colleagues show that the hemodynamic estimates provided by cSVD are not weighted by the tracer arrival time, thus overcoming the SVD delay problem. Therefore, cSVD is a model-independent technique insensitive to the tracer arrival time differences. It also performs comparably to the standard SVD when there are no differences between the tracer arrival time of the AIF and the tissue signal. In particular, Wu and colleagues' findings suggest that even without tracer arrival time differences, SVD obtained CBF values are underestimated.

The same work also investigates the effects of changing the sampling rate, and their implications in the flow determination. As the  $TR$  increases, the performance of SVD and cSVD degrades, because the temporal sampling is not sufficient to properly characterize the tissue hemodynamic properties. Furthermore, the optimal cSVD threshold also changes: it becomes less stringent and more data points are kept. If the arrival time differences are not multiples of  $TR$ , then cSVD exhibits slight oscillations. These are smaller in magnitude than those due to noise or obtained with SVD. Moreover, Wu and colleagues compare a fixed global threshold block-Circulant SVD (cSVD) and a block-Circulant SVD technique using SVD threshold varying on an individual pixel basis. They found out that oSVD performs better than cSVD. Since it is based on an *adaptive local threshold*, oSVD provides additional accuracy for different tissue types. cSVD results obtained in clinical images show promise in providing tracer arrival time-insensitive flow estimates. Therefore, it gives a more specific indicator of ischemic injury. The delay-insensitive CBF estimates using oSVD may provide results that are not only robust to differences in tracer arrival time, but also to AIF selection. If the contamination of flow estimates by tracer arrival time differences between the AIF and tissue signals is reduced, improved identification of salvageable tissue may be obtained.

Furthermore,  $t_d$  shift maps can contribute to provide a sensitive reflection of disturbed hemodynamics, while the CBF maps obtained with oSVD provide a more specific snapshot of the severity of ischemia in tissue at risk of infarction. The shift maps can represent tissue that is downstream from an occlusion or stenosis, but which may still receive sufficient flow at the time of imaging.

The CBF maps, on the other hand, represent the instantaneous flow at the acquisition time. Since CBF is a dynamic process, a single snapshot may not be a sensitive predictor of future infarction.

cSVD looks promising in providing time-insensitive tracer-arrival flow estimates, but more work is necessary to better define its domain of validity. Furthermore, it shows some limitations. First of all, cSVD and oSVD concentrate only on the CBF estimation and use the estimated values to discriminate among tissue types and characteristics. However, some situations in the clinical context require the whole shape of the Residue function and not only the CBF. Besides, these techniques do not consider the problem of bolus *dispersion*. The characterization of the deconvolved  $R(t)$  is therefore poor and shows the presence of negative values in the deconvolved curve.

As for standard SVD, both cSVD and oSVD need to fix a *threshold* to eliminate the spurious oscillation in the deconvolved  $R(t)$ . In the cSVD case, the optimal threshold value was found *a posteriori* by minimizing the average error in the flow estimation on a simulated data set. This approach cannot be applied on subject data. In oSVD, this problem can be partly overcome by means of an adaptive threshold selection technique as the one proposed in [46], which is based on pixel concentration characteristics. However, the presence of oscillations in the estimated  $R(t)$  shape still remain.

### 3.2.3 Non linear Stochastic Regularization

The *Nonlinear Stochastic Regularization* (NSR) [6, 94] is a nonlinear Bayesian deconvolution method that introduces the non-negative constrain and exploits the advantages of the Bayesian framework in the  $R(t)$  estimation process.

NSR provides a residue function model (in the stochastic sense) that prevents the negative values and ensures the smoothness of the estimated function. In particular, the unknown  $CBF \cdot R(t)$  is described by the convolution of the exponential of a *Brownian* motion with a deterministic exponential function

$$CBF \cdot R(t) = d(t) \otimes e^{R_1(t)} \quad (3.19)$$

where

$$d(t) = \frac{1}{\theta_1} e^{-\frac{t}{\theta_1}} \quad (3.20)$$

and

$$R_1(t) = \alpha + \theta_2 \beta(t) \quad (3.21)$$

with  $\beta(t)$  Brownian motion [9, 90, 91].

Moreover, in the Bayesian estimation context the covariance matrix of the measurement noise  $\Sigma_\nu$  is needed. The tissue concentration weight model used in NSR is the following

$$SD(t) = \frac{\theta_3}{1 + C_{VOI}(t)} \quad (3.22)$$

Summarizing the unknown parameters to be estimated in the NSR model are  $\mathbf{p} = [\theta_1, \theta_2, \theta_3, \alpha]$ .

Let  $\mathbf{y}$  be the vector containing the measurements of tissue concentration  $C_{VOI}(t)$  and  $\mathbf{G}$  the linear operator which models the relationship between  $CBF \cdot R(t)$  and tissue concentration. Then, once determined  $\theta_1$ ,  $\theta_2$ ,  $\theta_3$  and  $\alpha$  by means of a maximum likelihood strategy as described in [6], the maximum *a posteriori* estimate of  $R_1$  is

$$\widehat{\mathbf{R}}_1 = \underset{\mathbf{R}_1}{\operatorname{argmin}} (\mathbf{y} - \mathbf{G}[\mathbf{d} \otimes \mathbf{e}^{\mathbf{R}_1}])^T \boldsymbol{\Sigma}_{\nu-1} (\mathbf{y} - \mathbf{G}[\mathbf{d} \otimes \mathbf{e}^{\mathbf{R}_1}]) + \gamma^{-2} \int (\dot{\mathbf{R}}_1)^2 dt \quad (3.23)$$

where  $\dot{\mathbf{R}}_1$  denotes the first derivative of  $\mathbf{R}_1$  and  $\gamma$  is the Regularization parameter which makes a trade-off between the adherence to the experimental data and the prior knowledge. It can be shown that the estimate can be efficiently obtained by generating a sequence of finite-dimensional problems whose solutions rapidly converge to the one of the correspondent infinite-dimensional problem [6].

For a more detailed description of the NSR theory and its application in the DSC-MRI context see [6, 9, 90, 91].

Notice that NSR, although requiring a model of the residue function, is not a deterministic parametric approach. The model in Eq. (3.19), (3.20) and (3.21) describes the residue function as a stochastic process having the property of non negativity and smoothness. This means that NSR is not comparable to deterministic and physiological parametric approaches, such as in [43, 53, 65, 93].

Noticeably, NSR can reconstruct the original *non dispersed* Residue function. This is possible because in Eq. (3.19) NSR considers the product function  $CBF \cdot R_{disp}(t)$  as the convolution of the exponential of a Brownian motion and a deterministic exponential function ( $d(t)$ ) accounting for the dispersion.

The parameter  $\theta_1$  accounts for the *level of dispersion* present in the data. When the estimated  $\theta_1$  is very close to zero, NSR considers no dispersion in the Residue function; when  $\theta_1$  increases, dispersion has occurred and it increases accordingly to the parameter.  $\theta_2$  describes the *non dispersed* and *non negative*  $R(t)$ : from its maximum the original non dispersed CBF can be calculated.  $\theta_3$  is an index of the *noise level* present in the data; it is substantially constant among tissue types, depending only on the noise level and increasing as it increases.

However, NSR bears some limitations. Firstly, it is *non linear*, hence computationally more expensive than SVD and cSVD, which are linear methods. Secondly, NSR reconstructs  $R(t)$  on a virtual grid which is indeed finer than the sampling grid but does not accept the time  $t = 0$  as the initial point. This means that, using NSR, the Residue function can be estimated very close to time  $t = 0$  (for example, by making the virtual grid much finer than the sampling grid), but not at time  $t = 0$ . Anyway, this limitation can be easily overcome by interpolating the estimate  $R(t)$  to the initial value or by translating the time

---

domain before applying NSR analysis. In the end NSR, like every method solving a minimization problem, needs the *initial value* of the parameters vector  $[\theta_1\theta_2\theta_3]$  to be specified. This value cannot be known *a priori* in the analysis of subjects DSC-MRI data. NSR can converge to the exact solution for the Residue function even if the parameters show bad initial (i.e.  $\theta_1$ ,  $\theta_2$  and  $\theta_3$  very different from their final estimated values). Yet, this requires higher computational time demand and, sometimes, implies the reaching of local instead of global minimum.



## Chapter 4

# The Arterial Input Function Selection

The AIF selection problem is thoroughly investigated in this chapter. Firstly, a new selection method combining anatomical information with MR-signal analysis is presented. Secondly, it is compared to the most interesting AIF selection algorithms proposed in literature on a simulated data set. Then, a comparison with the manual selection method on a clinical data set is performed and the AIF selection impact on CBF, CBV and MTT estimate is investigated.

### 4.1 Theory

AIF is estimated on the slice containing the Middle Cerebral Artery (MCA). Since the author's interest is focused on the whole brain analysis, the MCA symmetrical position relatively guarantees to minimize the delay between AIF and voxels.

The methodology for selecting the arterial voxels can be summarized in the following steps [66]:

1. drawing a region of interest (ROI);
2. exclusion of voxels with poor gamma-fit;
3. candidate voxels selection;
4. iterative cluster analysis.

In the first step, a region of interest containing the selected artery is automatically drawn. The MCA arises from the internal carotid and continues into the lateral sulcus. Here, it branches and projects to many parts of the lateral cerebral cortex (Figure 4.1). Thus, the MCA main segment is expected to be located in the middle of the slice, with anterior-posterior direction. The algorithm detects the brain edge and selects the expected MCA location through an elliptical ROI.

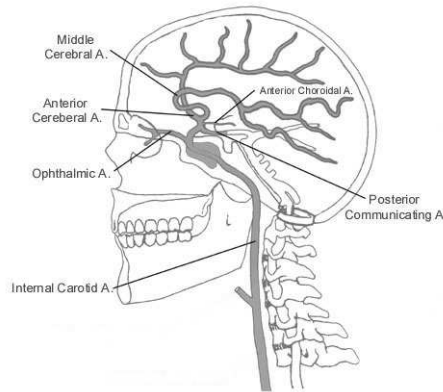


Figure 4.1: Major arteries supplying blood to the brain.

Successively, the fit between the concentration samples and the gamma-variate curve is evaluated for each voxel in the ROI to eliminate recirculation (see subsection 2.3.3, page 12). Once the fit is computed, the algorithm considers only the gamma-variate curve for each voxel. Thus, voxels presenting a poor fit are discarded on the basis of the following exclusion criteria:

- convergence is not reached during the fit estimate;
- the maximum values of the gamma-variate function differ from the maximum concentration sample by more than 10%;
- the difference norm between the gamma-variate and the concentration curves in the main peak is computed. Then, 2% of voxels with the largest norm are discarded.

The remaining voxels are all potential arterial voxels, so they are called candidate voxels. As mentioned before, AIF is computed on the basis of the signal measured from one of the main arterial vessels. Therefore, the tracer bolus is expected to arrive earlier in the arterial voxels than in the tissue ones. Moreover, the tracer bolus is likely to present a low dispersion level, because it still has to pass through the small vessels and the capillaries. Consequently, the arterial concentration curve should present a smaller Time To Peak (TTP), a greater Maximum Concentration (MC) and a smaller Full Width at Half Maximum (FWHM) than the tissue ones. Therefore, the following criteria are used to reduce the candidate arterial voxels:

- the area under the curve (AUC) is computed for each voxel. Then, the  $P_{AUC}$  of voxels with the smallest AUC are discarded to minimize the partial volume effect;
- TTP is computed for each voxel. Since voxels with delayed TTP are assumed to reflect large venous structures, the  $P_{TTP}$  of voxels with the largest TTP are discarded.

A cluster analysis of the candidate voxels is performed to estimate the AIF. Firstly, a hierarchical clustering algorithm separates the candidate voxels into two cluster on the basis of the Euclidian distance between curves. Secondly, the centroid, i.e. the mean cluster curve, is computed and the cluster presenting the highest centroid peak is selected. If the difference between two peaks is smaller than 5%, then the cluster with the smallest TTP is selected. Iteratively, a new cluster analysis is performed on the selected cluster until it contains less than 6 voxels.

Finally, the AIF is estimated by averaging the voxels in the last cluster.

Noticeably, the algorithm restricts the searching area through anatomical knowledge. This solution has already been used in literature [35, 55], but the searching area was always manually drawn by a physician. Here, anatomical knowledge is instead integrated for the first time in a fully automated method to select the arterial voxels in a reliable brain area. Moreover, even if the algorithm is developed to extract MCA, it can be easily modified to consider different arteries.

The parameters  $P_{AUC}$  and  $P_{TTP}$  must be fixed before applying the AIF extraction algorithm. They depend mostly on the acquisition sequence and on the artery site of interest. However, once they are optimized, they keep constant for a particular scanning protocol.

## 4.2 Simulation: Set up

The simulated data set was obtained starting from a known AIF, achieved as suggested in [84]. The AIF concentration curve ( $C_{AIF}(t)$ ) was divided into two components, the principal peak ( $C_P(t)$ ) and the subsequent recirculation ( $C_R$ ).  $C_P(t)$  was modelled as a gamma-variate function. The recirculation consists of a copy of the principal peak, translated and convolved with an exponential function. Figure 4.2 shows the components of the simulated AIF.

$$C_{AIF}(t) = C_P(t) + C_R(t) \quad (4.1)$$

$$C_P(t) = \begin{cases} 0 & t < t_0 \\ (t - t_0)^\alpha \cdot e^{-\frac{t-t_0}{\beta}} & \text{otherwise} \end{cases} \quad (4.2)$$

$$C_R(t) = k \cdot C_P(t - t_D) \otimes e^{-\frac{t}{\tau_R}} \quad (4.3)$$

where  $t_0$  is the contrast arrival time,  $\alpha$  is a measure of the inflow velocity steepness,  $\beta$  is the washout velocity,  $t_D$  is the delay between the principal peak and the recirculation,  $\tau_R$  is the time constant of the exponential function accounting for the recirculation dispersion and  $k$  is a proportionality constant selected so that the recirculation peak is the third part of the main peak. The simulation parameter values are reported in table 4.1. Different parameter values have been used to generate many *false AIF* (fAIF). Figure 4.3 shows a comparison between the true and the false AIFs. Table 4.3 reports the fAIF simulation parameters.

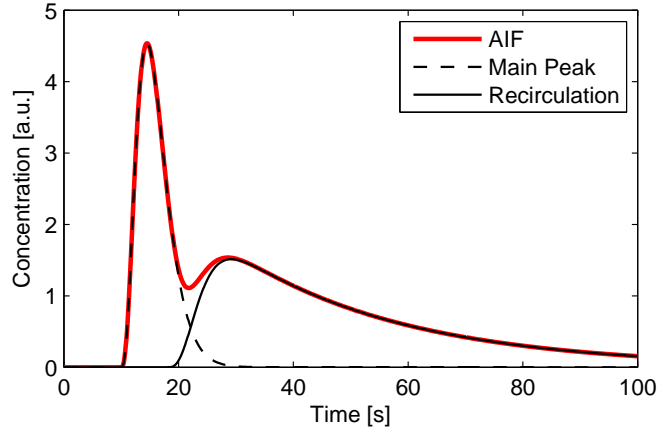


Figure 4.2: Structural elements in the simulated AIF.

The *Residue function*  $R(t)$  was modelled with a gamma-variate function, as suggested in [17]. The gamma-variate function was selected among the proposed Residue functions to simulate the presence of bolus dispersion in the arteries feeding the tissue volumes. Figure 4.4 shows an example of the gamma-variate Residue function.

$$R(t) = t \cdot e^{-\frac{t}{\sqrt{MTT}}} \quad (4.4)$$

Notice that, as required by the definition of the dispersed Residue function,  $R(0) = 0$  and  $\int_0^\infty R(t)t = MTT$ .

Tissue concentration time curves ( $C_{VOI}(t)$ ) were obtained from Eq. 2.12, considering a time range between 0 and 100 seconds. Three different combina-

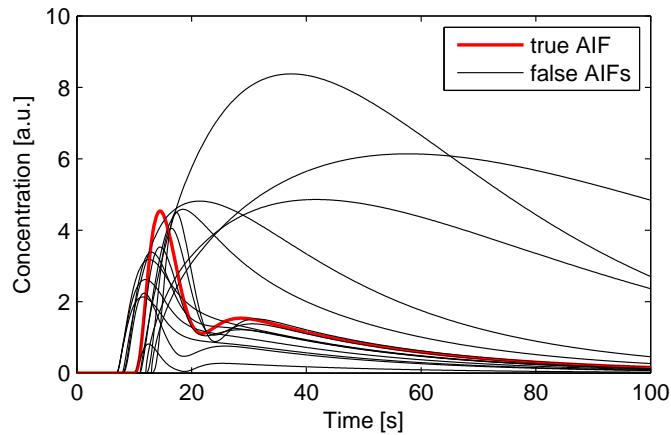


Figure 4.3: Comparison between the true and the false AIFs.

tions between tissue type and pathological state were simulated: normal and pathological gray matter and normal white matter. CBV and MTT values in the different combinations are reported in Table 4.2. Notice that MTT is assumed to be Gaussian to generate different realizations of the tissue. As CBF is obtained from Eq. (2.11), it is also assumed to be Gaussian. A comparison between the different tissue curves is reported in Figure 4.5.

The corresponding MR signal was obtained deriving Eq. 2.17

$$S_{VOI}(t) = S_0 e^{-k_{VOI} \cdot TE \cdot C_{VOI}(t)} \quad (4.5)$$

where  $S_0$  is the baseline signal, TR and TE are the acquisition sequence parameters. Typical parameter values are chosen; they are reported in Table

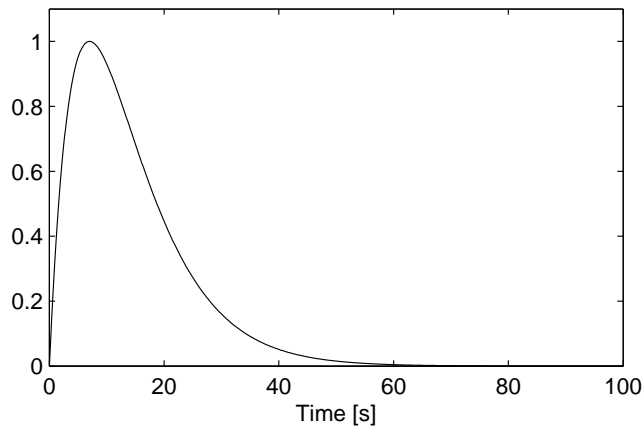


Figure 4.4: Example of the gamma-variate Residue function.

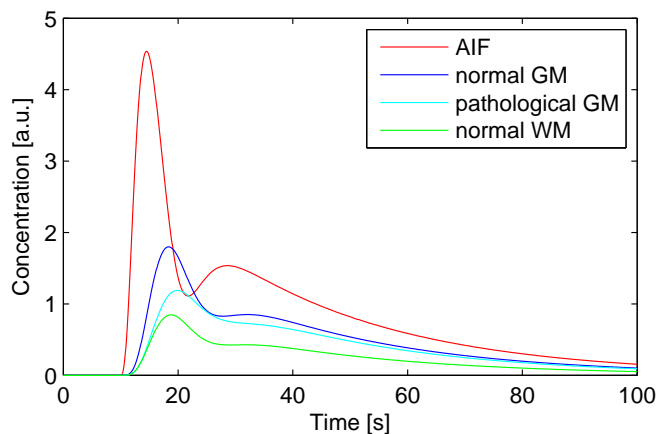


Figure 4.5: Comparison between the true AIF and the concentration curve of the different tissues.

4.1. The proportionality factor  $k_{VOI}$  was selected so that the signal presents a 40% peak signal drop from the baseline in the normal gray matter, which corresponds to values typically found in clinical cases [89].

Several linear combinations between the arterial signal and the different tissue type signals were generated to simulate the partial volume effect.

Summarizing, each realization of the simulated data set contains:

- 6 arterial voxels;
- 14 false AIF voxels;
- 440 voxels representing normal gray matter tissue;
- 440 voxels representing pathological gray matter tissue;
- 600 voxels representing normal white matter tissue;
- 400 voxels representing the partial volume effect.

For each realization, noise was added to generate 100 different noisy curves. Noise was modelled as a zero mean Gaussian noise with standard deviation  $SD_{noise}$  chosen to create signal to noise ratios (i.e.  $SNR = S_0/SD_{noise}$ ) of 5, 10, 20, 50, thus including the SNR values typically found in DSC-MRI clinical practise (SNR~20) [17]. Figure 4.6 reports voxel signals in a realization at SNR=20.

Five different automatic AIF selection methods were applied to this simulated data set:

- the novel approach proposed in this work (see section 4.1), which will be called HIER;
- the method proposed by Mouridsen and colleagues in [52], called in this work K-MEANS;
- the method proposed by Butman and colleagues in [12], called in this work SD-MAP;
- the method proposed by Rempp and colleagues in [72], called in this work REMPP;
- the method proposed by Ibaraki and colleagues in [35], called in this work PEAK;

All methods were implemented as proposed in the original publications. The only exception was the final step. In each method, a gamma variate function was used to fit the arterial concentration curve. The gamma variate function is assumed to be the AIF. In the HIER method, the first step, i.e. the detection of the searching area, was not performed in the simulated data analysis.

AIF was also estimated by manual selection of the six arterial voxels. The selected voxels contain only the arterial signal, thus such AIF is not biased by the partial volume effect. This AIF will be called *best AIF*.

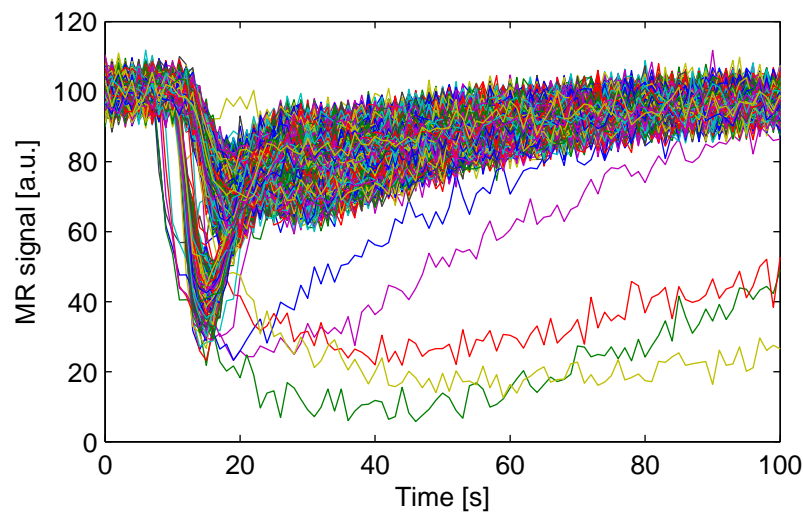


Figure 4.6: Simulated data set realization.

Simulation Parameters	
$t_0$	10 s.
$t_D$	8 s.
$\alpha$	3 adim.
$\beta$	1.5 s.
$\tau_R$	30 s.
$\rho$	$0.0104 \frac{100g}{ml}$
$k_H$	0.73
$S_0$	100 a.u.
$T_E$	50 ms.
$T_R$	1 s.

Table 4.1: Parameter values in the simulated data generation.

Tissue Simulation Parameters		
Tissue Clinical State	CBV [ml/100g]	MTT (mean $\pm$ SD) [s.]
Normal Gray Matter	4	$4 \pm 0.33$
Pathological Gray Matter	3.3	$10 \pm 0.7$
Normal White Matter	2	$5.45 \pm 0.33$

Table 4.2: Hemodynamic parameters

False AIF Simulation Parameters			
	$t_0$ [s.]	$\alpha$ [adim.]	$\beta$ [s.]
fAIF <sub>1</sub>	7	1.5	3
fAIF <sub>2</sub>	7	1.6	3.1
fAIF <sub>3</sub>	7	1.6	3.5
fAIF <sub>4</sub>	8	2	2.5
fAIF <sub>5</sub>	8	2.5	1.5
fAIF <sub>6</sub>	8	1.1	10
fAIF <sub>7</sub>	10	2.5	1
fAIF <sub>8</sub>	10	2.5	1.8
fAIF <sub>9</sub>	11	1.5	5
fAIF <sub>10</sub>	11	1	20
fAIF <sub>11</sub>	12	0.7	30
fAIF <sub>12</sub>	12	2.8	1.6
fAIF <sub>13</sub>	13	3.3	1.3
fAIF <sub>14</sub>	13	0.65	50

Table 4.3: False AIF simulation parameters.

## 4.3 Simulation: Results

### 4.3.1 Arterial Input Function reconstruction

Figures 4.7 - 4.12 show the mean AIF computed using the different methods in different noise conditions. Moreover, the arterial voxels were manually selected and an AIF is estimated. Since it is not biased by the partial volume effect, it represents the best obtainable solution (*best AIF*).

- The HIER method (Figure 4.7) precisely reconstructs the arterial curve in high, normal and low noise conditions (SNR 10, 20, 50), whereas it overestimates the peak at a very high noise level (SNR 5). Moreover, it presents good confidence bands at SNR 10, 20 and 50, showing a high reproducibility level.
- K-MEANS performs less satisfactorily than HIER (Figure 4.8). Solutions usually underestimate the true AIF and present wider confidence bands than HIER.
- The SD-MAP method provides good AIF assessment and good confidence bands at high, normal and low noise levels (Figure 4.9). But its performances crumble when noise considerably increases. Moreover, the estimated arterial curve peaks are usually delayed with respect to the true AIF ones.
- REMPP (Figure 4.10) shows quite good solutions at low and normal noise level (SNR 20 and 50). However, it overestimates the peak and provides very narrow curves at a high noise level. The PEAK method exhibits good mean AIF estimates among all SNRs (Figure 4.11). However, it presents wide confidence bands, particularly in the final part of the arterial curve (i.e. after the main peak) at SNR 10 and 20. Remarkably, the CBV, CBF and MTT quantification depends on the whole AIF, not only on its principal peak.
- The Best AIF method usually provides very good mean solutions and confidence intervals, but it overestimates the peak at high noise level (SNR 50) (Figure 4.12).

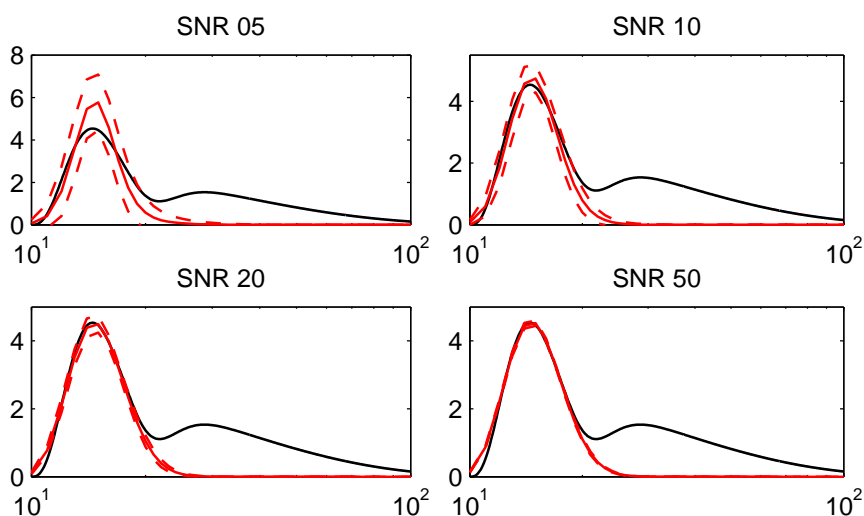


Figure 4.7: AIFs reconstructed with the hierarchical cluster method (Hier). Black solid lines indicate the true AIF, red solid lines the mean of reconstructed AIFs and dashed lines the mean  $\pm$  SD of reconstructed AIFs. The horizontal axes are time [s.] in logarithmic scale and time scale was shifted by 10 seconds to improve visualization. The vertical axes are concentration [a.u.].

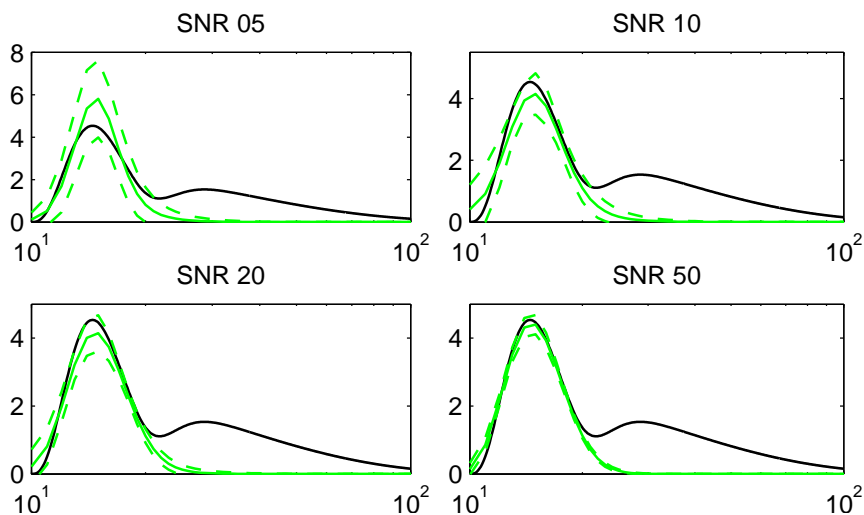


Figure 4.8: AIFs reconstructed using [52] (K-means). Black solid lines indicate the true AIF, red solid lines the mean of reconstructed AIFs and dashed lines the mean  $\pm$  SD of reconstructed AIFs. The horizontal axes are time [s.] in logarithmic scale and time scale was shifted by 10 seconds to improve visualization. The vertical axes are concentration [a.u.].

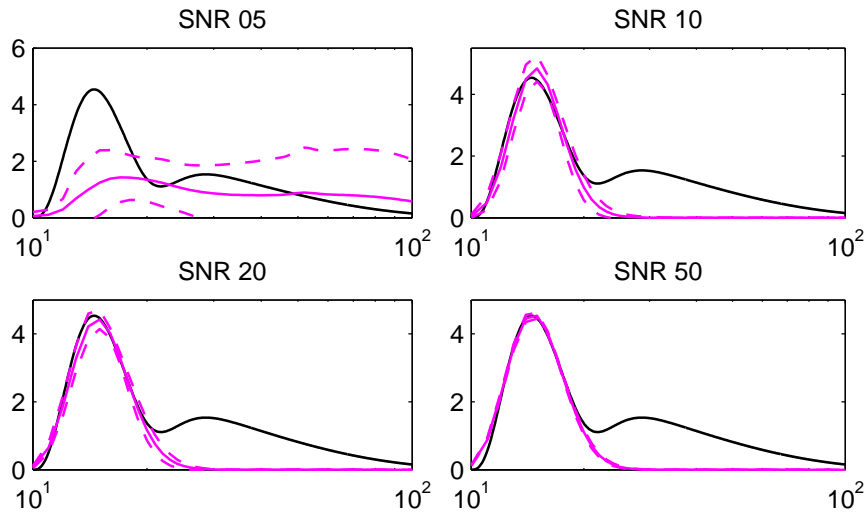


Figure 4.9: AIFs reconstructed by the SD map method (SD map) [12]. Black solid lines indicate the true AIF, red solid lines the mean of reconstructed AIFs and dashed lines the mean  $\pm$  SD of reconstructed AIFs. The horizontal axes are time [s.] in logarithmic scale and time scale was shifted by 10 seconds to improve visualization. The vertical axes are concentration [a.u.].

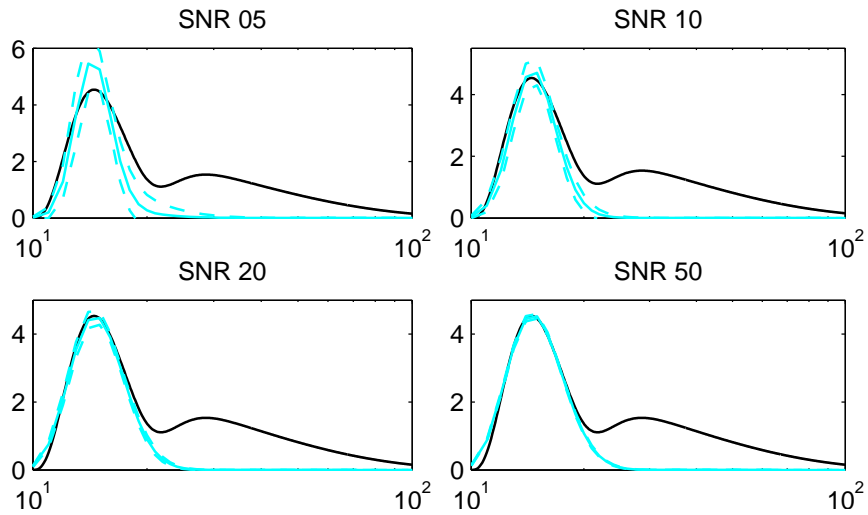


Figure 4.10: AIFs reconstructed by Rempp method (Rempp) [72]. Black solid lines indicate the true AIF, red solid lines the mean of reconstructed AIFs and dashed lines the mean  $\pm$  SD of reconstructed AIFs. The horizontal axes are time [s.] in logarithmic scale and time scale was shifted by 10 seconds to improve visualization. The vertical axes are concentration [a.u.].

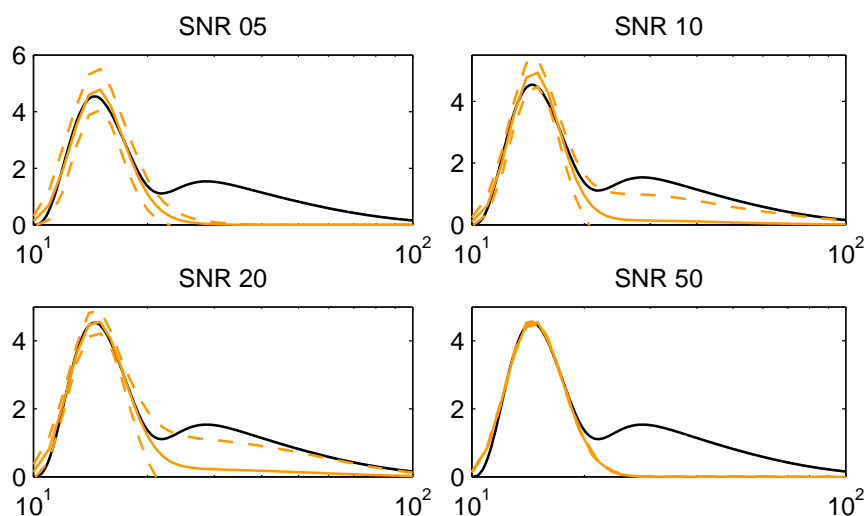


Figure 4.11: AIFs reconstructed using [72] (Peak). Black solid lines indicate the true AIF, red solid lines the mean of reconstructed AIFs and dashed lines the mean  $\pm$  SD of reconstructed AIFs. The horizontal axes are time [s.] in logarithmic scale and time scale was shifted by 10 seconds to improve visualization. The vertical axes are concentration [a.u.].

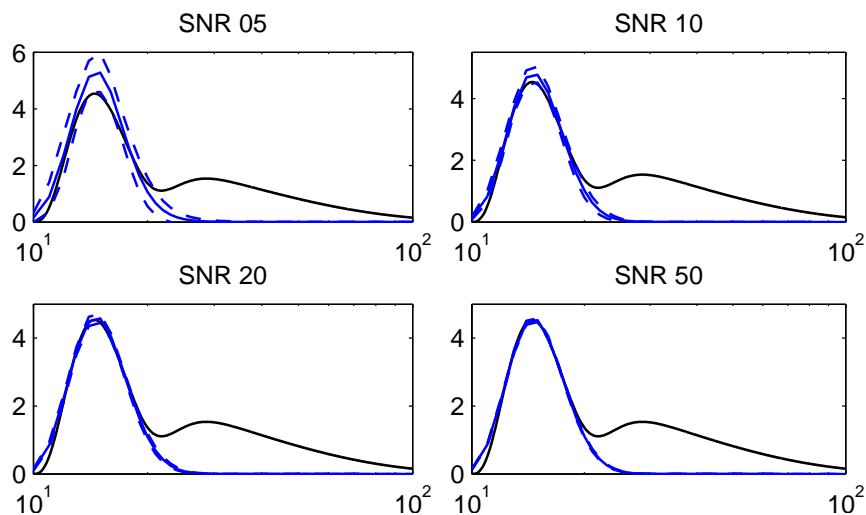


Figure 4.12: AIFs reconstructed by selecting only arterial voxels (best solution). Black solid lines indicate the true AIF, red solid lines the mean of reconstructed AIFs and dashed lines the mean  $\pm$  SD of reconstructed AIFs. The horizontal axes are time [s.] in logarithmic scale and time scale was shifted by 10 seconds to improve visualization. The vertical axes are concentration [a.u.].

In each method, the mean partial volume in the selected voxels was computed and reported in Figure 4.13. At a very high noise level (SNR 5), PEAK performs best, SD-MAP is significantly affected by partial volume and the other methods exhibit comparable performances. At SNR 10 and 20, HIER and PEAK provide comparable results and show the best scores. At low noise levels (SNR 50), all methods have good performances with the exception of K-MEANS, that is the worst method at SNR 10, 20 and 50. HIER is the best method at the noise level typically present in the clinical practice (SNR 20).

The performances of the different algorithms to estimate the AIF were also assessed by measuring the difference between the estimated AIF and both the true and the best AIFs. The difference was computed as *Root Mean Square Error* (RMSE) in each realization of the simulated data as

$$RMSE = \sqrt{\frac{\sum_{i=1}^n [AIF_{estimated}(t_i) - AIF_{true/best}(t_i)]^2}{n}} \quad (4.6)$$

where  $n = 100$  is the number of samples in the simulated data,  $AIF_{estimated}(t)$  is the arterial curve provided by each method and  $AIF_{true/best}(t)$  is the true AIF or the best AIF.

Mean RMSE indices between the best AIF and the estimated ones are reported in Figure 4.14. At a very high noise level, PEAK shows the best result, SD-MAP the worst and the other methods have similar RMSE values. In other conditions, all methods exhibit comparable performances, but HIER reaches the best results. At typical SNR, the HIER method has the smallest RMSE and PEAK the largest one.

Figure 4.15 shows the mean difference, expressed as RMSE, between the true and the estimated AIFs. The difference between the best and the true AIFs was also reported. All methods asymptotically come close to the best AIF results, with the exception of PEAK. At SNR 5, the PEAK method provides good performance, its reconstructed AIF is nearer to the true one than the best AIF. At lower noise levels (SNR 10, 20), PEAK RMSE is higher than best AIF one. Then, at SNR 50, PEAK result is comparable to the other methods. At typical SNR, HIER method has the smallest RMSE and PEAK the largest one.

Since the CBV quantification depends on the AIF integral (from Eq. (2.4)), the area under the concentration curve is an important parameter to assess the estimated AIFs. Figure 4.16 reports the mean AUC computed in each estimated AIF. Results are compared to the AUC of the true AIF main peak, i.e. the AIF without recirculation. At SNR 10, 20, 50, all methods underestimate the AUC, with the exception of PEAK. PEAK shows a very high difference from the true AUC in SNR 10 and 20, whereas it provides AUC very close to the true one at SNR 5 and 50. Remarkably, SD-MAP exhibits a very high difference from the true AIF AUC at SNR 5, but it performs well at other noise levels. SD-MAP and HIER provide the closest value to the true ones at the typical SNR used in clinical practice.

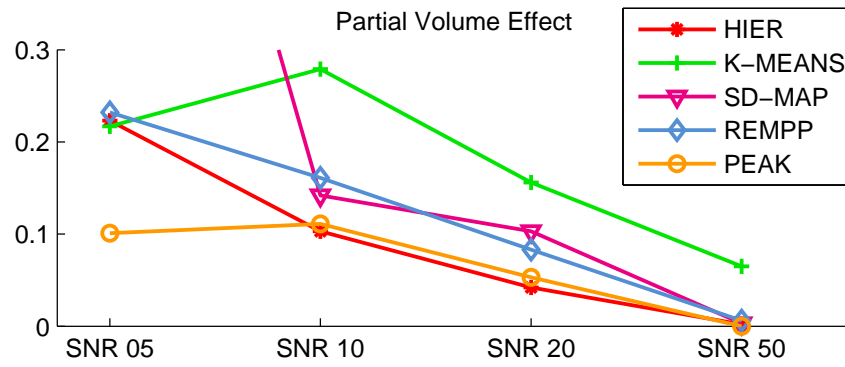


Figure 4.13: Partial volume effect in arterial voxel selection.

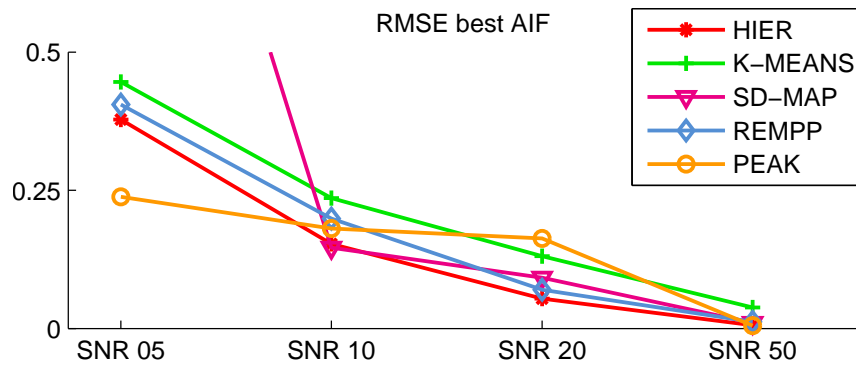


Figure 4.14: Root Mean Square Error computed between the estimated AIF and the best possible AIF.

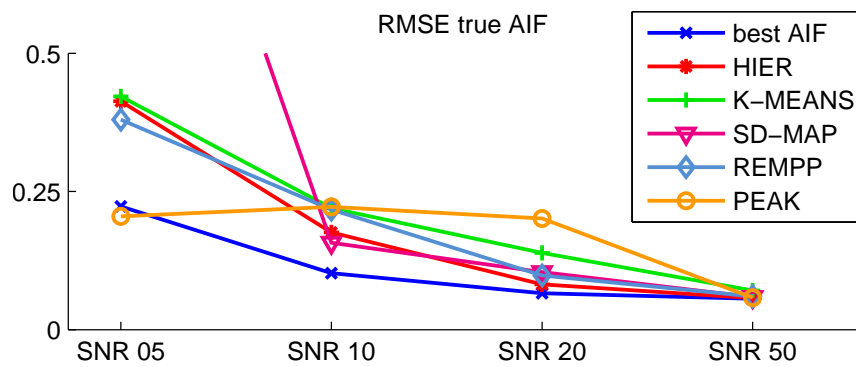


Figure 4.15: Root Mean Square Error computed between the estimated and the true AIFs.

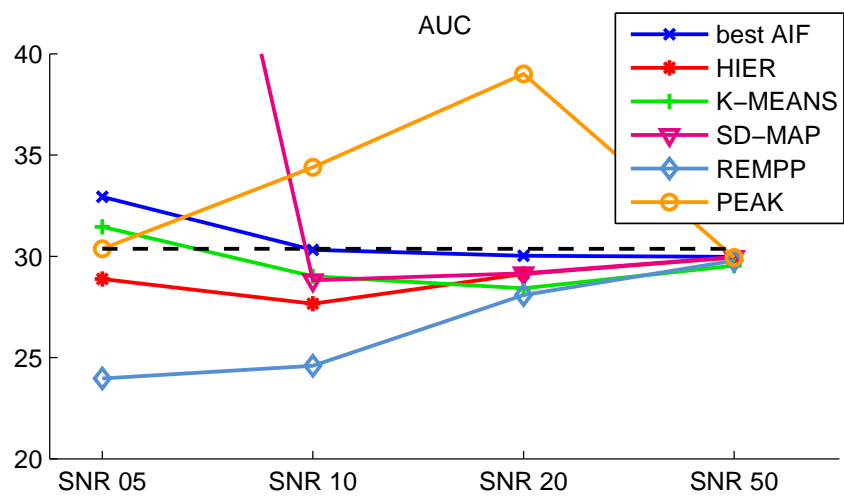


Figure 4.16: Area Under the Curve computed on the estimated AIF. The dashed black line indicates the AUC of the true AIF without recirculation.

### 4.3.2 Impact of the Arterial Input Function on estimating the hemodynamic parameters

Cerebral Blood Flow (CBF), Volume (CBV) and Mean Transit Time (MTT) have been computed in order to evaluate the impact of the AIF on DSC-MRI image quantification. CBV was computed according to Eq. (2.4). SVD deconvolution was performed to estimate CBF from the Residue function. Then, MTT was obtained from Eq. (2.11). AIF was estimated on simulated data at SNR 20, i.e. the typical noise level in clinical practice.

CBF, CBV and MTT were estimated from both noisy and non noisy data. Thus, both the impact of the AIF selection and the combination of the AIF selection with the noise in data can be evaluated. This allows to assess the different AIF dependencies and their combination with the noise effects. Normal and pathological *gray matter* (GM) and normal *white matter* (WM) were simulated to account for the different tissue clinical states.

#### Tissue without noise

For each AIF selection method, ratios between estimated and true CBFs in each tissue type were reported in the upper panel of Figure 4.17 (mean  $\pm$  SD). Ratios obtained from the best AIF are the closest to the unity in normal white matter and pathological gray matter, whereas HIER performs best in the normal gray matter CBF quantification. Except for the PEAK approach, all automatic AIF selection algorithms overestimate CBF in each tissue type. PEAK leads to a large CBF underestimate instead. Among all different methods, HIER is the most accurate in each tissue type,  $1.0042 \pm 0.0001$  in normal gray matter,  $1.0123 \pm 0.0003$  in pathological gray matter and  $1.0125 \pm 0.0002$  in normal white matter.

In the middle panel of Figure 4.17 CBV ratios were reported (mean  $\pm$  SD). Since the CBV estimate depends only on the AIF integral on time, the ratio between the estimated and the true CBV equals the ratio between the estimated and the true AIF integrals on time. The best AIF method leads to the best CBV ratio (1.01). Among all methods, HIER and SD-MAP present the best CBV ratio (1.04) and PEAK the worst one (0.78). PEAK method provides a large CBV underestimate, whereas all other algorithms overestimate it.

The lower panel in Figure 4.17 shows ratios between the estimated and the true MTT (mean  $\pm$  SD). With the exception of PEAK, all methods quite overestimate MTT and exhibit comparable results. MTT ratios range from  $1.011 \pm 0.005$  (K-MEANS in pathological gray matter) to  $1.0386 \pm 0.0002$  (HIER in normal gray matter). On the contrary, MTT ratios computed by using PEAK method are very small (about 0.81), showing a large MTT underestimate.

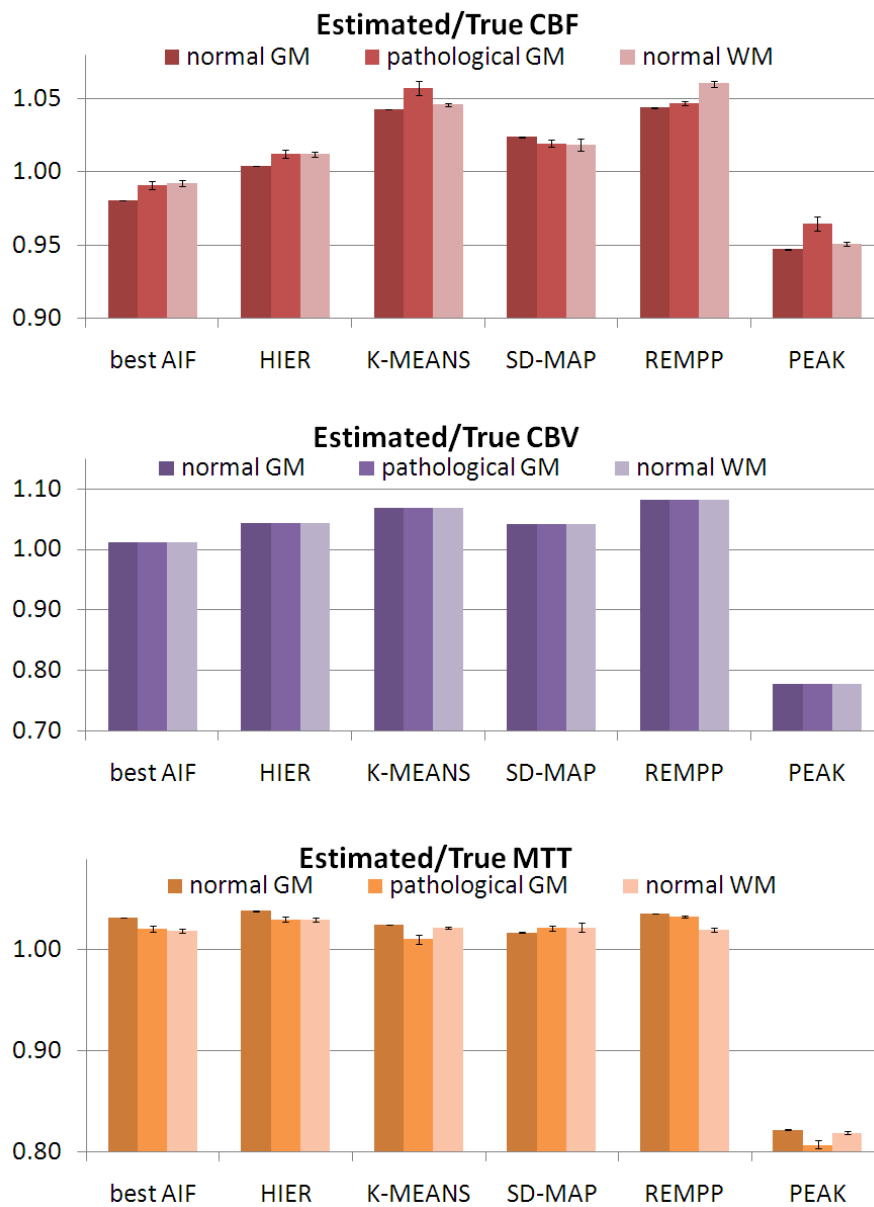


Figure 4.17: Mean CBF, CBV and MTT ratio computed by using the estimated and the true AIFs. The AIF estimation was performed on data at SNR 20. The Residue function quantification was performed using SVD on non noisy tissue data.

### Noisy tissue

Estimated and true CBF mean ratio and SD was reported in Figure 4.18 (upper panel), divided into AIF selection method and tissue type. The CBF values obtained using the best AIF are very close to the true ones. Among all other methods, HIER shows the best results considering both the normal and the pathological gray matter ( $1.02 \pm 0.06$  and  $1.02 \pm 0.11$ , respectively), whereas in the normal white matter the PEAK method performs best ( $1.02 \pm 0.11$ ). The worst mean ratios were obtained using K-MEANS and REMPP algorithms, but REMPP also presents the largest SD in each tissue type ( $1.07 \pm 0.07$ ,  $1.06 \pm 0.12$  and  $1.08 \pm 0.14$  in normal GM, pathological GM and normal WM, respectively).

The middle panel in Figure 4.18 reports the estimated and true CBV mean ratio and SD. As previously argued, CBV depends only on the AIF integral on time. Thus, only the mean CBV ratio is affected by the AIF, whereas the SD is caused by noise in the data. In this case, the best AIF provides the best CBV values (1.01 mean ratio). Among all other methods, HIER and SD-MAP provide comparable ratios (1.046 and 1.045 mean value, respectively). PEAK is the only method affected by CBV underestimate, showing 0.78 as mean CBV ratio.

Mean ratio and SD computed between the estimated and the true MTT are showed in Figure 4.18. With the exception of PEAK, all methods provided comparable results, ranging from  $0.99 \pm 0.15$  (SD-MAP method on normal WM) to  $1.04 \pm 0.14$  (REMPP on pathological GM). As in non noisy data analysis, AIF computed using PEAK method leads to underestimates in MTT values (MTT ratios:  $0.81 \pm 0.06$ ,  $0.81 \pm 0.10$  and  $0.81 \pm 0.12$  in normal GM, pathological GM and normal WM, respectively).

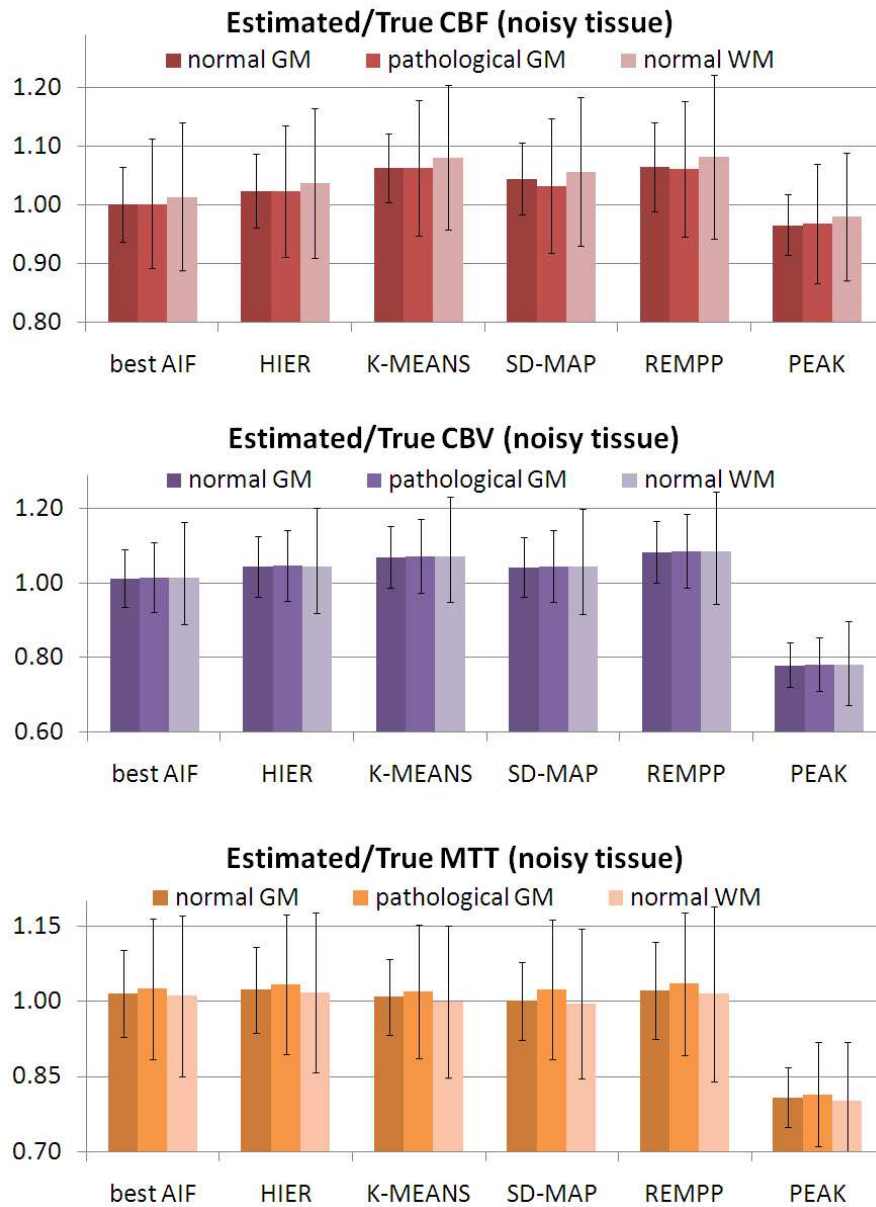


Figure 4.18: Mean CBF, CBV and MTT ratio computed by using estimated and true AIFs. The AIF estimation was performed on data at SNR 20. The Residue function quantification was performed using SVD on noisy tissue data (SNR 20).

## 4.4 Simulation: Discussion

The AIF selection is a critical step in the CBF, CBV and MTT quantification from DSC-MRI images. For routine clinical use, an automatic, rapid and objective method to obtain the AIF is essential. In this work, a novel fully automated algorithm for the AIF estimate was presented and compared to the most famous methods proposed in literature. The comparison has been made on a large data set including 3 different tissue types, 4 different noise levels and the partial volume effect.

The HIER method has been shown to precisely reconstruct the AIF. The algorithm provides accurate AIF estimates and it is robust against the different noise level. Thus, it increases the reproducibility level in DSC-MRI image quantification. At the noise level typically found in DSC-MRI images, the HIER method provides excellent performances. It presents very narrow confidence bands, hence has a remarkably good reproducibility level. Among all tested algorithms, it shows the lowest partial volume effect. Moreover, it records the lowest RMSE from both the true and the best AIF, thus it is able to reconstruct the true AIF shape. In addition, its AUC is the closest to the true one. Therefore, it is not very biased by the partial volume effect and its estimate is very close to the true AIF.

The SD-MAP algorithm provides reliable AIF estimates, too. It presents narrow confidence bands. It can reconstruct a good AIF shape, close to the true one. It is more affected by the partial volume effect than the HIER method, even if its AUC is very close to the true value. The main problem of the SD-MAP algorithm is its sensitiveness to the noise level, in particular if this is very high. At very low SNR, the concentration curve SD depends mainly on the noise, thus standard deviation maps obtained with the SD-MAP method are not correlated to the vasculature location.

The REMPP method can well characterize the AIF at normal and low noise levels. Moreover, it is very accurate and presents narrow confidence bands. Nonetheless, it is noise sensitive. When the SNR decreases, REMPP estimates become sharper than the true AIF and this leads to underestimate the AUC.

K-MEANS estimates are not satisfactory. They seem highly influenced by the partial volume effect. It usually underestimates the true AIF, thus providing low AUC. It presents high RMSE from both the true and the best AIF. Therefore, it is not able to reconstruct the true AIF shape. Moreover, it provides wide confidence bands, and this underlines its lack of accuracy in the arterial voxel selection.

Considering the mean of estimated AIFs, the PEAK method can reliably reconstruct the arterial curve and it is not particularly affected by the partial volume effect. Nonetheless, it is characterized by very wide confidence bands at normal and high noise level, especially in the final part of the curve, after the main peak. Moreover, it shows high RMSE from both the true and the best AIF and it widely overestimates the AUC. Therefore, the PEAK method is not accurate and has a very low reproducibility level.

All methods remarkably overestimate the main peak in very noisy conditions (SNR 05), also when selecting only the arterial voxels (best AIF). This

is caused by the fit operation. In each method, the estimated arterial concentration curve is fitted with a gamma variate function in order to eliminate the recirculation. The main peak is the most interesting part of the curve: the higher the concentration value, the larger the weight. In the fit operation, samples whose value was significantly increased by noise may lead to overestimate the concentration peak. Since this effect becomes evident only at very high noise levels, the bias introduced by the fit operation is lower than the bias due to the recirculation when considering real data noise levels.

The impact of the AIF selection was also assessed by CBF, CBV and MTT quantification both in noisy and non noisy data. Since the CBV quantification depends only on the AIF integral, it is not affected by the arterial curve shape. On the contrary, a deconvolution operation must be performed to obtain the CBF value. Deconvolution is very sensitive to the AIF shape, thus the AIF selection has a large impact on the CBF quantification. The ratios between the estimated and the true CBF, CBV and MTT values were computed to compare the investigated algorithms. HIER provides the best CBF ratios both in presence and in absence of noise. When considering noisy data, HIER presents the lowest difference among the different tissue errors. Therefore, HIER is able to reconstruct accurate and reliable AIFs, very close to the true one. PEAK provides significantly underestimated CBV values. This leads to very underestimated MTT values, whereas the CBF quantification errors are comparable to the other method ones. This underlines that PEAK is very affected by the partial volume. REMPP shows the highest SD values in CBF, CBV and MTT ratios in noisy data analysis. This means that it is very sensitive to noise and it has a low reproducibility level. SD-MAP provides the best CBV ratios both in presence and absence of noise, comparable to the HIER ones. But its performances are worse than the HIER ones in CBF quantification and in MTT quantification in normal WM and pathological GM. K-MEANS provides good CBV and MTT ratios, but also poor CBF ones. This underlines that K-MEANS estimated AIF is biased by the partial volume effect and it is not reliable.

Summarizing, HIER has demonstrated to be a robust method to estimate the AIF. At the noise level typically present in DSC-MRI images, it provides the best performances among the implemented methods. Other algorithms appear to be more sensitive to noise and show a lower reproducibility level than HIER. Then, HIER is able to extract reliable arterial curves, thus providing accurate estimates of CBF, CBV and MTT.

The simulation study allowed to test the AIF selection algorithms in a controlled environment and to thoroughly analyse their performances. HIER method has been shown to perform best among the implemented methods. It can reconstruct a reliable AIF and provide accurate estimates of the hemodynamic parameters. The next step in the validation process is its application on clinical data. Since the true AIF is not known in clinical data, the AIF provided by HIER algorithm is compared to the one obtained by manual selection.

## 4.5 Clinical data: Experimental set up and subjects

The clinical data set was provided by Doctor Mirco Cosottini, of the Department of Neuroscience, University of Pisa, Italy. It is composed by DSC-MRI data from 11 patients with severe atherosclerotic unilateral stenosis of the internal carotid artery. All subjects were submitted to conventional angiography with digital subtraction technique to confirm the stenosis grading. Examinations were executed with MR equipment Signa Horizon CV 1.5 T GE Medical System using a dedicated phased array neurovascular coil. DSC-MRI imaging was performed with a single shot EPI GE sequence along the bicommissural axis ( $TE = 51$  ms and  $TR = 1560$  ms). The injection rate was 5 ml/sec with a total amount of 14 ml, using a 18 gauge intravenous access connected to an automated injector. In 8 out of the considered subjects, DSC-MRI acquisition was repeated 6 months after the surgery intervention to completely or partially eliminate the stenosis. For subject n° 10, only the acquisition after surgery was available. In total, 18 different clinical cases were considered (i.e. 10 pre-surgery and 8 post-surgery).

Subject ID	Age [years]	Weight [kg]	Gender	Stenosis Loc. [Rad]	Pre/Post-Surgery Imaging
#1	72	69	M	dx	Pre/Post
#2	77	85	M	sx	Pre/Post
#3	81	62	M	sx	Pre/Post
#4	78	60	F	dx	Pre
#5	75	74	M	dx	Pre/Post
#6	59	73	M	sx	Pre/Post
#7	77	83	M	dx	Pre/Post
#8	58	78	M	sx	Pre
#9	81	79	F	dx - sx	Pre/Post
#10	70	72	M	sx	Post
#11	76	85	M	dx	Pre/Post

Table 4.4: Age, weight, gender, stenosis location and presence of post-surgery acquisition of the eleven considered subjects. Noticeably, the stenosis location is in radiological convention (i.e. the right hemisphere is seen on the left side of the image).

Table 4.4 shows age, weight, gender of the eleven subjects together with the stenosis location and the presence of a second DSC-MRI acquisition after

surgery.

Noticeably, a subset of the whole data set was considered in the comparison between automatic AIF and manual AIF. It includes subjects #1 pre and post; #2 pre and post; #3 pre and post and #4 pre.

## 4.6 Clinical Data: Results

In each subject, automatic and manual AIFs were extracted. The *automatic AIF* was computed using the HIER algorithm presented in this work. The *manual AIF* was computed by a physician, who selected the arterial voxels on the DSC-MRI images.

Figures 4.19 - 4.25 show AIF computed in each subject. The upper panel shows the slice selected for the automatic AIF extraction, the searching area drawn by the algorithm and the selected voxel location. In the middle and lower panel, respectively, the automatic and the manual selection results are presented. The AIF gamma function is compared to the selected voxel gamma functions and to the concentration mean samples of the selected voxels. The abscissa axes (i.e. the time axes) are in logarithmic scale and they are also shifted by 10 seconds to improve the visualization and to emphasize the curve differences.

A clinician is asked to examine the selected voxel location to evaluate the algorithm ability to select voxels containing arterial vessels. For each selected voxel, he concluded that its position is compatible with the arterial structures of the subject.

Since DSC-MRI images have a low spatial resolution and are affected by the partial volume effect, the clinician may select some voxels that are very different one from each other. For example, he can select voxels with a low concentration peak (e.g. subject #1 pre surgery, Figure 4.19), very dispersed ones (e.g. subject #2 pre surgery, Figure 4.21), or delayed ones (e.g. subject #3 pre surgery, Figure 4.23). Therefore, the manual AIF curve shows a higher noise level than the automatic one, or at least the same (e.g. subject #1 post surgery, #3 pre and post surgery, Figures 4.20, 4.23 and 4.24). The automatic algorithm thus selects voxels with lower variation one from each other than the manual selection, with the only exception of the subject #1 post surgery.

Differences between manual and automatic AIFs can also be found in the concentration peak, in the time to peak and in the concentration peak width. In pre surgery subjects, the automatic algorithm provides a higher AIF than the manual selection, whereas the state reverses in the post surgery subjects. The manual AIF is also affected by delay and dispersion in subjects #1, #3, #4 pre surgery (Figures 4.19, 4.23 and 4.25), whereas all AIFs present comparable time to peak and width in the other subjects. Ideally, AIF should present a high and fast peak concentration, followed by one or more little peaks caused by recirculation. For example, in subject #2 pre surgery (Figure 4.21) a second small peak, following the main one, can be easily found. Moreover, the AIF time to peak should be anticipated than the tissue one, to preserve the causality between AIF and tissue. Noticeably, delay and dispersion have been shown to provide very biased CBF values when using the standard quantification techniques.

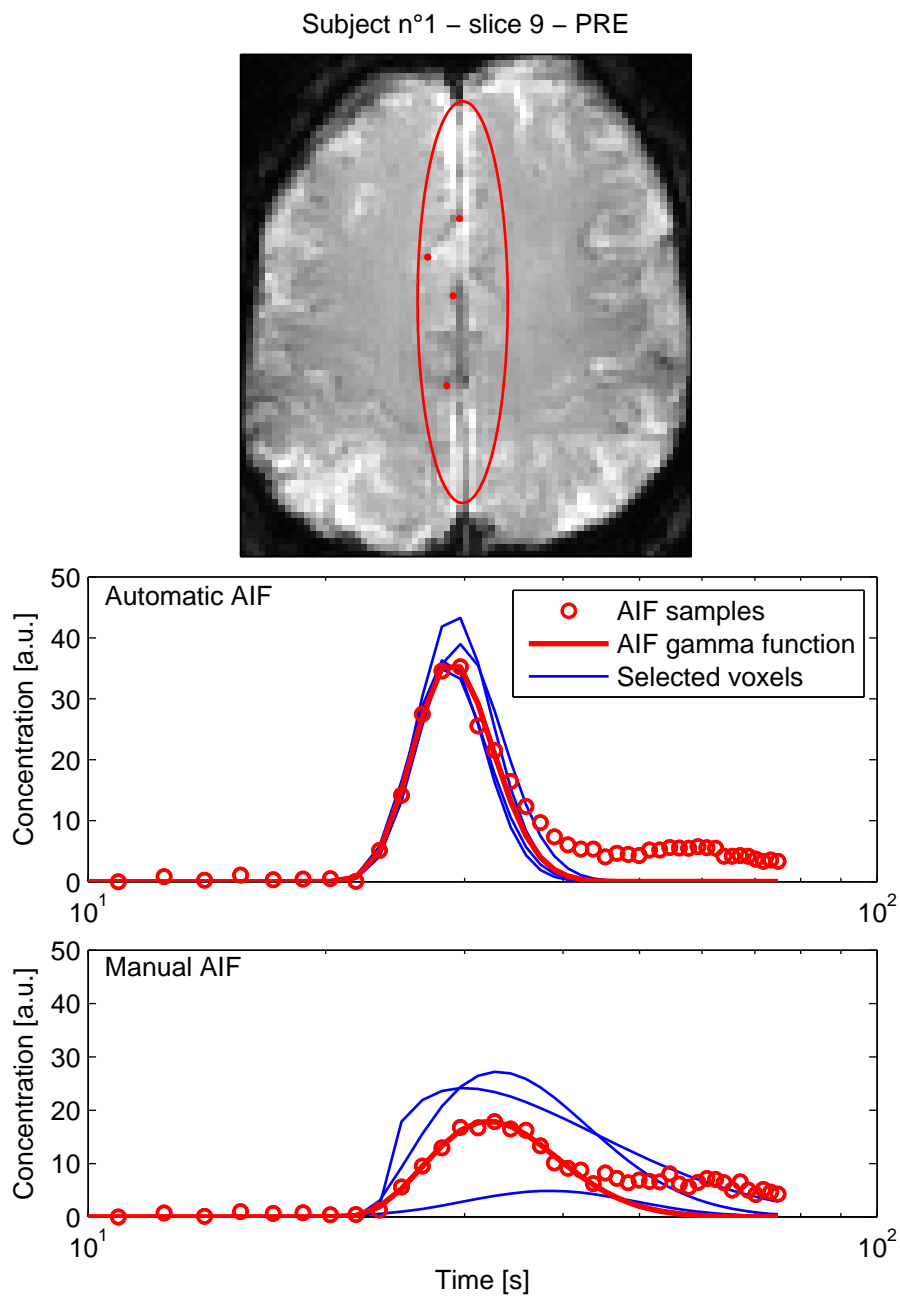


Figure 4.19: Selected AIFs in subject #1 pre surgery. The upper panel shows the slice containing MCA, the searching area (red line) and the selected voxel location (red dot). The middle and lower panels report automatic and manual AIF, respectively. Results are presented as a comparison among the estimated AIF, the selected voxels and the concentration mean samples. Horizontal axes are set in logarithmic scale and shifted by 10 seconds in order to emphasize the curve differences.

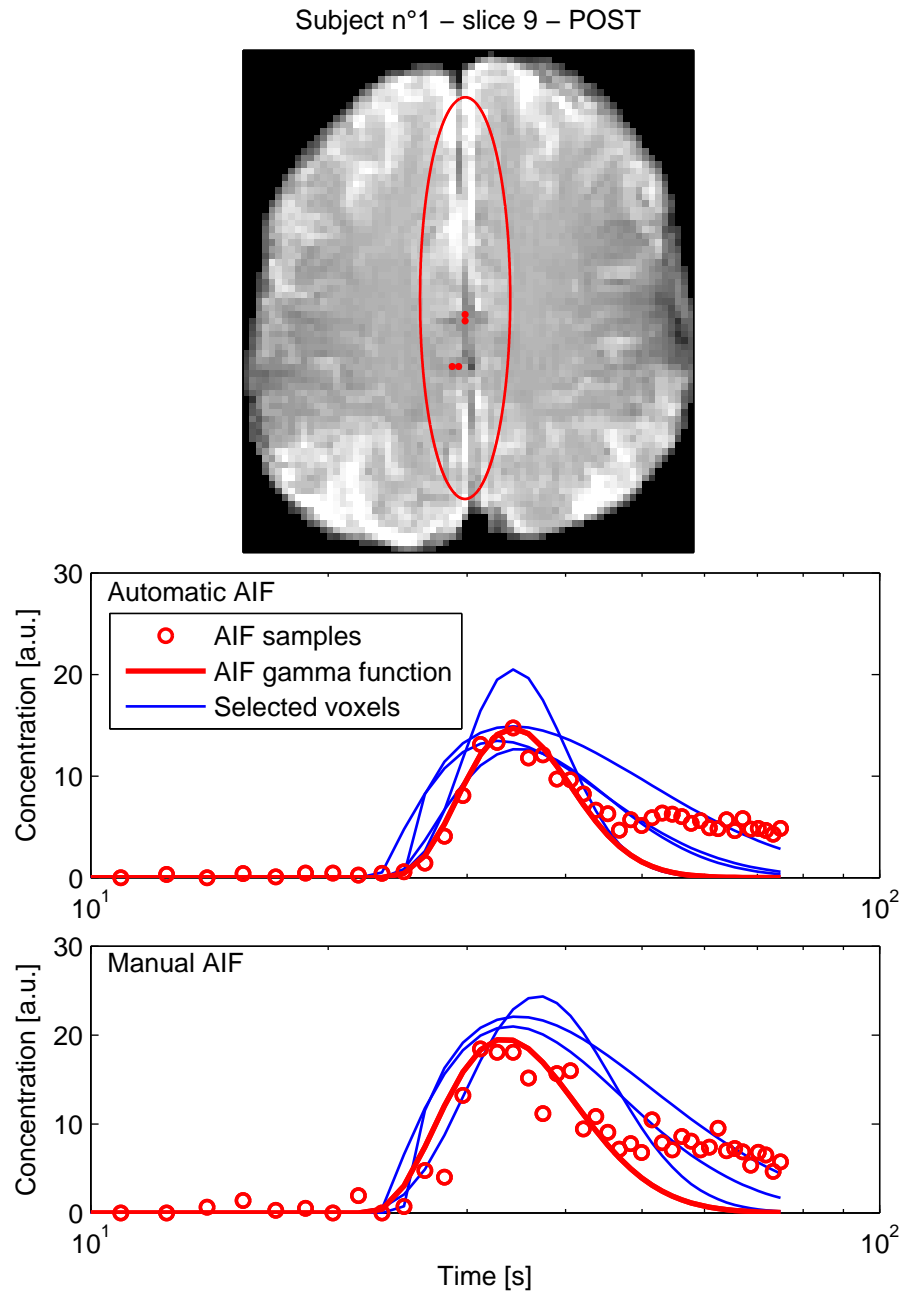


Figure 4.20: Selected AIFs in subject #1 post surgery. The upper panel shows the slice containing MCA, the searching area (red line) and the selected voxel location (red dot). The middle and lower panels report automatic and manual AIF, respectively. Results are presented as a comparison among the estimated AIF, the selected voxels and the concentration mean samples. Horizontal axes are set in logarithmic scale and shifted by 10 seconds in order to emphasize the curve differences.

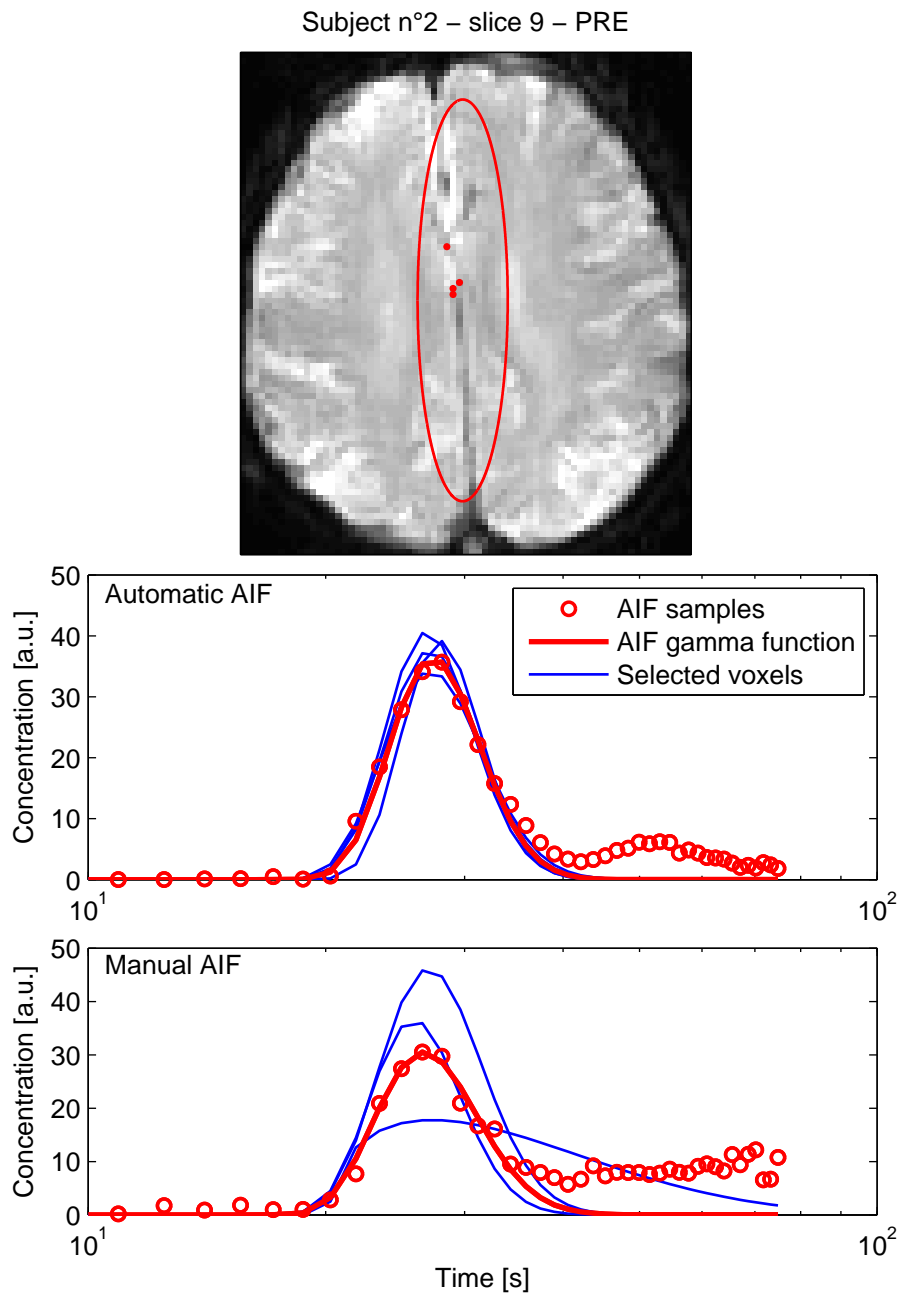


Figure 4.21: Selected AIFs in subject #2 pre surgery. The upper panel shows the slice containing MCA, the searching area (red line) and the selected voxel location (red dot). The middle and lower panels report automatic and manual AIF, respectively. Results are presented as a comparison among the estimated AIF, the selected voxels and the concentration mean samples. Horizontal axes are set in logarithmic scale and shifted by 10 seconds in order to emphasize the curve differences.

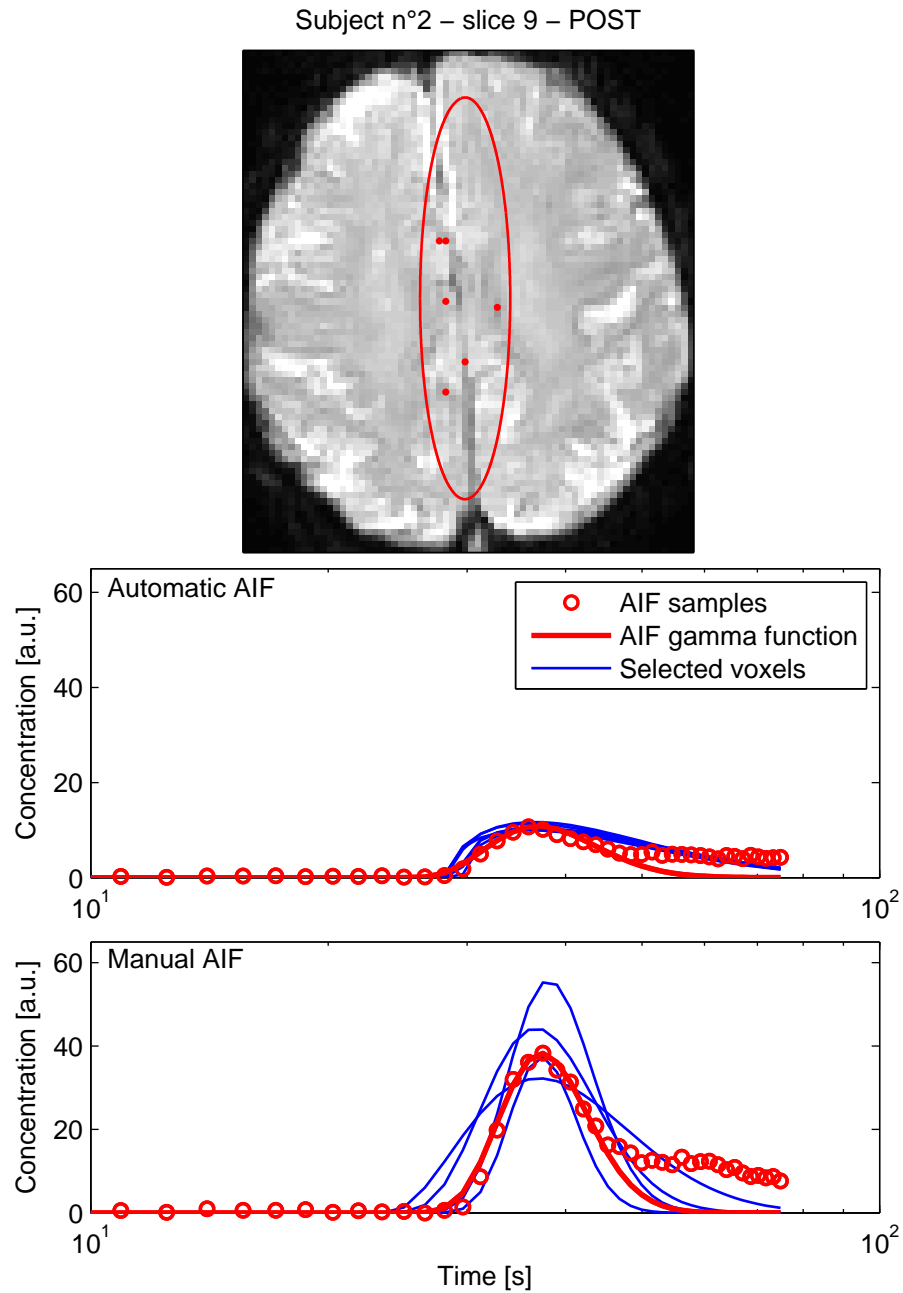


Figure 4.22: Selected AIFs in subject #2 post surgery. The upper panel shows the slice containing MCA, the searching area (red line) and the selected voxel location (red dot). The middle and lower panels report automatic and manual AIF, respectively. Results are presented as a comparison among the estimated AIF, the selected voxels and the concentration mean samples. Horizontal axes are set in logarithmic scale and shifted by 10 seconds in order to emphasize the curve differences.

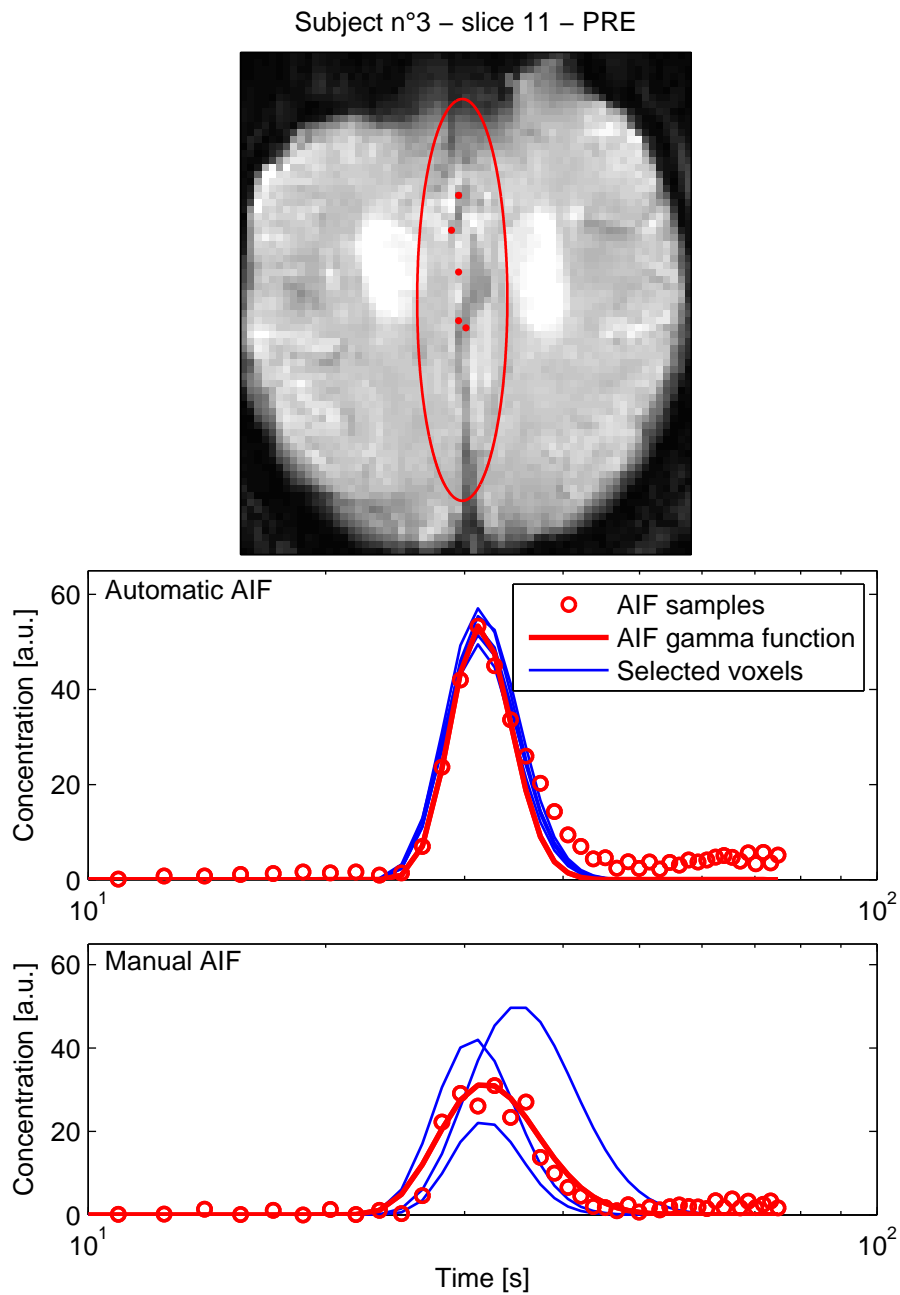


Figure 4.23: Selected AIFs in subject #3 pre surgery. The upper panel shows the slice containing MCA, the searching area (red line) and the selected voxel location (red dot). The middle and lower panels report automatic and manual AIF, respectively. Results are presented as a comparison among the estimated AIF, the selected voxels and the concentration mean samples. Horizontal axes are set in logarithmic scale and shifted by 10 seconds in order to emphasize the curve differences.

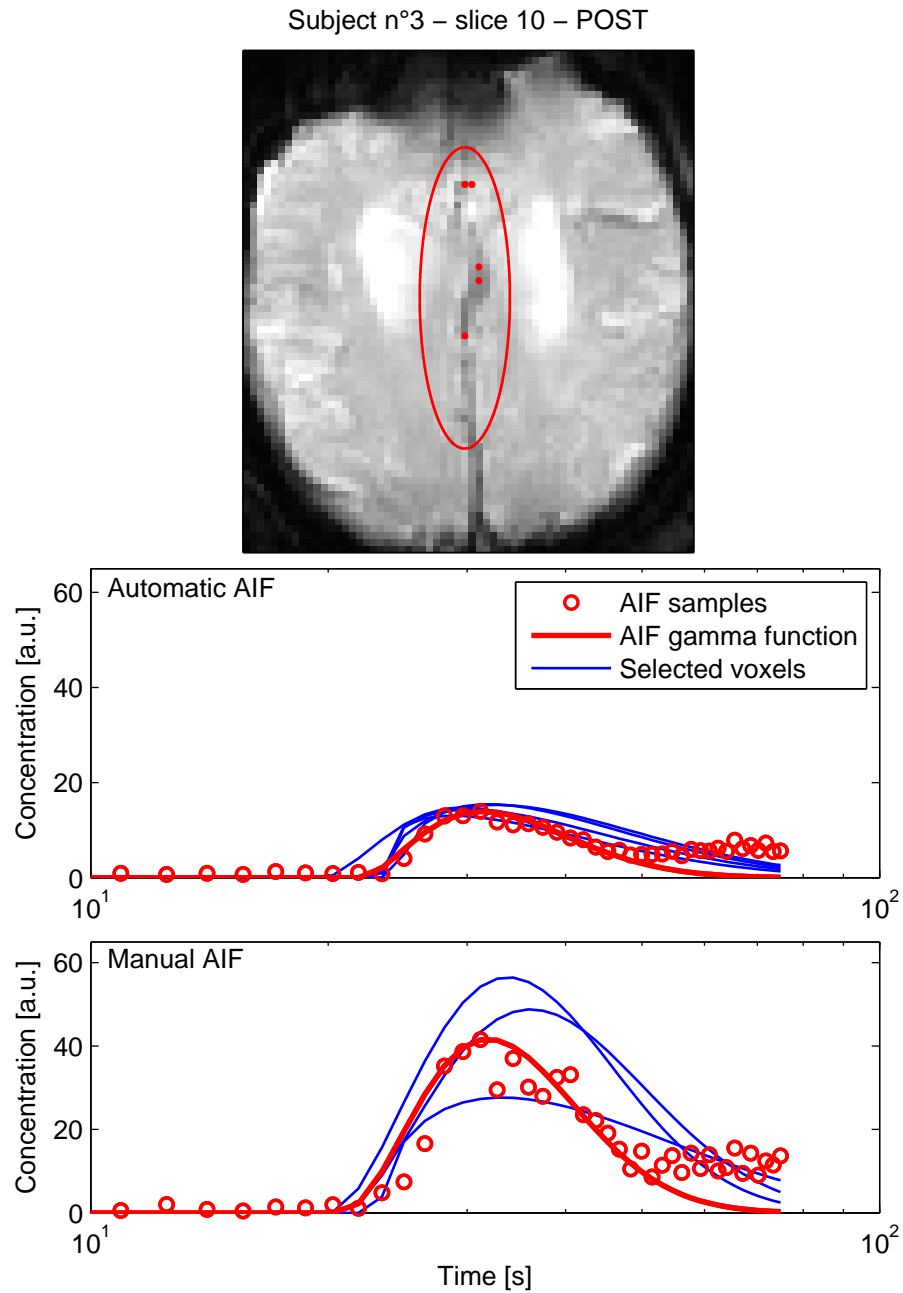


Figure 4.24: Selected AIFs in subject #3 post surgery. The upper panel shows the slice containing MCA, the searching area (red line) and the selected voxel location (red dot). The middle and lower panels report automatic and manual AIF, respectively. Results are presented as a comparison among the estimated AIF, the selected voxels and the concentration mean samples. Horizontal axes are set in logarithmic scale and shifted by 10 seconds in order to emphasize the curve differences.

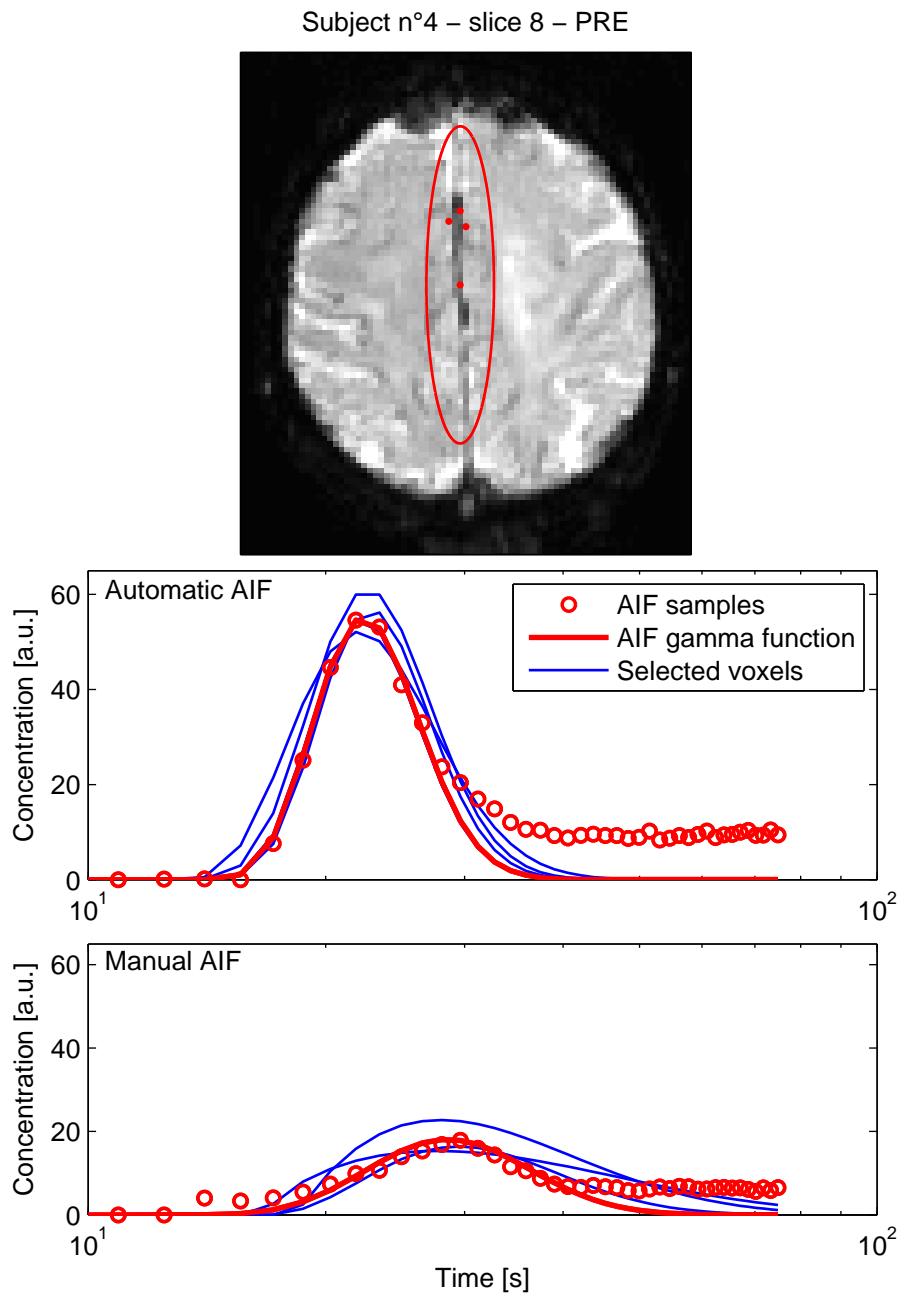


Figure 4.25: Selected AIFs in subject #4 pre surgery. The upper panel shows the slice containing MCA, the searching area (red line) and the selected voxel location (red dot). The middle and lower panels report automatic and manual AIF, respectively. Results are presented as a comparison among the estimated AIF, the selected voxels and the concentration mean samples. Horizontal axes are set in logarithmic scale and shifted by 10 seconds in order to emphasize the curve differences.

CBF and MTT values were estimated using both manual and automatic AIF in order to evaluate the AIF selection impact in the clinical image quantification. CBF and MTT maps were computed in each slice for all subjects by SVD applied voxel by voxel. In each slice, two large ROIs were manually drawn by a trained physician on the left and on the right hemisphere. The ROIs are delimited by the inter-hemispheric scissure and by the cerebral external border. Each ROI is drawn to contain only white and gray matter. Thus, if other structures (e.g, the basal ganglia) are visible, they are not included in the ROIs. Mean CBF and MTT values were computed in each ROI and a laterality percentage index was defined as follows:

$$\begin{aligned} CBF_{LI} &= \frac{CBF_{ROI_{DX}} - CBF_{ROI_{SX}}}{CBF_{ROI_{DX}}} \\ MTT_{LI} &= \frac{MTT_{ROI_{DX}} - MTT_{ROI_{SX}}}{MTT_{ROI_{DX}}} \end{aligned} \quad (4.7)$$

where  $CBF_{ROI_{DX}}$ ,  $CBF_{ROI_{SX}}$ ,  $MTT_{ROI_{DX}}$  and  $MTT_{ROI_{SX}}$  represent the CBF and MTT mean values in the right and left ROIs. CBV was also evaluated in order to obtain the MTT maps. However, CBV was not considered in the AIF impact analysis because it depends only on the AIF integral and AIF does not affect the CBV laterality index.

CBF and MTT laterality indices can be used to detect disease affected regions. Consider a patient with a stenosis in a carotid. The disease reduces the hematic support in the pathologic hemisphere: this is revealed by lower CBF values and higher MTT values than healthy hemisphere ones. Positive CBF laterality index indicates a higher mean CBF value in the right hemisphere than in the left one, suggesting a pathologic condition in the left hemisphere. Likewise, negative CBF laterality index points out a difference in CBF values in favour of the left hemisphere. Opposite remarks have to be done considering the MTT laterality index. Pathologic tissue is characterized by a slow blood flow, thus by a higher MTT than the healthy hemisphere. Therefore, positive MTT laterality index indicates higher MTT values in the right hemisphere than in the left one, thus suggesting that the right hemisphere is the pathologic one. Negative MTT laterality index indicates a higher MTT in the left hemisphere than in the right and that the disease is localized in the left hemisphere. Moreover, high absolute values in the laterality indices indicate a prominent hemodynamic difference between the two hemispheres, whereas small values characterize a healthy condition. Therefore, laterality indices can be used to evaluate both the disease severity and its localization.

Figures 4.26-4.29 report the CBF and the MTT laterality indices estimated in each slice and in each subject using both the manual and the automatic AIFs. The slice index indicates the slice position in the head: slice 1 is the nearest to the neck, whereas slice 12 is on the top of the head. The first and the last slices are usually very noisy, thus their results are less reliable than the ones of other slices. Pre surgery results are in the upper panels, whereas the post surgery analysis are in the lower ones. The CBF laterality indices are in the left panels and the right ones report the MTT laterality indices.

The CBF laterality indices obtained using the automatic AIF in subject #1 pre surgery indicate a wide difference in slices 6, 7 and 10 in favour of the left hemisphere (Figure 4.26). In these slices the difference is larger than 22% (slice

10), up to 47% in slice 6. Therefore, CBF is larger in the left hemisphere than in the right one. The MTT laterality index obtained with the automatic AIF is larger than 10% in all slices, with the exception of slices 1, 2 and 11. The largest MTT laterality indices are achieved in slices 6, 7 and 10. Therefore, both CBF and MTT laterality indices suggest that the disease is localized in the right hemisphere of slices 6, 7 and 10. The angiography examination confirms the information provided by the automatic AIF laterality indices. Analysis carried out using the automatic AIF also agree with the physician's diagnosis, but the differences are less marked than those provided by the automatic AIF analysis.

Laterality indices obtained using the automatic AIF change after the surgery treatment. CBF laterality indices decrease significantly in the slices affected by the disease: -28% in slice 6, -29% in slice 7 and -18% in slice 10. Generally, the CBF laterality index decreases also in the other slices. The MTT laterality index decreases in all slices, with the exception of slice 2 and 11. The largest decrease is registered in slices 5, 6, 7, 10 (-11% up to -16%). Therefore, the automatic AIF analysis suggests a significant improvement in the patient clinical picture. On the contrary, laterality indices obtained with the manual AIF do not significantly change before and after surgery. They rather suggest a disease aggravation in some slices, e.g. the CBF laterality index shows a 10% increase in slice 6 and the MTT one gets worse in all central slices.

Automatic and manual AIFs provide comparable results in subject #2, both in pre and post surgery analysis (Figure 4.27). CBF laterality indices present large negative values in slices 2 and 7 (-97% and -49% respectively), but they are coupled to small MTT laterality indices. On the contrary, slices 3, 4, 5 present large positive CBF laterality indices (15%, 27%, 18% respectively) and also large negative MTT laterality indices (-10%, -29%, -16%, respectively). Large negative MTT laterality indices are also registered in the upper slices, but the corresponding CBF indices are very small. Results provided by both manual and automatic AIF agree with the physician diagnosis, that localizes a stenosis in the left hemisphere.

After the surgery treatment, the anomalous CBF laterality indices almost disappear. The asymmetry in the pathological slices is recovered both in the CBF and in the MTT laterality indices. The MTT laterality indices show a small inversion in the asymmetry, but all values are smaller than 12

Automatic and manual AIFs perform comparably also in subject #3 (Figure 4.28). All slices present positive CBF and negative MTT laterality indices, with the only exception of slice 4 (CBF) and 6 (MTT). Therefore, both analyses suggest that the disease is in the left hemisphere, in agreement with the angiographic examination.

After the treatment the clinical picture appears not to change significantly. On the one hand, some slices present almost worse CBF laterality index (e.g. slice 5, 7, 10); on the other hand, other slices show improved CBF laterality indices (e.g. slice 8, 9, 11). All MTT laterality indices are still negative and they do not present significant differences between pre and post surgery analysis.

Manual and automatic AIFs provide very different laterality index results in subject #4 (Figure 4.29). A severe stenosis in the right hemisphere was pointed out by the physician using the conventional angiography. The analysis obtained using automatic AIF presents large negative CBF laterality indices,

most of all in slices 2, 6, 8, 9, 10. Moreover, very large positive MTT laterality indices are registered in all slices (all larger than 20%). Therefore, both the CBF and the MTT laterality indices suggest that the disease is localized in the right hemisphere, as in the diagnosis. On the contrary, the manual AIF analysis provides large positive CBF laterality indices in all slices except for slice 2, suggesting a disease in the left hemisphere. However, MTT laterality indices are also positive in all slices, suggesting a disease in the right hemisphere. Information provided by the manual AIF analysis are thus conflicting and in disagreement with the clinical diagnosis considering the CBF values.

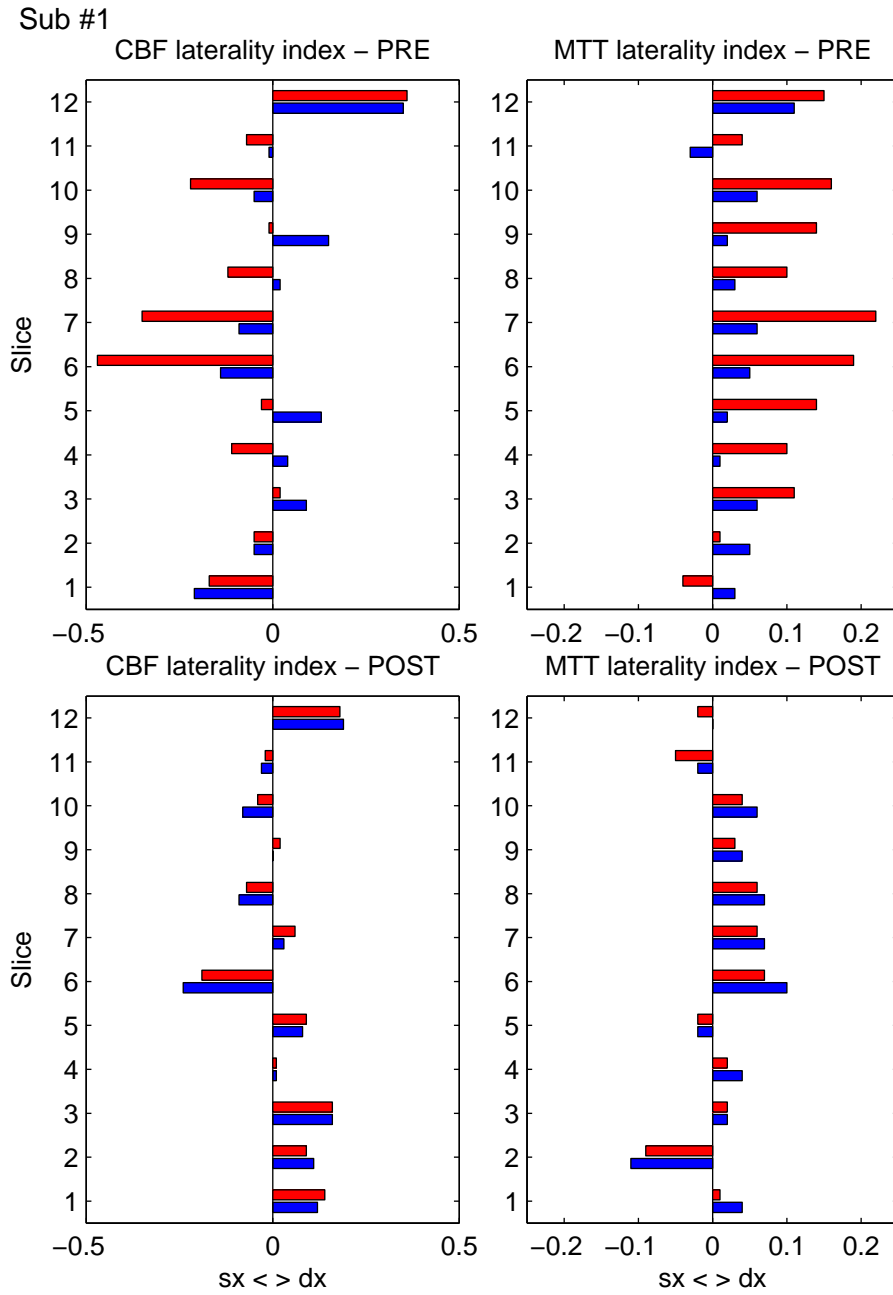


Figure 4.26: CBF and MTT laterality indices in subject #1. Results obtained using automatic AIF are reported with the red bars, whereas blue bars indicate the results obtained using manual AIF.

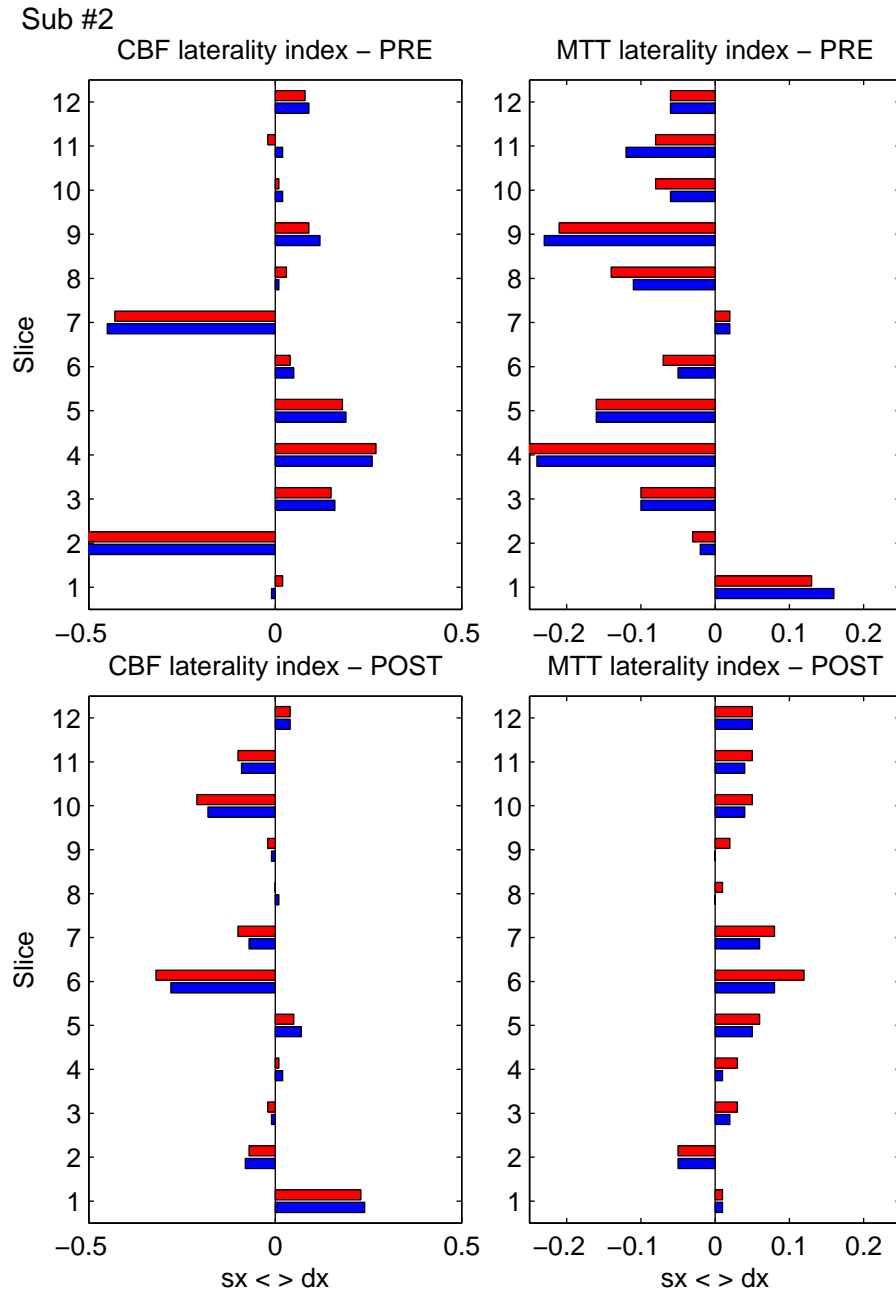


Figure 4.27: CBF and MTT laterality indices in subject #2. Results obtained using automatic AIF are reported with the red bars, whereas blue bars indicate the results obtained using manual AIF.

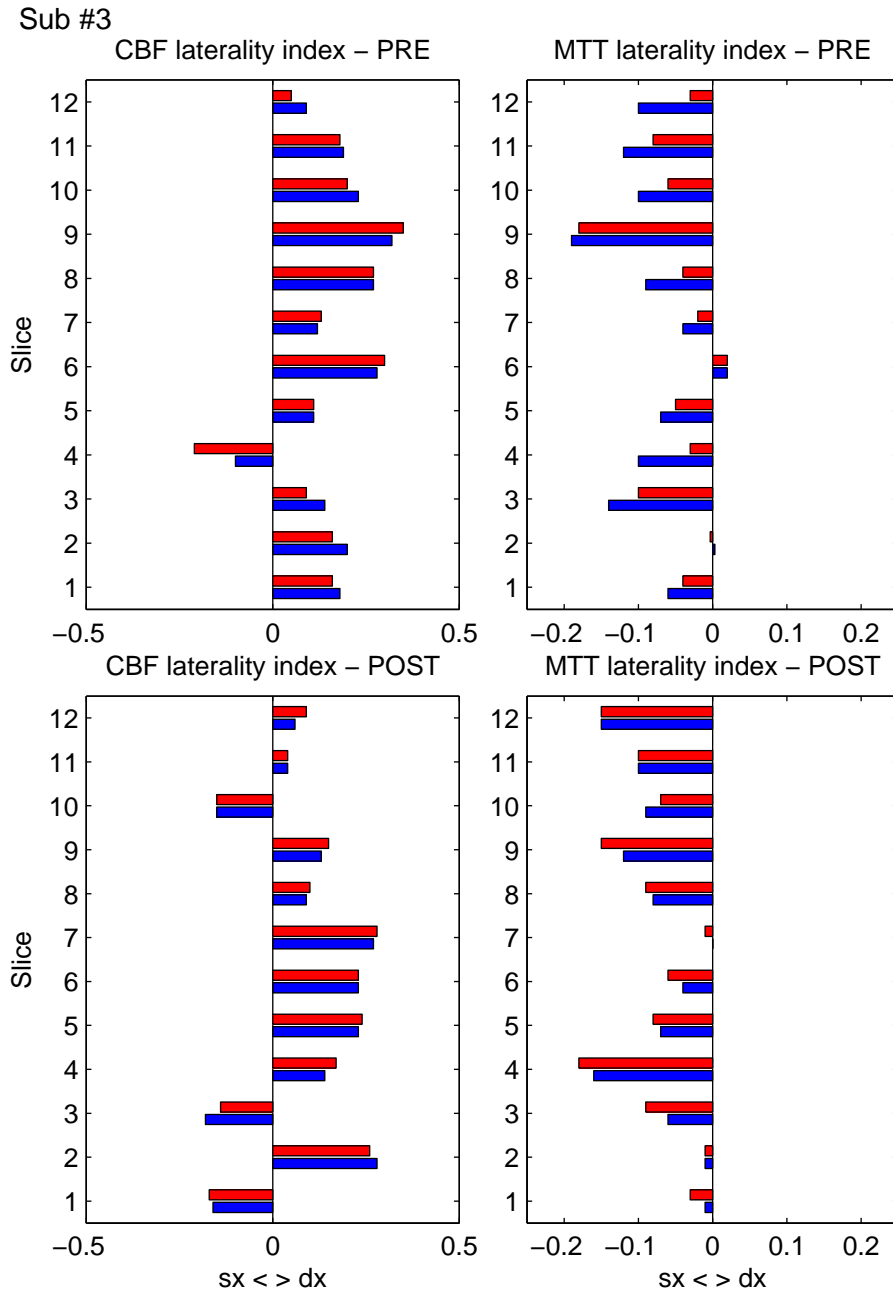


Figure 4.28: CBF and MTT laterality indices in subject #3. Results obtained using automatic AIF are reported with the red bars, whereas blue bars indicate the results obtained using manual AIF.

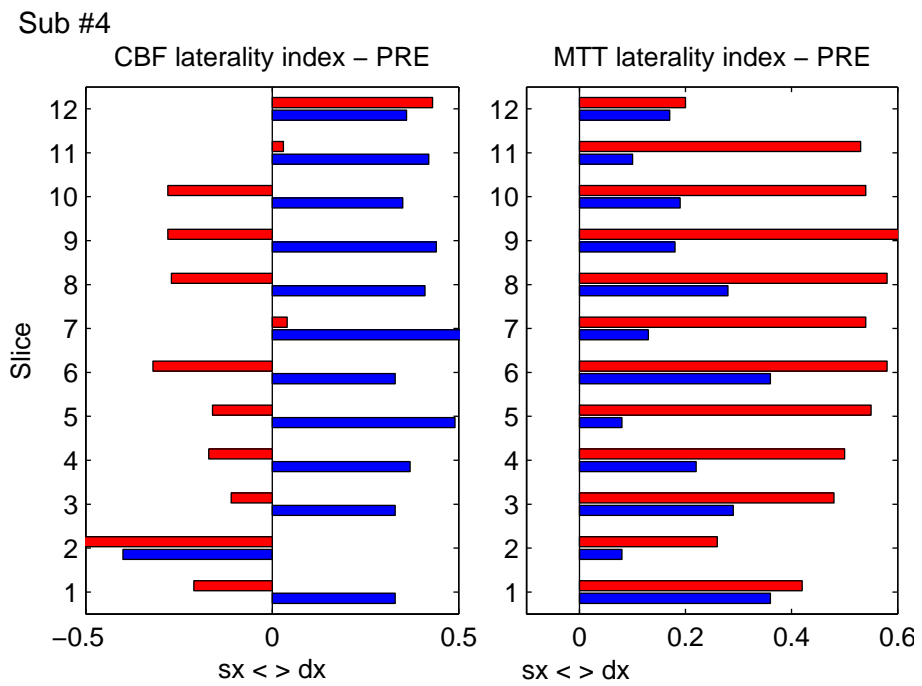


Figure 4.29: CBF and MTT laterality indices in subject #4. Results obtained using automatic AIF are reported with the red bars, whereas blue bars indicate the results obtained using manual AIF.

## 4.7 Clinical Data: Discussion

The automatic algorithm (HIER) for the arterial function selection has been proposed and applied to clinical DSC-MRI data. The clinical data set includes 11 patients with atherosclerotic unilateral stenosis of the internal carotid artery. In 8 out of the considered subjects, the DSC-MRI examination was repeated 6 months after the surgery intervention to completely or partially eliminate the stenosis. In 4 subjects, the AIF was detected both with automatic and manual methods, to compare their performances. 3 subjects of this subset also have post surgery examination.

*Manually selected AIF* is currently the gold standard in the DSC-MRI image quantification. However, it requires trained staff and it is scarcely reproducible as it is operator dependent. Arterial voxels can be selected either directly on the DSC-MRI images, or on the anatomical MRI images. Yet, in the first case images feature low spatial resolution, whereas in the second case, the coregistration problem between anatomical and functional images needs to be solved.

In this work, manual AIF performances were not optimal. Manually selected voxels are significantly different in their time-concentration curve. For instance, they present different dispersion levels, they are delayed or they feature different concentration peaks. This leads to a global AIF with a high noise level and an irregular shape. Therefore, it appears to be highly affected by partial volume effect and it is not reliable.

The *automatic AIF* selection algorithm detects the middle cerebral artery (MCA) in the first slice above the corpus callosum. Firstly, it highlights the region where the MCA is expected to be. Then, it extracts the AIF by a dichotomously applied hierarchical clustering. Therefore, it integrates anatomical and functional information in the arterial voxel detection. Many other methods work on the restricted area containing the artery, but the area is manually selected. Here, an automatic method to detect the searching area has been proposed and validated for the first time.

HIER has been shown to select almost identical voxels. Moreover, the obtained AIF presents a very regular shape, sometimes with the typical secondary peak in recirculation. Therefore, HIER demonstrated to provide an AIF which is not biased by partial volume effect.

Both automatic and manual AIFs have been used to compute CBF, CBV and MTT maps using SVD; CBF and MTT laterality indices have been defined. The laterality indices obtained through automatic AIF offer information which confirm the patient clinical picture provided by a physician with a standard angiography. Although laterality indices provided by manual AIF do confirm the clinical picture, pathology may be less evident, and information may even be inconsistent.

In conclusion, automatic AIF stands out as an innovative method to overcome manual AIF shortcomings and gather useful information for the diagnosis in atherosclerotic patients.



## Chapter 5

# Dynamic Susceptibility Contrast -MRI: Population Deconvolution

A new deconvolution method for DSC-MRI image quantification is presented here, the *Population Deconvolution* (PD) method. First of all, the deconvolution method theory is explained, pointing out how it applies the population approach to the problem. After describing the simulation set up and assessment criteria, PD is validated on the simulated data and compared to SVD and cSVD. Subsequently, SVD, cSVD, NSR and PD are assessed and compared on clinical data.

### 5.1 Theory

One of the main issues in the deconvolution operation is *ill-conditioning*. This means that the deconvolution is highly biased by the noise in the data. Low noise levels in the sampled data lead to high errors in the estimated results; for instance, unphysiological oscillations or negative values in the estimated residue function ( $R(t)$ ). Furthermore, ill-conditioning gets worse as the sampling rate increases and in case of low kinetic systems.

The SVD method reduces the noise impact in the estimated  $R(t)$  by using a threshold to eliminate small eigenvalues in matrix  $\mathbf{W}$  (see section 3.2.1, page 23). SVD is based on the hypothesis that small eigenvalues in ( $W$ ) are due to noise in the data., It reduces the noise impact in  $R(t)$ , thus increasing the solution regularity by eliminating these eigenvalues.

All deconvolution methods proposed in DSC-MRI image quantification are voxel based. This means that the deconvolution operation is performed in each voxel separately from the others. However, the idea that similar voxels are characterized by similar residue functions can be easily assumed. Moreover, tackling the deconvolution problem on a population basis increases the available information amount available.

The PD method, proposed in [27, 59], exploits the population approach to estimate the residue function using a minimum variance estimator. Firstly, it reconstructs the voxel concentration curve without noise, taking advantage from the population approach. Then, it obtains the minimum variance  $R(t)$  for each voxel.

Let us consider a population of  $m$  voxels with the sampling grid  $\{t_k\}$ ,  $k = 1 : n$ . The concentration samples can be modelled as follows

$$\begin{aligned} y_k^j &= c^j(t_k) + v_k^j & j = 1, \dots, m \text{ and } k = 1, \dots, n \\ c^j(t) &= \bar{c}(t) + \tilde{c}^j(t) \end{aligned} \quad (5.1)$$

where  $y_k^j$  are the noisy concentration samples of  $j$ -th voxel;  $c^j(t)$  are the concentration samples without noise;  $v_k^j$  are the noise samples. The noise vectors  $\{v^j\} = [v_1^j \dots v_n^j]^T$  are assumed independent and normally distributed with  $E[v_k^j] = 0$  and variance matrix  $\Sigma_v^j$ . It is assumed that the individual curve  $c^j(t)$  can be decomposed in an average curve  $\bar{c}(t)$  and an individual shift from the average  $\tilde{c}^j(t)$ . Both the average curve and the individual shift are assumed to be zero-mean Gaussian stochastic processes.

The first step of the PD method provides the estimate of the average curve and the shift from the average for each voxel. In other words, it computes  $E[\bar{c}(\tau)|y]$  and  $E[\tilde{c}^j(\tau)|y]$  for  $j = 1 \dots m$ , where  $y = [y_1^1, y_2^1, \dots, y_n^1, y_1^2, \dots, y_n^m]^T$  is a column vector containing the whole voxel population samples. Noticeably,  $\tau$  is a generic temporal instant, thus PD allows to reconstruct the voxel concentration curve and the residue function on a generic temporal grid.

The average curve is computed starting from the known formula on the joint Gaussian vectors

$$E[\bar{c}(\tau)|y] = cov[\bar{c}(\tau), y] \cdot Var[y]^{-1} \cdot y \quad (5.2)$$

Where  $cov[q, w] = E[(q - E[q])(w - E[w])^T]$  and  $Var[q] = E[(q - E[q])(q - E[q])^T]$ . Let define the following symbols

$$\begin{aligned} \bar{c} &= [\bar{c}(t_1) \dots \bar{c}(t_n)]^T \\ \bar{c}_\tau &= [\bar{c}(t_\tau) \bar{c}(t_1) \dots \bar{c}(t_n)]^T \\ \tilde{c}^j &= [\tilde{c}^j(t_1) \dots \tilde{c}^j(t_n)]^T \\ \bar{Q} &= Var[\bar{c}] \\ \tilde{Q} &= Var[\tilde{c}^j] \\ \bar{q}_\tau &= cov[\bar{c}(\tau), \bar{c}] \\ \xi_\tau &= E[\bar{c}(\tau)|y] \\ \xi &= E[\bar{c}|y] \\ \tilde{Q}_v^j &= \tilde{Q} + \Sigma_v^j \\ F &= \sum_{i=1}^m (\tilde{Q}_v^i)^{-1} \end{aligned} \quad (5.3)$$

The solution of Eq. (5.2) can be proved to be

$$\begin{aligned}\xi_\tau &= E[\bar{c}(\tau)|y] = \bar{q}_\tau b \\ b &= \left[ \sum_{i=1}^m (\tilde{Q}_v^i)^{-1} y^i \right] - F(\bar{Q}^{-1} + F)^{-1} \sum_{j=1}^m (\tilde{Q}_v^j)^{-1} y^j\end{aligned}\quad (5.4)$$

If we consider Eq. (5.2), it seems that the computation of  $E[\bar{c}(\tau)|y]$  calls for the inversion of an  $nm$ -th order matrix. However, the relationships reported in Eq. (5.4) demonstrate that only  $n$ -th order inverses are required.

The individual curve of the  $j$ -th voxel can be computed on a arbitrary temporal grid as follows

$$E[c^j(\tau)|y] = \xi_\tau + \tilde{q}_\tau \cdot (\tilde{Q} + \Sigma_v^j)^{-1} \cdot (y^j - \xi) \quad (5.5)$$

Eq. (5.5) provides the minimum variance estimate of each voxel concentration curve. From it, the minimum variance estimate of each voxel residue function can be easily obtained using the simple raw deconvolution method.

Now, the problem is estimating the covariance matrices defined in Eq. (5.3). Starting from Eq. (2.12) the residue function can also be decomposed into a typical curve and an individual shift

$$\begin{aligned}R(t) &= \bar{R}(t) + \tilde{R}(t) \\ c(t) &= \bar{c}(t) + \tilde{c}(t) \approx CBF \cdot AIF(t) \otimes (\bar{R}(t) + \tilde{R}(t)) \\ \text{from which} & \\ \bar{c}(t) &\approx CBF \cdot AIF(t) \otimes \bar{R}(t) \\ \tilde{c}(t) &\approx CBF \cdot AIF(t) \otimes \tilde{R}(t)\end{aligned}\quad (5.6)$$

Now, the  $R(t)$  stochastic model has to be introduced.  $R(t)$  is expected to be a decreasing function and to tend to zero. However, a stochastic model whose variance increases with time is easier to define than the contrary. Therefore, a time transformation is performed so that the new time  $\tilde{t}$  ranges from 0 to 1, according to the formula  $\tilde{t} = 1/(1+t/\gamma)$ . Parameter  $\gamma$  was set to the value that maximizes the minimum distance between each pair of transformed sampling instants. Noticeably,  $t = 0$  corresponds to  $\tilde{t} = 1$  and  $t = \gamma$  to  $\tilde{t} = 0.5$ , hence the time axes is inverted in the new temporal space with respect to the old temporal space. A stochastic model with a variance increasing with time in the new temporal space corresponds to a stochastic model with a variance decreasing with time in the old temporal space. Consequently, the time transformation allows to simply define a stochastic model for a decreasing function tending to zero. Both the typical residue curve and the individual shifts are modelled as integrated Wiener processes. For instance, in the case of  $\bar{R}(t)$ , it is

$$\begin{cases} \dot{\bar{z}}(\tilde{t}) = \mathbf{A}\bar{z}(\tilde{t}) + \bar{\lambda}\mathbf{B}\bar{\omega}(\tilde{t}) \\ \bar{R}(\tilde{t}) = \mathbf{C}\bar{z}(\tilde{t}) \end{cases} \quad (5.7)$$

where  $\bar{\lambda}$  is an unknown hyper-parameter ( $\bar{\lambda}$  estimate problem will be discussed later),  $\bar{\omega}$  is a unit intensity white noise and

$$A = \begin{pmatrix} 0 & 1 \\ 0 & 0 \end{pmatrix} \quad B = \begin{pmatrix} 0 \\ 1 \end{pmatrix} \quad C = ( 0 \quad 1 ) \quad (5.8)$$

Therefore, the covariances of the residue function average curve and individual shifts are

$$\begin{aligned} \text{cov} [\bar{R}(s), \bar{R}(\tau)] &= \bar{\lambda}^2 \begin{cases} \frac{s^2}{2}(\tau - \frac{s}{3}) & s \leq \tau \\ \frac{\tau^2}{2}(s - \frac{\tau}{3}) & s > \tau \end{cases} \\ \text{cov} [\tilde{R}^j(s), \tilde{R}^j(\tau)] &= \tilde{\lambda}^2 \begin{cases} \frac{s^2}{2}(\tau - \frac{s}{3}) & s \leq \tau \\ \frac{\tau^2}{2}(s - \frac{\tau}{3}) & s > \tau \end{cases} \end{aligned} \quad (5.9)$$

To obtain the  $\bar{c}(t)$  and  $\tilde{c}(t)$  covariance from the  $\bar{R}(t)$  and  $\tilde{R}(t)$  ones, the discrete formulation of the convolution in Eq has to be considered. (5.6). Let  $\bar{\mathbf{C}}$  be a square matrix containing the  $\bar{c}(t)$  covariance values,  $\mathbf{AIF}$  the square Toeplitz matrix containing the AIF samples for the discrete convolution and  $\bar{\mathbf{R}}$  be a square matrix containing the  $\bar{R}(t)$  covariance values. Then,

$$\bar{\mathbf{C}} = CBF \cdot (\mathbf{AIF} \cdot \bar{\mathbf{R}} \cdot \mathbf{AIF}^T) \quad (5.10)$$

A similar relationship can be derived for the process  $\tilde{c}(t)$  and  $\tilde{R}(t)$ .

The  $\bar{R}(t)$  and  $\tilde{R}(t)$  models depend on the hyper-parameters  $p = [\bar{\lambda}, \tilde{\lambda}]^T$ . They account for the amplitude of the stochastic processes that model  $\bar{R}(t)$  and  $\tilde{R}(t)$ . However, they are not known in the real data and have thus to be estimated. The problem can be solved resorting to a Maximum Likelihood (ML) estimator. The hyper-parameters are estimated by minimizing the following objective function:

$$\hat{p} = \underset{p}{\text{argmin}} L(y; p) \quad (5.11)$$

with

$$L(y; p) = \log [\det (\text{Var}[y])] + y^T \text{Var}[y]^{-1} y \quad (5.12)$$

where the likelihood component estimate can be obtained from

$$\begin{aligned} y^T \text{Var}[y]^{-1} y &= \sum_{i=1}^m m(y^i)^T d^i \\ d^i &= \left[ (\tilde{Q}_v^i)^{-1} y^i - (\tilde{Q}_v^i)^{-1} (\bar{Q}^{-1} + F)^{-1} \sum_{j=1}^m (\tilde{Q}_v^j)^{-1} y^j \right] \end{aligned} \quad (5.13)$$

and

$$\det (\text{Var}[y]) = \left( \prod_{i=1}^m \det(C_{ii}) \right)^2 \quad (5.14)$$

with  $C_{ii}$   $n \times n$  matrices such that

$$\begin{aligned} C_{ii} &= \text{chol}[A_{ii} - D_i] & C_{(i+1)i} &= (\bar{Q} - D_i)(C_{ii}^T)^{-1} \\ C_{ki} &= C_{(i+1)i} \quad k > i + 1 & D_{i+1} &= D_i + C_{(i+1)i} C_{(i+1)i}^T \\ D_1 &= 0 & C_{21} &= \bar{Q}(C_{11}^T)^{-1} \end{aligned}$$

where  $chol[K]$  denotes the Cholesky factorization of the matrix  $K$ ,  $A_{kk} = \bar{Q} + \tilde{Q} + \Sigma_v^k$  indicates the  $k$ -th  $n \times n$  block of the main diagonal of  $Var[y]$ .

Once the hyper-parameters are estimated, they can be substituted in the equations (5.4) and (5.5) to obtain the individual concentration curve  $c^j(t)$  and consequently, the individual residue function  $R^j(t)$ . This technique is usually called Empirical Bayes method.

Refer to [27, 59] for a more precise formulation of the PD method and for the proposed result proofs.

The main feature of the PD method is the *population approach*. Performing the deconvolution operation of several voxels at the same time allows the algorithm to exploit a large amount of information. The larger the voxel number simultaneously analyzed, the greater the available information. However, large populations may also become a source of errors. If the analysed voxels belong to two different populations, then a bias is introduced to the noise free concentration curve. As a consequence, the estimated residue function is also biased. The larger the voxel number simultaneously analyzed, the greater the risk that different population are considered. Therefore, a good method to separate the different voxel populations is necessary.

As previously described, PD allows to reconstruct the concentration curve and the residue function of each voxel on an arbitrary time grid. Thus, PD is not influenced by the sampling frequency. Furthermore, it can reconstruct the residue function on a fine temporal grid, which is very useful when the whole  $R(t)$  shape is of interest.

PD is a linear deconvolution method, with the exception of the hyper-parameters computation step. Thus, it is computationally not much expensive. However, the hyper-parameters estimation is the most computationally expensive and crucial step in the PD method because provided results are heavily influenced by the hyper-parameter estimate.

Another important feature of PD is that a noise statistical description ( $\Sigma_v$ ) is required. Currently, no standard method to evaluate the noise statistical description from data has been achieved, yet. Since PD results are also influenced by the noise statistical description, a suitable model is necessary to describe noise.

## 5.2 Simulation: Set up

The simulated data set was obtained starting from a known AIF, obtained as suggested in [17, 61, 88]. The AIF concentration curve was modelled as a gamma-variate function

$$C_P(t) = \begin{cases} 0 & t < t_0 \\ A \cdot (t - t_0)^\alpha \cdot e^{-\frac{t}{\beta}} & \text{otherwise} \end{cases} \quad (5.15)$$

where  $A$  is a proportionality constant,  $t_0$  is the contrast arrival time,  $\alpha$  is a measure of the inflow velocity steepness and  $\beta$  is the washout velocity. The simulation parameter values are reported in table 4.2. Differently from the

simulation set up in section 4.2 (page 33), the simulated AIF does not present recirculation, but only the principal peak. Since the deconvolution operation has to be performed on the data without recirculation, a suitable strategy has to be adopted to eliminate recirculation. In this work, a fit with a Gamma-variate function is computed for each voxel concentration curve and for each AIF before applying the deconvolution algorithm when considering real data. Thus, this section will not dwell on simulating the recirculation. Four different residue functions were simulated, as suggested in [17]:

1. *Exponential function*  $R(t) = e^{-\frac{t}{MTT}}$ ;
2. *Lorentzian function*  $R(t) = \frac{1}{[1+(0.5\pi\frac{t}{MTT})^2]}$ ;
3. *Gamma-variate function*  $R(t) = t \cdot e^{-\frac{t}{\sqrt{MTT}}}$ ;
4. *Dispersed Exponential function*  $R(t) = \frac{e^{-\frac{t}{3}} - e^{-\frac{t}{MTT}}}{\frac{3}{MTT} - 1}$ ;

The Exponential and the Lorentzian functions were selected to simulate the *dispersion absence* in the data, whereas the Gamma-variate and the Dispersed Exponential were selected to simulate the *dispersion presence*. As required by the residue function definitions,  $R(t=0) = 1$  and  $\int_0 R(t)t = MTT$  in absence of dispersion; whereas  $R(t=0) = 1$  and  $\int_0 R(t)t = MTT$  in presence of dispersion.

Tissue concentration time curves ( $C_{VOI}(t)$ ) were obtained from Eq. 2.12 considering a time range between 0 and 120 seconds. CBF was assumed to be a stochastic Gaussian process with  $22 \pm 3, 52$  ml/100g/min as mean and standard deviation, respectively. MTT was assumed to be a stochastic Gaussian process too, with  $6, 3 \pm 1$  sec as mean and standard deviation, respectively. Simulation parameter settings correspond to values typically found in clinical data white matter [88] and are reported in table 5.1.

Noisy time concentration curves were obtained adding a zero mean Gaussian noise. Noise standard deviation was varied to simulate different *signal to noise ratio* (SNR). SNR is defined as the ratio between the signal power (meaningful information) and the noise power. Four different noise conditions were generated: clinical data noise typical level (SNR 10), high noise level (SNR 5), low noise level (SNR 50), virtually non noisy data (SNR 500).

PD was compared to the most applied deconvolution methods in DSC-MRI image quantification to validate the method. In particular, the simulated data were analyzed using the following algorithms, implemented as proposed in the original publications

- *Singular value decomposition* (SVD) as in [61, 62];
- *Block-circulant singular value decomposition* (cSVD), as in [88]
- *Population deconvolution* (PD).

Simulation Parameters	
$t_0$	10 s.
$A$	8
$\alpha$	3 adim.
$\beta$	1.5 s.
$\rho$	$0.0104 \frac{100g}{ml}$
$k_H$	0.73

Table 5.1: Parameter values in the simulated data generation.

## 5.3 Simulation: Results

### 5.3.1 Residue Function Reconstruction

The residue function was successfully estimated for each simulated voxel using PD, SVD and cSVD methods.

The *root mean square error* (RMSE) between each estimated  $R(t)$  and the true  $R(t)$  was computed to evaluate the ability of each algorithm to reconstruct the true residue function. RMSE was computed using Eq. (4.6). Figure 5.1 reports the RMSE mean and standard deviation (SD) obtained by SVD, cSVD and PD in each residue function model and in each noise level. The PD method always provides the best results. Its estimated  $R(t)$ s are more similar to the true ones than the SVD and cSVD ones. In each noise level, PD and SVD present constant performances in reconstructing exponential, lorentzian and dispersed exponential residue functions, whereas results get worse when considering the gamma-variate model for the residue function. Differently, cSVD performs best when estimating dispersed exponential  $R(t)$ , whereas its results get worse when considering the other  $R(t)$  models. As expected, SVD performs significantly better than cSVD when considering non dispersed  $R(t)$ , whereas the situation reverses when a dispersed model is considered. Nevertheless, SVD and cSVD provide very similar results in the dispersed models.

Some realizations of estimated residue functions at the noise level typically present in the clinical data (SNR 10) are reported in Figure 5.2. The voxel with the best results and the one with the worst results were chosen in each residue function model on the basis of the distance between the true  $R(t)$  and the estimated one. In each panel, the true  $R(t)$  is compared to the ones reconstructed by using PD, SVD and cSVD. PD always provides  $R(t)$ s which are closer to the true ones than those obtained by SVD and cSVD. The residue functions estimated using PD present indeed very small and damped oscillation if compared to the SVD and cSVD ones, providing a more reliable  $R(t)$ . In the worst cases,  $R(t)$ s given by SVD and cSVD present non reliable shapes, with wide oscillations and negative values. Similar results were obtained considering other noise levels (data not shown).

### 5.3.2 Impact on Cerebral Blood Flow Estimates

CBF was computed for each voxel as the maximum of the estimated residue function. Remember that, when dispersion is present in the residue function,

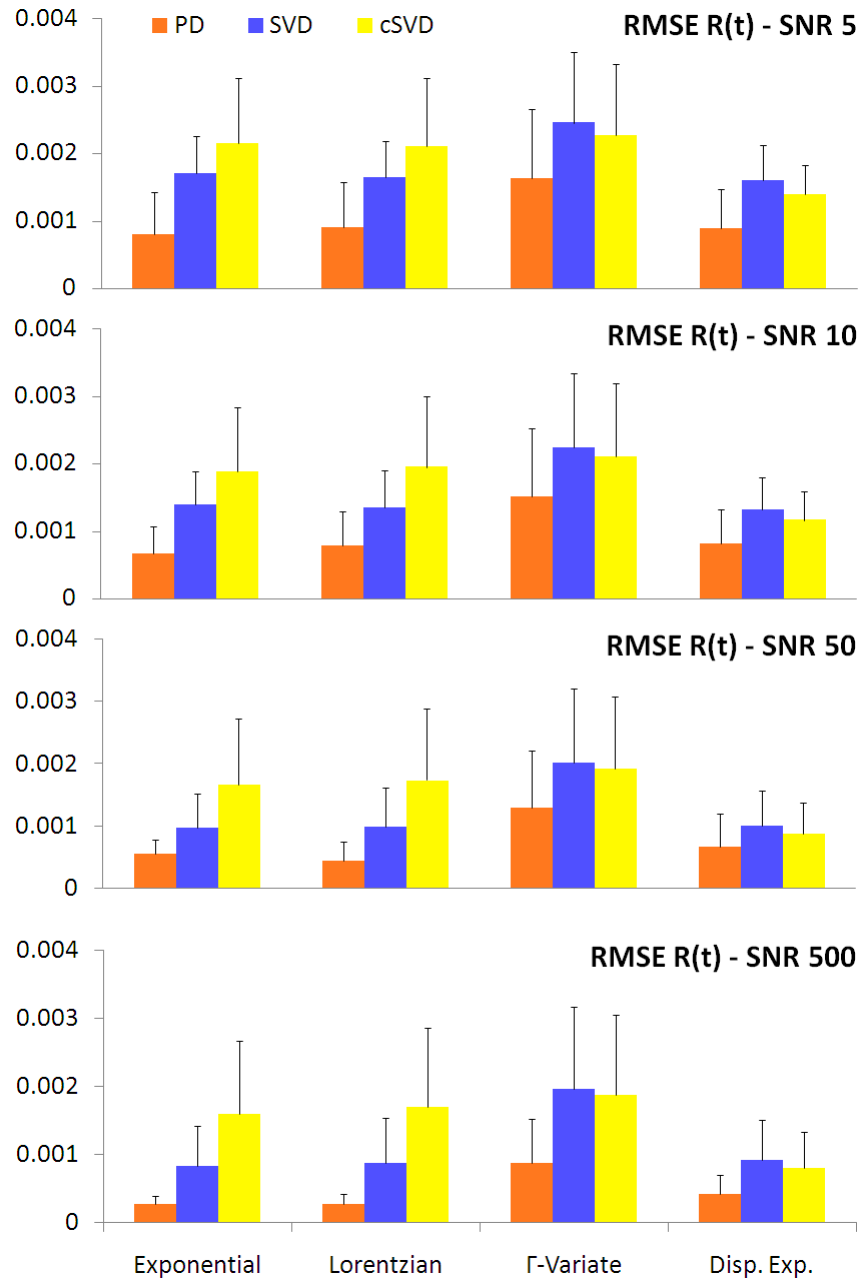


Figure 5.1: RMSE between the reconstructed and the true residue functions.

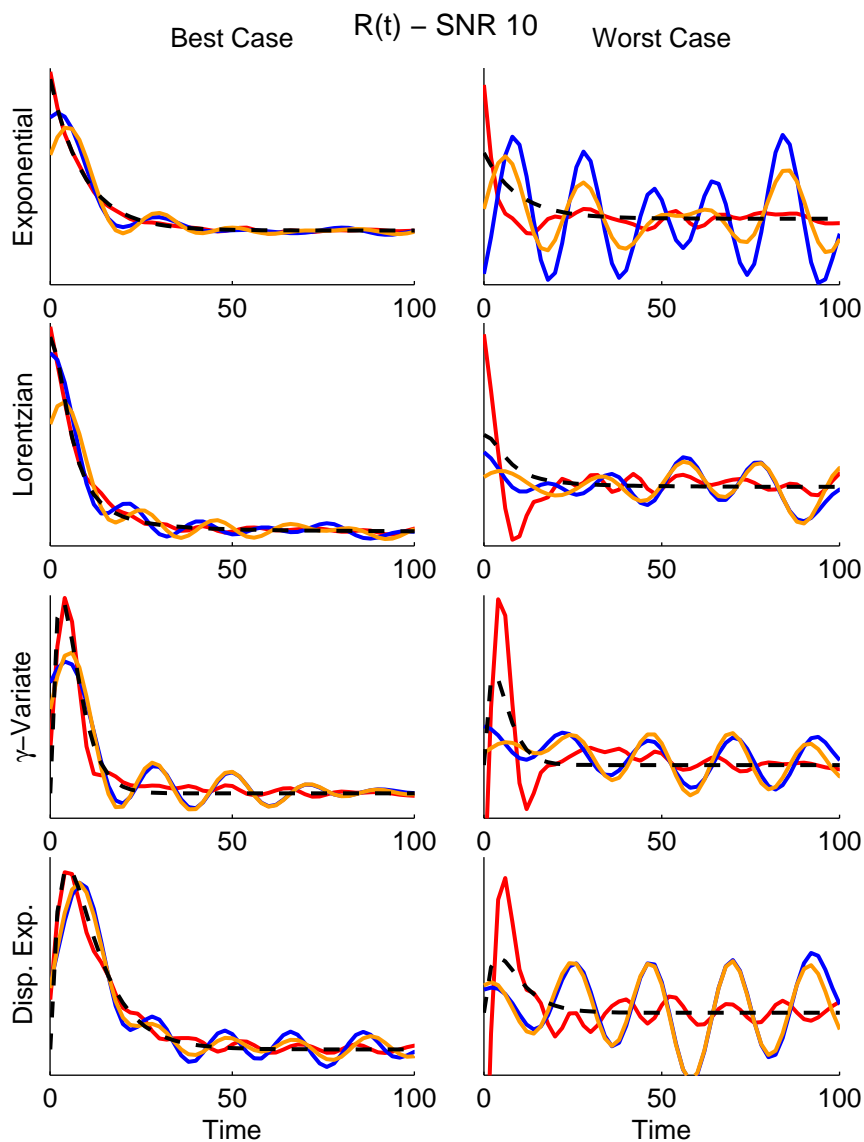


Figure 5.2: Examples of reconstructed residue functions at SNR 10. Red lines represent the PD reconstructed  $R(t)$ , the blue lines represent the SVD reconstructed  $R(t)$  and yellow lines represent the cSVD results. True  $R(t)$  is reported using black dashed lines.

estimated CBFs are intrinsically biased by underestimation. The percentage error between the estimated CBF and the real CBF was computed for each voxel. Figure 5.3 shows the percentage error mean and SD obtained using the different deconvolution methods. Results are subdivided into the different residue function models and noise levels. PD presents the smallest mean error in all cases, with the exception of Lorentzian  $R(t)$  at SNRs 5 - 10 and dispersed exponential  $R(t)$  at SNR 500. In these cases, SVD provides a smaller mean error than PD. PD is characterized by a larger SD than SVD and cSVD. When considering non dispersed residue functions, SVD performs significantly better than cSVD, providing very small mean error, whereas they provide comparable results when dispersion is present in the residue function. SVD and cSVD always underestimate the true CBF for each residue function model. PD presents overestimated CBF for the exponential, Lorentzian and Gamma-variated  $R(t)$ , whereas it underestimates the true CBF when a dispersed exponential  $R(t)$  has to be reconstructed. Across the different  $R(t)$  models, the dispersed exponential residue function is characterized by the worst mean error for each deconvolution method, with the only exception of SNR 500, when SVD provides very good CBF estimates.

Considering the whole simulated cases, Figure 5.4 shows the relative percentage of the three deconvolution methods in providing the best CBF estimate. For each noise level, PD provides the best CBF estimates in the majority of the cases, from 58% at SNR 5 to 79% at SNR 50. SVD is the second best method, but its percentage results are less than half of the PD ones.

Figure 5.5 compares the true CBF with the ones obtained using PD, SVD and cSVD at the typical noise level present in the clinical data (SNR 10). As expected, SVD and cSVD always underestimate the true CBF; moreover, the larger the true CBF, the larger the bias in the estimates. Differently, PD overestimates the small CBF values, whereas it underestimates the large ones. Nevertheless, considering the mean true CBF value (i.e. 22 ml/100g/min) PD estimates are closer to the true CBF than those provided by SVD and cSVD.

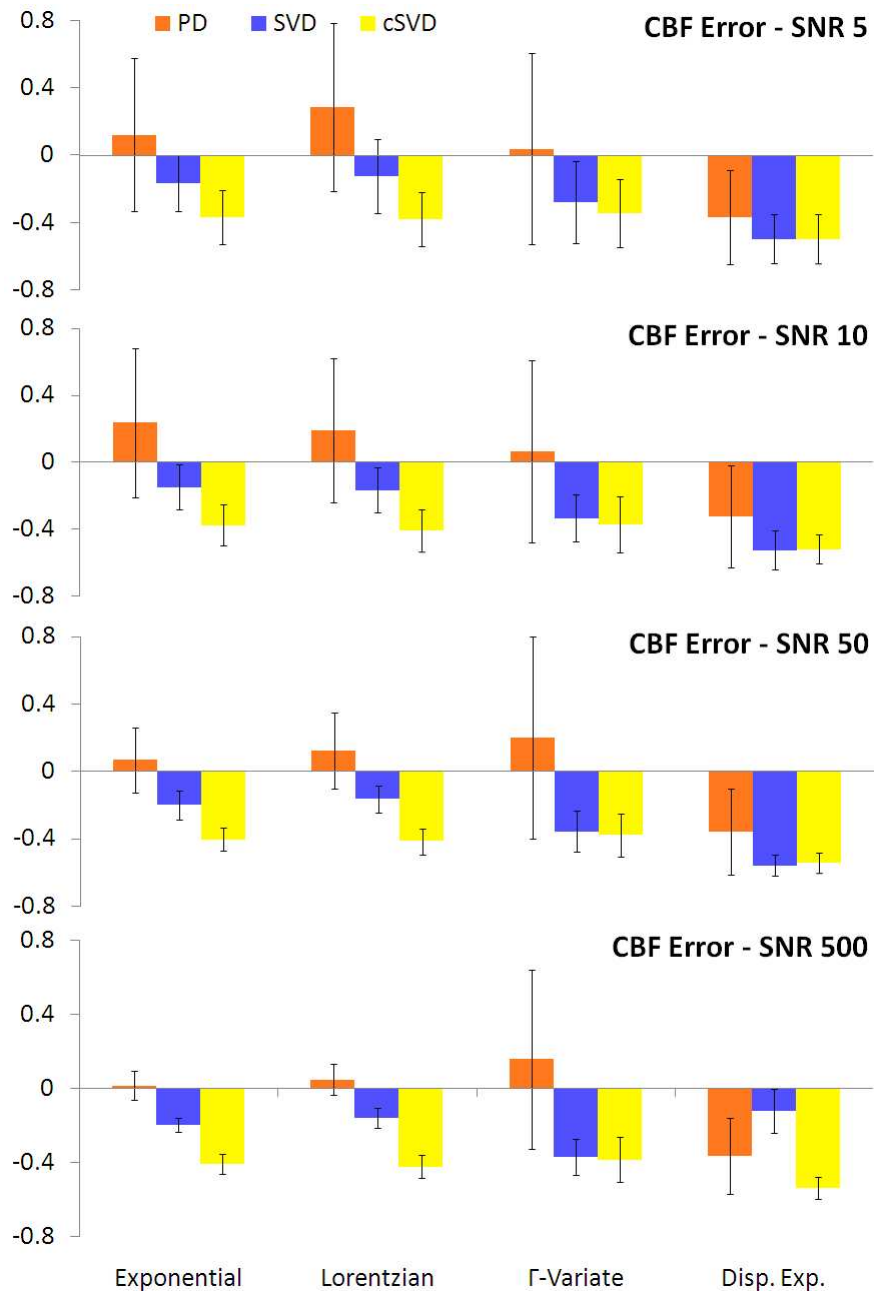


Figure 5.3: Estimated CBF percentage error.

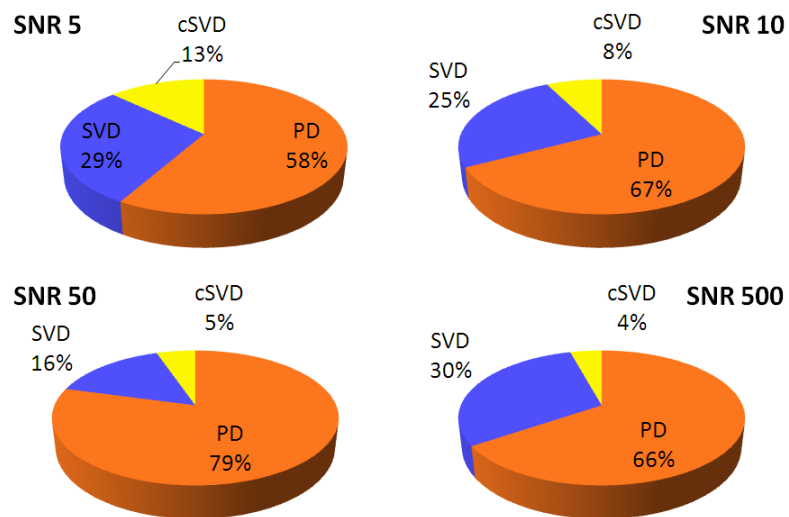


Figure 5.4: Method providing the best CBF estimate. For each method, the percentage of cases in which it provides the best CBF estimate is reported at each noise level.

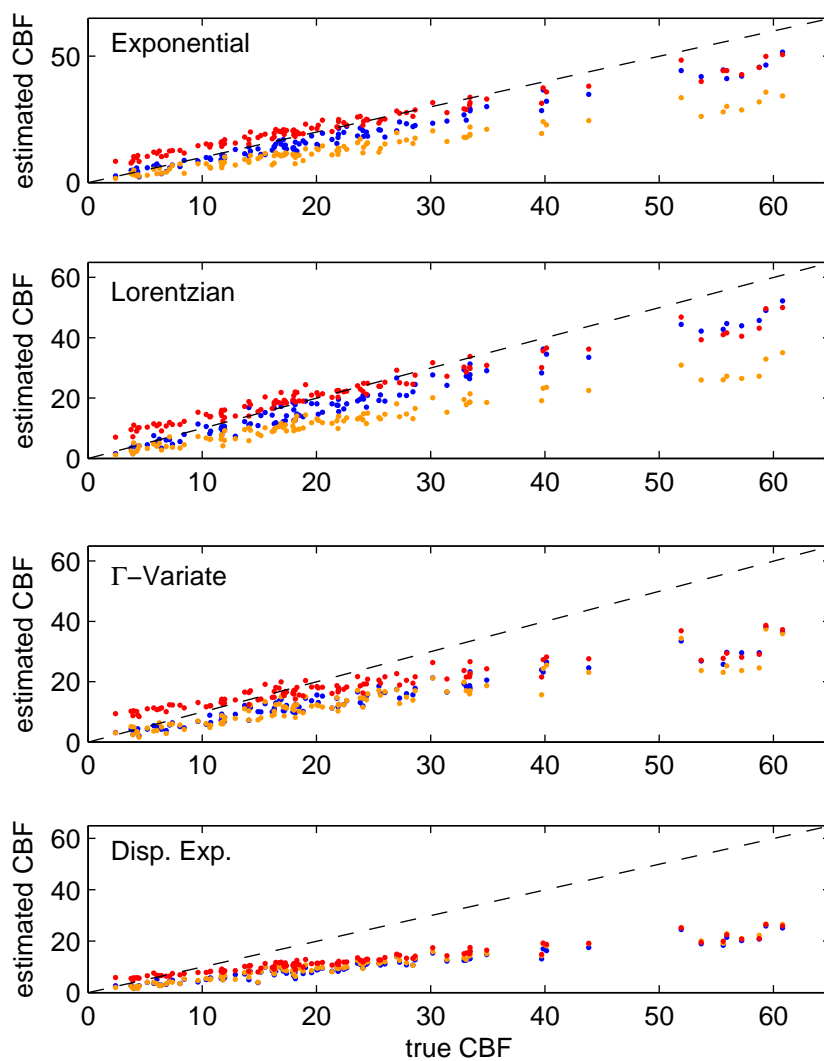


Figure 5.5: PD (red dots), SVD (blue dots) and cSVD (yellow dots) CBF estimates (vertical axes) versus true CBF (horizontal axes) at SNR 10 for the four different  $R(t)$  models.

## 5.4 Simulation: Discussion

A novel deconvolution method (PD) has been proposed and compared with the most popular deconvolution approaches for DSC-MRI image quantification: SVD and cSVD. The comparison has been made on a large simulated data set, including 4 different residue function models and 4 different noise levels. Summarizing, 1600 different situations were considered (100 CBF and MTT instances  $\times$  4 R(t) models  $\times$  4 SNR). Simulated data analysis was performed to validate the PD method and evaluate its performances.

PD has been shown to well characterize the residue function and accurately estimate the CBF, both in presence and absence of dispersion. PD performs better than SVD and cSVD, providing residue function estimates less biased by oscillation. Therefore, PD results are more physiologic and reliable.

SVD and cSVD provide unphysiological residue functions and fail to characterize the initial part of R(t) in presence of dispersion. Their estimates present oscillations and negative values and appear to be more sensitive to noise level than PD. As noise increases, oscillations become wider and not damped. Furthermore, one of the most important open issues in SVD and cSVD method is the threshold value set up. As reported in literature [46, 56], it is a critical step in both algorithms: small thresholds lead to good CBF estimates, but extremely noisy R(t) curves, whereas larger ones provide smoother R(t), but heavily underestimate the CBF.

PD, SVD and cSVD ability to reconstruct the true residue function was assessed by computing the root mean square error (RMSE). PD provides the best RMSE index in all cases and the best, or at least a comparable, standard deviation. Thus, PD provides a better estimation of the peak with respect to the other methods.

PD also provides the best CBF estimates in most cases. Considering the different noise level, PD is characterized by the smallest percentage error in at least 58% of the cases. At the noise level commonly present in clinical data, PD provides the best CBF estimates in 67% of the cases, SVD in 25% and cSVD in 8%. SVD and cSVD always underestimate the true CBF values and bias increases with the true CBF values. This means that tissues with high blood flow (i.e. gray matter) will be more biased than the other ones. Differently, PD estimates CBF in all the voxels of the same tissue at the same time. Estimate percentage error is very close to zero for the CBF population main value, smaller CBF values are usually overestimated and larger ones are underestimated. In presence of dispersion, the underestimation problem gets worse: PD underestimates also the population main value, but the bias is smaller than in SVD and cSVD estimates.

However, the more concentrated the population CBF values, the smaller the CBF estimate percentage error. Therefore, the impact of the over/underestimation problem can be reduced by analyzing more populations. The most appealing PD feature is the population approach. Estimating a large number of voxels at the same time increases the amount of available information, thus reducing the noise effects. The hypothesis that similar concentration time curves present similar CBF values is not so binding, but a robust method to divide all

voxels in the different populations is needed. Moreover, PD is a linear deconvolution method, as are SVD and cSVD, so it is not computationally expensive. An other important PD feature is that it does not require any threshold, as in SVD and cSVD. The hyper parameters describing the stochastic process that model the residue function are estimated in the algorithm. The price is the introduction of a non linear step before applying the estimating linear algorithm.

Summarizing, a novel deconvolution method has been proposed and validated on a simulated data set. PD provides more physiological and accurate residue function estimates than SVD and cSVD. Therefore, it gives higher quality information than the most popular methods for DSC-MRI image quantification. In the next sections, PD will be tested on a clinical data set and compared to SVD, cSVD and a deconvolution method recently proposed in this researching group, nonlinear stochastic regularization (NSR).

## 5.5 Clinical Data: Analysis

The clinical data set is the same proposed in section 4.5 (page 52). In summary, it includes 18 different clinical cases (11 subjects: 10 pre-surgery examinations and 8 post-surgery examination). Each examination contains 12 slices. A global AIF was computed for each examination by using the method presented in chapter 4. Furthermore, a Gamma-variate fitting procedure was performed on the arterial and on each voxel concentration curve to eliminate the presence of recirculation.

CBV maps were calculated pixel-by-pixel in each slice for each clinical case according to Eq. (2.4). The tissue brain density  $\rho$  and the proportionality constant  $k_H = (1 - H_{art})/(1 - H_{cap})$  were fixed to the commonly used values of 1.04 g/ml and 0.73, respectively. Summarizing, 216 CBV maps were generated (i.e. 18 examinations  $\times$  12 slices).

In each slice, two large ROIs were manually drawn by a trained physician on the left and on the right hemisphere. The ROIs are delimited by the inter-hemispheric scissure and by the cerebral external border. Each ROI is drawn to contain only white and gray matter. Thus, if other structures (e.g. the basal ganglia) are visible, they are not included in the ROIs. In total, 432 ROIs were generated (i.e. 18 examinations  $\times$  12 slices  $\times$  2 hemispheres). In each ROI, CBV mean was estimated and the ratio between the right and the left hemisphere was computed to evaluate the differences in blood volume distribution. CBV ratio mean and SD were computed in all 12 slices for each subject.

According to Eq. (2.12), CBF is defined as the maximum of the  $CBF \cdot R(t)$  function obtained by a deconvolution operation. CBF values were computed pixel-by-pixel using five different deconvolution methods: SVD, cSVD, NSR, dispersion corrected NSR (dcNSR) and PD. In total, 1080 CBF maps were generated (i.e. 18 examinations  $\times$  12 slices  $\times$  5 deconvolution methods).

Since the PD algorithm is expected to analyse only a voxel population at time, a preliminary step is required before performing the deconvolution to divide the different voxel populations. Voxels are subdivided in several populations by mean of a clustering approach. A K-means clustering algorithm subdivides all the voxels of the same slice into 10 clusters on the basis of the Euclidean distance among all voxel concentration curves. Each cluster is assumed to contain a unimodal voxel population, thus all voxels in each cluster are analyzed at the same time using the PD algorithm. Clusters containing less than 25 elements were discarded because the population is too poor to allow an accurate residue function estimate.

As previously pointed out, a statistical description of the noise ( $\Sigma_v$ ) is required to perform PD. The noise is assumed to be Gaussian, with zero mean and constant variance. ( $\Sigma_v$ ) is computed separately for each cluster because of PD sensitivity to it. Firstly, the population mean signal is computed and it is subtracted from each voxel signal. Then, the obtained signal is assumed to be a noise realization and the statistical analysis is performed. Noticeably, only the samples acquired before the tracer injection are considered in this step, in order to exclude the tracer arrival effects in the noise variance matrix estimate. Moreover, the variance of the peak sample and of the surrounding ones is reduced by a factor of 10 to increase the weight of the peak over the other samples.

The first PD algorithm step is the estimate of the hyper parameters characterizing the stochastic processes that model the residue function. Since it is the most computationally expensive step of the method, an ad hoc strategy was adopted to reduce the computation costs. If the considered population contains more than 100 elements, then the hyper parameter estimate step is performed only on a subpopulation of 100 randomly chosen elements.

Since a gold standard for the CBF absolute quantification has not been achieved yet, relative CBF values were considered and ratios between different ROIs were computed to compare the different deconvolution algorithms. As previously described for CBV, a ROI was drawn in the both hemispheres for each slice. CBF mean was computed on each ROI and the ratio between the right and the left hemisphere was also evaluated. Then, CBF ratio mean and SD was computed across all 12 slices for each deconvolution method.

Moreover, CBF percentage SD was computed in each ROI as

$$CBF_{SD\%} = 100 \cdot \frac{SD_{CBF}}{mean_{CBF}} \quad (5.16)$$

where  $mean_{CBF}$  and  $SD_{CBF}$  are the CBF mean and SD in the ROI, respectively.  $CBF_{SD\%}$  was computed to evaluate the ability of each deconvolution algorithm to provide reliable CBF estimates.

MTT was obtained as the ratio between CBV and CBF, according to the Central Volume theorem (Eq. (2.11)). Absolute MTT values were calculated pixel-by-pixel using the CBF values provided by SVD, cSVD, NSR, dcNSR and PD. In total, 1080 MTT maps were generated (i.e. 18 examinations  $\times$  12 slices  $\times$  5 deconvolution methods). Noticeably, absolute MTT values were obtained starting from relative CBV (i.e. without accounting for the constant  $\rho$  and  $k_H$ ) and CBF values.

As described previously for CBF and CBV analysis, MTT mean was computed on each ROI and the ratio between the right and the left hemisphere was obtained. Then, MTT ratio mean and SD was computed on all 12 slices. Moreover, MTT percentage SD was computed in each ROI as

$$MTT_{SD\%} = 100 \cdot \frac{SD_{MTT}}{mean_{MTT}} \quad (5.17)$$

where  $mean_{MTT}$  and  $SD_{MTT}$  are the MTT mean and SD in the ROI, respectively.

CBF and MTT *laterality indices* were computed in each slice according to Eq. (4.7), here reported

$$CBF_{LI} = \frac{CBF_{DX} - CBF_{SX}}{CBF_{DX}} \\ MTT_{LI} = \frac{MTT_{DX} - MTT_{SX}}{MTT_{DX}}$$

where  $CBF_{DX}$ ,  $CBF_{SX}$ ,  $MTT_{DX}$  and  $MTT_{SX}$  represent the CBF and MTT mean values in the right and left ROIs. CBF and MTT laterality indices allow to easily detect the brain region which presents high differences in CBF and MTT distribution. Laterality indices can be used to identify pathologic regions,

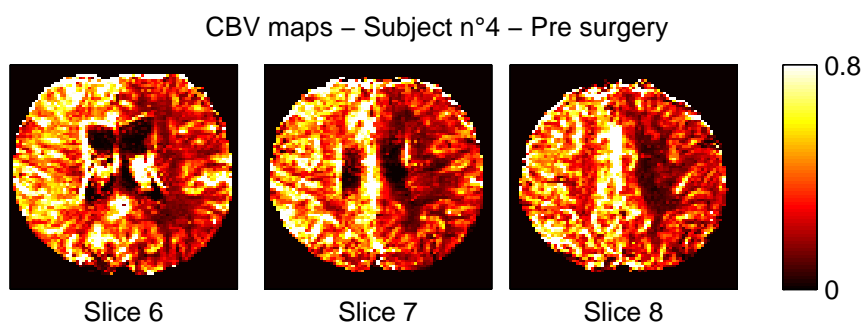


Figure 5.6: CBV maps obtained for subject n°4 before surgery.

since the stenosis disease is characterized by a low CBF and a high MTT in the pathologic area compared to the healthy one. Here, laterality indices will be used to evaluate the ability of the different deconvolution methods to detect pathologic cases.

## 5.6 Clinical Data: Results

### 5.6.1 Cerebral Blood Volume maps

Table 5.2 reports the mean and SD of CBV ratios between the right and the left hemisphere in all slices for each subject, both in the pre-surgery and post-surgery examination. In subjects n° 1 - 2 - 3 - 5 - 6, the post-surgery CBV ratio is closer to the unity than the pre-surgery one, suggesting a recovery from the disease after the treatment. SD is smaller in the post-surgery examination than in the pre-surgery one for all subjects, too, with the exception of subject n° 7. This remarks the improvement in the subject clinical state after the surgery. Subject n° 7 presents also an inversion of the blood volume distribution after the treatment: initial CBV ratio of 0.96 becomes 1.22. This indicates that shun introduction has modified the blood volume distribution across the brain. Subject n° 9 shows an equal CBV ratio and a smaller SD before and after surgery, suggesting that the treatment had not the desired effects.

Noticeably, subject n° 4 present a very high CBV ratio, suggesting a high impairment in the right hemisphere, the pathologic one. Stenosis thus causes an accumulation of blood in the pathologic tissues, suggesting that the disease has probably lead to a blood-brain barrier disruption. Figure 5.6 shows the high asymmetry in the blood volume distribution in subject n° 4. The left hemisphere (i.e. the healthy one) appears shadowed in all reported slices. According to the radiologic convention, the left hemisphere is located in the right side of the figure, whereas the right hemisphere is located in the left side.

In figures 5.7 - 5.8 CBV maps obtained for subject n° 6 before surgery and n° 9 after surgery are presented. CBV values are expressed in ml/g percentage, as commonly done in literature. They are comparable to the ones reported in

other works, but still outside the ideal range because of the DSC-MRI absolute quantification problem.

CBV Dx/Sx Subject	Pre Surgery		Post Surgery	
	mean	SD	mean	SD
1	1,28	0,31	1,04	0,29
2	1,18	0,29	1,03	0,21
3	1,07	0,40	0,86	0,23
4	1,67	0,58	#	#
5	0,94	0,33	1,00	0,29
6	1,17	0,36	1,10	0,33
7	0,96	0,26	1,22	0,38
8	1,05	0,33	#	#
9	1,08	0,45	1,08	0,31
10	#	#	1,10	0,22
11	1,14	0,16	#	#

Table 5.2: Mean CBV ratios and standard deviations (SD) between the right and the left hemisphere before and after surgery.

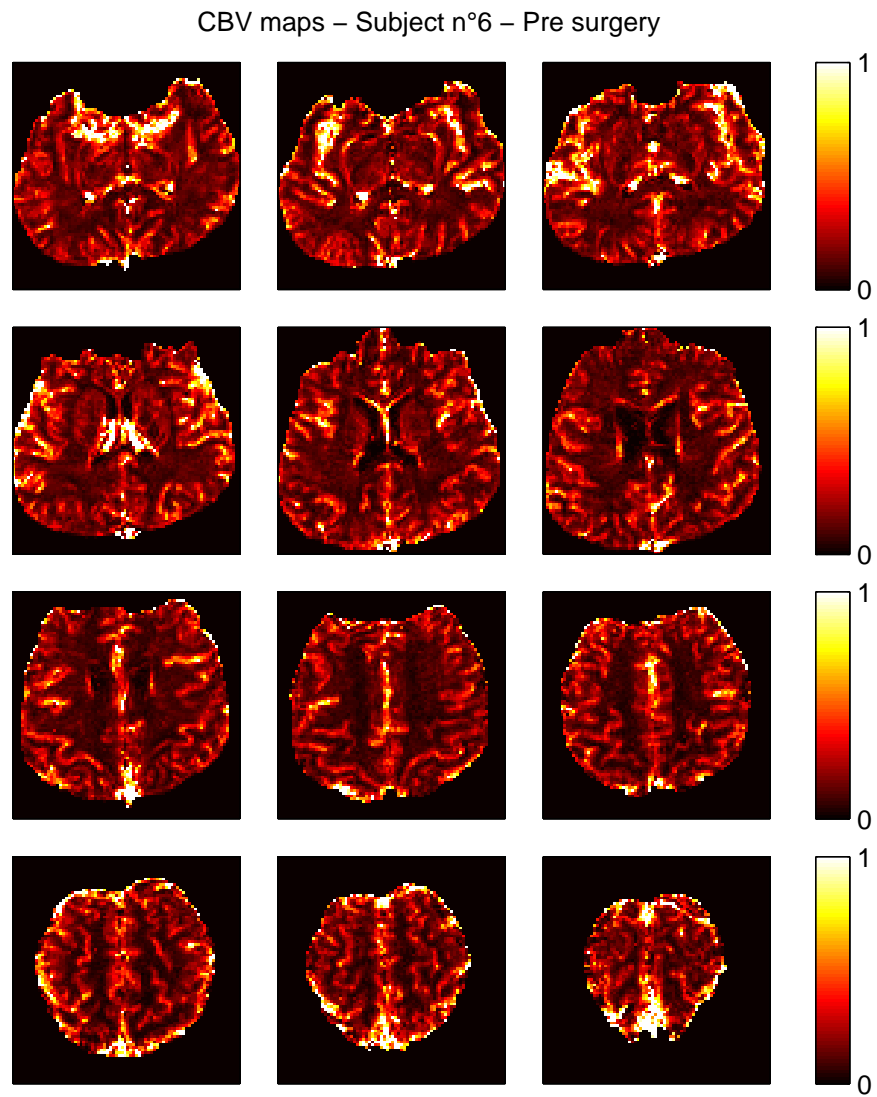


Figure 5.7: CBV maps obtained for subject n° 6 before surgery.

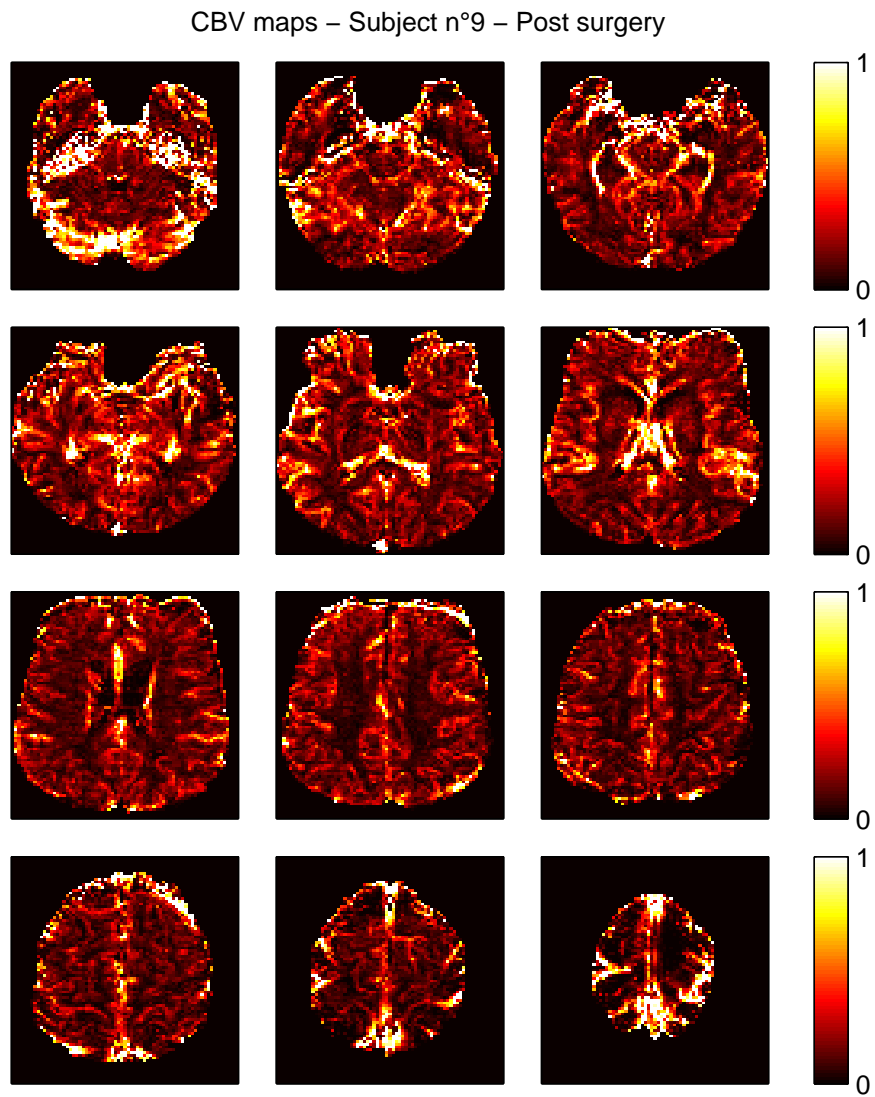


Figure 5.8: CBV maps obtained for subject n° 9 after surgery.

### 5.6.2 Cerebral Blood Flow maps

Tables 5.3 show the mean CBF ratio between the right and the left hemisphere obtained by using SVD, cSVD, NSR, dispersion corrected NSR (dcNSR) (i.e. CBF was computed on the non dispersed residue function) and PD in all subject before surgery. Mean CBF ratio was computed on all 12 slices for each examination. Stenosis disease commonly generates differences in CBF distribution, thus the CBF ratio can be used to investigate the subject clinical state. For instance, the CBF ratio allows to locate the disease. A CBF ratio greater than 1 indicates that the CBF is larger in the right hemisphere than in the left one. Therefore, it suggests that the left hemisphere is affected by the pathology. Vice versa, a CBF ratio smaller than 1 suggests a larger CBF in the left hemisphere than in the right one, thus locating the pathology in the right hemisphere. Moreover, the CBF ratio allows to quantify the disease degree. The further the CBF ratio from unity, the more serious the pathology.

CBF Dx/Sx - Pre surgery										
Sub.	SVD		cSVD		NSR		dcNSR		PD	
	mean	SD	mean	SD	mean	SD	mean	SD	mean	SD
1	1,08	0,21	1,07	0,19	0,73	0,23	1,27	0,47	1,01	0,12
2	1,02	0,23	0,95	0,18	1,29	0,59	1,26	0,41	1,01	0,24
3	1,20	0,20	1,13	0,14	1,34	0,50	1,83	1,07	1,27	0,27
4	1,09	0,25	1,11	0,25	0,77	0,29	0,70	0,33	1,03	0,29
5	1,03	0,19	1,00	0,14	1,00	0,24	0,91	0,37	1,02	0,22
6	0,96	0,11	1,02	0,10	0,71	0,19	0,81	0,20	0,82	0,16
7	0,93	0,08	1,01	0,07	1,22	0,71	0,81	0,27	0,94	0,12
8	1,46	0,27	1,33	0,22	2,01	1,27	2,35	1,54	1,77	0,70
9	0,97	0,15	1,06	0,10	0,76	0,29	0,80	0,30	0,93	0,17
10	#	#	#	#	#	#	#	#	#	#
11	1,02	0,18	1,00	0,14	1,17	0,60	1,32	0,56	0,99	0,22

Table 5.3: Mean CBF ratios and standard deviations (SD) between the right and the left hemisphere before surgery.

In all cases, NSR provides the highest difference between the right and left hemisphere, thus suggesting a more serious pathologic state than in the other deconvolution methods. In six cases (i.e. subjects n° 1 - 3 - 4 - 5 - 8 - 11), the CBF distribution difference obtained considering the dispersion corrected NSR is larger than the one obtained considering the dispersed residue function. cSVD CBF ratio is the closest to the unity in six cases (i.e. subjects n° 3 - 5 - 6 - 7 - 8 - 11), thus making the pathology identification more difficult than in other methods. Subject n° 8 presents the largest difference from the unity in the CBF ratio: this suggests the presence of a high impairment in the pathological hemisphere.

For 7 patients, the DSC-MRI examination was repeated after the surgery. The mean CBF ratio and SD of the post treatment examinations are reported in table 5.4. NSR still provides the largest difference between the two hemispheres in each subject. In most cases, post surgery CBF ratio is closer to the unity than the pre surgery one, suggesting a recovery from the disease. Only subject n° 5 shows a significant deterioration of the CBF distribution after the shunt

CBF Dx/Sx - Post surgery										
Sub.	SVD		cSVD		NSR		dcNSR		PD	
	mean	SD	mean	SD	mean	SD	mean	SD	mean	SD
1	1,04	0,12	1,07	0,10	1,21	0,47	1,42	0,80	1,07	0,17
2	0,97	0,14	1,01	0,11	1,48	0,87	1,04	0,61	1,00	0,19
3	1,11	0,19	1,12	0,17	1,51	0,74	1,33	0,90	1,12	0,25
4	#	#	#	#	#	#	#	#	#	#
5	1,13	0,18	1,13	0,19	1,23	0,26	1,36	0,70	1,27	0,35
6	1,05	0,12	1,02	0,08	1,17	0,28	1,13	0,27	1,08	0,14
7	0,92	0,26	0,95	0,25	0,80	0,33	0,84	0,40	0,91	0,35
8	#	#	#	#	#	#	#	#	#	#
9	1,01	0,08	1,04	0,07	0,89	0,21	1,05	0,41	0,98	0,11
10	1,25	0,28	1,15	0,25	1,95	0,97	1,73	1,13	1,60	0,54
11	#	#	#	#	#	#	#	#	#	#

Table 5.4: Mean CBF ratios and standard deviations (SD) between the right and the left hemisphere after surgery.

introduction, remarked by all methods. In some cases, a CBF ratio inversion is recorded in the post surgery examination compared to the pre surgery one, suggesting that the treatment has modified the blood flow across the brain.

However, the different deconvolution methods do not lead to the same diagnosis. For instance, in subject n° 4 SVD, cSVD and PD indicate a higher blood flow in the right hemisphere than in the left one, whereas NSR suggests a lower blood flow in the right hemisphere. Moreover, in subjects n° 1 and 7 NSR and dcNSR provide dissonant CBF ratios between the two hemispheres. In subject n° 1 NSR provides a CBF ratio of 0.73, whereas dcNSR records 1.27. In other words, NSR suggests that the left hemisphere has a higher CBF than the right one, whereas dcNSR leads to the opposite conclusion. In subject n° 7 a similar situation is recorded: NSR suggests a larger CBF in the right hemisphere (mean CBF ratio is 1.22), whereas dcNSR indicates that the left hemisphere is characterized by a larger CBF (mean CBF ratio is 0.81). Therefore, results provided in table 5.3 and 5.4 are to be carefully examined because they are obtained averaging all 12 slices, thus representing the global blood flow state. Very low CBF values located in a small brain area can almost disappear when considering the whole brain CBF ratio. Furthermore, very high differences from the unity of the mean CBF ratio can appear unphysiological if considering the collateral circulation presence.

The SD values reported in table 5.3 and 5.4 indicate that the CBF ratio across slices is not constant in the same subject. NSR and dcNSR present the largest SD in each subject, suggesting that the CBF ratio presents a large variation across slices. This confirms that particular care is needed when considering global hemodynamic parameters. Therefore, a way to examine CBF differences in small brain areas, such as the laterality indices, is advisable.

Table 5.5 shows mean percentage SD obtained by SVD, cSVD, NSR, dcNSR and PD in the right and left hemisphere in each subject before surgery. NSR and dcNSR show the highest values in all cases, suggesting a quite noisy characterization of CBF maps. As expected, SVD and cSVD always present the

lowest percentage SD values, since they commonly provide uniform CBF maps. PD shows SD values higher than SVD and cSVD ones and lower than NSR and dcNSR ones. Hence, PD provides CBF maps with a higher contrast level than SVD and cSVD, but not too high as in NSR maps.

CBF SD - Pre surgery										
Subject	SVD		cSVD		NSR		dcNSR		PD	
	Dx	Sx	Dx	Sx	Dx	Sx	Dx	Sx	Dx	Sx
1	70	68	69	69	237	274	496	456	111	97
2	83	83	70	71	329	254	381	259	120	122
3	103	88	85	78	185	288	511	469	159	147
4	73	79	68	68	128	146	327	437	97	101
5	99	106	88	91	173	218	270	353	125	132
6	75	70	69	67	136	104	313	317	119	106
7	90	83	81	71	505	314	632	858	151	144
8	79	90	74	77	243	359	422	591	123	147
9	86	89	75	79	204	303	502	486	122	114
10	#	#	#	#	#	#	#	#	#	#
11	86	91	72	78	669	574	645	658	111	111

Table 5.5: Mean percentage standard deviation (SD) of CBF obtained by SVD, cSVD, NSR, dcNSR, PD in the left and right hemisphere of each subject before surgery.

Results do not change in the post-surgery situation. Figure 5.6 shows mean percentage SD obtained by SVD, cSVD, NSR, dcNSR and PD in the right and left hemisphere in each subject after surgery. NSR and dcNSR show the highest values in all the considered subjects; PD presents higher values than SVD and cSVD ones but lower than NSR and dcNSR ones.

CBF SD - Post surgery										
Subject	SVD		cSVD		NSR		dcNSR		PD	
	Dx	Sx	Dx	Sx	Dx	Sx	Dx	Sx	Dx	Sx
1	89	75	72	60	552	310	524	377	109	102
2	98	94	74	70	871	569	773	825	142	141
3	104	97	82	72	534	562	622	753	159	163
4	#	#	#	#	#	#	#	#	#	#
5	83	85	83	83	111	144	450	463	102	109
6	89	81	73	66	197	183	287	313	125	115
7	78	98	72	98	138	114	268	278	115	103
8	#	#	#	#	#	#	#	#	#	#
9	82	85	75	81	234	233	322	334	90	93
10	81	88	76	82	368	534	392	596	92	92
11	#	#	#	#	#	#	#	#	#	#

Table 5.6: Mean percentage standard deviation (SD) of CBF obtained by SVD, cSVD, NSR, dcNSR, PD in the left and right hemisphere of each subject after surgery.

Particular slices have been selected in each subject to further investigate

the performances of the deconvolution methods. CBF maps obtained by SVD, cSVD, NSR, dcNSR and PD in these slices are presented in next pages (Figures from 5.9 to 5.26). All methods provide only relative CBF values; therefore, all CBF maps were normalized to the same pixel to allow a direct comparison across the methods. The pixel selection has been manually performed by considering the white matter in the non pathologic hemisphere. As expected, PD maps are comparable to those provided by SVD and cSVD, but they present a higher contrast level, thus emphasizing the differences in the CBF distribution. NSR and dcNSR present even higher contrasted CBF maps. Sometimes, NSR and dcNSR allow to easily detect disease affected areas because of the very high contrast level. On the other hand, they sometimes provide very noisy maps, which are difficult to analyse.

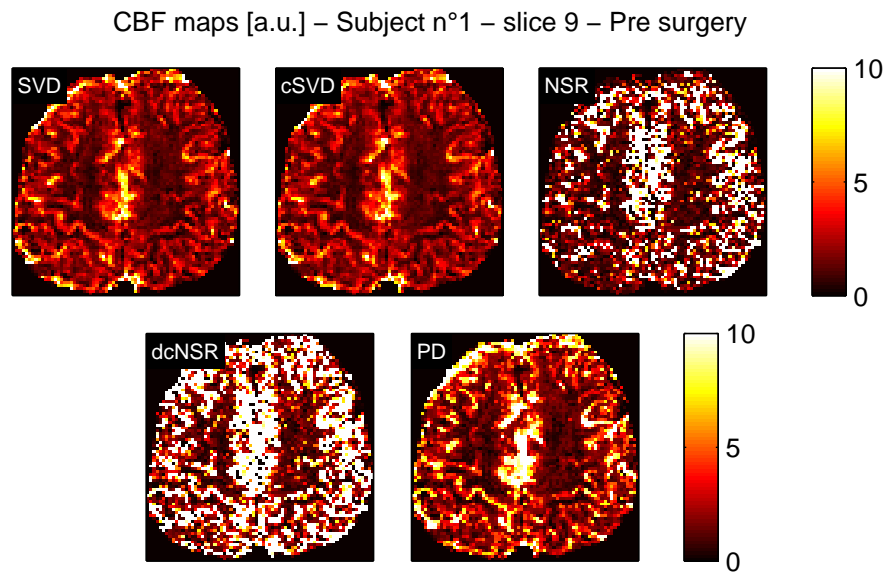


Figure 5.9: CBF maps obtained by SVD, cSVD, NSR, dcNSR and PD in subject n° 1 before surgery. Relative CBF values are normalized to the same reference region in each map.

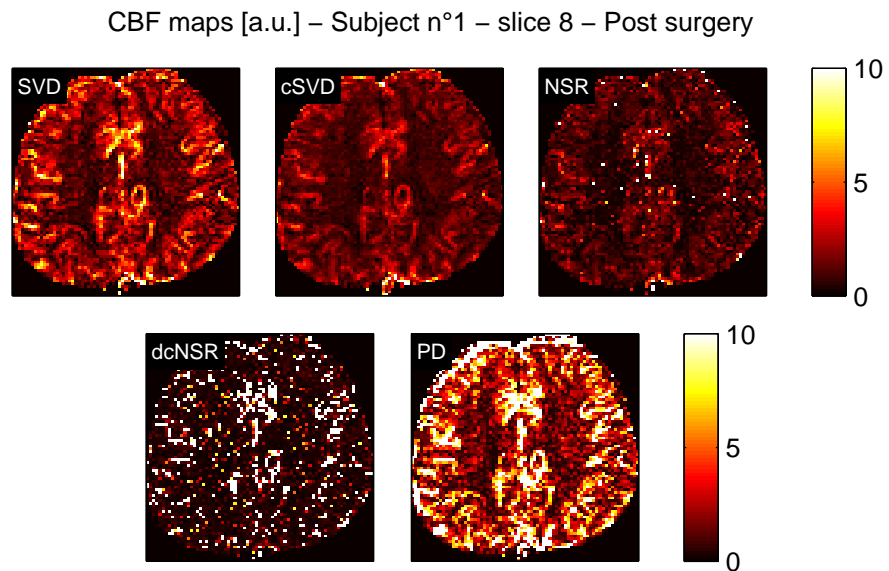


Figure 5.10: CBF maps obtained by SVD, cSVD, NSR, dcNSR and PD in subject n° 1 after surgery. Relative CBF values are normalized to the same reference region in each map.

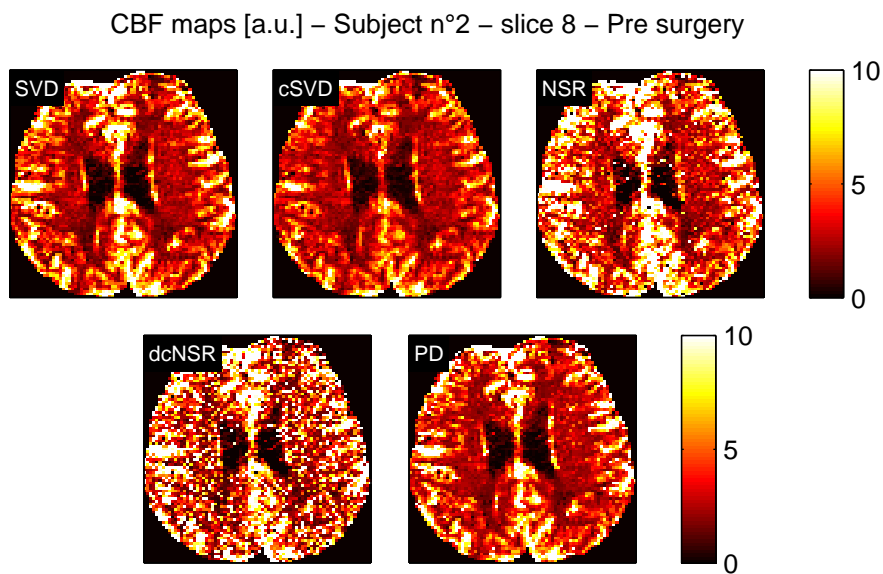


Figure 5.11: CBF maps obtained by SVD, cSVD, NSR, dcNSR and PD in subject n° 2 before surgery. Relative CBF values are normalized to the same reference region in each map.

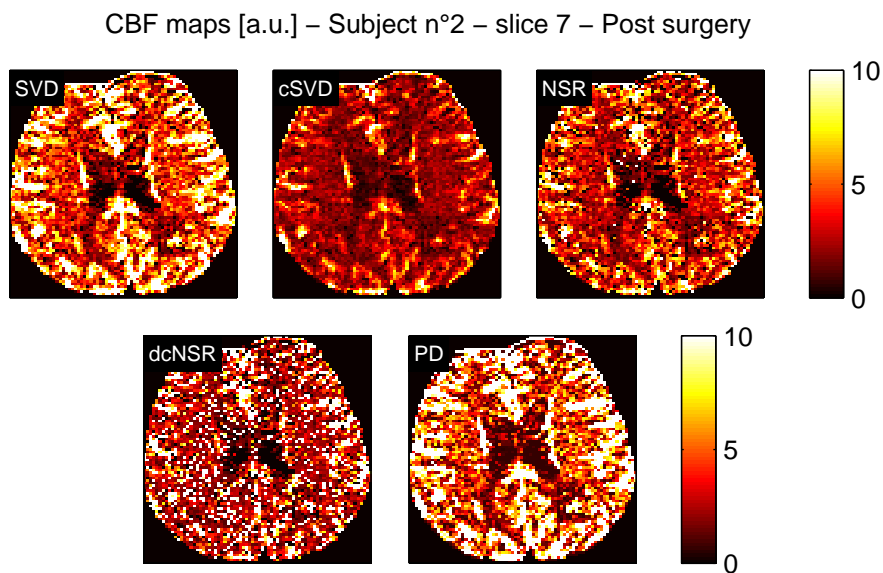


Figure 5.12: CBF maps obtained by SVD, cSVD, NSR, dcNSR and PD in subject n° 2 after surgery. Relative CBF values are normalized to the same reference region in each map.

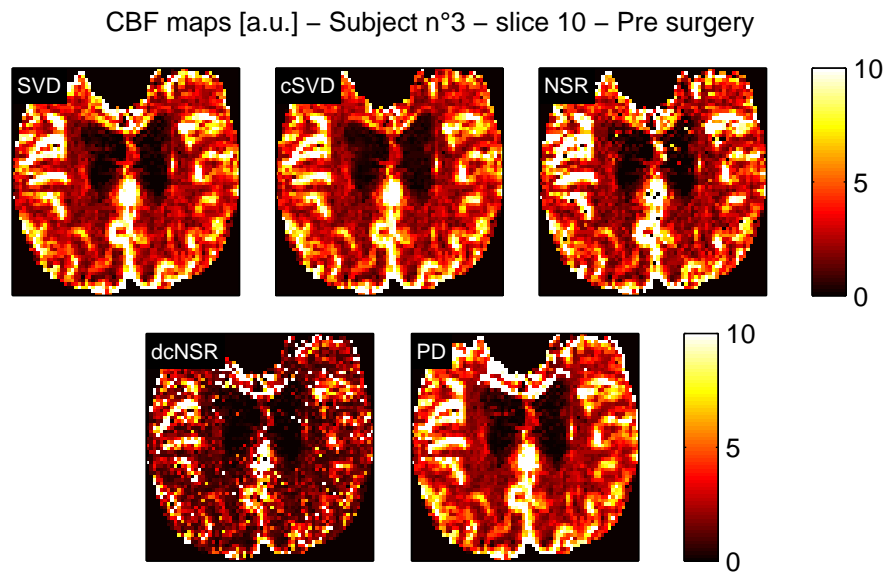


Figure 5.13: CBF maps obtained by SVD, cSVD, NSR, dcNSR and PD in subject n° 3 before surgery. Relative CBF values are normalized to the same reference region in each map.

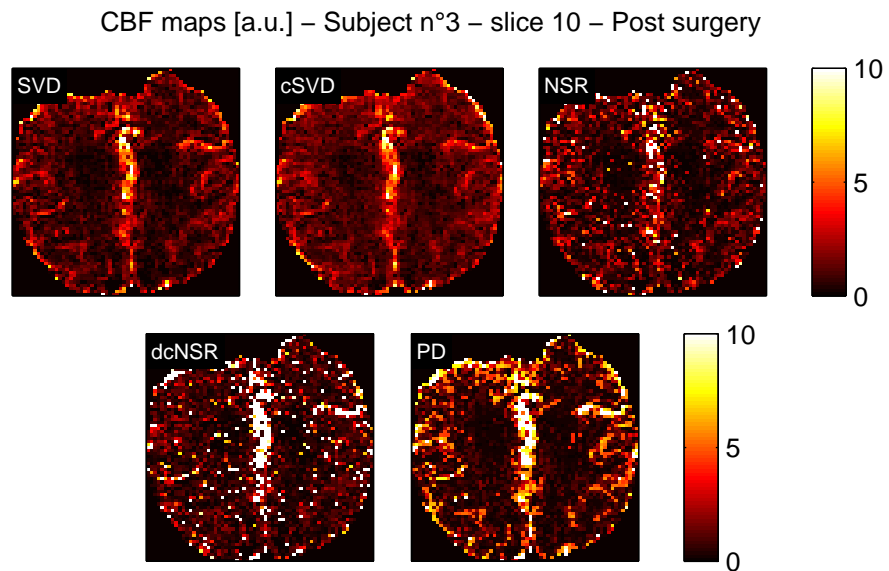


Figure 5.14: CBF maps obtained by SVD, cSVD, NSR, dcNSR and PD in subject n° 3 after surgery. Relative CBF values are normalized to the same reference region in each map.

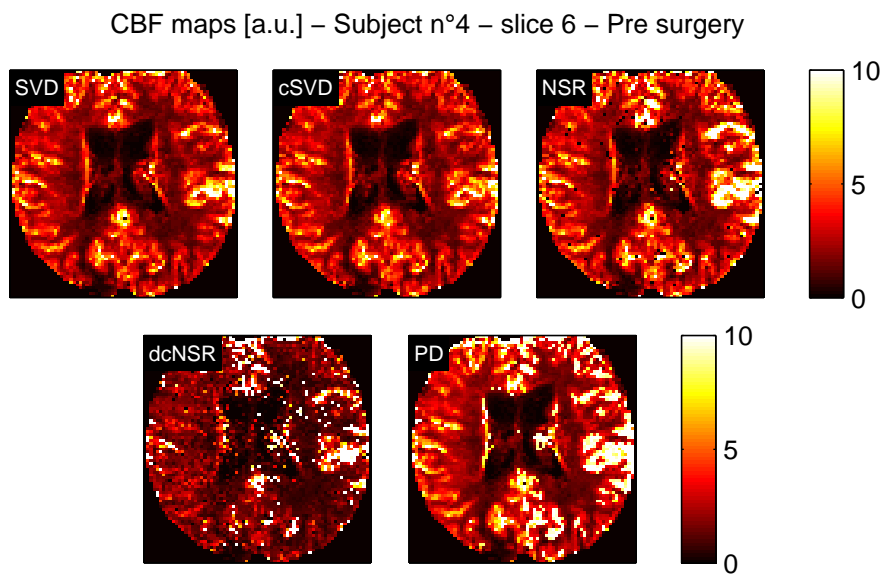


Figure 5.15: CBF maps obtained by SVD, cSVD, NSR, dcNSR and PD in subject n° 4 before surgery. Relative CBF values are normalized to the same reference region in each map.

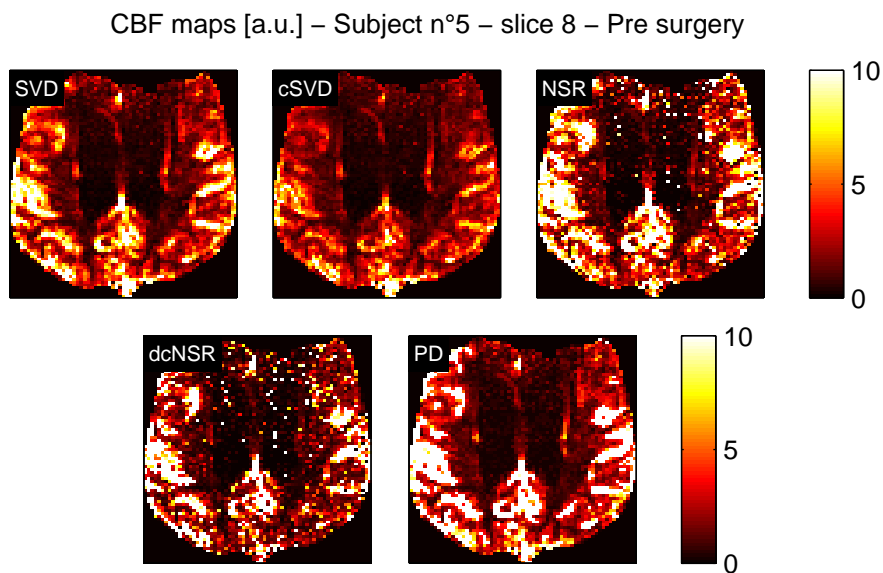


Figure 5.16: CBF maps obtained by SVD, cSVD, NSR, dcNSR and PD in subject n° 5 before surgery. Relative CBF values are normalized to the same reference region in each map.

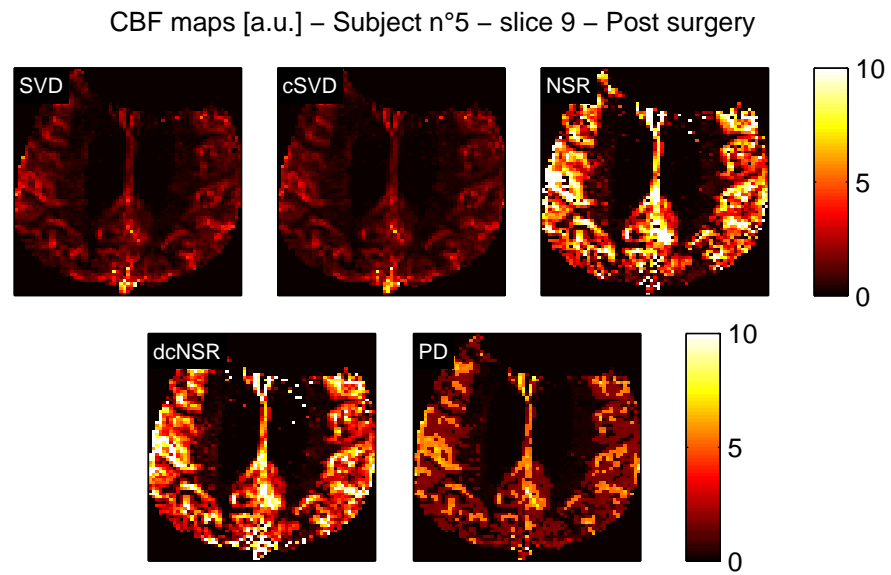


Figure 5.17: CBF maps obtained by SVD, cSVD, NSR, dcNSR and PD in subject n° 5 after surgery. Relative CBF values are normalized to the same reference region in each map.

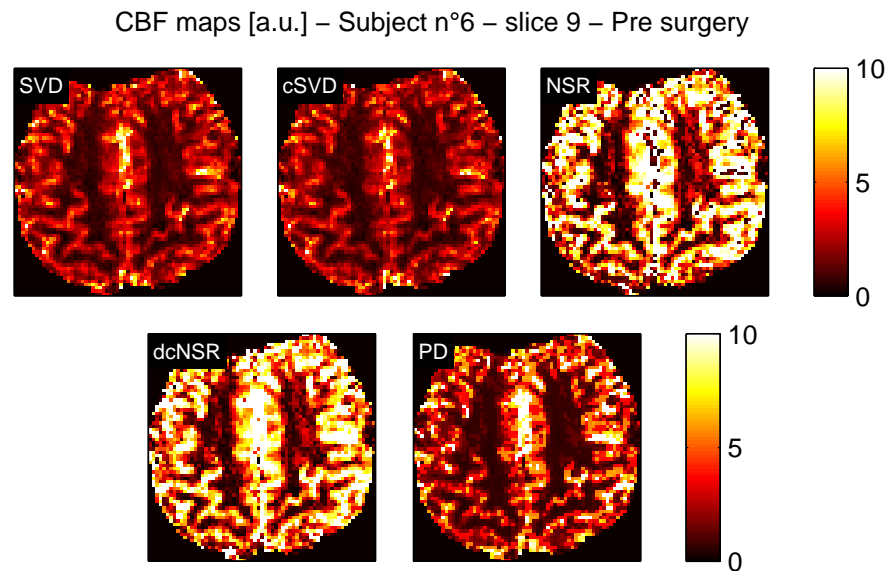


Figure 5.18: CBF maps obtained by SVD, cSVD, NSR, dcNSR and PD in subject n° 6 before surgery. Relative CBF values are normalized to the same reference region in each map.

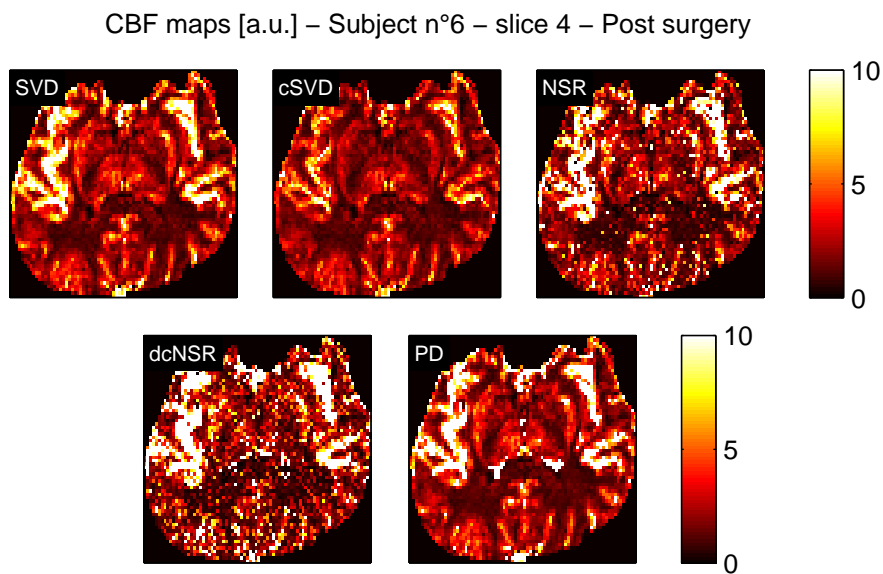


Figure 5.19: CBF maps obtained by SVD, cSVD, NSR, dcNSR and PD in subject n° 6 after surgery. Relative CBF values are normalized to the same reference region in each map.

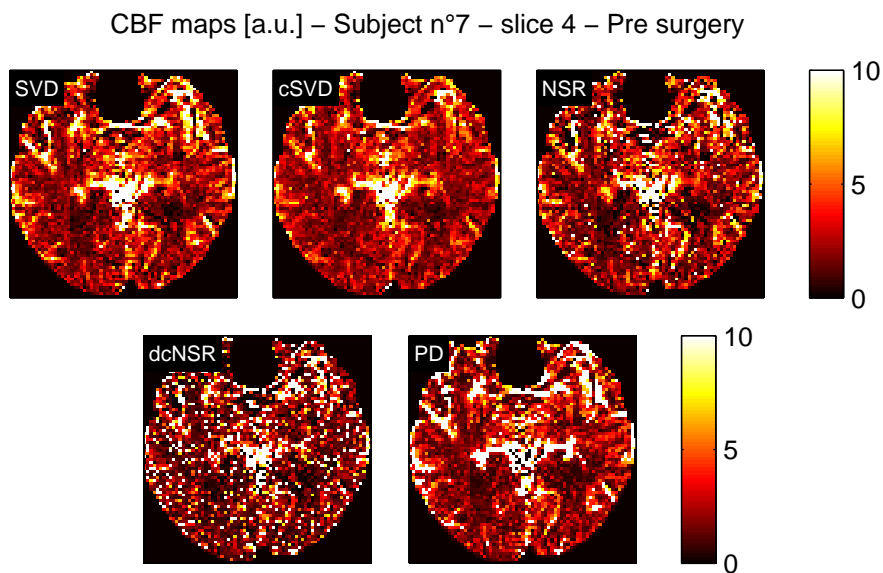


Figure 5.20: CBF maps obtained by SVD, cSVD, NSR, dcNSR and PD in subject n° 7 before surgery. Relative CBF values are normalized to the same reference region in each map.

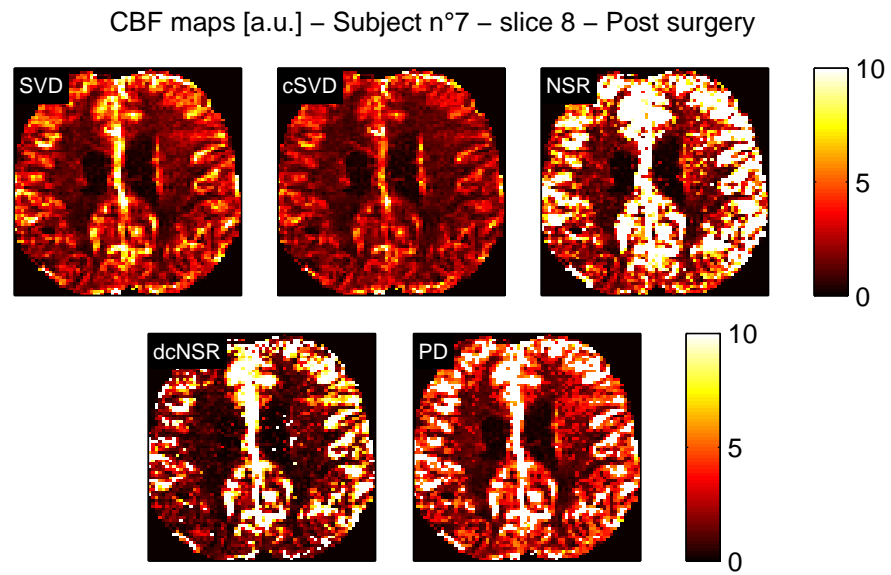


Figure 5.21: CBF maps obtained by SVD, cSVD, NSR, dcNSR and PD in subject n° 7 after surgery. Relative CBF values are normalized to the same reference region in each map.

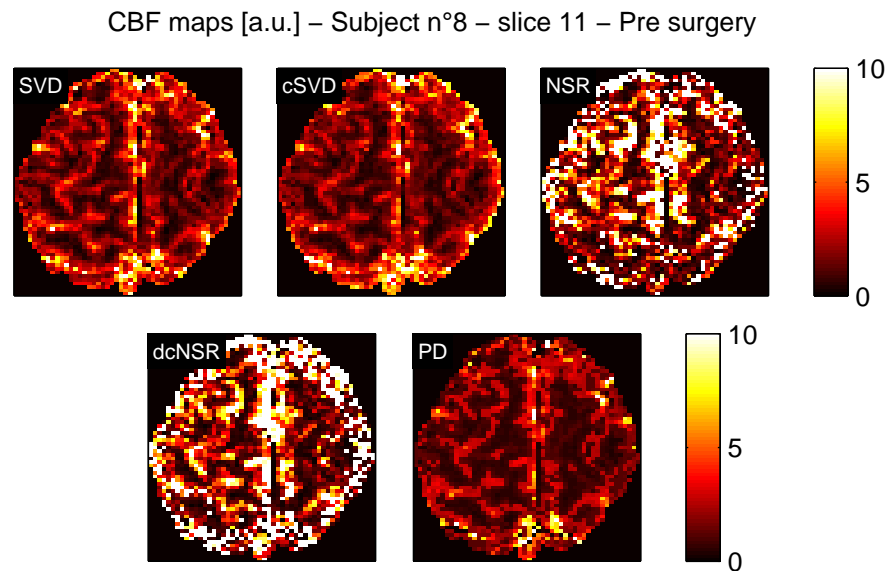


Figure 5.22: CBF maps obtained by SVD, cSVD, NSR, dcNSR and PD in subject n° 8 before surgery. Relative CBF values are normalized to the same reference region in each map.

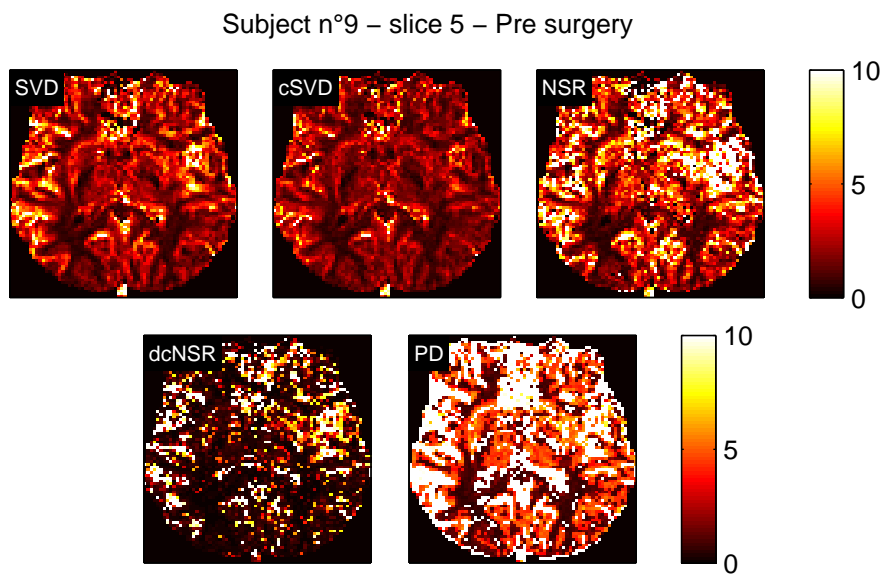


Figure 5.23: CBF maps obtained by SVD, cSVD, NSR, dcNSR and PD in subject n° 9 before surgery. Relative CBF values are normalized to the same reference region in each map.

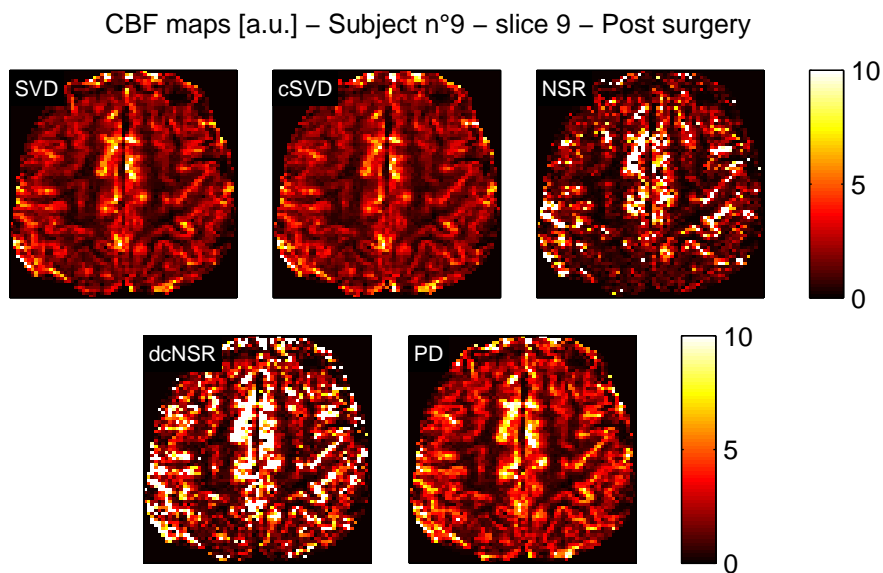


Figure 5.24: CBF maps obtained by SVD, cSVD, NSR, dcNSR and PD in subject n° 9 after surgery. Relative CBF values are normalized to the same reference region in each map.

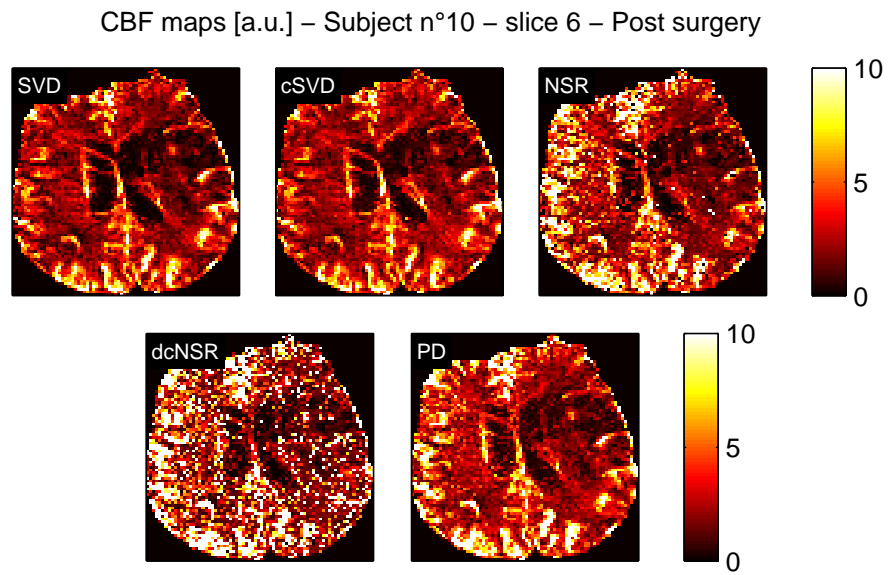


Figure 5.25: CBF maps obtained by SVD, cSVD, NSR, dcNSR and PD in subject n° 10 after surgery. Relative CBF values are normalized to the same reference region in each map.

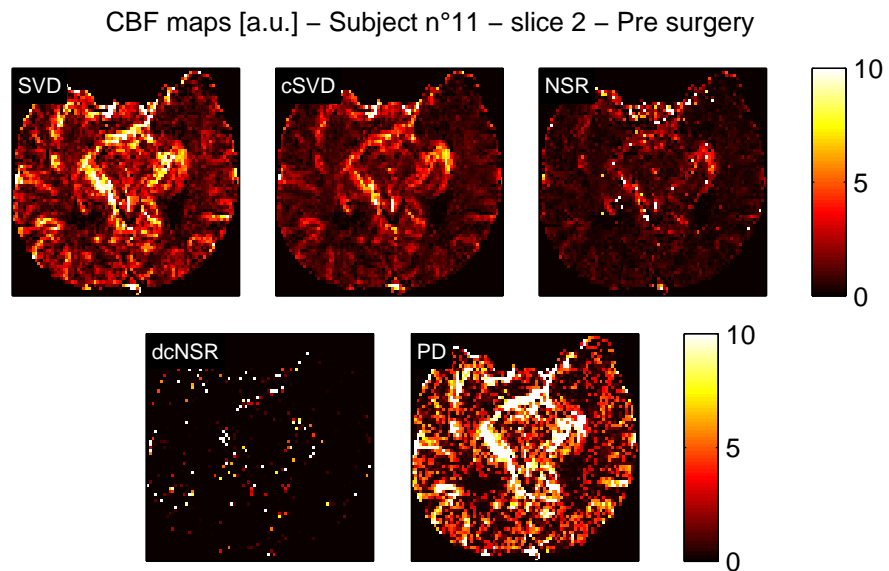


Figure 5.26: CBF maps obtained by SVD, cSVD, NSR, dcNSR and PD in subject n° 11 before surgery. Relative CBF values are normalized to the same reference region in each map.

### 5.6.3 Mean Transit Time maps

Table 5.7 shows mean MTT ratios and SD between the right and left hemisphere obtained in each subject by using SVD, cSVD, NSR, dcNSR and PD. Mean ratios are obtained averaging all 12 slices of each examination. As for CBF, mean MTT ratios can be used to investigate the stenosis disease. Pathologic brain areas are usually characterized by a slow blood flow, thus obtaining a larger mean transit time than normal one. MTT ratios larger than one indicate that MTT in the right hemisphere is larger than in the left one, thus suggesting that pathology affects the right brain area. Vice versa, if MTT is larger in the left hemisphere than in the right one, MTT ratio becomes smaller than one, thus indicating that the stenosis is located in the left hemisphere. Moreover, the further the MTT ratio from the unity, the more serious the pathology. Therefore, MTT ratios can be used to locate and assess the disease.

MTT Dx/Sx - Pre surgery										
Sub.	SVD		cSVD		NSR		dcNSR		PD	
	mean	SD	mean	SD	mean	SD	mean	SD	mean	SD
1	1,01	0,04	1,02	0,07	1,19	0,16	1,20	0,21	1,11	0,14
2	0,92	0,09	0,97	0,09	0,87	0,14	0,91	0,15	0,93	0,13
3	0,96	0,07	0,99	0,06	0,90	0,10	0,91	0,09	0,94	0,05
4	1,69	0,24	1,69	0,25	1,99	0,46	1,66	0,27	1,85	0,27
5	0,94	0,08	0,97	0,06	0,88	0,15	0,90	0,12	0,90	0,10
6	1,18	0,06	1,06	0,04	1,72	0,37	1,77	0,29	1,43	0,16
7	1,06	0,06	1,00	0,04	1,08	0,07	1,10	0,11	1,07	0,07
8	0,87	0,16	0,97	0,08	0,70	0,31	0,67	0,27	0,74	0,15
9	1,08	0,12	1,02	0,04	1,23	0,23	1,29	0,27	1,16	0,14
10	#	#	#	#	#	#	#	#	#	#
11	1,01	0,05	1,01	0,05	1,00	0,07	0,98	0,07	1,07	0,11

Table 5.7: Mean MTT ratios and standard deviations (SD) between the right and left hemisphere before surgery.

In all cases, with the exception of subject n° 11, NSR and dcNSR provide the largest mean MTT ratio estimates, thus suggesting a more serious pathologic state than the other deconvolution methods. In 5 cases (i.e. subjects n° 1 - 6 - 7 - 8 - 9), dcNSR MTT ratio is larger than the NSR one, whereas in subjects n° 2 - 3 - 4 - 5 the NSR presents the largest MTT ratio. PD presents the largest MTT ratio only in subject n° 11, but in this subject all methods result in a very close to the unity MTT ratio. As expected, cSVD MTT ratios are the closest to the unity across all methods, thus making the disease detection difficult. However, differences in MTT distribution are commonly smaller than differences in CBF distribution, for all deconvolution methods. This is not unexpected because of the brain hemodynamic behaviour in the pathologic state. When stenosis reduces the lumen of a large vessel feeding a brain area, changes happen in the local hemodynamic. Commonly, CBV increases and CBF decreases to ensure the hematic support to the pathologic area. Therefore, MTT usually presents significant variations between healthy and pathologic areas only in peripheral or heavily impaired areas. For instance, subject n° 8 presents very high differences in CBF distribution between the right and left hemisphere (see

table 5.3), whereas difference in MTT values is less marked. Another example is represented by subject n° 6. It shows significant differences from the unity both in mean MTT and CBF ratio (table 5.3), suggesting a high impairment in the right hemisphere. Noticeably, subject n° 4 is characterized by the highest difference in MTT distribution between the two hemispheres (see also MTT maps in Figure 5.33). However, particular attention is necessary in interpreting results because it can be affected by BBB disruption, as reported in the CBV maps results.

The SD values reported in table 5.7 confirm that MTT ratios remain quite constant across the slices. NSR and dcNSR present the largest SD values in all cases with the exception of subject n° 11, in which PD is characterized by the largest SD value.

MTT Dx/Sx - Post surgery										
Sub.	SVD		cSVD		NSR		dcNSR		PD	
	mean	SD	mean	SD	mean	SD	mean	SD	mean	SD
1	1,03	0,05	0,99	0,04	1,03	0,08	1,01	0,13	1,02	0,08
2	1,04	0,06	0,99	0,04	1,04	0,05	1,02	0,05	1,04	0,06
3	1,00	0,10	0,98	0,09	0,97	0,14	1,05	0,20	1,04	0,14
4	#	#	#	#	#	#	#	#	#	#
5	1,01	0,13	1,02	0,09	1,03	0,36	0,96	0,30	0,96	0,17
6	0,95	0,09	0,97	0,10	0,97	0,17	0,95	0,18	0,96	0,08
7	1,07	0,18	1,01	0,10	1,35	0,53	1,32	0,55	1,14	0,27
8	#	#	#	#	#	#	#	#	#	#
9	1,01	0,04	0,99	0,05	1,10	0,09	1,03	0,16	1,02	0,08
10	0,89	0,08	0,99	0,04	0,76	0,18	0,77	0,20	0,78	0,12
11	#	#	#	#	#	#	#	#	#	#

Table 5.8: Mean MTT ratios and standard deviations (SD) between the right and left hemisphere after surgery.

Table 5.8 shows the mean MTT ratios and SD between the right and left hemisphere in each subject after the surgery treatment. In almost all cases, MTT ratio after surgery is closer to the unity than before, suggesting a recovery in hemodynamic. Only subject n° 7 presents a significant MTT deterioration after surgery, suggesting that the shunt introduction has modified the blood dynamic. As in pre-surgery results, NSR and dcNSR usually provide the furthest from the unity MTT ratios. However, all methods provide comparable results in most cases. NSR and dcNSR are characterized by the largest SD values, but they also present a reduction in SD values before and after surgery. cSVD still presents very close to one MTT ratios and the smallest SD values.

Table 5.9 reports the mean percentage SD obtained by SVD, cSVD, NSR, dcNSR and PD across all slices in each subject before surgery. NSR and dcNSR show the largest values in all cases, suggesting that they provide noisy MTT maps. As expected, SVD and cSVD present the smallest SD values, thus indicating that their MTT maps are very uniform and with low contrast. As in the CBF percentage SD, PD shows values higher than SVD and cSVD, but also smaller than NSR and dcNSR.

Results do not change in the post-surgery situation (table 5.10). In each

MTT SD - Pre surgery										
Subject	SVD		cSVD		NSR		dcNSR		PD	
	Dx	Sx	Dx	Sx	Dx	Sx	Dx	Sx	Dx	Sx
1	48	46	43	44	132	152	147	162	61	60
2	54	53	57	56	96	88	117	119	55	55
3	46	44	51	47	67	63	80	76	45	42
4	46	48	46	50	56	71	73	86	52	55
5	75	78	62	65	163	157	184	187	93	94
6	47	33	36	30	153	175	157	133	65	77
7	70	72	67	65	101	105	130	133	97	99
8	54	53	50	49	151	125	155	142	76	69
9	42	49	44	47	73	90	91	116	53	67
10	#	#	#	#	#	#	#	#	#	#
11	67	65	41	40	89	95	122	128	97	97

Table 5.9: Mean percentage standard deviation (SD) of MTT obtained by SVD, cSVD, NSR, dcNSR, PD in the left and right hemisphere of each subject before surgery.

MTT SD - Post surgery										
Subject	SVD		cSVD		NSR		dcNSR		PD	
	Dx	Sx	Dx	Sx	Dx	Sx	Dx	Sx	Dx	Sx
1	70	70	61	60	82	85	113	116	79	78
2	64	67	55	56	64	68	99	100	66	67
3	90	83	73	70	116	106	148	135	122	120
4	#	#	#	#	#	#	#	#	#	#
5	78	71	66	60	273	251	301	290	164	144
6	62	69	58	63	157	149	167	175	64	66
7	72	73	56	57	206	234	202	239	84	95
8	#	#	#	#	#	#	#	#	#	#
9	58	63	54	55	127	139	159	177	65	71
10	64	66	49	50	103	86	146	127	80	72
11	#	#	#	#	#	#	#	#	#	#

Table 5.10: Mean percentage standard deviation (SD) of MTT obtained by SVD, cSVD, NSR, dcNSR, PD in the left and right hemisphere of each subject after surgery.

subject, NSR and dcNSR present the largest SD values, whereas SVD and cSVD provide the smallest one. PD percentage SD are smaller than NSR and dcNSR ones, but larger than the SVD and cSVD ones.

Particular slices have been selected in each subject to further investigate the performances of the deconvolution methods. MTT maps obtained by SVD, cSVD, NSR, dcNSR and PD in these slices are presented in next pages (Figures from 5.27 to 5.44). Absolute MTT maps are expressed in seconds. As for the CBF maps, PD MTT maps are comparable to those provided by SVD and cSVD, but they present a higher contrast level, thus emphasizing the differences in the MTT distribution. NSR and dcNSR present even higher contrasted MTT maps. On the one hand, NSR and dcNSR allow to easily detect disease affected areas. On the other hand, they sometimes provide very noisy maps, which are difficult to analyse.

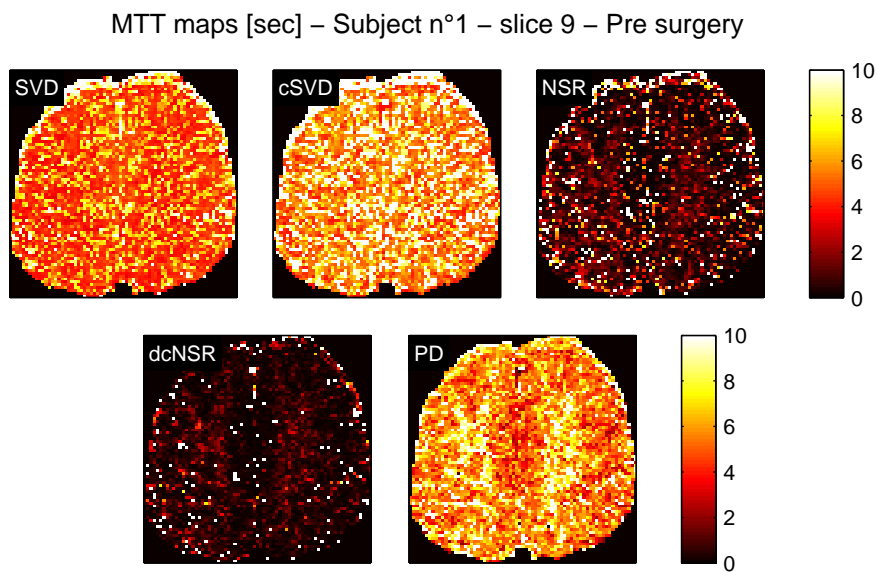


Figure 5.27: MTT maps obtained by SVD, cSVD, NSR, dcNSR and PD in subject n° 1 before surgery. Relative MTT values are normalized to the same reference region in each map.

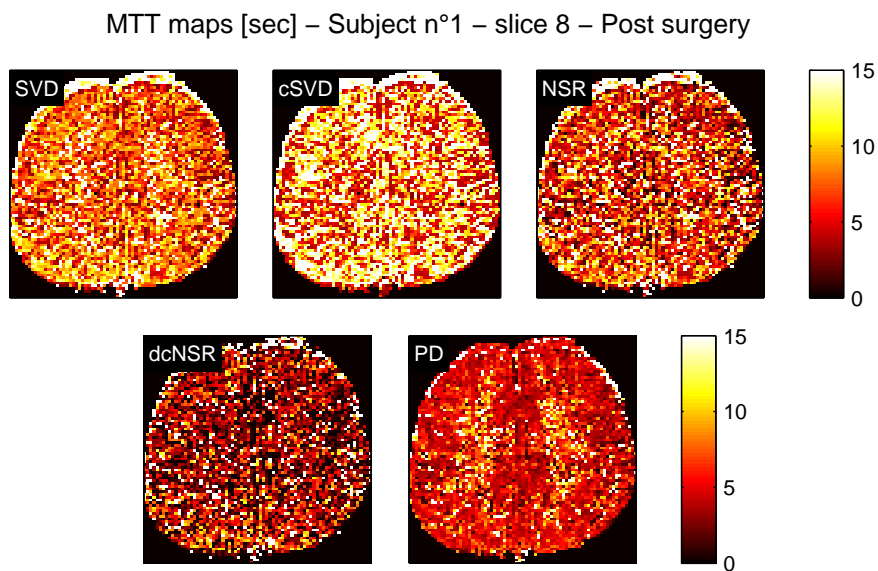


Figure 5.28: MTT maps obtained by SVD, cSVD, NSR, dcNSR and PD in subject n° 1 after surgery. Relative MTT values are normalized to the same reference region in each map.

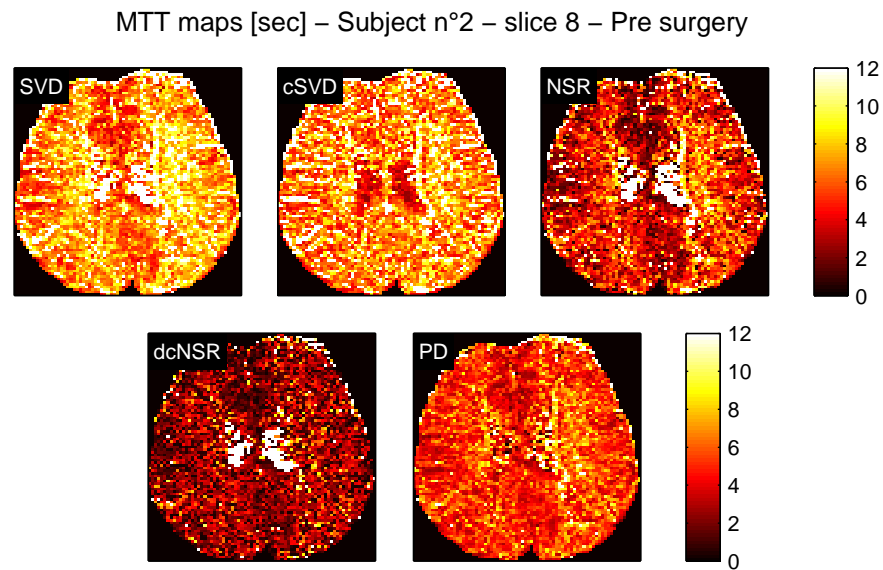


Figure 5.29: MTT maps obtained by SVD, cSVD, NSR, dcNSR and PD in subject n° 2 before surgery. Relative MTT values are normalized to the same reference region in each map.

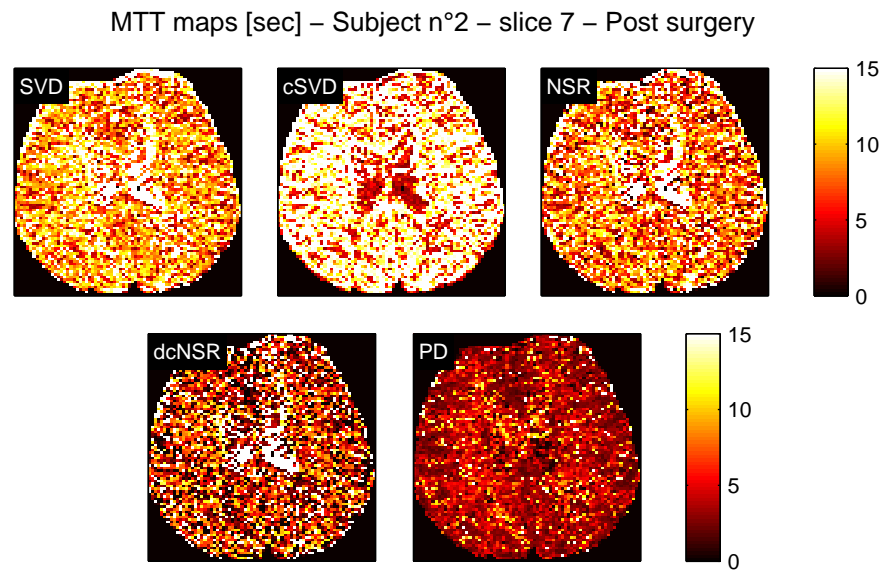


Figure 5.30: MTT maps obtained by SVD, cSVD, NSR, dcNSR and PD in subject n° 2 after surgery. Relative MTT values are normalized to the same reference region in each map.

MTT maps [sec] – Subject n°3 – slice 10 – Pre surgery

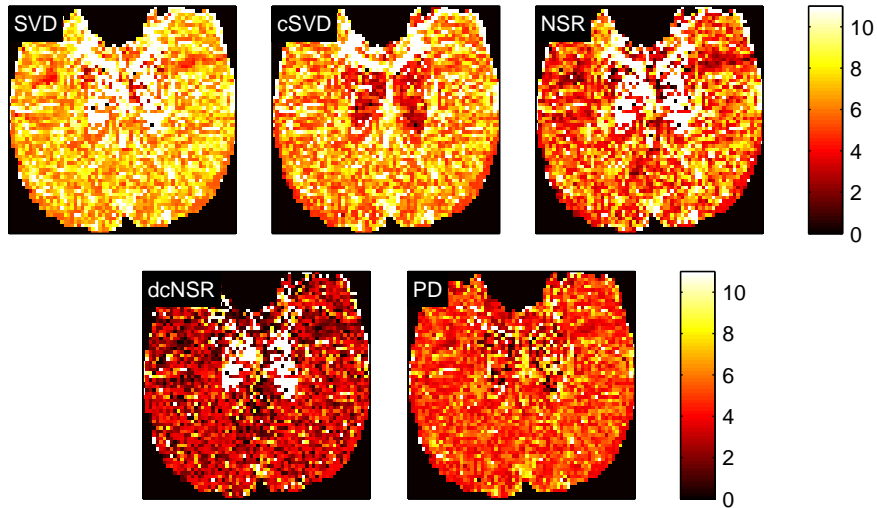


Figure 5.31: MTT maps obtained by SVD, cSVD, NSR, dcNSR and PD in subject n° 3 before surgery. Relative MTT values are normalized to the same reference region in each map.

MTT maps [sec] – Subject n°3 – slice 10 – Post surgery

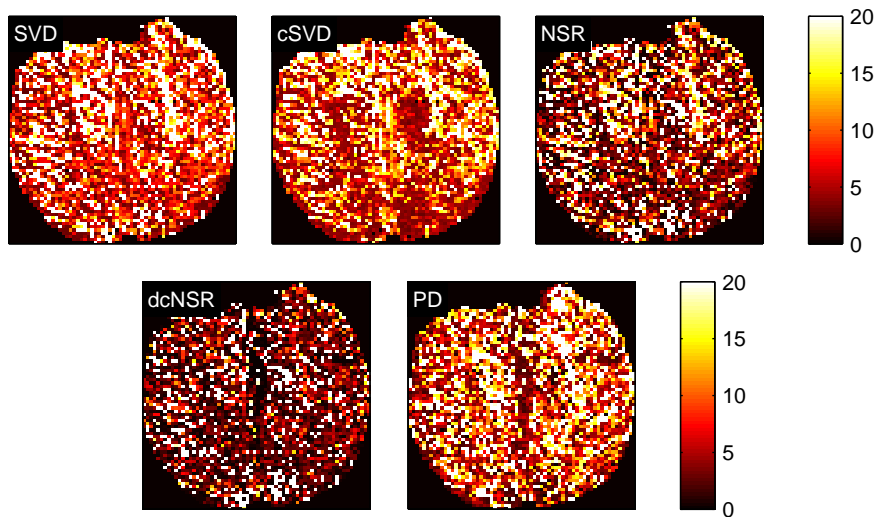


Figure 5.32: MTT maps obtained by SVD, cSVD, NSR, dcNSR and PD in subject n° 3 after surgery. Relative MTT values are normalized to the same reference region in each map.

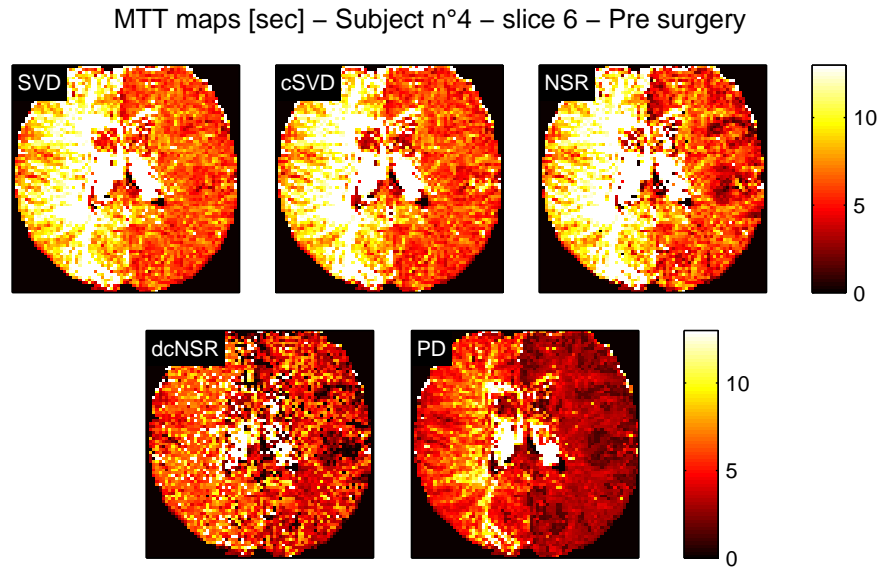


Figure 5.33: MTT maps obtained by SVD, cSVD, NSR, dcNSR and PD in subject n° 4 before surgery. Relative MTT values are normalized to the same reference region in each map.

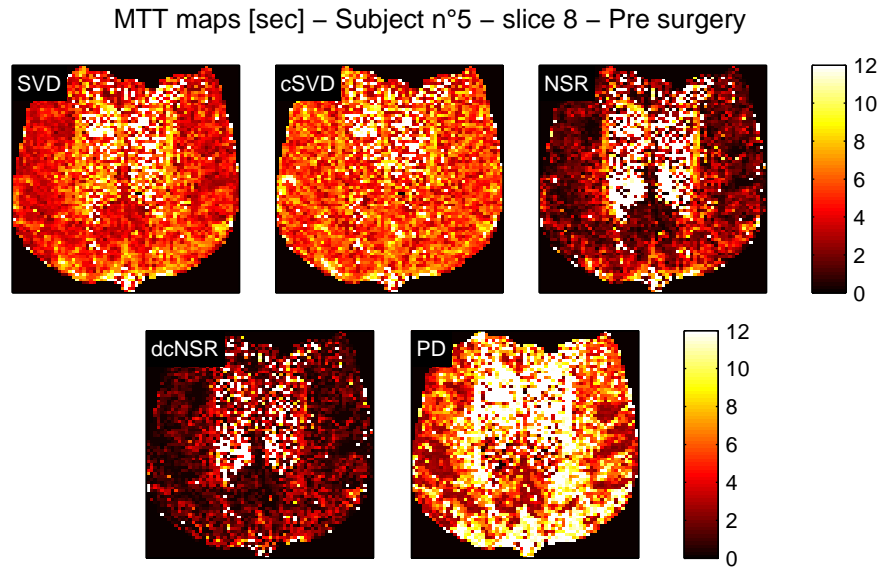


Figure 5.34: MTT maps obtained by SVD, cSVD, NSR, dcNSR and PD in subject n° 5 before surgery. Relative MTT values are normalized to the same reference region in each map.

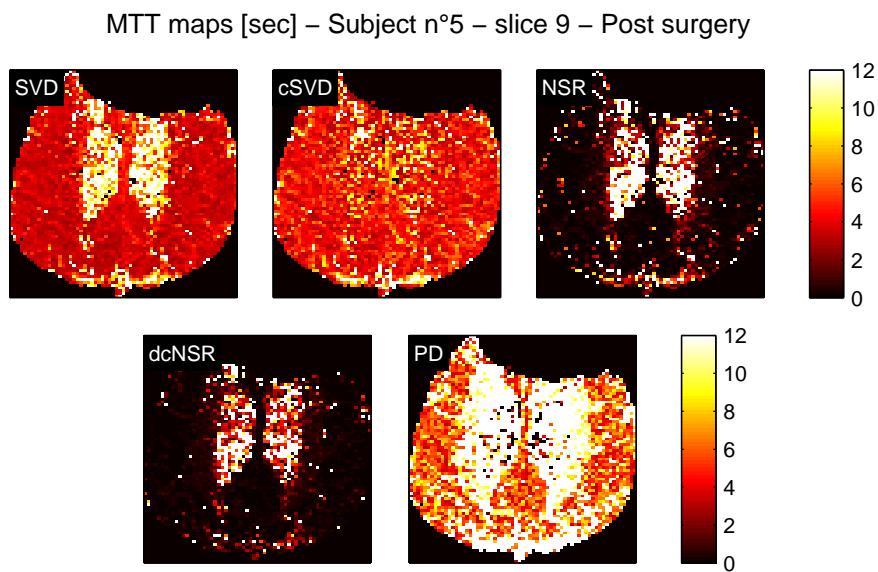


Figure 5.35: MTT maps obtained by SVD, cSVD, NSR, dcNSR and PD in subject n° 5 after surgery. Relative MTT values are normalized to the same reference region in each map.

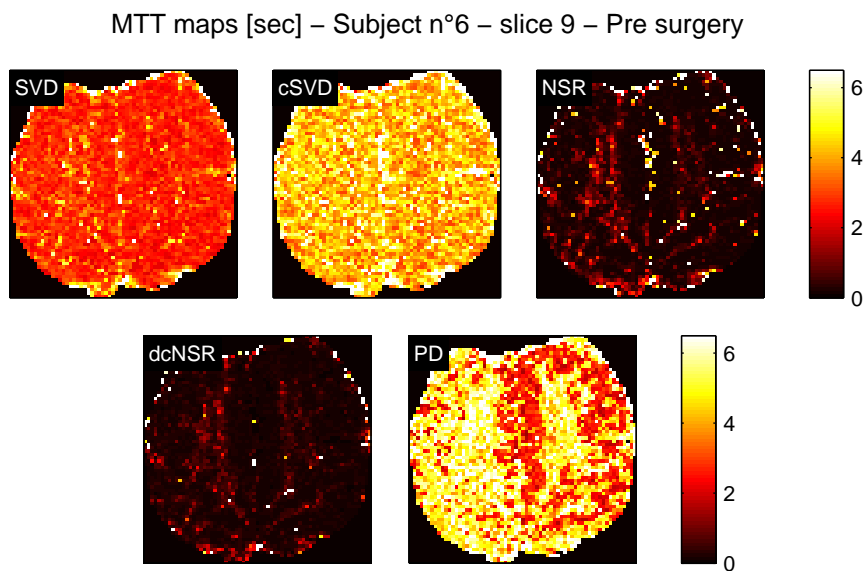


Figure 5.36: MTT maps obtained by SVD, cSVD, NSR, dcNSR and PD in subject n° 6 before surgery. Relative MTT values are normalized to the same reference region in each map.

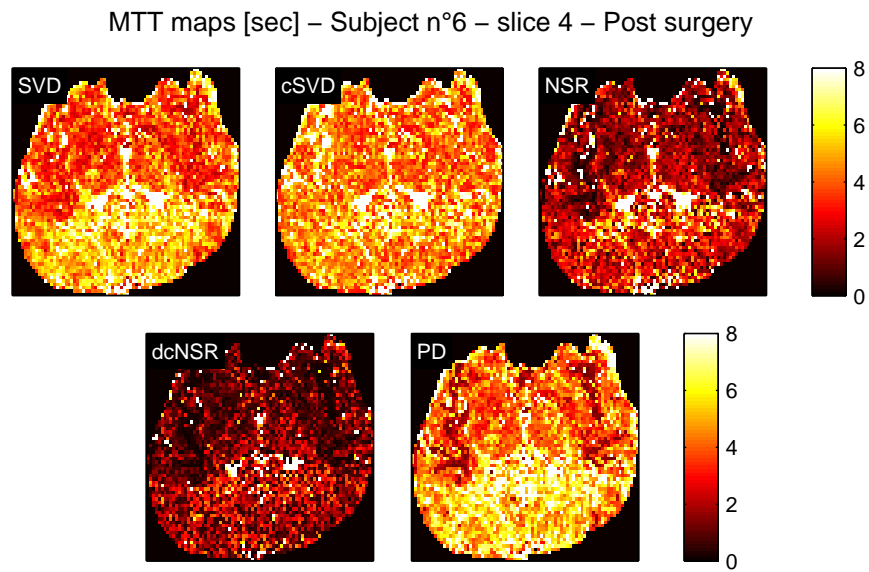


Figure 5.37: MTT maps obtained by SVD, cSVD, NSR, dcNSR and PD in subject n° 6 after surgery. Relative MTT values are normalized to the same reference region in each map.

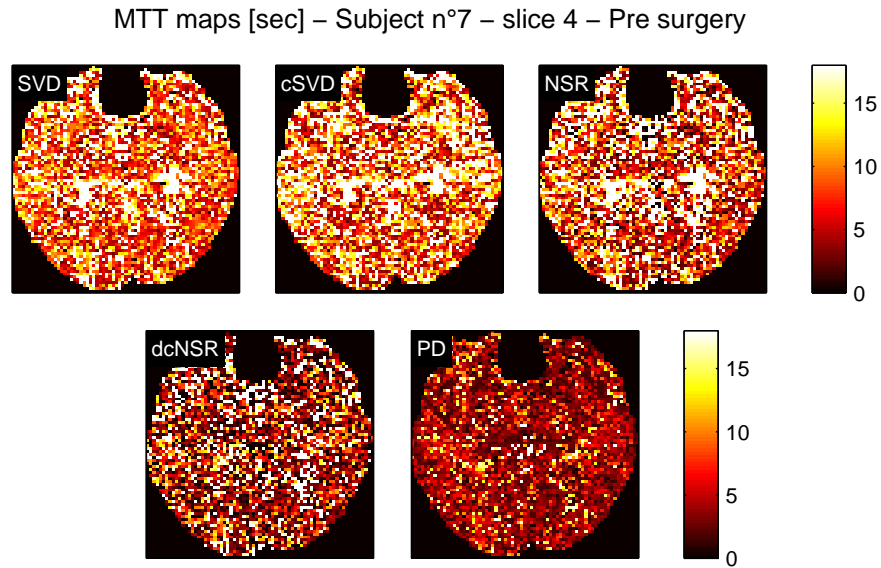


Figure 5.38: MTT maps obtained by SVD, cSVD, NSR, dcNSR and PD in subject n° 7 before surgery. Relative MTT values are normalized to the same reference region in each map.

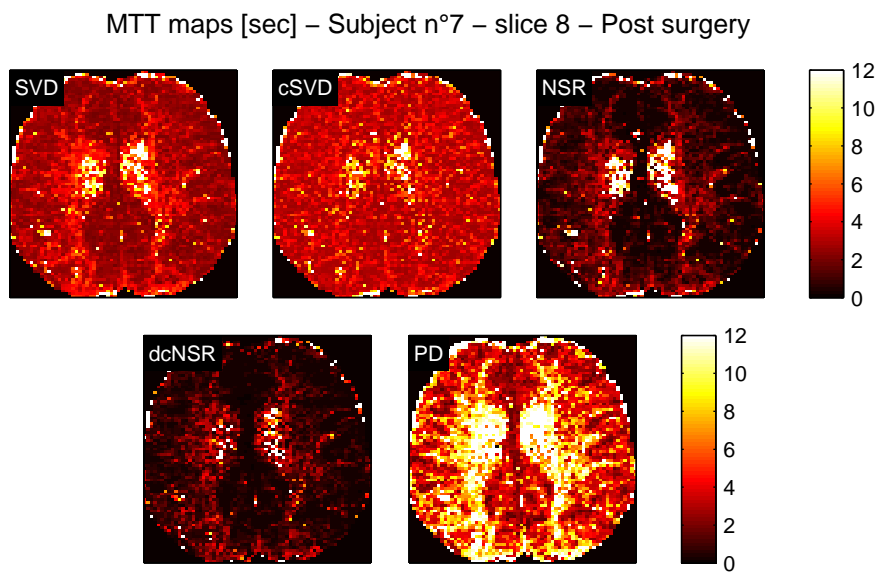


Figure 5.39: MTT maps obtained by SVD, cSVD, NSR, dcNSR and PD in subject n° 7 after surgery. Relative MTT values are normalized to the same reference region in each map.

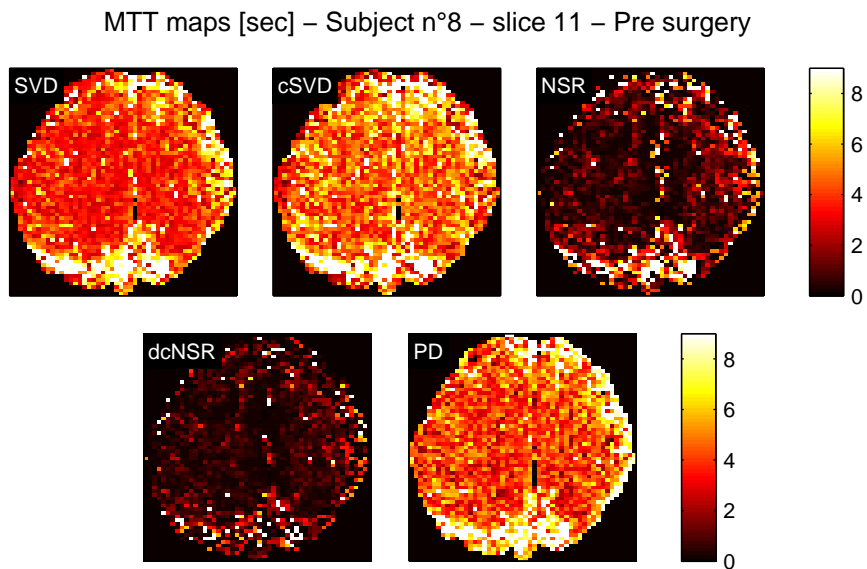


Figure 5.40: MTT maps obtained by SVD, cSVD, NSR, dcNSR and PD in subject n° 8 before surgery. Relative MTT values are normalized to the same reference region in each map.

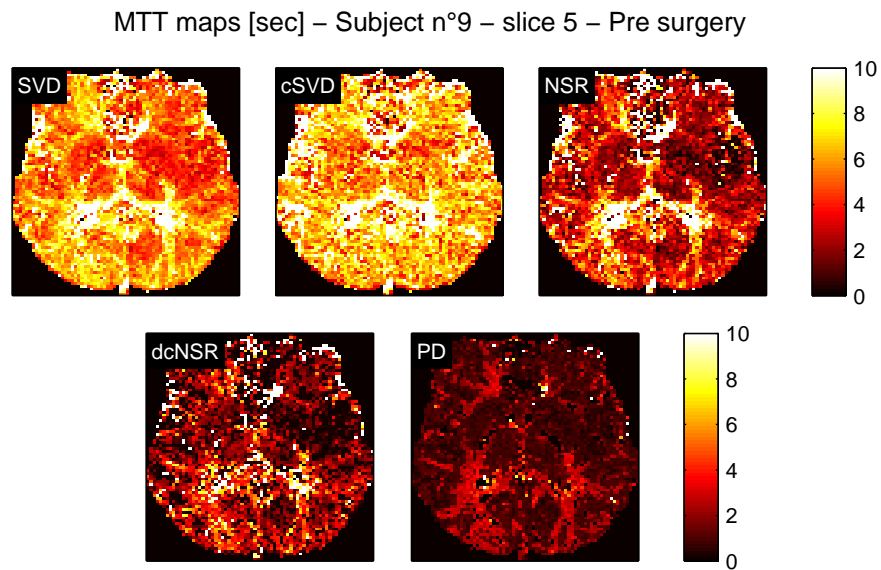


Figure 5.41: MTT maps obtained by SVD, cSVD, NSR, dcNSR and PD in subject n° 9 before surgery. Relative MTT values are normalized to the same reference region in each map.

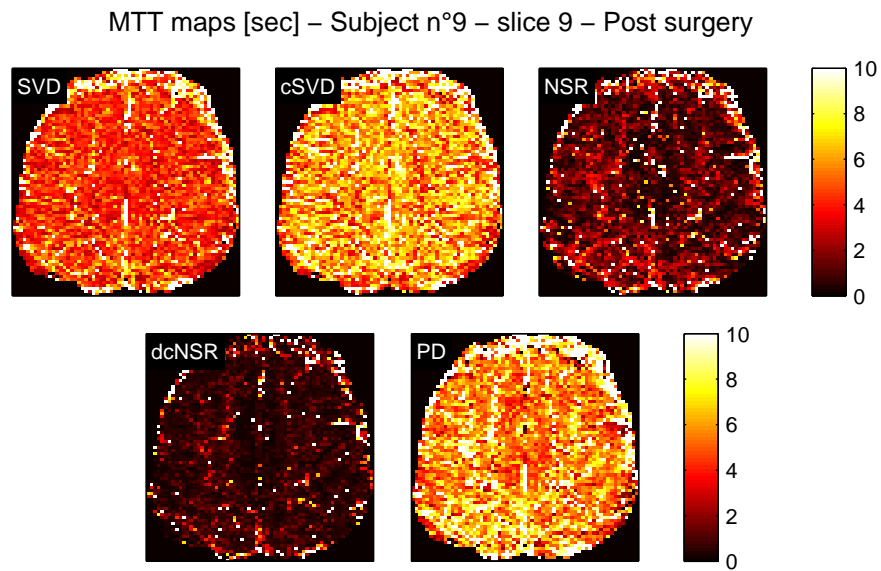


Figure 5.42: MTT maps obtained by SVD, cSVD, NSR, dcNSR and PD in subject n° 9 after surgery. Relative MTT values are normalized to the same reference region in each map.

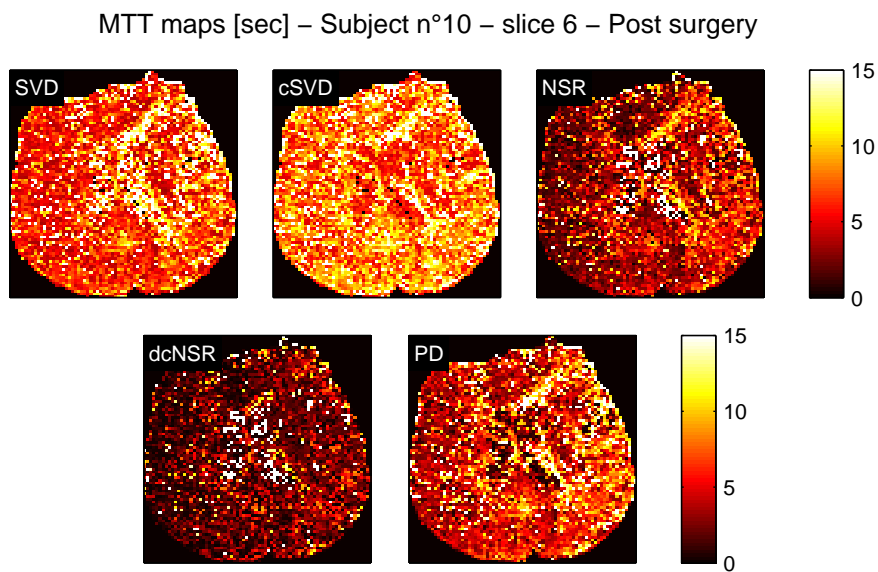


Figure 5.43: MTT maps obtained by SVD, cSVD, NSR, dcNSR and PD in subject n° 10 after surgery. Relative MTT values are normalized to the same reference region in each map.

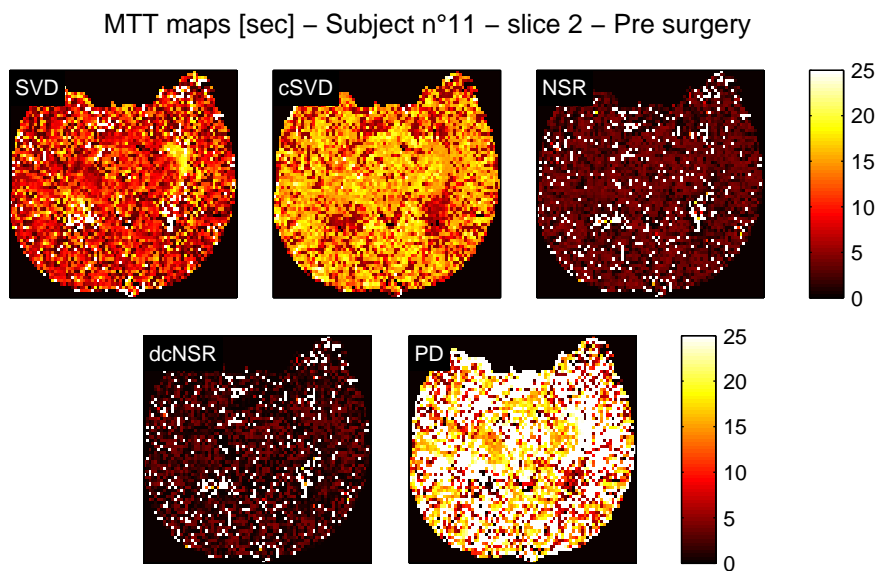


Figure 5.44: MTT maps obtained by SVD, cSVD, NSR, dcNSR and PD in subject n° 11 before surgery. Relative MTT values are normalized to the same reference region in each map.

### 5.6.4 Laterality Indices

MTT and CBF laterality indices were computed for all subjects, before and after surgery. They are a graphical representation of the CBF and MTT distribution across all slices. Thus, they allow an easy and immediate interpretation of the information provided by CBF and MTT maps. Furthermore, they can be used to monitor the recovery after the surgical treatment. As expected, MTT laterality indices are commonly smaller than CBF ones. As discussed previously, MTT distribution differences are usually smaller than the CBF ones because of the compensation mechanisms in cerebral hemodynamic. However, MTT laterality indices increase the clinical information in DSC-MRI image quantification, thus leading to a more accurate disease detection and characterization.

As example of the laterality indices interpretation consider a patient with a stenosis in a carotid. The disease reduces the hematic support in the pathologic hemisphere: this is revealed by lower CBF values and higher MTT values than healthy hemisphere ones. Positive CBF laterality index indicates a higher mean CBF value in the right hemisphere than in the left one, suggesting a pathologic condition in the left hemisphere. Likewise, negative CBF laterality index points out a difference in CBF values in favour of the left hemisphere. Opposite remarks have to be done considering the MTT laterality index. Pathologic tissue is characterized by a slow blood flow, thus by a higher MTT than the healthy hemisphere. Therefore, positive MTT laterality index indicates higher MTT values in the right hemisphere than in the left one, thus suggesting that the right hemisphere is the pathologic one. Negative MTT laterality index indicates a higher MTT in the left hemisphere than in the right and that the disease is localized in the left hemisphere. Moreover, high absolute values in the laterality indices indicate a prominent hemodynamic difference between the two hemispheres, whereas small values characterize a healthy condition. Therefore, laterality indices can be used to evaluate both the disease severity and its localization.

NSR and dcNSR commonly provide very large laterality indices, which are usually larger than those obtained by SVD, cSVD and PD. Wide laterality indices emphasize anomalies in CBF and MTT distribution, thus allowing to easily detect the pathologic brain areas. However, NSR and dcNSR laterality indices are sometimes too large and loose any physiological meaning. Moreover, NSR and dcNSR sometimes provide dissonant results. This can be due to the high contrast level in NSR and dcNSR CBF and MTT maps; low variations in CBF and MTT distribution are highlighted, whereas high variations lead to very noisy maps.

SVD and cSVD laterality indices are usually very close to zero, thus concealing the differences between the left and right hemisphere. Moreover, results do not change after the treatment; rather, they sometimes get worse in the post-surgery examination.

PD laterality indices are usually smaller than the NSR and dcNSR ones, but also larger than the SVD and cSVD ones. They do not present unphysiologically high values as in NSR and dcNSR results, but they still underline differences in CBF and MTT distribution between the two hemispheres. Moreover, PD usually presents significant changes in the post-surgery results, allowing to evaluate the improvement in the patient clinical state.

Figures 5.45-5.48 show the CBF and MTT laterality indices obtained by SVD, cSVD, NSR, dcNSR and PD in subjects n° 3 and 9, before and after surgery. As pointed out previously, cSVD and SVD laterality indices are usually close to 0, whereas NSR and dcNSR show the largest ones. Furthermore, NSR and dcNSR sometimes provides very high results, without any physiological meaning (e.g. Figure 5.46 slices n° 3 - 10 - 11 - 12).

In subject n° 3, laterality indices detect a pathological area in slice n° 9 (Figure 5.45). CBF laterality indices also indicate an irregular flow distribution in slices n° 2 - 6 - 8 - 10, but they are not supported by the MTT laterality indices. On the one hand, differences in slices n° 8 - 10 confirm the pathological state in slice n° 9. On the other hand, the integration between CBF and MTT laterality indices allow to ignore false positive results obtained in slices n° 2 - 6. In the post surgery examination (Figure 5.46) an improvement in CBF and MTT laterality indices is pointed out by all methods.

Similar results are obtained in subject n° 9. The pre-surgery examination confirms the physician diagnosis, whereas an improvement is shown in the post-surgery one. Considering the slice n° 7 in Figure 5.47, all methods detect the anomaly in the CBF and MTT distribution, but they do not provide the same results. On the one hand, NSR and dcNSR report CBF laterality index larger than 1, thus quite unreliable. On the other hand, the disease is not very emphasized by SVD and cSVD. PD results are smaller than the NSR and dcNSR ones and larger than the SVD and cSVD ones, thus providing a good emphasis without losing the laterality index physiological meaning.

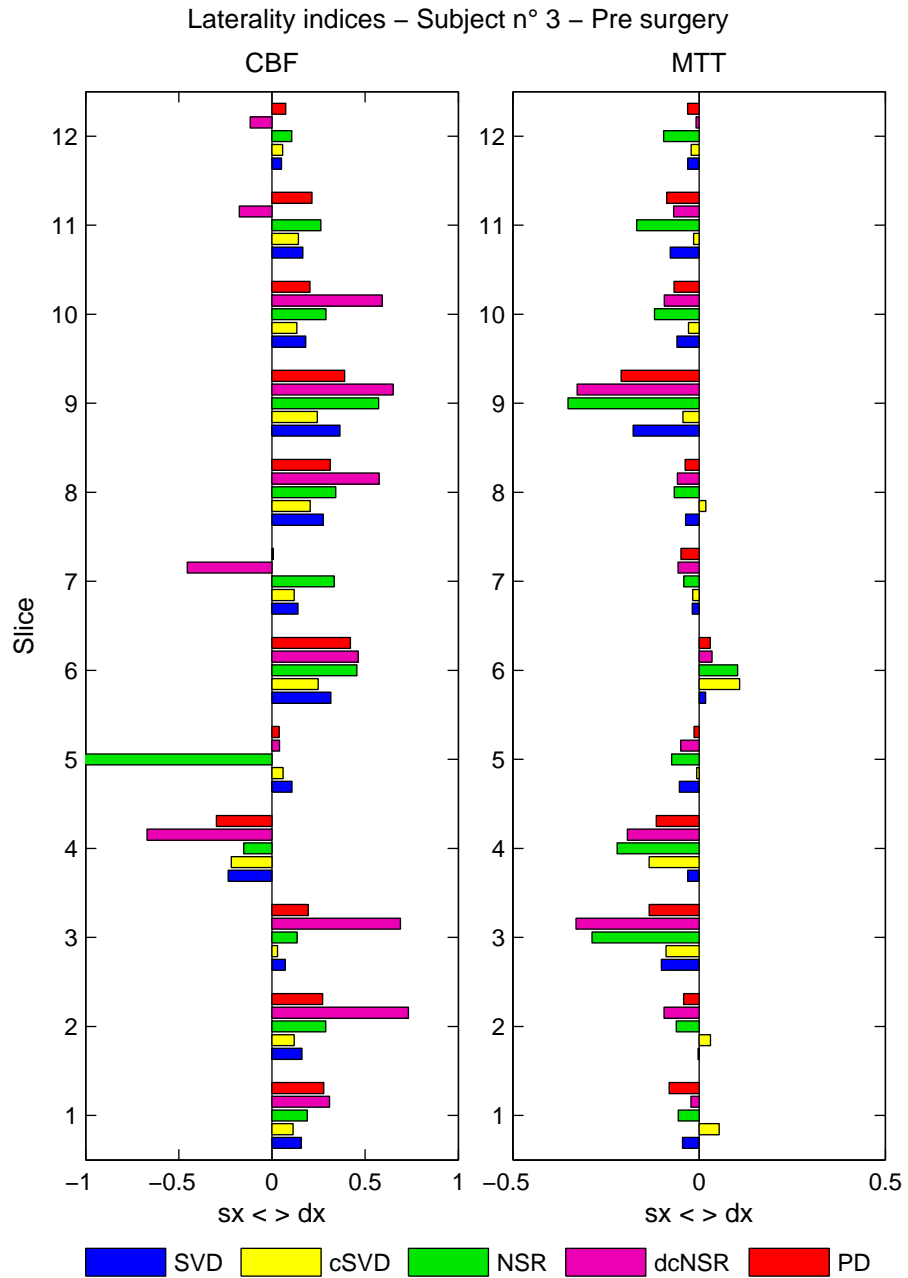


Figure 5.45: CBF and MTT laterality indices obtained in subject n° 3 before surgery.

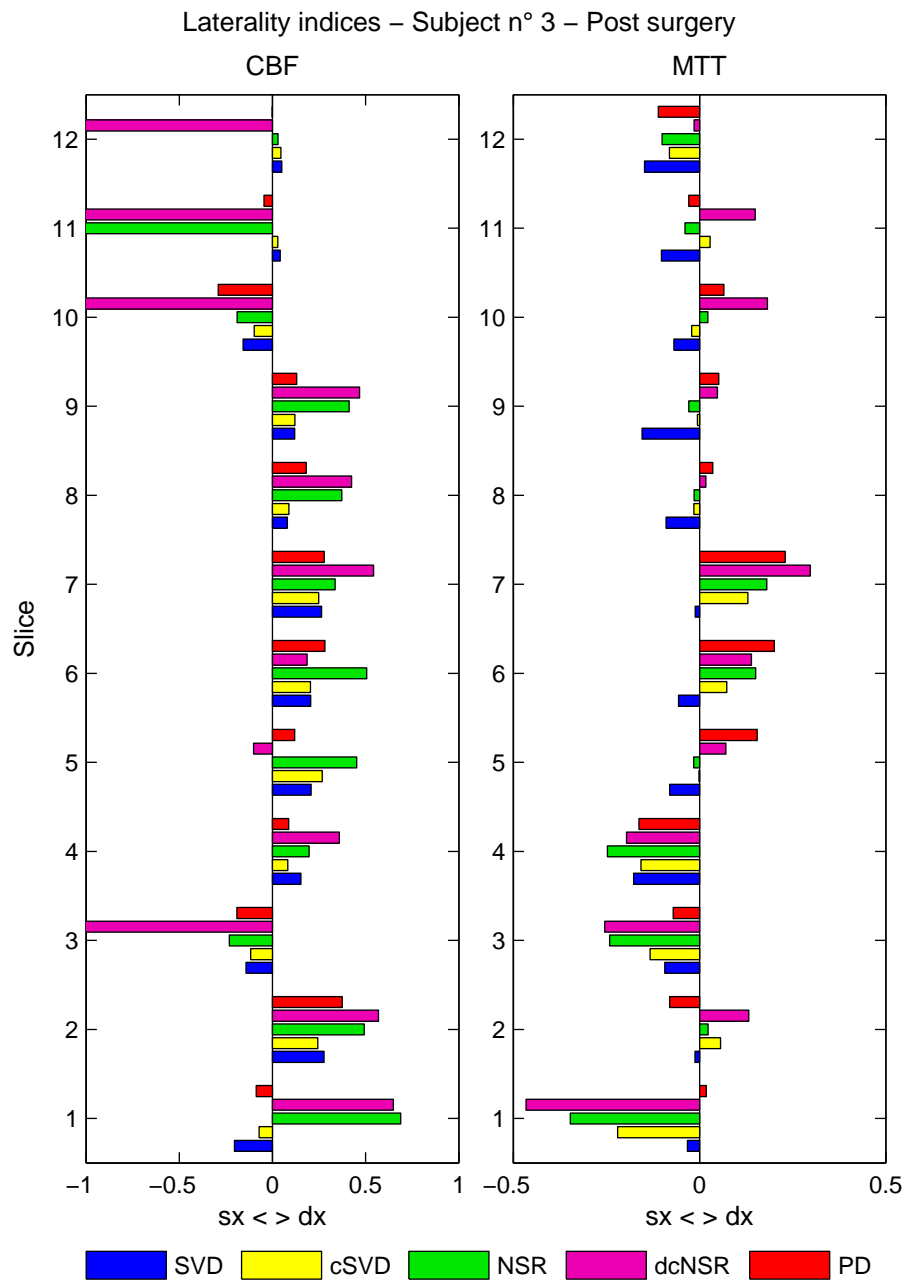


Figure 5.46: CBF and MTT laterality indices obtained in subject n° 3 after surgery.

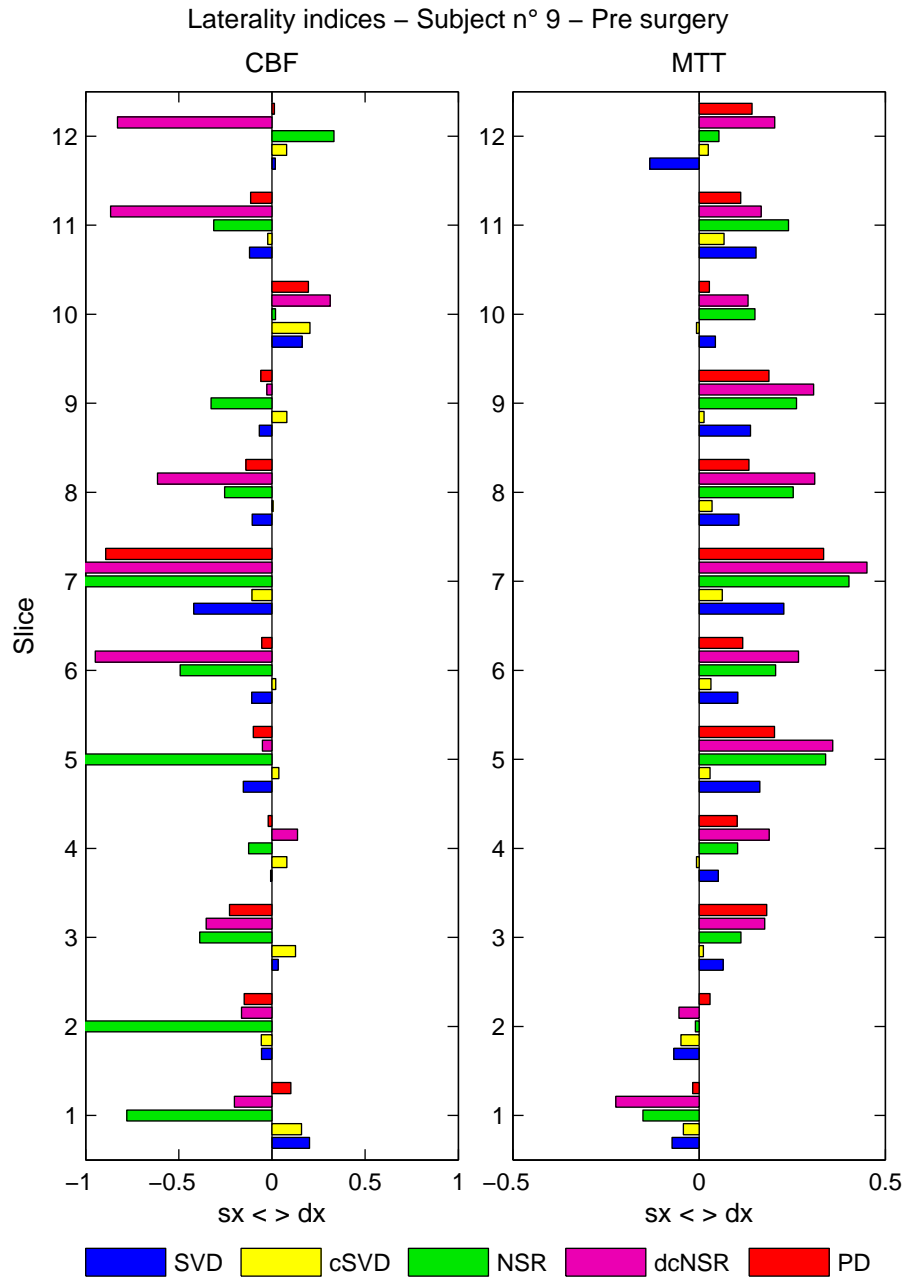


Figure 5.47: CBF and MTT laterality indices obtained in subject n° 9 before surgery.

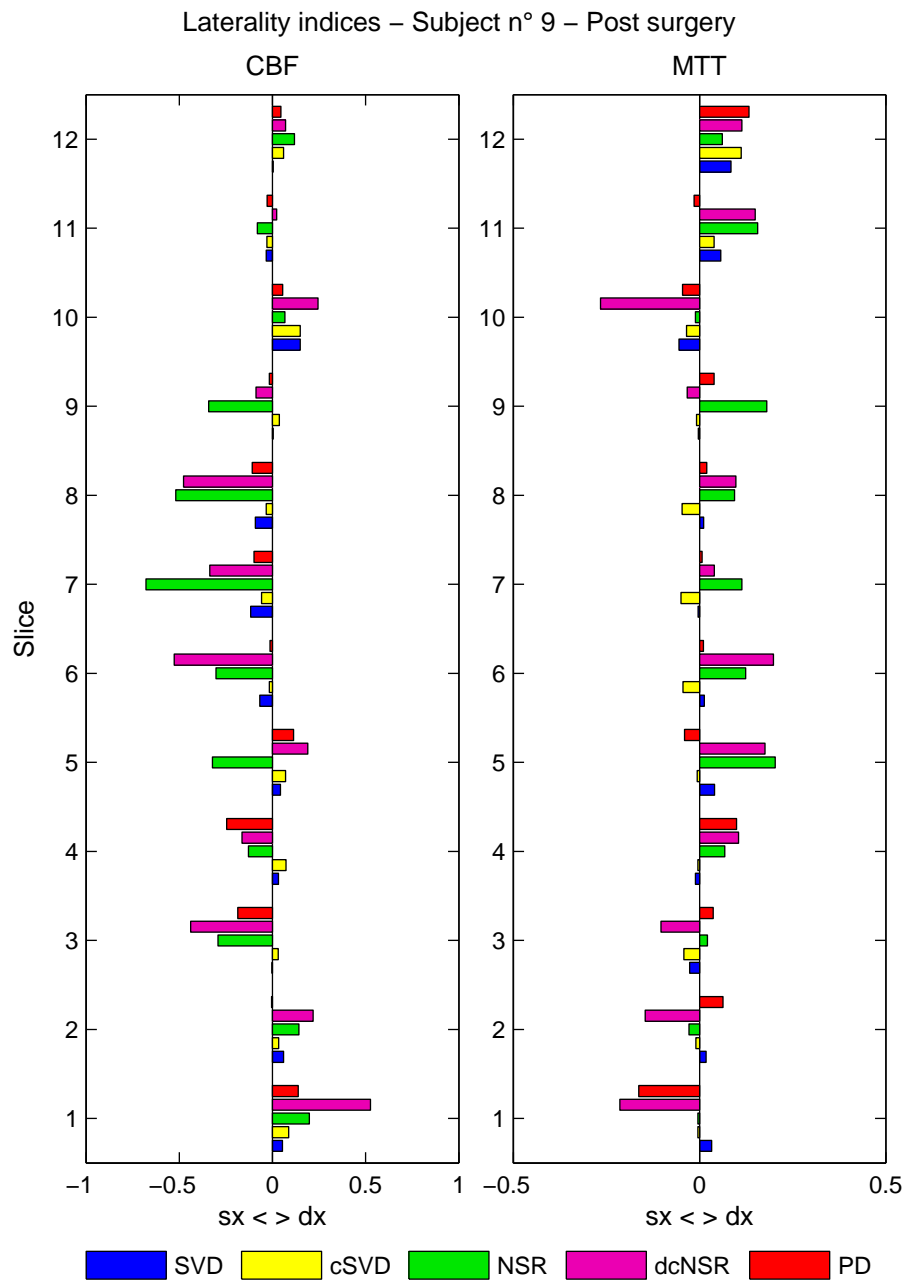


Figure 5.48: CBF and MTT laterality indices obtained in subject n° 9 after surgery.

## 5.7 Clinical Data: Discussion

SVD, cSVD, NSR, dcNSR and PD have been compared on a clinical DSR-MRI image data set. The data set includes 11 patients with severe atherosclerotic unilateral stenosis of the internal carotid artery. For 8 of the considered subjects, examination was repeated 6 months after the surgical introduction of a shunt to eliminate or reduce the pathology.

In each subject, a global AIF was automatically detected using the method proposed in chapter 4. According to [72], a Gamma-variate fit was performed on each voxel concentration curve to eliminate recirculation. In each slice, two ROIs were considered in the left and in the right hemisphere to investigate the deconvolution method performances.

216 CBV maps were obtained according to Eq. (2.4). Ratios between the right and left hemisphere were computed to investigate the differences in blood volume distribution between the two hemispheres. Reported CBV maps are expressed in ml/g percentage as commonly done in literature; results are comparable to the values reported in literature, but they are still far from ideal due to the DSC-MRI absolute quantification problem.

1080 relative CBF maps were obtained by applying SVD, cSVD, NSR, dcNSR and PD. The ratios between the right and left hemisphere were calculated (i.e. ROI analysis) to investigate the differences in the estimated blood flow. In general, NSR and dcNSR show the highest CBF ratios, thus significantly emphasizing the CBF distribution anomaly. However, the difference between the CBF ratio and the unit is sometimes very high, due to the very high contrast level in the NSR and dcNSR CBF maps. cSVD ratios are very close to unit, hence make the identification of pathological areas more difficult. PD and SVD provide comparable CBF ratios, closer to the unit than the NSR and dcNSR ones, but less than the cSVD ones. In the post-surgery situation, the different methods provide a closer to unit CBF ratio, suggesting that pathologic situation has been recovered. Normalized relative CBF maps obtained by PD are comparable in term of values to those provided by SVD and cSVD, but they show more contrasted areas, emphasizing the flow differences. NSR and dcNSR maps are extremely contrasted, but appear noisier than the PD ones.

1080 absolute MTT maps were computed as the ratio between CBV and CBF. The ratio between the right and left hemisphere was computed in each slice to investigate the differences in the blood transit time. As expected, differences in MTT distribution are generally smaller than differences in CBF distribution, for all deconvolution methods. As in the CBF ratio, NSR and dcNSR show the highest MTT ratios, thus significantly emphasizing the MTT distribution anomaly. cSVD MTT ratios are very close to unit, whereas SVD and PD underline the differences in MTT distribution better than cSVD. PD MTT ratios are also slightly further from unit than SVD, but always closer to unit than NSR and dcNSR. MTT ratios sometimes do not lead to the same diagnosis than CBF ones. This because of the compensation mechanisms present in patients affected by stenosis. MTT maps provided by PD are comparable to the SVD ones, but present a higher contrast level. Therefore, the pathologic area detection is easier in PD maps than in SVD ones. cSVD maps are extremely uniform, pathologic areas are very difficult to detect. NSR and dcNSR maps appear to be very

noisy, thus they are difficult to interpret.

Laterality indices were computed to provide a graphical representation of the CBF and MTT map information. Since cerebral auto-regulation and compensation mechanisms can modify CBF, CBV and MTT, the integration of the whole information provided by the different parameters leads to a more accurate diagnosis. NSR and dcNSR provide very large laterality indices, thus emphasizing the disease affected regions. Nevertheless, they sometimes present too high and unphysiological indices. Moreover, healthy areas are still characterized by laterality indices not close to 0. SVD and cSVD laterality indices are generally very close to 0 and they make the disease detection difficult. PD laterality indices are usually larger than the SVD and cSVD ones, but smaller than the NSR and dcNSR ones. Therefore, it meets the need to underline the pathologic areas without showing false positive results.

The most crucial step in the PD method is the preliminary elaboration. If the PD algorithm is provided with a multimodal population, then a bias is introduced on residue function estimates. If a population is much larger than the other ones, then it includes the smaller ones, whose residue function estimates are not accurate. Moreover, including a small population in a larger one means losing part of its information because of the mean population curve computed in the initial steps of the algorithm. If two or more populations present a comparable number of voxel, then the hyper parameter estimate fails. In this case, the hyper parameter describing the residue function individual shift increases and the oscillations in the estimated  $R(t)$  get wider. Therefore, population division has to be carefully performed.

Summarizing, a novel method (PD) for the DSC-MRI image quantification has been proposed, validated and compared to two classic methods (SVD, cSVD) and to a recently proposed method (NSR, dcNSR). PD can provide reliable residue function estimates and high quality CBF and MTT maps. ROI analysis and laterality indices obtained by PD show that PD is a valid alternative for the DSC-MRI image quantification.



## Chapter 6

# Dynamic Susceptibility Contrast -MRI: a New Kernel-Based Deconvolution Approach

This chapter introduces a novel deconvolution approach, which has been recently proposed and is still being developed. The method has been tested on simulated data, providing quite good results. A first attempt on clinical data has been also performed. This method differs from the PD method proposed in chapter 5 both in the problem approach and in the application field. Thanks to its population approach, PD is suitable for large voxel set analysis, providing good results and a short computation time. However, PD is not applicable when only a small brain region is considered because the population approach is no longer valid. On the other hand, the new method is voxel based and can be applied also on a small brain region. Although it is still under refinement, the obtained results are promising and make it very interesting. It has therefore been included in this work.

### 6.1 Theory

The most crucial step in the DSC-MRI image quantification is the residue function identification. In other words, the impulsive response of a time-invariant linear system has to be estimated starting from the noisy output samples (i.e. the voxel concentration samples) and the system input (i.e. the arterial input).

In literature, the most used methods for the system identification start from identifying a low-order model by using standard techniques, such as maximum likelihood or predictor error methods [31, 32, 47]. Then, they proceed to quantify bias and variance errors on the basis of the model. In the stochastic embedding approaches, the a priori knowledge is usually formulated on the bias

error. Here, a new kernel-based approach is applied to formulate the probabilistic prior directly on the unknown residue function. The a priori knowledge is hence used to provide a model of  $R(t)$ , rather than the errors of measure and model.

Let us begin from the problem statement. In DSC-MRI, the model associated to the measurements is

$$c(t_i) = \int_0^{t_i} R^*(t_i - \tau - \Delta) \cdot AIF(\tau) d\tau + v_i = L_i^{AIF}[R, \Delta] + v_i \quad (6.1)$$

where  $\{c(t_i)\}$  are the concentration samples obtained on the temporal grid  $\{t_i\}_{i=1}^n$ ;  $R^*(t)$  is the residue function multiplied by CBF and the proportionality constant (i.e.  $R^*(t) \sim CBF \cdot R(t)$ );  $\Delta$  accounts for a possible time-delay in the system and  $\{v_i\}$  is a white Gaussian noise with variance  $\sigma^2$ . From now on,  $L_i^{AIF}[R, \Delta]$  indicates the model prediction at time  $t = t_i$ , i.e. the convolution computed at time  $t = t_i$  between AIF and  $R(t)$ , with a delay of  $\Delta$ .

In a kernel based approach a prior is assumed; it consists of a stochastic model for  $R^*(t)$ . Commonly, the prior consists of a Gaussian measure in an infinite-dimensional function space. Such prior can be used to define a transformation from the normal space to a Hilbert space  $\mathcal{H}$ . Since the transformation between space is uniquely identified by its kernel, the prior can be represented also by the kernel itself. If the prior is indeed composed by a Gaussian measure, then the associated kernel is a Mercer kernel and the Hilbert space is a reproducing kernel Hilbert space (RKHS). A RKHS satisfies two proprieties: the pointwise evaluation is a continuous linear functional space and the inner product satisfies the reproducing property. Thus, a RKHS is equipped by a norm, which derives from the inner product.

Let us assume that  $R^*(t)$  and  $\{v_i\}$  are jointly normal and there is no feedback in the system (these assumptions are fair in the DSC-MRI context). If the prior associated to  $R^*(t)$  can be represented as a Mercer kernel, then the minimum variance estimate of the residue function can be proved to be given by

$$\hat{R}^* = \arg \min_{R^*} \sum_{i=1}^n (c_i - L_i^{AIF}[R^*; \Delta])^2 + \gamma \|\mathbf{P}[R^*]\|_{\mathcal{H}}^2 \quad (6.2)$$

where  $\mathbf{P}$  denotes the orthogonal projection of  $R^*$  onto  $\mathcal{H}$ ;  $\|\cdot\|_{\mathcal{H}}$  is the norm associated with  $\mathcal{H}$ ;  $\gamma$  is the so-called regularization parameter, which has to correctly balance the expected regularity of the solution and the adherence to experimental data.

Typical choices are Gaussian or polynomial kernels. In DSC-MRI context, the residue function is known to be regular, thus the most popular approach is to model it as an integrated Wiener process with unknown initial conditions. The kernel (W) associated to this statistical assumption is

$$W(s, \tau) = cov\left(\tilde{R}(s), \tilde{R}(\tau)\right) = \begin{cases} \frac{s^2}{2} \left(\tau - \frac{s}{3}\right) & s \leq \tau \\ \frac{\tau^2}{2} \left(s - \frac{\tau}{3}\right) & s > \tau \end{cases} \quad (6.3)$$

and  $\tilde{R}$  is a zero-mean Gaussian process with auto-covariance  $\lambda^2 W$ .

The regularization method described in Eq (6.2) is a Tikhonov-type problem, thus it presents an explicit solution for every given  $\gamma$ . Kernel based regularization methods are widely employed in the nonparametric system identification, but they are not suitable to reconstruct the impulse response in a physical context because of several limitations. For instance, they are not able to obtain unbiased estimates of functions defined on a noncompact domain, such as an exponential on  $X = [0, +\infty)$ . Moreover, the variance of the processes associated with the most used kernels increases over time (e.g.  $W$ ). However, in a physical context, the impulse response variability is larger in the first time instants and decreases over time. In particular, the prior defined by  $W$  does not include the BIBO-stability constraint.

The prior defined in the DNP method overcomes these limitations. Firstly, it defines a time transformation that maps the noncompact domain  $X$  into  $S = [0, 1]$  and the exponential functions on  $X$  into straight lines on  $S$ . Such time transformation is

$$\tau = e^{-\beta t} \quad t \in X \quad (6.4)$$

Then, the prior is defined on the new coordinates. It is exactly the integrated Wiener process with zero initial value and arbitrary first-order derivative at zero. The resulting kernel ( $K$ ) is

$$K(s, t) = W(e^{-\beta t}, e^{-\beta s}) \quad (s, t) \in X \times X \quad (6.5)$$

The stochastic model for the residue function becomes

$$R^*(t) = \begin{cases} 0 & t < 0 \\ \theta e^{-\beta t} + \tilde{R}(t) & t \in X \end{cases} \quad (6.6)$$

where  $\theta \in \mathbb{R}$  and  $\tilde{R}(t)$  is now a zero-mean Gaussian process with auto-covariance  $\lambda^2 K$ .

The residue function stability can be proved to be guaranteed if the function value is imposed to be null at zero in the new coordinates or, equivalently, that  $R^*(t) = 0$  for  $t \rightarrow +\infty$  in the old coordinates.

Once the prior is defined, the residue function estimate can be obtained from the Tikhonov estimator defined in Eq. (6.2). However, such estimator requires the knowledge of the parameter vector  $\eta = [\lambda, \beta, \sigma, \Delta, \theta]$ .  $\eta$  is treated as possibly unknown hyper-parameter vector and it is determined via maximum likelihood. Once  $\eta$  is determined, the estimator presents an explicit solution

$$\hat{R}^*(t) = \hat{\theta} e^{-\hat{\beta} t} + \hat{\lambda}^2 \sum_{i=1}^n b_i L_i^{AIF} [K(s, t; \hat{\beta}); \hat{\Delta}] \quad (6.7)$$

where  $\hat{\eta} = [\hat{\lambda}, \hat{\beta}, \hat{\sigma}, \hat{\Delta}, \hat{\theta}]$  is the  $\eta$  estimate and  $\{b_i\}$  are the elements of vector  $b \in \mathbb{R}^n$  given by

$$b = \text{Var} [y|\eta = \hat{\eta}]^{-1} \psi(\hat{\eta}) \quad (6.8)$$

where  $\text{Var} [y|\eta = \hat{\eta}]$  denotes the auto-covariance of the concentration samples given  $\eta$  and  $\psi(\eta) \in \mathbb{R}^n$  is the vector whose  $i$ -th component is  $y_i - L_i^{AIF} [\theta e^{-\beta t}; \Delta]$ .

A more accurate formulation and the complete proofs of the proposed method can be found in [28, 68, 69].

The most appealing feature of the DNP approach is that it was developed in a fully Bayesian context. The prior is defined directly on the residue function, whereas the most common stochastic methods base their model on the bias error. DNP assumes that the residue function is regular and it tends to zero for  $t \rightarrow +\infty$ . These constraints are very light and, most of all, they are physiologic and reflect the properties of the residue function defined in the dilution theory.

Another interesting feature of DNP is the delay problem treatment. Not only is DNP insensitive to it, but it can also estimate the delay between the AIF and the tissue concentration curve. In [14], the authors have shown that a delay of 1 to 2 seconds can introduce a 40% underestimation of CBF and a 60% underestimation of MTT. Furthermore, such delays are common in cerebral regions affected by vascular diseases. Therefore, a delay estimate can improve the CBF estimate accuracy and increase the information provided to the physician.

Moreover, DNP requires no parameter optimisation to provide suitable results. This makes the method very flexible because it can be applied on different data sets without a preliminary tuning step.

Although DNP has many advantages, it suffers from a shortcoming: the hyper-parameter number. DNP has to estimate the delay, the noise variance and the parameters embedded in the  $R(t)$  model. On the one hand, this increases the method flexibility; on the other hand, it increases the dimensionality problem. The hyper-parameters have to be estimated for each voxel and their estimate is obtained via non-linear methods. Therefore, DNP is computationally more expensive than the linear methods, such as SVD or cSVD.

## 6.2 Simulation: Set up

The simulated data set was generated as described in section 5.2 (page 75). Briefly, four different models for the residue function were considered (i.e. Exponential, Lorentzian, Gamma-variate and Dispersed Exponential functions), accounting both for the presence and the absence of dispersion.

Different CBF and MTT combinations were used to generate 100 simulated voxels for each residue function model. Then, a translation was performed on simulated voxels to replicate the delay effects. Delay of 0, 1, 2 samples were considered.

Gaussian noise was added to the concentration curves to generate four different noise conditions (SNR 5, 10, 50, 500), including the noise level which is commonly presents in patient data (SNR 10).

Summarizing, the simulated data set contains 4800 situations (4  $R(t)$  models  $\times$  100 CBF & MTT combinations  $\times$  3 delay  $\times$  4 SNR).

DNP was compared to the most applied deconvolution methods in DSC-MRI image quantification to be validated. In particular, the simulated data were analyzed using the following algorithms, implemented as proposed in the original publications

- *Singular value decomposition* (SVD) as in [61, 62];
- *Block-circulant singular value decomposition* (cSVD), as in [88]
- *De Nicolao & Pillonetto* system identification method (DNP).

### 6.3 Simulation: Results

The residue function was successfully estimated for each simulated voxel using the PD, SVD and cSVD methods.

The *root mean square error* (RMSE) between each estimated  $R(t)$  and the true  $R(t)$  was computed to evaluate the ability of each algorithm to reconstruct the true residue function. RMSE was computed using Eq. (4.6). Figure 6.1 reports the RMSE mean and standard deviation (SD) obtained by SVD, cSVD and DNP. Results are divided into residue function model and delay. The DNP method always provides the worst results, with the exception of the dispersed exponential  $R(t)$  with a 2 sample delay. However, its performances become comparable to the SVD and cSVD ones as delay increases. As expected, cSVD performs better than SVD when there is dispersion or delay between AIF and voxel curves. SVD results get significantly worse as delay increases, whereas cSVD appears to be quite insensitive to delay. DNP and cSVD provide their best results when considering a dispersed exponential  $R(t)$  and the worst ones when considering a Gamma-variate  $R(t)$ .

Figure 6.2 reports some instances of estimated residue functions at the noise level typically presents in the clinical data (SNR 10) when no delay is present, whereas Figure 6.3 shows some results obtained when a 2 sample delay is present between the AIF and the concentration data. The voxel with the best results and the one with the worst results were chosen in each residue function model. In each panel, the true  $R(t)$  is compared to the ones reconstructed by using DNP, SVD and cSVD. DNP provides very good results in the best cases, performing better than SVD and cSVD, both in presence and in absence of delay. However, in the worst cases, DNP shows both over and underestimation of the residue function peak. Noticeably, residue functions reconstructed using DNP never present oscillations after the main peak, whereas SVD and cSVD ones are characterized by a large number of unphysiological oscillations. In many cases, the spurious oscillations in the SVD and cSVD estimates make the detection of the residue function main peak very difficult. Thus, DNP provides more physiological and reliable  $R(t)$  than SVD and cSVD.

CBF was computed for each voxel as the maximum of the estimated residue function. The estimated CBF percentage error was computed for each voxel. Figure refCBFerrDNP shows the percentage error mean and SD obtained using the different deconvolution methods. Results are subdivided into the different residue function models and delay. DNP presents the smallest mean error in

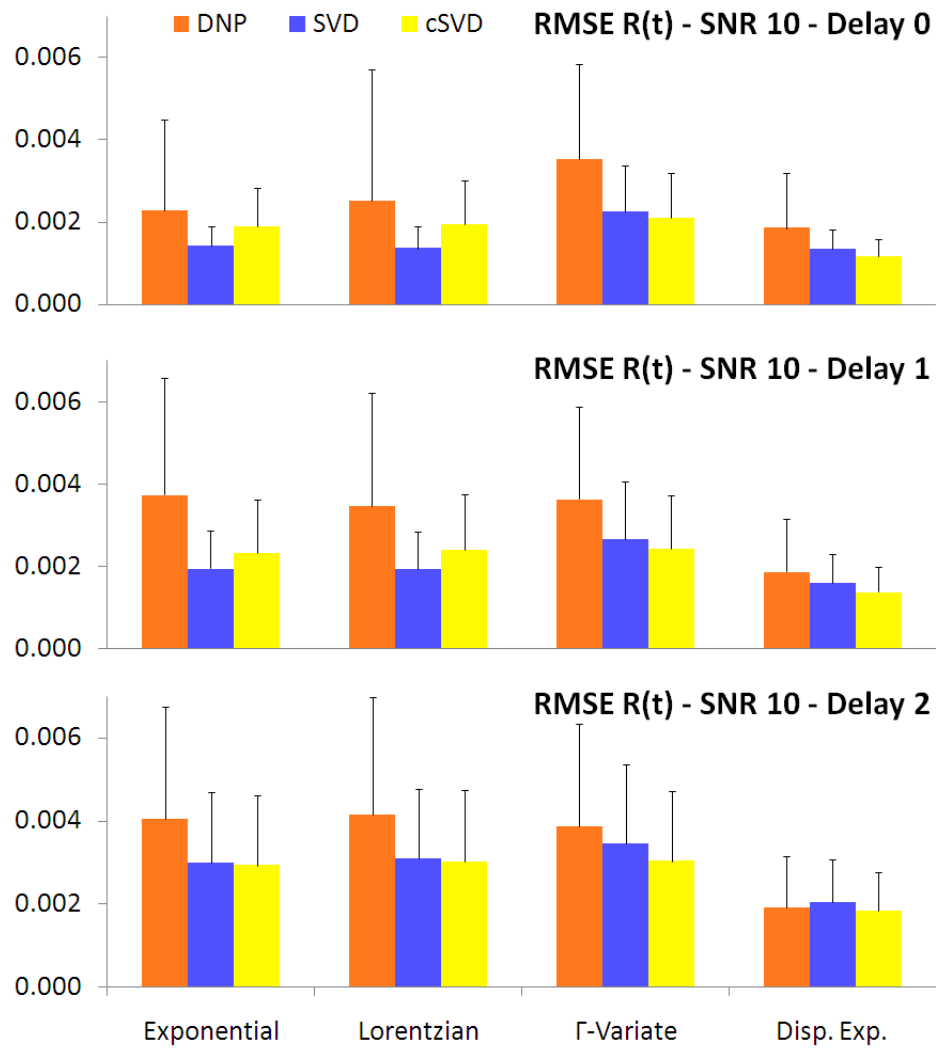


Figure 6.1: RMSE between the reconstructed and the true residue functions.

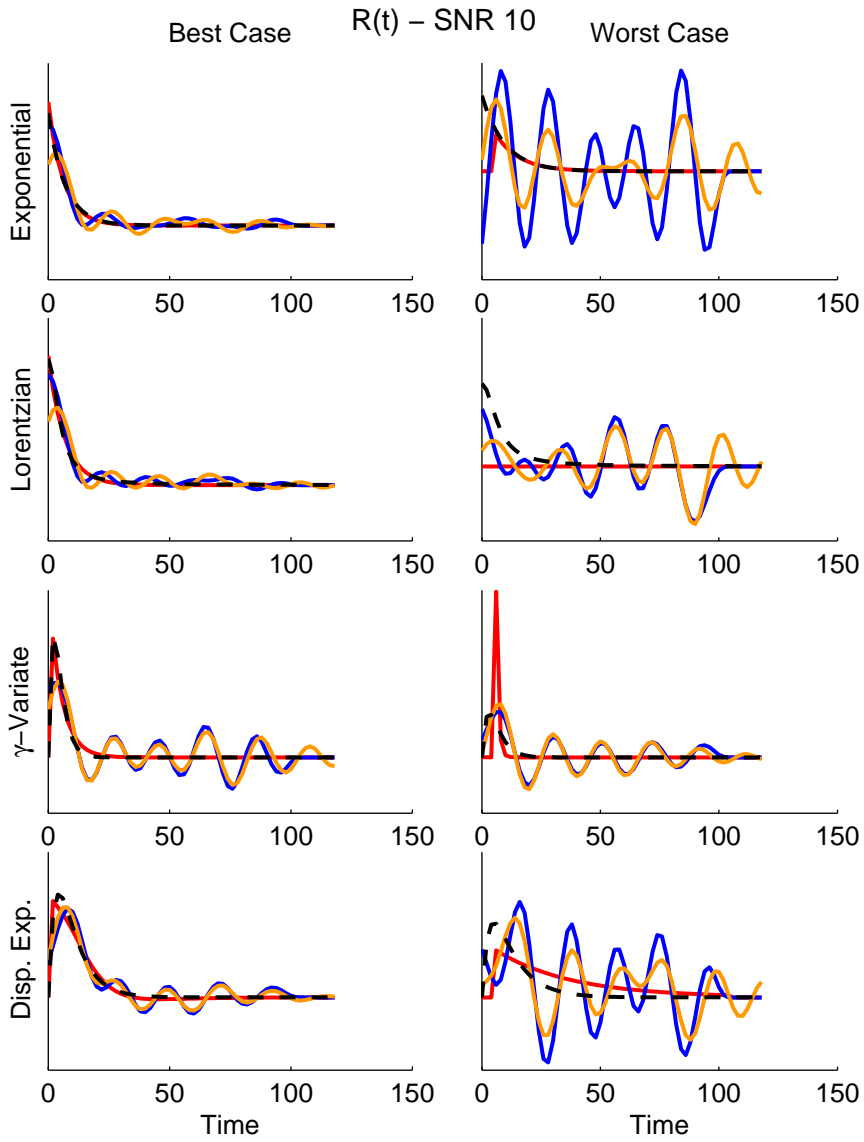


Figure 6.2: Examples of reconstructed residue functions at SNR 10 without delay. Red lines represent the DNP reconstructed  $R(t)$ , blue lines represent the SVD reconstructed  $R(t)$  and yellow lines represent the cSVD results. True  $R(t)$  is reported using black dashed lines.



all cases, with the exception of Gamma-variate  $R(t)$  with 0 and 1 sample delays. In the first case, SVD and cSVD show a significantly smaller mean error than DNP, whereas in the second case all methods provide comparable results. DNP is characterized by a larger SD than SVD and cSVD. When considering non dispersed and non delayed residue functions, SVD performs significantly better than cSVD, providing a very small mean error, whereas they provide comparable results in the other cases. SVD and cSVD always underestimate the true CBF for each residue function model. PD presents overestimated CBF for the exponential, Lorentzian and Gamma-variated  $R(t)$ , whereas it underestimates the true CBF when a dispersed exponential  $R(t)$  has to be reconstructed. Remember that, when dispersion is present in the residue function, estimated CBFs are intrinsically biased by underestimation.

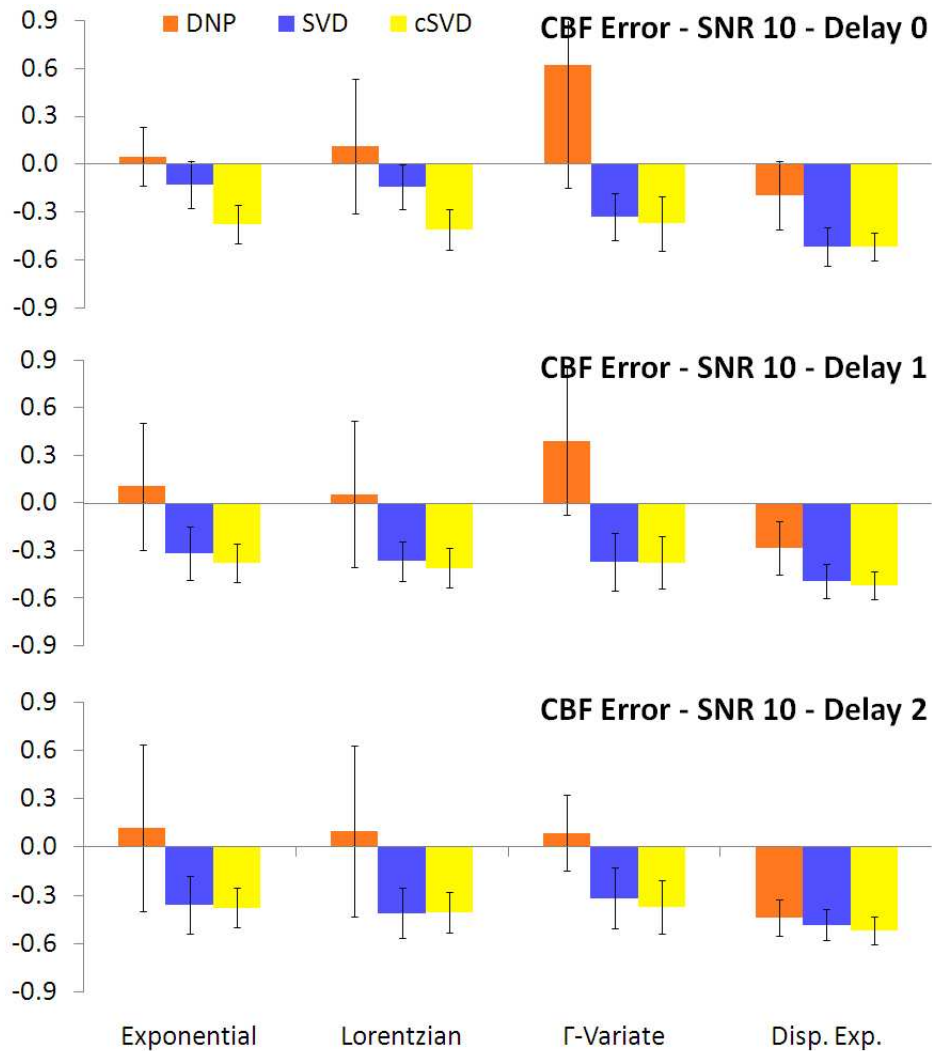


Figure 6.4: Estimated CBF percentage error at SNR 10.

Considering the whole simulated cases at SNR 10, figure 6.5 shows the relative percentage of the three deconvolution methods in providing the best CBF estimate. For each delay level, DNP provides the best CBF estimates in the majority of cases, from 67% at 1 sample delay to 79% when there is no delay. SVD is the second method, but it results the best method in less than 25% of cases.

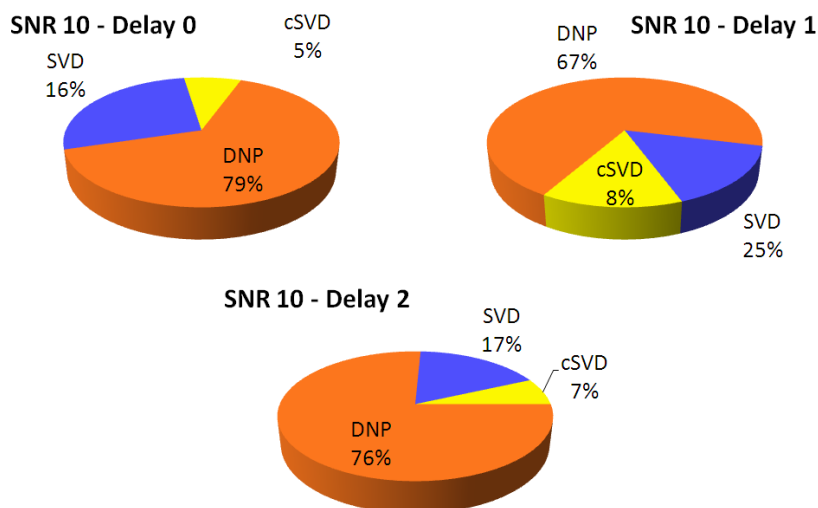


Figure 6.5: Percentage for the three deconvolution methods in providing the lowest CBF estimate error at SNR 10.

Figure 6.6 compares the true CBF with the ones obtained using DNP, SVD and cSVD at the typical noise level present in the clinical data (SNR 10), without delay. As expected, SVD and cSVD always underestimate the true CBF; moreover, the larger the true CBF, the larger the bias in the estimates. Differently, DNP presents both underestimation and overestimation of the true CBF. Especially, the difference between the true and the estimated CBF is not influenced by the true CBF value. Furthermore, considering the mean true CBF value (i.e. 22 ml/100g/min), the DNP estimates are closer to the true CBF than those provided by SVD and cSVD, with the exception of the Gamma-variate residue function. In such cases, the DNP estimates are characterized by a wide overestimation and SVD provides the best CBF estimate.

Similar results can be found in 6.7, which shows a comparison between the true CBF and the ones obtained using DNP, SVD and cSVD at the SNR 10 and with a 2 sample delay. SVD and cSVD always underestimate the true CBF; as expected, SVD estimates get worse because of the delay presence, whereas cSVD provides similar results in presence or absence of delay. DNP usually presents both underestimation and overestimation of the true CBF and the estimate error is not influenced by the CBF value. However, when considering the dispersed exponential  $R(t)$ , DNP always underestimates CBF and it provides performances comparable to the SVD and cSVD ones. Considering the mean true CBF value (i.e. 22 ml/100g/min) DNP estimates are closer to the true

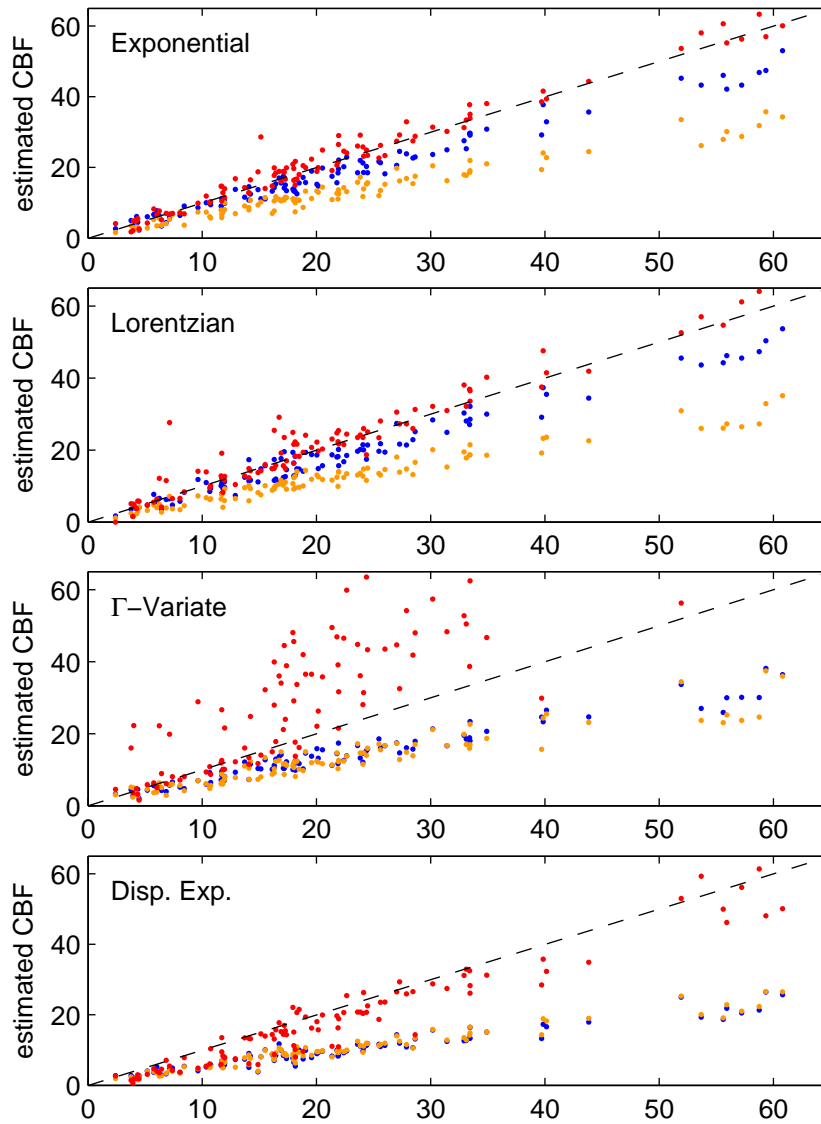


Figure 6.6: PD (red dots), SVD (blue dots) and cSVD (yellow dots) CBF estimates (vertical axes) versus true CBF (horizontal axes) for the four different  $R(t)$  models at SNR 10, without delay.

CBF than those provided by SVD and cSVD.

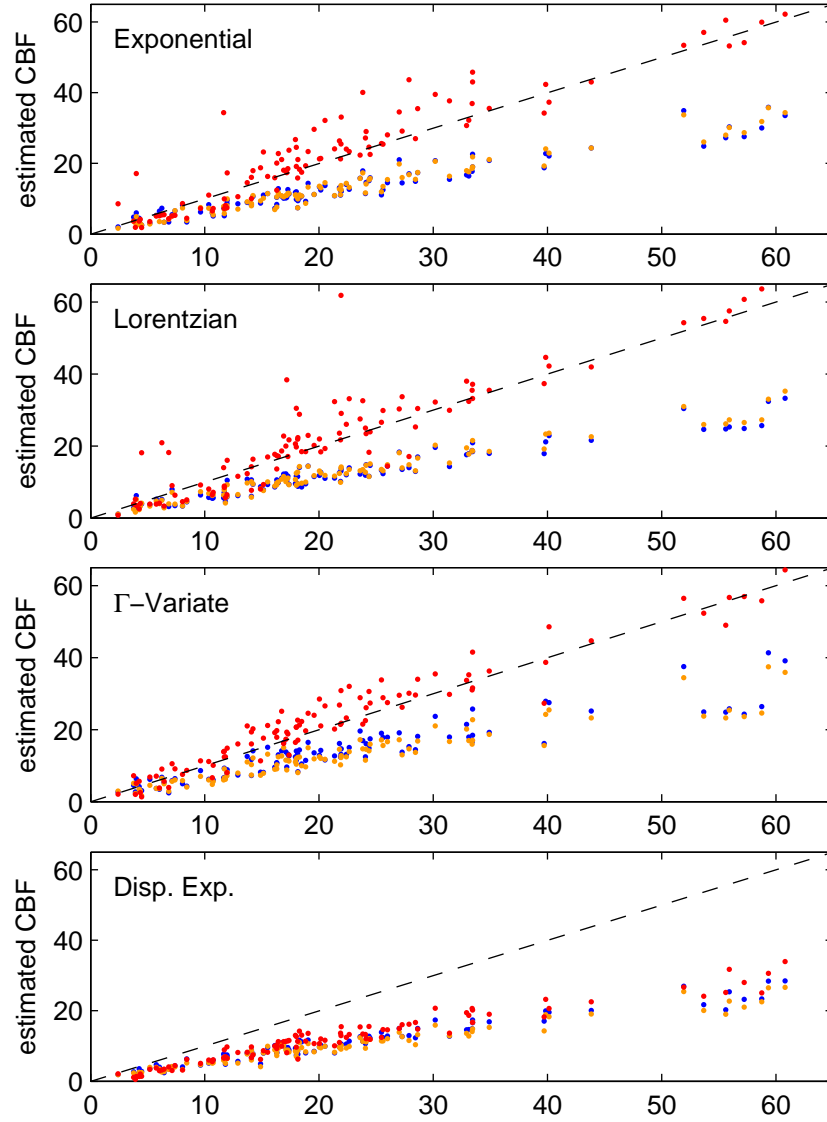


Figure 6.7: PD (red dots), SVD (blue dots) and cSVD (yellow dots) CBF estimates (vertical axes) versus true CBF (horizontal axes) for the four different  $R(t)$  models at SNR 10, with a 2 sample delay between the AIF and the concentration curves.

Figure 6.8 shows the mean delay values obtained by DNP compared to the true ones for the four different  $R(t)$  models at SNR 10. DNP always overestimates the delay, most of all in presence of dispersion. Moreover, delay estimates get better as delay increases.

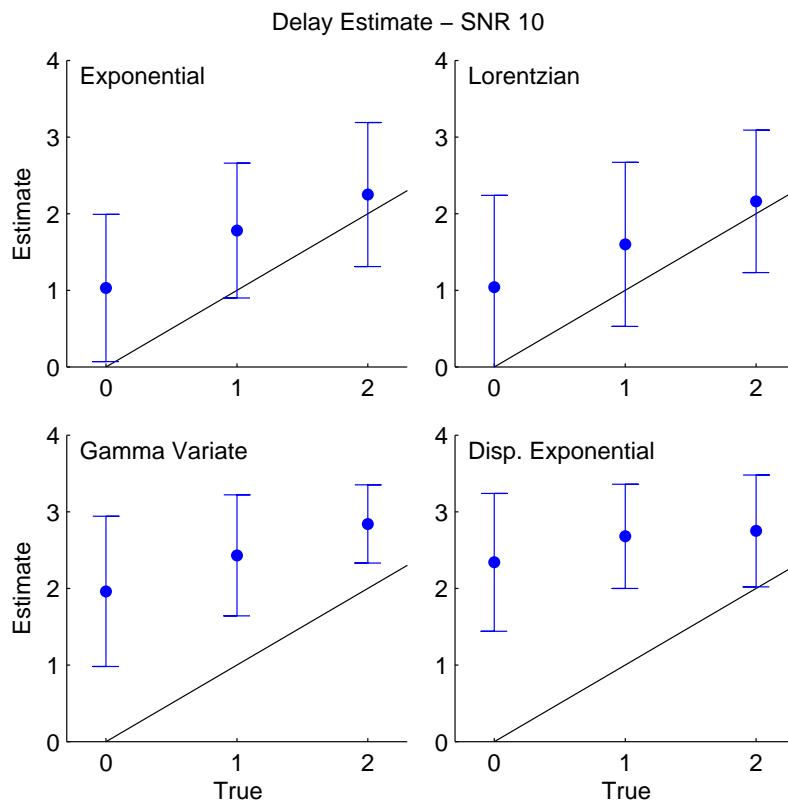


Figure 6.8: DNP delay estimates (vertical axis) versus true delay (horizontal axis) at SNR 10. Identity line (black line) is reported as term of comparison.

## 6.4 Assessment on Clinical Data

Even if DNP has not been validated yet and it is not yet optimized, a first attempt at a clinical data analysis was performed to evaluate the DNP estimate quality.

### 6.4.1 Data Set & Analysis

The clinical data set is the same proposed in section 4.5 (page 52). In summary, it includes 18 different clinical cases (11 subjects: 10 pre-surgery examinations and 8 post-surgery examination). Each examination contains 12 slices. A global AIF was computed for each examination by using the method presented in chapter 4. Furthermore, a Gamma-variate fitting procedure was performed on the arterial and on each voxel concentration curve to eliminate the presence of recirculation.

According to Eq. (2.12), *Cerebral blood flow* (CBF) is defined as the maximum of the  $CBF \cdot R(t)$  function obtained by a deconvolution operation. CBF values were computed pixel-by-pixel using three different deconvolution methods: SVD, cSVD and DNP.

*Mean transit time* (MTT) was obtained as the ratio between CBV and CBF, according to the Central Volume theorem (Eq. (2.11)). Absolute MTT values were calculated pixel-by-pixel using the CBF values provided by SVD, cSVD, and DNP and the CBV maps computed in section 5.5. Noticeably, absolute MTT values were obtained starting from relative CBV (i.e. without accounting for the constant  $\rho$  and  $k_H$ ) and CBF values.

### 6.4.2 Results

CBF maps were computed for each subject using the SVD, cSVD and DNP deconvolution algorithms. All methods provide only relative CBF values; therefore, all CBF maps were normalized to the same pixel to allow a direct comparison between the methods. The pixel selection has been manually performed by considering the white matter in the non pathologic hemisphere.

Figures 6.9 and 6.10 show the CBF maps obtained for particular slices selected in subjects n° 1 and 3 before surgery. In subject n° 1, the CBF map provided by DNP presents a very high CBF and appears to be characterized by a higher noise level than SVD and cSVD ones. In subject n° 3 all methods provide comparable CBF maps, with the same contrast and noise levels. Results obtained in the other subjects are similar to those presented for subjects n° 1 and 3. They can be very similar to SVD and cSVD ones, or provide higher CBF values and noise level.

Figures 6.11 and 6.12 show the MTT maps obtained for particular slices selected in subjects n° 1 and 3 before surgery. In both cases DNP provides smaller MTT values than SVD and cSVD, but all maps present similar contrast and noise levels.

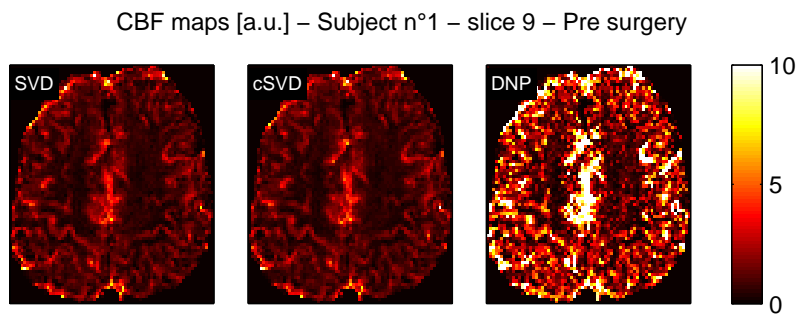


Figure 6.9: CBF maps obtained by SVD, cSVD and DNP in subject n° 1 before surgery. Relative CBF values are normalized to the same reference region in each map.

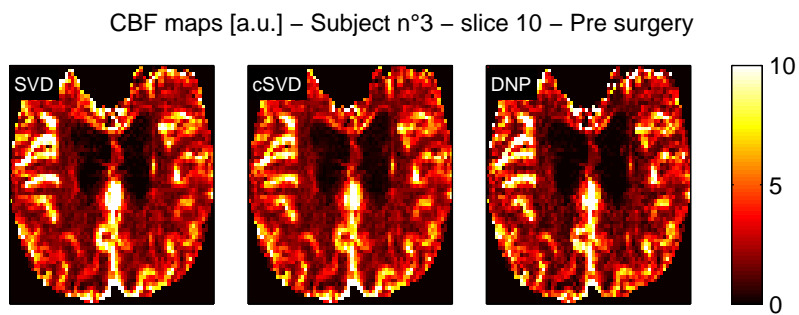


Figure 6.10: CBF maps obtained by SVD, cSVD and DNP in subject n° 3 before surgery. Relative CBF values are normalized to the same reference region in each map.

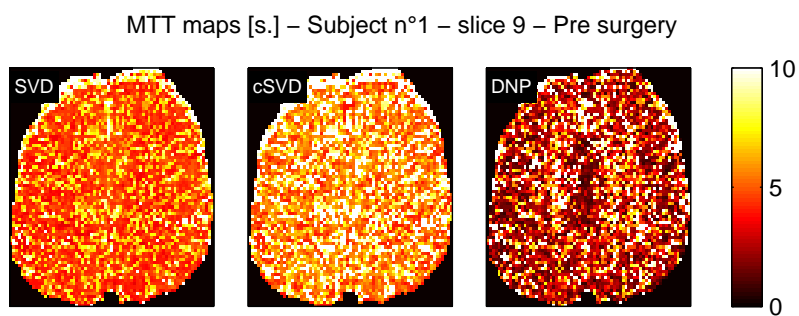


Figure 6.11: MTT maps obtained by SVD, cSVD and DNP in subject n° 1 before surgery. MTT values are expressed in seconds.

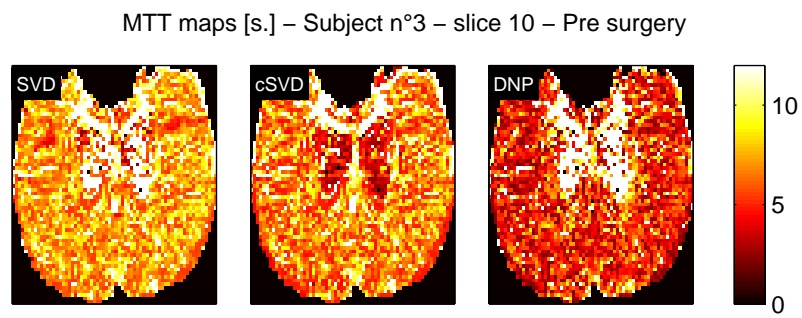


Figure 6.12: MTT maps obtained by SVD, cSVD and DNP in subject n° 3 before surgery. MTT values are expressed in seconds.

## 6.5 Discussion

In Chapter 5 a novel deconvolution method (PD) has been proposed and validated both on simulated and clinical data. PD exploits the population approach to improve the residue function estimates and, consequently, the CBF ones. However, in some occasions, the analysis of a small number of voxels is required. In other occasions, only a region of interest (ROI) mean curve has to be examined. In such situations, a population approach cannot be applied because of the considered voxel small number, hence a pixel based deconvolution algorithm has to be used. SVD and cSVD are the most used pixel based deconvolution methods, but they present some limitations, such as unphysiological oscillations and negative values in the estimated residue function. Furthermore, their CBF estimates depend on the choice of a threshold value and are influenced by the presence of delay and dispersion in the AIF.

A novel deconvolution method (DNP) has been proposed to overcome the SVD and cSVD limitations. DNP tackles the problem in a fully Bayesian framework. In particular, a new probabilistic prior has been defined directly on the unknown residue function, rather than on the bias error. The prior includes information on both  $R(t)$  continuity and on the system BIBO-stability. The minimum variance estimate is obtained with a Tikhonov estimator defined on a RKHS which has been fully characterized.

DNP has been compared to SVD and cSVD on simulated data. The data set includes 4800 different situations (4  $R(t)$  models  $\times$  100 CBF & MTT value combinations  $\times$  4 SNR  $\times$  3 delay).

DNP has been shown to provide more accurate CBF estimates than SVD and cSVD. It provides the best CBF estimate in at least 67% of cases at the typically SNR found in clinical practice (i.e. SNR 10). Furthermore, the advantage of DNP on SVD and cSVD becomes more marked as the delay increases. As expected, SVD performances get worse in presence of delay, whereas cSVD appears to be insensitive to delay. As for DNP, not only is it insensitive to delay; it can also assess the delay, thus improving the quality of the information provided to the physician. superiority

As DNP includes the BIBO-stability and the  $R(t)$  continuity information in the prior, it can provide physiological  $R(t)$  estimate. The DNP reconstructed residue functions do not show negative values or spurious oscillations, which are instead present in SVD and cSVD ones. Thus, DNP provides more reliable  $R(t)$  estimates than SVD and cSVD.

Another important feature of DNP is that it requires no parameter optimization before the analysis. All the stochastic model parameters, such as the delay, the noise variance or the time transformation parameter, are computed by the algorithm. Differently, when applying SVD or cSVD, a threshold value has to be determined before performing the analysis. Therefore, DNP is a more flexible method than SVD and cSVD.

However, DNP presents some limitations, too. In some occasions, the bias in the peak estimation is very large. Considering the RMSE between the true residue function and the estimated one, SVD and cSVD show to better characterize the true residue function, in particular in absence of dispersion. DNP

appears not to assess the true time to peak; therefore, DNP  $R(t)$  estimates are usually translated, if compared to the true one. This is due to a non accurate delay estimation. More precisely, DNP usually overestimates the delay, most of all when dispersion is present in the residue function.

Another DNP limitation is its being a non linear algorithm. Even if the Tikhonov estimator has an explicit solution, the stochastic model parameter vector estimation requires a non linear step. Therefore, DNP is computationally more expensive than SVD and cSVD and it will require much time if a large data set has to be analysed.

DNP has also been compared to SVD and cSVD also on a clinical data set. The CBF maps obtained by DNP have usually a higher contrast level than the SVD and cSVD ones, but they appear to be noisier, too. However, DNP provides more physiological MTT values than SVD and cSVD.

In conclusion, a new pixel based deconvolution method has been proposed and compared to two classical methods. DNP is very promising and provides an accurate CBF value estimate, but it presents also some limitations. Therefore, some optimization work has to be done yet.

# Chapter 7

## Conclusions

Magnetic resonance imaging techniques measuring the cerebral hemodynamic have developed rapidly in the last decade, resulting in a wide range of available methods. The most successful approach is based on dynamic tracking of a bolus of a paramagnetic contrast agent, commonly gadolinium. In *Dynamic Susceptibility Contrast - Magnetic Resonance Imaging* (DSC-MRI), Gadolinium contrast agent is injected and a time series of fast  $T_2^*$ -weighted images is acquired. As Gadolinium passes through the tissues, it produces a reduction of  $T_2^*$  intensity depending on the local concentration. The acquired data are then post-processed to obtain perfusion maps with different parameters, such as the *Cerebral Blood Flow* (CBF), the *Cerebral Blood Volume* (CBV), the *Mean Transit Time* (MTT). However, there are still some difficulties for an accurate and absolute quantification of perfusion parameters due, for example, to the presence of bolus delay and dispersion, to the *Arterial Input Function* (AIF) measurement, to the partial volume effect. In this work, two of the most important limitations in DSC-MRI images quantification have been considered.

A significant DSC-MRI open issue is the estimation of the AIF, that is the tracer concentration curve in the vessels feeding the tissue. Currently, AIF is estimated directly on MR images by selection of a few number of voxels containing one of the principal arterial vessels. An automatic, rapid and objective method to select the arterial voxels is essential for routine clinical use. In this work a novel fully automated algorithm for the AIF estimate was presented. It exploits anatomical information to detect a small brain area where one of the principal arterial vessels is expected to locate. Then, it use a hierarchical clustering approach to select voxels characterized by a high, narrow and early-appeared shape for the concentration time curve. The mean concentration curve over these voxels is taken as the global AIF, which therefore is expected to reflect primarily normal arteries. This new method, called HIER, was compared on simulated data to the most interesting methods proposed in literature. HIER has been shown to well reconstruct the true AIF, providing accurate estimates and very narrow confidence bands. Moreover, it is robust against the different noise levels. Thus, it has shown to be less influenced by partial volume artefacts than other automatic methods and to increase the reproducibility level in DSC-MRI image quantification. AIFs obtained by HIER on a clinical data set have also been compared to the manual one, provided by a physician. HIER selected

arterial voxels are characterized by a smaller intra-variability than the manual ones; furthermore, HIER AIFs have been shown to lead to a more accurate diagnosis than manual ones.

Another critical step in DSC-MRI data analysis is the estimation of the *residue function*  $R(t)$ , that is the fraction of contrast agent remaining inside the tissue at time  $t$  following a tracer bolus injection. A deconvolution operation, which is a well known mathematical problem, has to be performed to estimate the residue function. Deconvolution methods have to face the operation intrinsic problems and the physiological system specific constraints. The deconvolution intrinsic problems are the ill-posedness and the ill-conditioning, whereas the most common physiological constraints are the smoothness and the non negativity of  $R(t)$ . Another important source of error is the possible presence of *delay* and/or *dispersion* in the AIF. Currently, the most used deconvolution methods are the *Singular Value Decomposition* (SVD) and the *block-Circulant Singular Value Decomposition* (cSVD). SVD is historically the first and the most important deconvolution method proposed in DSC-MRI context and it is currently the reference method. During the last decade, SVD performances have been deeply analysed and its limitations have been largely pointed out. The cSVD method is the natural SVD evolution, that is less biased by the presence of delay in the AIF than the original SVD. Other methods have been proposed to provide an accurate quantification of the hemodynamic parameters, such as the *Nonlinear Stochastic Regularization* (NSR). NSR is a recently proposed method, that accounts for both the smoothness and the non-negativity constraints of the residue function.

In this work, we have discussed also a deconvolution method based on a population approach. The *Population Deconvolution* (PD) method exploits a population approach to analyse a large set of similar voxels at the same time, thus improving the data quality in the deconvolution operation. PD has been validated and compared to SVD and cSVD on a simulated data set. As already reported in literature, SVD has been shown to not be able to provide physiological results. Its  $R(t)$  estimates present wide oscillations, negative values and they are largely biased in presence of dispersion in the AIF. cSVD has proved to achieve time-shift insensitive, but unphysiological oscillations and negative values still remain in the estimated  $R(t)$ . Residue functions obtained using PD present very small and damped oscillations, thus resulting less biased than SVD and cSVD ones. Furthermore, PD has been shown to accurately estimate the CBF both in presence and in absence of dispersion, providing better results than SVD and cSVD. Therefore, PD improves quality of the information obtained in the DSC-MRI images analysis.

SVD, cSVD and PD have been compared also to NSR on clinical data. CBF and MTT maps and *laterality indices* (LI) were computed using all these methods. CBF and MTT maps provided by PD are comparable to those obtained by SVD and cSVD, but show more contrasted areas, emphasizing the flow and transit time differences. Commonly, NSR maps are extremely contrasted, but appear noisier than the PD ones. Laterality indices provide a graphical representation of the CBF and MTT map information, integrating the whole information provided by the different parameters. NSR provides very large laterality indices, thus emphasizing the disease affected regions. Nevertheless, the detection of the pathological areas is not easy because of the large LI variability

---

also in the healthy regions. On the contrary, SVD and cSVD laterality indices make the disease detection difficult because they do not emphasize the pathological areas. PD meets the need to underline the pathologic areas without showing false positive results, providing larger LIs than the SVD and cSVD ones, but smaller than the NSR. Therefore, PD have been shown to lead to a more accurate diagnosis than the other methods. The most crucial step in the PD method is the preliminary elaboration. If the PD algorithm is provided with a multimodal population, then a bias is introduced on residue function estimates. Therefore, population division has to be carefully performed.

The most interesting PD feature is the population approach. However, it provides good results when a large voxel set is considered. In some cases, only a small number of voxels or a ROI average curve have to be analyse. In these cases, PD cannot be applied and a voxel based method is required. In this work a new deconvolution method, called DNP, is presented and its preliminary results are shown. DNP formulates the stochastic prior directly on the residue function and it includes information on both  $R(t)$  continuity and system BIBO-stability. An important DNP feature is that it can estimate the AIF delay, thus improving the accuracy in the  $R(t)$  estimation. Moreover, DNP does not require to fix any threshold value, which is known to affect SVD and cSVD estimates.

DNP has been compared to SVD and cSVD on a simulated data set, at noise level typically found in clinical data. Preliminary results have shown that DNP provide more accurate CBF estimates than SVD and cSVD, both in presence and absence of delay and dispersion. Furthermore, thanks to the prior, the DNP reconstructed residue functions do not show negative values or spurious oscillations, thus providing more physiologic  $R(t)$  estimates than SVD and cSVD. However, DNP is still under refinement because it presents some limitations, too. Currently, the most important DNP limitation is the delay estimation. DNP usually overestimates the delay, above all in presence of dispersion, thus providing a non accurate characterization of the residue function. Considering the RMSE between the true residue function and the estimated one, SVD and cSVD provide better results than DNP. Another DNP problem is that the hyper-parameter quantification requires a non-linear step, thus increasing the computation time of the algorithm. DNP has also been compared to SVD and cSVD also on a clinical data set. The CBF maps obtained by DNP have usually a higher contrast level than the SVD and cSVD ones, but they appear to be noisier, too. However, DNP provides more physiological MTT values than SVD and cSVD. Summarizing, DNP provides very promising results, but it has still to be optimized to improve the residue function characterization.

In conclusion, although it presents some limitation in the post-processing analysis, DSC-MRI techniques are becoming an important tool in the medical research and clinical practice. The development of a fully automatic algorithm for the AIF selection and of a deconvolution method based on a population approach, would improve the clinical and scientific information provided by DSC-MRI analysis.



# Bibliography

- [1] Alsop D.C., Detre J.A. Reduced Transit-time Sensitivity in Noninvasive Magnetic Resonance Imaging of Human Cerebral Blood Flow. *Journal of Cerebral Blood Flow and Metabolism* 16: 1236-1249 (1996).
- [2] Alsop D.C., Wedmid A., Schlaug G. Defining a Local Input Function for Perfusion Quantification with Bolus Contrast MRI. Proceedings of 10<sup>th</sup> Annual Meeting ISMRM, pag. 659, Honolulu, Haway, USA (2002).
- [3] Andersen I.K., Szymkowiak A., Rasmussen C.E., Hanson L.G., Marstrand J.R., Larsson H.B.W., Hansen L.K. Perfusion Quantification Using Gaussian Process Deconvolution. *Magnetic Resonance in Medicine* 48: 351-361 (2002).
- [4] Axel L. Cerebral Blood Flow Determination by Rapid-Sequence Computed Tomography. A Theoretical Analysis. *Radiology* 137: 679-686 (1980).
- [5] Barbier E.L., Lamalle L., Decorsp M. Methodology of Brain Perfusion Imaging. *Journal of Magnetic Resonance Imaging* 13: 496-520 (2001).
- [6] Bell B.M., Pillonetto G. Estimating Parameters and Stochastic Functions of One Variable Using Nonlinear Measurements Model. *Inverse Problems* 20: 627-646 (2004).
- [7] Benner T., Heiland S., Erb G., Forsting M., Sartor K. Accuracy of Gamma-variate Fits to Concentration-time Curves from Dynamic Susceptibility-Contrast Enhanced MRI: Influence of Time Resolution, Maximal Signal Drop and Signal-to-noise. *Magnetic Resonance in Medicine* 15: 307-317 (1997).
- [8] Bertoldo A., Corazza S., Zanderigo F., Pillonetto G., Cosottini M., Cobelli C. Assessment of Regional Cerebral Blood Flow By Bolus-Tracking MRI Images: Characterization of the Tissue Residue Function Using Nonlinear Stochastic Regularization Method. Proceedings of MEDICON Ischia (NA), Italy, 31 July-5 August (2004).
- [9] Bertoldo A., Zanderigo F., Cobelli C. Assessment of Cerebral Blood Flow, Volume, and Mean Transit Time from Bolus-tracking MRI Images: Theory and Practise. In *Advanced Image Processing in Magnetic Resonance Imaging*, L. Landini Editor, Marcel Dekker Signal Processing and Communications Series, New York, NY, USA (2005).

- [10] Boxerman J.L., Hamberg L.M., Rosen B.R., Weisskoff R.M. MR Contrast due to Intravascular Magnetic Susceptibility Perturbations. *Magnetic Resonance in Medicine* 34: 555-566 (1995).
- [11] Brunecker P., Villringer A., Schultze J., Nolte C.H., Jungehulsing G.J., Endres M., Steinbrink J. Correcting saturation effects of the arterial input function in dynamic susceptibility contrast-enhanced MRI - a Monte Carlo simulation. *Magnetic Resonance Imaging* 25: 1300-1311 (2007).
- [12] Butman J.A., Tasciyan T. Automated computation of the arterial input function for dynamic susceptibility bolus tracking brain perfusion MRI. *Proceedings of ISMRM 13<sup>th</sup> Scientific Meeting and Exhibition*, Miami, Florida, USA, 7-13 May (2005).
- [13] Calamante F., Thomas D.L., Pell G.S., Wiersma J., Turner R. Review Article: Measuring Cerebral Blood Flow Using Magnetic Resonance Imaging Techniques. *Journal of Cerebral Blood Flow and Metabolism* 19: 701-735 (1999).
- [14] Calamante F., Gadian D.G., Connelly A. Delay and Dispersion Effects in Dynamic Susceptibility Contrast MRI: Simulations using Singular Value Decomposition. *Magnetic Resonance in Medicine* 44: 466-473 (2000).
- [15] Calamante F., Ganesan V., Kirkham F.J., Jan W., Chong W.K., Gadian D.G., Connelly A. MR Perfusion Imaging in Moyamoya Syndrome: Potential Implications for Clinical Evaluation of Occlusive Cerebrovascular Disease. *Stroke* 32: 2810-2816 (2001).
- [16] Calamante F., Gadian D.G., Connelly A. Quantification of Perfusion using Bolus Tracking Magnetic Resonance Imaging in Stroke: Assumptions, Limitations, and Potential Implications for Clinical Use. *Stroke* 33: 1146-1151 (2002).
- [17] Calamante F., Gadian D.G., Connelly A. Quantification of Bolus-Tracking MRI: Improved Characterization of the Tissue Residue Function Using Tikhonov Regularization. *Magnetic Resonance in Medicine* 50: 1237-1247 (2003).
- [18] Calamante F., Yim P.J., Cebral J.R. Estimation of Bolus Dispersion Effects in Perfusion MRI using Image-based Computational Fluid Dynamics. *NeuroImage* 19: 341-353 (2003).
- [19] Calamante F., Willats L., Gadian D.G., Connelly A. Bolus Delay and Dispersion in Perfusion MRI: Implications for Tissue Predictor Models in Stroke. *Magnetic Resonance in Medicine* 55: 1180-1185 (2006).
- [20] Calamante F., Morup M., Hansen L.K. Defining a Local Arterial Input Function for Perfusion MRI using Independent Component Analysis. *Magnetic Resonance in Medicine* 52: 789-797 (2004).
- [21] Carpenter T.K., Armitage P.A., Bastin M.E., Wardlaw J.M. Dsc Perfusion MRI - Quantification and Reduction of Systematic Errors Arising in Areas of Reduced Cerebral Blood Flow. *Magnetic Resonance in Medicine* 55: 1342-1349 (2006).

- [22] Carroll T.J., Teneggi V., Jobin M., Squassante L., Treyer V., Hany T.F., Burger C., Wang L., Bye A., Von Schulthess G.K., Buck A. Absolute Quantification of Cerebral Blood Flow with Magnetic Resonance: Reproducibility of the Method, and Comparison with H<sub>2</sub>(15)O Positron Emission Tomography. *Journal of Cerebral Blood Flow and Metabolism* 22: 1149-1156 (2002).
- [23] Carroll T.J., Rowley H.A., Haughton V.M. Automatic Calculation of the Arterial Input Function for Cerebral Perfusion Imaging with MR Imaging. *Radiology* 227:593-600 (2003).
- [24] Cha S., Lu S., Johnson G., Knopp E.A. Dynamic Susceptibility Contrast MR Imaging: Correlation of Signal Intensity Changes with Cerebral Blood Volume Measurements. *Journal of Magnetic Resonance Imaging* 11: 114-119 (2000).
- [25] De Nicolao G., Sparacino G., Cobelli C. Nonparametric Input Estimation in Physiological Systems: Problems, Methods, and Case Studies. *Automatica* 33: 851-870 (1997).
- [26] De Nicolao G., Sparacino G., Cobelli C. Stima di Secrezione di Ormoni e Produzione di Substrati Mediante Deconvoluzione. In *Bioingegneria dei Sistemi Metabolici*, GNB, Patron Editore, Bologna, Italy, p. 137-150 (1998).
- [27] De Nicolao G., Pillonetto G., Chierici M., Cobelli C. Efficient Nonparametric Population Modeling for Large Data Sets. Proceedings of *American Control Conference*, New York City, New York, USA, July 9-13 (2007).
- [28] De Nicolao G., Pillonetto G. A new kernel-based approach for system identification. Proceedings of *American Control Conference*, Seattle, Washington, USA, June 11-13 (2008).
- [29] Duhamel G., Schlaug G., Alsop D.C. Measurement of Arterial Input Functions for Dynamic Susceptibility Contrast Magnetic Resonance Imaging using Echo-Planar Images: Comparison of Physical Simulations with in Vivo Results. *Magnetic Resonance in Medicine* 55: 514-523 (2006).
- [30] Ellinger R., Kremser C., Schocke M.F., Kolbitsch C., Griebner J., Felber S.R., Aichner F.T. The Impact of Peak Saturation of the Arterial Input Function on Quantitative Evaluation of Dynamic Susceptibility Contrast-enhanced MR Studies. *Journal of Computer Assisted Tomography* 24: 942-948 (2000).
- [31] Garulli A., Vicino A., Zappa G. Conditional central algorithms for worst-case set- membership identification and filtering. *IEEE Transactions on Automatic control* 45(1): 14-23 (2000).
- [32] Goodwin G., Braslavsky J., Seron M. Non-stationary stochastic embedding for transfer function estimation. *Automatica* 38: 47-62 (2002).
- [33] Grüner R., Bjørnarå B.T., Moen G., Taxt T. Magnetic Resonance Brain Perfusion Imaging with Voxel-Specific Arterial Input Functions. *Journal of Magnetic Resonance Imaging* 23: 273-284 (2006).

- [34] Hoppel B.E., Weiskoff R.M., Thulborn K.R., Moore J.B., Kwong K.K., Rosen B.R. Measurement of regional blood oxygenation and cerebral hemodynamics. *Magnetic Resonance in Medicine*, 30: 715-723 (1993).
- [35] Ibaraki M., Shimosegawa E., Toyoshima H., Takahashi K., Miura S., Kanno I. Tracer Delay Correction of Cerebral Blood Flow with Dynamic Susceptibility Contrast-enhanced MRI. *Journal of Cerebral Blood Flow and Metabolism* 25: 378-390 (2005).
- [36] Ibaraki M., Ito H., Shimosegawa E., Toyoshima H., Ishigame K., Takanashi K., Kanno I., Miura S. Cerebral Vascular Mean Transit Time in Healthy Humans: a Comparative Study with PET and Dynamic Susceptibility Contrast-enhanced MRI. *Journal of Cerebral Blood Flow and Metabolism* 1-10 (2006).
- [37] Ito H., Kanno I., Kato C., Sasaki T., Ishii K., Ouchi Y., Iida A., Okazawa H., Hayashida K., Tsuyuguchi N., Ishii K., Kuwabara Y., Senda M. Database of Normal Human Cerebral Blood Flow, Cerebral Blood Volume, Cerebral Oxygen Extraction Fraction and Cerebral Metabolic Rate of Oxygen measured by Positron Emission Tomography with  $^{15}\text{O}$ -labelled Carbon Dioxide or Water, Carbon Monoxide and Oxygen: a Multicenter Study in Japan. *European Journal of Nuclear Medicine and Molecular Imaging* 31(5): 635-643 (2004).
- [38] Kennan R.P., Jäger H.R.  $T_2$ - and  $T_2^*$ -W DCE-MRI: Blood Perfusion and Volume Estimation using Bolus Tracking. In *Quantitative MRI of the Brain*, Edited by Paul Tofts, John Wiley and Sons, Ltd, p. 365-412 (2003).
- [39] Kiselev V.G. On the Theoretical Basis of Perfusion Measurements by Dynamic Susceptibility Contrast MRI. *Magnetic Resonance in Medicine* 46: 1113-1122 (2001).
- [40] Kiselev V.G. Transverse Relaxation Effect of Contrast Agent: a Crucial Issue for Quantitative Measurements. In *Proceedings of ISMRM Workshop on Quantitative Cerebral Perfusion Imaging Using MRI: A Technical Perspective*, Venice, Italy, March 21-23, pp. 6-9 (2004).
- [41] Kjølbj B.F., Østergaard L., Kiselev V.G. Theoretical Model of Intravascular Paramagnetic Tracers Effect on Tissue Relaxation. *Magnetic Resonance in Medicine* 56: 187-197 (2006).
- [42] Landis C.S., Li X. et al. Determination of the MRI Contrast Agent Concentration Time Course In Vivo following Bolus Injection: Effect of Equilibrium Transcytolemmal Water Exchange. *Magnetic Resonance in Medicine* 44: 563-574 (2000).
- [43] Larson K.B., Perman W.H., Perlmutter J.S., Gado M.H., Zierler, K.L. Tracer-kinetic Analysis for Measuring Regional Cerebral Blood Flow by Dynamic Nuclear Magnetic Resonance Imaging. *Journal of Theoretical Biology* 170: 1-14 (1994).
- [44] Leenders K.L., Perani D., Lammertsma A.A., Heather J.D., Buckingham P., Healy M.J., Gibbs J.M., Wise R.J., Hatazawa J., Herold S., Beany

- R.P., Brooks D.J., Sprinks T., Rhodes C., Franckowiak R.S.J., Jones T. Cerebral blood flow, blood volume and oxygen utilization. Normal values and effect of age. *Brain* 113: 27-47 (1990).
- [45] Lin W., Celik A., Derdeyn C., An H., Lee Y., Videen T., Østergaard L., Powers W.J. Quantitative Measurements of Cerebral Blood Flow in Patients with Unilateral Carotid Artery Occlusion: a PET and MR Study. *Journal of Magnetic Resonance Imaging* 14: 659-667 (2001).
- [46] Liu H.L., Pu Y., Liu Y., Nickerson L., Andrews T., Fox P.T., Gao J.H. Cerebral Blood Flow Measurement by Dynamic Contrast MRI using Singular Value Decomposition with an Adaptive Threshold. *Magnetic Resonance in Medicine* 42: 167-172(1999).
- [47] Ljung L. Model validation and model error modelling. Proceedings of *Astrom symposium on control, Studentlitteratur*, Lund, Sweden. 15-42 (1999).
- [48] Lorenz C., Benner T., Lopez C.J., Ay H., Zhu M.W., Aronen H., Karonen J., Liu Y., Nuutinen J., Sorensen A.G. Effect of Using Local Arterial Input Functions on Cerebral Blood Flow Estimation. *Journal of Magnetic Resonance Imaging* 24: 57-65 (2006).
- [49] Marstrand J.R., Rostrup E., Rosenbaum S., Garde E., Larsson H.B. Cerebral hemodynamic changes measured by gradient-echo or spin-echo bolus tracking and its correlation to changes in ICA blood flow measured by phase-mapping. *Journal of Magnetic Resonance Imaging* 14: 391-400 (2001).
- [50] Meier P., Zierler K.L. On the Theory of the Indicator-Dilution Method for Measurement of Blood Flow and Volume. *Journal of Applied Physiology* 6: 731-744 (1954).
- [51] Mlynash M., Eyngorn I. Bammer R., Moseley M., Tong D.C. Automated Method for Generating the Arterial Input Function on Perfusion-weighted MR Imaging: Validation in Patients with Stroke. *American Journal of Neuroradiology* 26: 1479-1486 (2005).
- [52] Mouridsen K., Christensen S., Gyldensted L., Østergaard L. Automatic Selection of Arterial Input Function using Cluster Analysis. *Magnetic Resonance in Medicine* 55: 524-531 (2006).
- [53] Mouridsen K., Friston K., Hjort N., Gyldensted L., Østergaard L., Kiebel S. Bayesian estimation of cerebral perfusion using a physiological model of microvasculature. *NeuroImage* 33:570-579 (2006).
- [54] Mukherjee P., Kang H.C., Videen T.O., McKinstry R.C., Powers W.J., Derdeyn C.P. Measurement of Cerebral Blood Flow in Chronic Carotid Occlusive Disease: Comparison of Dynamic Susceptibility Contrast Perfusion MR Imaging with Positron Emission Tomography. *American Journal of Neuroradiology* 24: 862-871 (2003).
- [55] Murase K., Kikuchi K., Miki H., Shimizu T., Ikezoe J. Determination of Arterial Input Function using Fuzzy Clustering for Quantification of Cerebral Blood Flow with Dynamic Susceptibility Contrast-enhanced MR Imaging. *Journal of Magnetic Resonance Imaging* 13: 797-806 (2001).

- [56] Murase K., Shinohara M., Yamazaki Y. Accuracy of Deconvolution Analysis Based on Singular Value Decomposition for Quantification of Cerebral Blood Flow using Dynamic Susceptibility Contrast-enhanced Magnetic Resonance Imaging. *Physics in Medicine and Biology* 46: 3147-3159 (2001).
- [57] Murase K., Yamazaki Y., Shinohara M. Autoregressive Moving Average (ARMA) Model Applied to Quantification of Cerebral Blood Flow Using Dynamic Susceptibility Contrast-enhanced Magnetic Resonance Imaging. *Magnetic Resonance in Medical Sciences* 2(2): 85-95 (2003).
- [58] Murase K., Yamazaki Y., Shohei M. Deconvolution Analysis of Dynamic Contrast-enhanced Data Based on Singular Value Decomposition Optimized by Generalized Cross Validation. *Magnetic Resonance in Medical Sciences* 3(4): 165-175 (2004).
- [59] Neve M., De Nicolao G., Marchesi L. Nonparametric Identification of Population Models via Gaussian Processes. *Automatica* 43: 1134-1144 (2007).
- [60] Newman G.C., Hospod F.E., Patlak C.S., Fain S.E., Pulfer K.A. Cool T.D., OSullivan F. Experimental Estimates of the Constants Relating Signal Change to Contrast Concentration for Cerebral Blood Volume by  $T_2^*$  MRI. *Journal of Cerebral Blood Flow and Metabolism* 26: 760-770 (2006).
- [61] Østergaard L., Weisskoff R.M., Chesler D.A., Gyldensted C., Rosen B.R. High Resolution Measurements of Cerebral Blood Flow using Intravascular Tracer Bolus Passages. Part I: Mathematical Approach and Statistical Analysis. *Magnetic Resonance in Medicine* 36: 715-725 (1996).
- [62] Østergaard L., Sorensen A.G., Kwong K.K., Weisskoff R.M., Gyldensted C., Rosen B.R. High Resolution Measurements of Cerebral Blood Flow using Intravascular Tracer Bolus Passages. Part II: Experimental Comparison and Preliminary Results. *Magnetic Resonance in Medicine* 36: 726-736 (1996).
- [63] Østergaard L., Johannsen P., Host-Poulsen P., Vestergaard-Poulsen P., Asboe H., Gee A.D., Hansen S.B., Cold G.E., Gjedde A., Gyldensted C. Cerebral Blood Flow Measurements by Magnetic Resonance Imaging Bolus Tracking: Comparison with  $[15O]H_2O$  Positron Emission Tomography in Humans. *Journal of Cerebral Blood Flow and Metabolism* 18: 935-940 (1998).
- [64] Østergaard L., Smith D.F., Vestergaard-Poulsen P., Hansen S.B., Gee A.D., Gjedde A., Gyldensted C. Absolute Cerebral Blood Flow and Blood Volume Measured by Magnetic Resonance Imaging Bolus Tracking: Comparison with Positron Emission Tomography Values. *Journal of Cerebral Blood Flow and Metabolism* 18: 425-432 (1998).
- [65] Østergaard L., Chesler D.A., Weisskoff R.M., Sorensen A.G., Rosen B.R. Modeling Cerebral Blood Flow and Flow Heterogeneity From Magnetic Resonance Residue Data. *Journal of Cerebral Blood Flow and Metabolism* 19: 690-699 (1999).

- [66] Peruzzo D., Bertoldo A., Zanderigo F., Cobelli C. Automatic Selection of Arterial Input Function on Dynamic Contrast-enhanced MRI Images: Comparison of Different Methods. Proceedings of *ISMRM 14<sup>th</sup> Scientific Meeting and Exhibition*, Seattle, Washington, USA, 6-12 May (2006).
- [67] Pillonetto G., Sparacino G., Cobelli C. Handling Non-Negativity in Deconvolution of Physiological Signals: a Nonlinear Stochastic Approach. *Annals of Biomedical Engineering* 30: 1077-1087 (2002).
- [68] Pillonetto G., Chiuso A., De Nicolao G. Identification and prediction of linear dynamical systems: a learning theory approach. Proceedings of *International Conference on Mathematical Problems in Engineering, Aerospace and Sciences*, Genova, Italy, June 25-27 (2008).
- [69] Pillonetto G., Chiuso A., De Nicolao G. Predictor estimation via Gaussian regression. Proceedings of *Conference on Control and Decision Systems*, Cancun, Mexico, (2008).
- [70] Porkka L., Neuder M., Hunter G., Weisskoff R.M., Belliveau J., Rosen, B.R. Arterial Input Function Measurement with MRI. In Proceedings of *The Society of Magnetic Resonance Medicine, 10<sup>th</sup> Annual Meeting*, San Francisco, California, USA, p. 120 (1991).
- [71] Rausch M. Scheffler K., Rudin M., Radu E.W. Analysis of Input Function from Different Arterial Branches with Gamma Variate Functions and Cluster Analysis for Quantitative Blood Volume Measurements. *Magnetic Resonance Imaging* 18: 1235-1243 (2000).
- [72] Rempp K.A., Brix G., Wenz F., Becker C.R., Gückel F., Lorenz W.J. Quantification of Regional Cerebral Blood Flow and Volume with Dynamic Susceptibility Contrast-enhanced MR Imaging. *Radiology* 193: 637-641 (1994).
- [73] Schreiber W.G., Guckel F., Stritzke P., Schmiedek P., Schwartz A., Brix G. Cerebral Blood Flow and Cerebrovascular Reserve Capacity: Estimation by Dynamic Magnetic Resonance Imaging. *Journal of Cerebral Blood Flow and Metabolism* 18: 1143-1156 (1998).
- [74] Simonsen C.Z., Østergaard L., Smith D.F., Vestergaard-Poulsen P., Gyldensted C. Comparison of Gradient- and Spin-Echo Imaging: CBF, CBV and MTT Measurements by Bolus Tracking. *Journal of Magnetic Resonance Imaging* 12: 411-416 (2000).
- [75] Smith A.M., Grandin C.B., Duprez T., Mataigne F., Cosnard G. Whole Brain Quantitative CBF and CBV Measurements using MRI Bolus Tracking: Comparison of Methodologies. *Magnetic Resonance in Medicine* 43: 559-564 (2000).
- [76] Smith M.R., Lu H., Frayne R. Signal-to-Noise Ratio Effects in Quantitative Cerebral Perfusion Using Dynamic Susceptibility Contrast Agents. *Magnetic Resonance in Medicine* 49: 122-128 (2003).
- [77] Sorensen A.G. What is the Meaning of Quantitative CBF? *American Journal of Neuroradiology* 22: 235-236 (2001).

- [78] Sourbron S., Luypaert R., Van Schuerbeek P., Dujardin, M. Stadnik, T. Osteaux M. Deconvolution of Dynamic Contrast-Enhanced MRI data by Linear Inversion: Choice of the Regularization Parameter. *Magnetic Resonance in Medicine* 52: 209-213 (2004).
- [79] Stewart G.N. Researches on the Circulation Time in Organs and on the Influences which affect it. Parts I-III. *Journal of Physiology* 15: 1-89 (1894).
- [80] Tofts P.S. Modeling Tracer Kinetics in Dynamic Gd-DTPA MR Imaging. *Journal of Magnetic Resonance Imaging* 7: 91-101 (1997).
- [81] Van Osch M.J., Vonken E.J., Bakker C.J., Viergever M.A. Correcting Partial Volume Artifacts of the Arterial Input Function in Quantitative Cerebral Perfusion MRI. *Magnetic Resonance in Medicine* 45: 477-485 (2001).
- [82] Van Osch M.J., Vonken E.J., Wu O., Viergever M.A., van der Grond J., Bakker C.J. Model of the Human Vasculature for Studying the Influence of Contrast Injection Speed on Cerebral Perfusion MRI. *Magnetic Resonance in Medicine* 50: 614-622 (2003).
- [83] Van Osch M.J.P., Vonken E.P.A. , Viergever M.A., Van Der Grond J., Bakker C.J.G. Measuring the Arterial Input Function with Gradient Echo Sequences. *Magnetic Resonance in Medicine* 49: 1067-1076 (2003).
- [84] Vonken E.P.A., Beekman F.J., Bakker C.J.G., Viergever M.A. Maximum Likelihood Estimation of Cerebral Blood Flow in Dynamic Susceptibility Contrast MRI. *Magnetic Resonance in Medicine* 41: 343-350 (1999).
- [85] Willats L., Connelly A., Calamante F. Improved Deconvolution of Perfusion MRI Data in the Presence of Bolus Delay and Dispersion. *Magnetic Resonance in Medicine* 56: 146-156 (2006).
- [86] Wirestam R., Andersson L., Østergaard L., Bolling M., Aunola J.P., Lindgren A., Geijer B., Holtas S., Stahlberg F. Assessment of Regional Cerebral Blood Flow by Dynamic Susceptibility Contrast MRI using Different Deconvolution Techniques. *Magnetic Resonance in Medicine* 43: 691-700 (2000).
- [87] Wirestam R., Stahlberg F. Wavelet-based Noise Reduction for Improved Deconvolution of Time-series Data in Dynamic Susceptibility-Contrast MRI. *MAGMA* 18: 113-118 (2005).
- [88] Wu O., Østergaard L., Weisskoff R.M., Benner T., Rosen B.R., Sorensen A.G. Tracer Arrival Timing-Insensitive Technique for Estimating Flow in MR Perfusion-Weighted Imaging Using Singular Value Decomposition with a Block-Circulant Deconvolution Matrix. *Magnetic Resonance in Medicine* 50: 164-174 (2003).
- [89] Wu O., Østergaard L., Koroshetz W.J., Schwamm L.H., O'Donnell J.O., Schaefer P.W., Rosen P., Weisskoff R.M., Sorensen A.G. Effects of Tracer Arrival Time on Flow Estimates in MR Perfusion-Weighted Imaging. *Magnetic Resonance in Medicine* 50: 856-864 (2003).

- [90] Zanderigo F., Bertoldo A., Pillonetto G., Cosottini M., Cobelli C. Non-linear Stochastic Regularization to Characterize Tissue Residue Function from Bolus-tracking MRI Images. In *Proceedings of ISMRM Workshop on Quantitative Cerebral Perfusion Imaging Using MRI: A Technical Perspective*, Venice, Italy, March 21-23, pp. 77-78 (2004).
- [91] Zanderigo F., Bertoldo A., Pillonetto G., Cobelli C. Nonlinear Stochastic Deconvolution of Bolus-Tracking MRI: Assessment and Comparison on Simulated Data vs other Methods in Presence/Absence of Dispersion. *Proceedings of ISMRM 13<sup>th</sup> Scientific Meeting and Exhibition*, Miami, Florida, USA, 7-13 May (2005).
- [92] Zanderigo F., Bertoldo A., Pillonetto G., Cobelli C. Detection of Dispersion from Bolus-tracking MRI Improves Cerebral Blood Flow Quantification: a Simulation Study. *Proceedings of ISMRM 14<sup>th</sup> Scientific Meeting and Exhibition*, Seattle, Washington, USA, 6-12 May (2006).
- [93] Zanderigo F., Bertoldo A., Cobelli C. A Log-normal dispersion model for parametric deconvolution of DSC-MRI images: assessment on simulated data. *ISMRM 15<sup>th</sup> Scientific Meeting and Exhibition*, Berlin, Germany, 19-25 May (2007).
- [94] Zanderigo F., Bertoldo A., Pillonetto G., Cobelli C. Nonlinear Stochastic Regularization to Characterize Tissue Residue Function in Bolus-Tracking MRI: Assessment and Comparison with SVD, Block-Circulant SVD and Tikhonov *IEEE Transactions on Biomedical Engineering*, in press (2009).
- [95] Zierler K.L. Theoretical Basis of Indicator-Dilution Methods for Measuring Flow and Volume. *Circulation Research* 10: 393-407 (1962).
- [96] Zierler K.L. Equations for Measuring Blood Flow by External Monitoring of Radioisotopes. *Circulation Research* 16: 309-321 (1965).



# List of Figures

2.1	A typical DSC-MRI acquisition protocol. . . . .	6
2.2	The quantification process of DSC-MRI image . . . . .	10
2.3	The effects of the passage of a paramagnetic agent bolus on MR signal. . . . .	11
2.4	A typical tissue concentration time course in presence of tracer recirculation and its gamma-variate fit. . . . .	13
3.1	Residue function in absence or presence of arterial dispersion. . .	17
4.1	Major brain arteries. . . . .	32
4.2	Simulated AIF generation. . . . .	34
4.3	Comparison between the true and the false AIFs. . . . .	34
4.4	Gamma-variate residue function. . . . .	35
4.5	Comparison between the true AIF and the concentration curve of the different tissues. . . . .	35
4.6	Simulated data set realization. . . . .	37
4.7	Hier method results. . . . .	40
4.8	K-means method results. . . . .	40
4.9	SD-map method results. . . . .	41
4.10	Rempp method results. . . . .	41
4.11	Peak method results. . . . .	42
4.12	Best solution results. . . . .	42
4.13	Partial volume in the AIF selection algorithms. . . . .	44
4.14	Distance from the best solution. . . . .	44
4.15	Distance from the true solution. . . . .	44
4.16	AUC of the estimated AIFs. . . . .	45
4.17	CBF, CBV and MTT ratio from the estimated AIFs and non noisy tissue data. . . . .	47
4.18	CBF, CBV and MTT ratio from the estimated AIFs and noisy tissue data. . . . .	49

4.19	Selected AIFs in subject #1 pre surgery. . . . .	55
4.20	Selected AIFs in subject #1 post surgery. . . . .	56
4.21	Selected AIFs in subject #2 pre surgery. . . . .	57
4.22	Selected AIFs in subject #2 post surgery. . . . .	58
4.23	Selected AIFs in subject #3 pre surgery. . . . .	59
4.24	Selected AIFs in subject #3 post surgery. . . . .	60
4.25	Selected AIFs in subject #4 pre surgery. . . . .	61
4.26	Laterality indices in subject #1. . . . .	65
4.27	Laterality indices in subject #2. . . . .	66
4.28	Laterality indices in subject #3. . . . .	67
4.29	Laterality indices in subject #4. . . . .	68
5.1	Distance between the reconstructed $R(t)$ and the true one. . . . .	78
5.2	Examples of reconstructed residue functions. . . . .	79
5.3	Estimated CBF percentage error. . . . .	81
5.4	Method providing the best CBF estimate. . . . .	82
5.5	Comparison between the true CBF and the estimated one. . . . .	83
5.6	CBV maps obtained for subject n°4 before surgery. . . . .	88
5.7	CBV maps obtained for subject n° 6 before surgery. . . . .	90
5.8	CBV maps obtained for subject n° 9 after surgery. . . . .	91
5.9	CBF maps in subject n° 1 before surgery. . . . .	96
5.10	CBF maps in subject n° 1 after surgery. . . . .	96
5.11	CBF maps in subject n° 2 before surgery. . . . .	97
5.12	CBF maps in subject n° 2 after surgery. . . . .	97
5.13	CBF maps in subject n° 3 before surgery. . . . .	98
5.14	CBF maps in subject n° 3 after surgery. . . . .	98
5.15	CBF maps in subject n° 4 before surgery. . . . .	99
5.16	CBF maps in subject n° 5 before surgery. . . . .	99
5.17	CBF maps in subject n° 5 after surgery. . . . .	100
5.18	CBF maps in subject n° 6 before surgery. . . . .	100
5.19	CBF maps in subject n° 6 after surgery. . . . .	101
5.20	CBF maps in subject n° 7 before surgery. . . . .	101
5.21	CBF maps in subject n° 7 after surgery. . . . .	102
5.22	CBF maps in subject n° 8 before surgery. . . . .	102
5.23	CBF maps in subject n° 9 before surgery. . . . .	103
5.24	CBF maps in subject n° 9 after surgery. . . . .	103
5.25	CBF maps in subject n° 10 after surgery. . . . .	104

---

5.26	CBF maps in subject n° 11 before surgery. . . . .	104
5.27	MTT maps in subject n° 1 before surgery. . . . .	109
5.28	MTT maps in subject n° 1 after surgery. . . . .	109
5.29	MTT maps in subject n° 2 before surgery. . . . .	110
5.30	MTT maps in subject n° 2 after surgery. . . . .	110
5.31	MTT maps in subject n° 3 before surgery. . . . .	111
5.32	MTT maps in subject n° 3 after surgery. . . . .	111
5.33	MTT maps in subject n° 4 before surgery. . . . .	112
5.34	MTT maps in subject n° 5 before surgery. . . . .	112
5.35	MTT maps in subject n° 5 after surgery. . . . .	113
5.36	MTT maps in subject n° 6 before surgery. . . . .	113
5.37	MTT maps in subject n° 6 after surgery. . . . .	114
5.38	MTT maps in subject n° 7 before surgery. . . . .	114
5.39	MTT maps in subject n° 7 after surgery. . . . .	115
5.40	MTT maps in subject n° 8 before surgery. . . . .	115
5.41	MTT maps in subject n° 9 before surgery. . . . .	116
5.42	MTT maps in subject n° 9 after surgery. . . . .	116
5.43	MTT maps in subject n° 10 after surgery. . . . .	117
5.44	MTT maps in subject n° 11 before surgery. . . . .	117
5.45	CBF and MTT laterality indices obtained in subject n° 3 before surgery. . . . .	120
5.46	CBF and MTT laterality indices obtained in subject n° 3 after surgery. . . . .	121
5.47	CBF and MTT laterality indices obtained in subject n° 9 before surgery. . . . .	122
5.48	CBF and MTT laterality indices obtained in subject n° 9 after surgery. . . . .	123
6.1	Distance between the DNP residue function and the true one. . . . .	132
6.2	Examples of reconstructed residue functions, without delay. . . . .	133
6.3	Examples of reconstructed residue functions, with a 2 samples delay. . . . .	134
6.4	DNP estimated CBF percentage error at SNR 10. . . . .	135
6.5	Method providing the best CBF estimate. . . . .	136
6.6	Comparison between the estimated CBF and the true one, without delay. . . . .	137
6.7	Comparison between the estimated CBF and the true one, with a 2 samples delay. . . . .	138
6.8	DNP delay estimates. . . . .	139

6.9	DNP CBF maps in subject n° 1 before surgery. . . . .	141
6.10	DNP CBF maps in subject n° 3 before surgery. . . . .	141
6.11	DNP MTT maps in subject n° 1 before surgery. . . . .	141
6.12	DNP MTT maps in subject n° 3 before surgery. . . . .	142

# List of Tables

1	Abbreviation table. . . . .	xi
4.1	AIF simulation set up . . . . .	37
4.2	AIF:tissue simulation parameters . . . . .	37
4.3	False AIF simulation set up . . . . .	38
4.4	Clinical data set social-demographic table. . . . .	52
5.1	AIF simulation set up . . . . .	77
5.2	CBV ratios between the right and the left hemisphere. . . . .	89
5.3	CBF ratios between the right and the left hemisphere before surgery. . . . .	92
5.4	CBF ratios between the right and the left hemisphere after surgery. . . . .	93
5.5	CBF percentage SD in the left and in the right hemisphere before surgery. . . . .	94
5.6	CBF percentage SD in the left and in the right hemisphere after surgery. . . . .	94
5.7	MTT ratios between the right and the left hemisphere before surgery. . . . .	105
5.8	MTT ratios between the right and the left hemisphere after surgery. . . . .	106
5.9	MTT percentage SD before surgery. . . . .	107
5.10	MTT percentage SD after surgery. . . . .	107